HIERARCHICAL MULTISCALE MATERIALS MODELING: CALIBRATION, UNCERTAINTY QUANTIFICATION, AND DECISION SUPPORT

A Dissertation
Presented to
The Academic Faculty

by

Aaron Ellis Tallman

In Partial Fulfillment
of the Requirements for the Degree
Doctor of Philosophy in the
School of Materials Science and Engineering

Georgia Institute of Technology
August 2018

HIERARCHICAL MULTISCALE MATERIALS MODELING: CALIBRATION, UNCERTAINTY QUANTIFICATION, AND DECISION SUPPORT

Approved by:

Dr. David L. McDowell, Advisor
George W. Woodruff School of Mechanical Engineering
Georgia Institute of Technology

Dr. Hamid Garmestani
School of Materials Science and Engineering
Georgia Institute of Technology

Dr. Yan Wang, Co-Advisor
George W. Woodruff School of Mechanical Engineering
Georgia Institute of Technology

Dr. Surya Kalidindi
George W. Woodruff School of Mechanical Engineering
Georgia Institute of Technology

Dr. Laura P. Swiler
Center for Computing Research
Sandia National Laboratories

Date Approved: July 15, 2018

The progress of science lies, essentially, in the evolution of its problems.

-Karl R. Popper

ACKNOWLEDGEMENTS

I would like to begin by thanking my advisor, Dr. David L. McDowell. It is a very rare thing to find people capable of immense vison and exacting quality of work who also generously give their time and energy to lift others to their level. Dr. McDowell is such a person, and it has been my great joy and privilege to have him as my advisor. I am grateful for the patience, wisdom, and sensitivity with which he guided me through this program. I wish to thank him for the example of his leadership, which will remain as a beacon for me in years to come.

I would also like to thank my co-advisor, Dr. Yan Wang, for his plentiful support and mentorship throughout my time in this program. I especially value our numerous discussions which often filled entire whiteboards with diagrams. I also thank him for encouraging me to consider my future with an open mind.

I give thanks also to Dr. Laura Swiler, who has been instrumental in the development of the work of this dissertation. I am grateful for the numerous constructive phone conversations, the important ontological discussions, and for the sincerity of her encouragement in stressful times. I would like to thank Dr. Swiler. along with Dr. Surya R. Kalidindi and Dr. Hamid Garmestani, for joining my reading committee and engaging with the content of my dissertation.

During my time at Georgia Tech, other individuals contributed meaningfully in mentoring me. I would like to thank Dr. Laurent Capolungo for being on the reading committee for my thesis proposal and for the coffee-fueled conversations we had

thereafter. The insights from those talks led to my first journal article publication. I would also like to thank Dr. Juan Rubio for a separate coffee-fueled conversation on Bayesian Inference. I would like to thank Michael Swanson for countless discussions which, over time, instilled in me a respect for the importance of ethics to the application of science.

Very special thanks are due to Dr. Jeffrey Donnell, for fostering my technical communication and my confidence, Sukanya Sharma, for being generous beyond measure with her time and expertise to facilitate the experimental portions of this work, and to the Georgia Tech Invention Studio, whose managers are some of the most generous and helpful people to be found on this campus.

The inhabitants of MRDC 3338 past were, to me, mentors and colleagues who contributed to my sense of belonging in this program. I wish to thank Dr. Anirban Patra, Dr. Matthew Priddy, Dr. Ashley Goulding, and Dr. Kyle Brindley, who each offered me unique and irreplaceable advice and help at different points throughout this process. I would also like to thank Paul Kern, Joel Blumer, Dr. Shuozhi Xu, Ben Smith, Conor Hennessey, Dr. Brett Ellis, and Dr. Shreevant Tiwari for their friendship and camaraderie.

The inhabitants of MRDC 3338, future, include my collaborators and friends. I believe the future of the office is a bright and verdant one. To Krzysztof Stopka, Theodore Zirkle, and Gary Whelan, I give my humble thanks for being more reliable, more engaged, and more supportive as collaborators than students have any business being. To them and to my other friends, Adrienne Muth, Luke Costello, Alex Semilov,

Kevin Chu, Dr. Tang Gu, and Dr. Dengke Chen, I give my thanks and my wish that this place continues to be as much a home to them as they have made it for me.

The Atlanta swing dance community has been a social scene, a creative outlet, and a source of some true friends. For the support, energy, and inspiration I have received from these remarkably earnest beings, I offer my thanks.

I dearly thank my sister Claire, for guiding me throughout my life (despite my willful nature) to respect the responsibility I have to myself and to the people near to me. In the same vein I thank Taylor, for being a shining example of what it is to honor those responsibilities.

Ali, who has entered my life in this most unusual of times, is deserving of uncountably many thanks. I wish to give her thanks for her crucial labor in keeping my living conditions from descending into utter disarray, for the practical help she provided on communicating clearly in my writing, and for the inspirational confidence she has in our trajectory together. As much as mere words can convey, I use them to give her my thanks.

My parents, to whom I owe everything, I wish to thank for their foundational support. As each new challenge tested my courage, it was their love, guidance, and support that let me re-shoulder my doubts and burdens and continue. They raised me well for this task. My mother Beth fostered in me courageous thinking--that every human structure can be rebuilt to be better. My father Ellis has given me a lifetime's example of honest thinking and honest action. I also thank my father for sharing with me the

perspective which comes with knowing that others have walked this path before, though it is a new one to me. For these gifts as well, I give them my gratitude.

This work was supported in part with funding granted under the DOE NEUP (NEAMS-3 CFP-12-3507: Uncertainty quantification and management for multiscale nuclear materials modeling). Continued work in this area was completed with funding granted under Sandia's Laboratory Directed Research and Development Academic Alliance program. Sandia National Laboratories is a multimission laboratory managed and operated by National Technology and Engineering Solutions of Sandia LLC, a wholly owned subsidiary of Honeywell International Inc. for the U.S. Department of Energy's National Nuclear Security Administration under contract DE-NA0003525.

TABLE OF CONTENTS

LIST OF TABLES

LIST OF FIGURES

LIST OF SYMBOLS

%MRE	Percent mean relative error.
2D	Two-dimensional.
3D	Three-dimensional.
ALO	Alumina.
AM	Additively manufactured.
ASTM	American Society for Testing and Materials.
BCC	Body-centered cubic.
BCJ	Bammann Chiesa Johnson.
BCJ-lv	Bammann Chiesa Johnson with local variation.
BU	Bottom-up.
C260	Cartridge brass.
CALPHAD	Calculation of phase diagrams.
CCD	Charge-coupled device.
CG	Coarse-grained
CLF	Constrained likelihood function.
CP	Crystal plasticity.
DDD	Discrete dislocation dynamics.
DI	De-ionized.
DNS	Direct numerical simulation.
DoE	Design of experiments
EBSD	Electron backscatter diffraction.
ECDF	Empirical cumulative distribution function.
FCC	Face-centered cubic.

FEM	Finite element method.
GP	Gaussian process.
GSH	Generalized spherical harmonic.
HCP	Hexagonal close-packed.
HMM	Hierarchical multiscale model
HPC	High performance computing.
ICME	Integrated computational materials engineering.
ISV	Internal state variable.
KDE	Kernel density estimate.
kMC	Kinetic Monte Carlo.
K-S	Kolmogorov-Smirnov.
LF	Likelihood function.
LOOCV	Leave-one-out cross validation.
MCMC	Markov chain Monte Carlo.
MD	Molecular dynamics.
MKS	Materials knowledge system.
ML	Maximum likelihood.
NEB	Nudged elastic band.
ODF	Orientation distribution function.
OFHC	Oxygen-free high thermal conductivity.
PC	Principal component.
PCA	Principal component analysis.
PCE	Polynomial chaos expansion.
PDF	Probability density function.
QoI	Quantity of interest.

RVE	Representative volume element.
SOR	Second order regression.
SSE	Sum of squared errors.
SVE	Statistical volume element.
SVENN	Statistical volume element nearest neighbor.
TD	Top-down
TDBU	Top-down bottom-up
Ti64	Ti-6Al-4V.
UMAT	User material subroutine.
UQ	Uncertainty quantification.
α-Ti	Hcp phase of Ti
$\forall$	For all.
$\in$	Element of.
$\otimes$	Tensor product.
$\prod$	Product.
$\langle\ \rangle$	Contents replaced by zero if less than zero.
$\mathbf{A}$	Matrix of regression data.
a	Distance moved by dislocation in one activation step.
a_0	Lattice parameter.
a_1^T, a_2^T, a_3^T	Non-Schmid coefficients.
A_{dir}	Direct back stress modulus.
A_{dyn}	Dynamic recovery coefficient of back stress.
A^α	Back stress of slip system α.

$\mathbf{A}^{\alpha\zeta}$	Matrix of slip system dislocation interaction coefficients.
b	Burgers vector magnitude.
$\mathbf{c}$	Vector of coefficients.
$\mathbf{C}$	GSH coefficients.
C_{ij}	Elastic constants of the elastic stiffness tensor.
C_l^{mn}	GSH coefficient.
d	Equivalent sphere diameter of grains.
d	Mean slip distance.
$\mathbf{D}^{in}$	Inelastic portion of the unrotated stretching tensor.
$D_{N,M}$	K-S statistic between first and second samples.
D^{α}	Drag stress of slip system α.
E	Young's modulus.
$\mathrm{E}[\ ]$	Expected value.
e_1, e_2, e_3	Euclidean mapping space coordinates.
E_{11}	Uniaxial elastic stiffness modulus.
f	BCJ rate sensitivity parameter.
f	Predicted response of a regression.
$\mathbf{F}^{e}$	Elastic portion of the deformation gradient.
f_i	Surrogate model of ith datum.
$\mathbf{F}^{in}$	Inelastic portion of the deformation gradient.
G	Shear modulus.
g_{dir}	Direct drag stress modulus.
g_{dyn}	Dynamic recovery coefficient of drag stress.

g_j	The jth orientation included in the texture.
g^{α}	Drag stress of slip system α.
H	BCJ direct isotropic hardening coefficient.
H	Stress dependent activation energy for unit dislocation slip.
h	BCJ direct kinematic hardening coefficient.
h	Scale hyperparameter.
h	Direct hardening coefficient of back stress.
H_0	Activation energy for unit dislocation slip at zero effective stress.
h_D	Dynamic recovery coefficient of back stress.
J	Total number of orientations in texture.
J_2	The second invariant of the deviatoric stress tensor.
k	Boltzmann constant.
k_{cs}	Material constant of mobile dislocation cross-slip.
k_{dyn}	Material constant of dynamic recovery of immobile dislocations.
k_{mul}	Material constant of mobile dislocation multiplication.
l	Length hyperparameter.
l	Lateral extent of kinks at the saddle point state.
l	Degree of GSH function.
$\tilde{L}$	GSH coefficient degree truncation.
$\mathbf{L}^{in}$	Inelastic portion of the velocity gradient.
m	Strain rate sensitivity exponent.
m	Mean of ensemble of responses.

m	Number of regression coefficients.
M	Strain rate sensitivity exponent.
m_i	Counting multiplier of ith grain.
$\mathbf{m}_0^\alpha$	Unit slip direction vector.
$N\left(\mu,\sigma^2\right)$	Normal distribution of mean μ and variance σ^2.
N_0	Number of ensembles in initial batch.
N_1	Number of ensembles in subsequent iterations.
N_{data}	Number of data.
N_{iter}	Number of iterative data selection steps.
$\mathbf{n}_{ns}^\alpha$	Unit vector normal to the 'non-slip' plane.
N_{runs}	Total number of CP model runs.
N_s	Number of slip systems.
n_s	Number of queries.
N_{SVE}	Number of SVEs in an ensemble.
n_v	Number of variables
$\mathbf{n}_0^\alpha$	Unit slip plane normal direction vector.
$Obj(\ )$	Objective function.
p	Shape factor, profiling parameter.
$\mathbf{p}$	Uniform density mapping parameters.
q	Shape factor, profiling parameter.
q_ρ	Dislocation barrier strength.
R	BCJ isotropic hardening ISV.

$\mathbb{R}$	The real numbers.
$\tilde{R}$	Number of included PCs.
R^2	Coeffiecient of determination.
R_c	Annihilation capture radius of dislocations.
R_d	BCJ dynamic recovery coefficient for isotropic hardening.
r_d	BCJ dynamic recovery coefficient for kinematic hardening.
R_s	BCJ static recovery coefficient for isotropic hardening.
r_s	BCJ static recovery coefficient for kinematic hardening.
s_a^α	Athermal slip resistance of slip system α.
s_t^α	Thermal slip resistance of slip system α.
s_{t0}	Thermal slip resistance at 0K (Peierls stress).
T	Temperature.
T_l^{mn}	GSH function.
u	Connection cost exponent.
V	BCJ rate sensitivity parameter.
V_a	Activation volume.
V_i	Volume of ith grain.
$\mathbf{x}$	Alignment variables.
Y	BCJ initial yield strength parameter.
Y^E	Experimental response.
Y^M	Model response.
α	Index for slip systems.

$\boldsymbol{\alpha}$	Kinematic hardening tensor.
α	Noise hyperparameter.
β_ρ	Dislocation trapping constant.
$\dot{\gamma}_0$	Pre-exponential factor, reference shearing rate.
$\dot{\gamma}^\alpha$	Shearing rate of crystallographic slip system α.
δ	Discrepancy, bias.
ΔF_g	Activation energy barrier to dislocation glide.
δ_{ij}	Kronecker delta.
ε	Measurement error.
ε	Strain.
$\varepsilon_{0,i}$	Decay constant.
ε_{33}	Axial strain.
ε_{eff}^{i}	Effective inelastic strain.
$\varepsilon_{\text{sur},i}$	Surrogate model error term.
$\boldsymbol{\theta}$	Calibration parameters.
$\hat{\boldsymbol{\theta}}_{\text{BU}}^{ref}$	Bottom-up reference estimates of calibration parameters θ.
$\hat{\boldsymbol{\theta}}_{\text{TD}}$	ML estimate of calibration parameters based on TD data.
$\hat{\boldsymbol{\theta}}_{\text{TD}}^{ref}$	Top-down reference estimates of calibration parameters θ.
$\overline{\boldsymbol{\theta}}$	Vector of regression terms.
$\boldsymbol{\theta}_{\max}$	Upper bounds of admissible parameter ranges.
$\boldsymbol{\theta}_{\min}$	Lower bounds of admissible parameter ranges.

κ_s^α	Softening term of threshold stress of slip system α.
κ_y	Hall-Petch slope.
κ^α	Threshold stress of slip system α.
λ^α	Mean free path of dislocation glide.
μ	Mean.
μ	Softening rate coefficient.
ν	Poisson's ratio.
υ_D	Debye frequency.
ρ	Dislocation density.
ρ_I	Immobile dislocation density.
ρ_M	Mobile dislocation density.
$\boldsymbol{\sigma}$	Cauchy stress.
σ	Stress.
σ	Standard deviation.
$\hat{\sigma}^2$	Unbiased predictor of population variance.
σ_{33}	Axial stress.
σ_e^2	Variance of errors.
$\sigma_{\text{exp},i}^2$	Expected variance of ith datum.
σ_{ns}^α	Contribution of non-Schmid stresses on slip system α.
σ_p^2	Variance of the penalty.
σ_Y	Yield strength.
$\sigma_{Y,0.2\%}$	0.2% offset yield strength.

σ_{θ}^{2}	Variance of parameter estimate, parameter uncertainty estimate.
τ	Resolved shear stress.
τ^{*}	Activation stress for dislocation cross-slip.
τ_{CRSS}^{α}	Critical resolved shear stress of slip system α.
τ_{eff}^{α}	Effective shear stress of slip system α.f
τf	Driving stress for dislocation glide.
φ1,ϕ,φ2	Euler angles.
χ	Misorientation angle.
χα	Back stress of slip system α.

SUMMARY

Computational material models help establish structure-property relationships by simulating properties, and are most effective when physically-based. The length and time scales of each simulation are constrained both by model type and computing power. Significant uncertainty can arise when models attempt to bridge across length and time scales, especially when using different model constructs. Hierarchical multiscale modeling (HMM) links models at different scales by informing parameters and form of higher scale models based on lower scale simulations, which can reduce uncertainty. The combination of diverse information sources in HMMs requires rigorous approaches to evaluate uncertainty propagation. In the pursuit of improved methods for empirical testing and development of model hierarchies, four approaches in which information is coordinated amongst multiple models are presented.

(1) In a reconciled top-down and bottom-up approach, a likelihood-based model calibration method is proposed, and bcc Fe crystal plasticity (CP) is used to demonstrate the compatibility of information pathways. (2) A statistical volume element (SVE) ensemble-based homogenization scheme of two models of cartridge brass polycrystal plasticity is used to inform a Bammann-Chiesa-Johnson macroplasticity model with a local variation in parameters. The effects of SVE size and model form on the performance of the homogenization in bridging microstructure variability to macroscale uncertainty are explored. (3) A multiscale model development framework is outlined for the reduced order modeling of mesoscale variability in cartridge brass. The variability in SVE simulations is included with the results of a series of spherical microindentation

experiments in a multiscale data collection. An initial study of the modeling involved in connecting the two length scales is performed. (4) In a CP-finite element method (FEM) based Materials Knowledge System model of α-Ti, the influence of texture is considered. Texture is parameterized using generalized spherical harmonics. The CP-FEM model is used with polycrystalline SVE-ensembles to calibrate the MKS model across different textures, sampled according to an uncertainty reduction criterion.

Results of the work suggest that data collection is an especially critical step in the formulation and deployment of hierarchical multiscale models. The use of bottom-up information in calibrating a multiscale model is shown to be susceptible to bias. A multiscale approach to coarse-grained simulations of polycrystals at the mesoscale is proposed. An approach to automating the data collection for a reduced-order model of microstructure sensitive response is shown to be competitive with manual data selection, prior to full optimization of the automated approach.

CHAPTER 1. INTRODUCTION

Scientific models infer knowledge from measurements. This relationship often limits insight to domains in which data can be readily gathered. Gathering data is a two-part problem. First, measurements must be obtained, often through demanding experimental procedures. Second, data must be selected which is relevant to the identified problem. In the multiscale modeling of material deformation, this second step becomes an increasingly complex consideration. With respect to the demands of this emerging challenge, the theme of this dissertation is data selection in multiscale materials science models of deformation. The following context is offered to motivate this theme.

1.1. Motivation

The frontier of human knowledge is continually changing. Scientists uncover knowledge by improving descriptions of reality. Technologists and engineers advance human knowledge by using knowledge to find improved solutions to the problems facing humanity. Materials scientists and engineers are tasked with both of these missions. For a materials scientist, a correct description is only half of the goal. In the work which follows, the fidelity and the usefulness of a solution are often considered jointly.

These attributes can be defined for this introduction. Fidelity refers to the extent to which a description of a given process reflects the most complete description of that process available. Usefulness indicates the extent to which the description can be used to inform decision-making. There are many types of decisions (e.g. materials design, research funding allocation, etc.) and each decision is accompanied by unique barriers to

the application of scientific knowledge. In materials science, a compromise between fidelity and usefulness is often made in the formulation of new descriptions of mechanisms.

Materials science has uncovered a diversity in the physical mechanisms which give rise to solid mechanics. These mechanisms often influence the properties of materials at length scales far removed from the length scale of their physical description. There exists ongoing research to refine the details of these individual mechanisms. The technology which is built on this knowledge must balance the influence of every relevant mechanism. The challenge of finding this balance grows more difficult as more materials knowledge is discovered.

Computational models of materials exemplify a tool built out of materials science knowledge. A simulation of a material can be beneficial when demanding industrial applications cause the material to fail. By using a simulation to investigate the failure, design variables can be explored systematically to find a solution, minimizing the expense of experimental trials. As computation has become increasingly capable, computational modeling research has produced increasingly nuanced descriptions of the deformation of materials. The growing category of microstructure sensitive models of material deformation demonstrate this trend. As model complexity increases, some approaches have emerged which connect multiple models across length scales in a multiscale treatment.

Multiscale modeling of materials is an approach to describing the multiscale interactions which are a hallmark of materials under deformation. In a multiscale

modeling approach, multiple material models are usually connected across length and time scales in either a concurrent or a hierarchical arrangement. In concurrent frameworks, the models' separate spatial domains are joined by a forced boundary solution. In a hierarchical framework, the models are joined through the values given to a parameter set which is used as a connection between models. While both formulations have been used in the field, the work of this dissertation addresses the hierarchical multiscale approach.

In 2008, integrated computational materials engineering (ICME) was designated as a major research objective in materials science (National Research Council, 2008). Numerous benefits were listed to motivate the pursuit of the integration of computational materials science tools into a holistic framework and engineering design in general. The development of connections between models was mentioned as a scientific and technological challenge among many others forecast in the report. The exploration of new model-model connection strategies is taken up in this dissertation in support of the larger goals of ICME.

Tools and companies which exemplify the goals of ICME have and continue to emerge. CALPHAD (which stands for calculation of phase diagrams) is a methodology which has given rise to many software tools which are important to ICME efforts (Spencer, 2008). Thermo-Calc Software is a company whose CALPHAD-based tools are used in research and in applications (Andersson et al., 2002).The work of QuesTek® Innovations LLC in computational materials design is innovative, and formalized the process structure property map as a means of arriving at a holistic consideration of the

mechanisms affecting a material (Kuehmann and Olson, 2009). No well-known commercial solution yet exists for the multiscale modeling of material deformation.

The development and improvement process of a model is specific to that model's intended application. Models are typically focused on either providing a scientific description of a phenomenon or extracting the relationships relevant to practical decision making. For the current discussion, these categories will be referred to as scientific models and design models. Models require calibration to make predictions. To improve those predictions a researcher may improve the calibration procedure, reduce the uncertainty of the model, or bring additional decision-relevant information to the decision maker, in the case of a design model. Each of these options is explored within this dissertation.

Multiscale modeling provides challenges to researchers in addition to the challenges of creating a model at a single scale. The most dramatic example of the issues facing multiscale modelers is taken from physics which govern the largest and smallest of scales. The cosmological constant problem is a reference to the 120 orders of magnitude difference between the quantum field predictions of vacuum energy density and the value which is consistent with astronomical observations (Adler et al., 1995). This stark disagreement has yet to be resolved, despite the fame of the problem. Additionally, the theories used in each approach have not been falsified by this predictive error. The length scales of concern to materials modelers are less dramatic in their range. Nevertheless, the multiscale modeling of solid mechanics presents the same epistemological problem: if two models from different scales are in disagreement, how can they be used appropriately in combination?

The specific applications of multiscale modeling of materials deformation include problems of data selection. In order to calibrate a multiscale model, data from many different sources might be considered. Guidance regarding the data appropriate for a given application has not yet been established for multiscale models. Broadly, the following chapters present specific examples of problems in multiscale modeling of the deformation of materials and the innovations in data selection approaches which inform these multiscale models.

1.2. Formal Objectives

In the spirit of ICME and in the pursuit of improved multiscale-specific methods of directing model improvement, the following objectives in the multiscale modeling of material deformation are addressed by this dissertation:

1. Develop a method for including information from multiple length scales in the calibration of a hierarchical multiscale model and demonstrate that method with a multiscale model of bcc Fe crystal plasticity
2. Explore reduced order modeling of microstructure sensitive response of cartridge brass to stress for the effects of model form and SVE size on the fidelity of mesoscale variability predictions
3. Investigate the feasibility of gathering data at multiple length scales for use in the development of a multiscale reduced order model of material deformation
4. Formulate a parameterized data selection method and apply it to a data-driven tool for homogenization of material response

1.3. Organization of Dissertation

The dissertation is organized into Chapters as follows. Chapter 2 provides a comprehensive literature review of the material related to the content of multiple chapters of work. Chapter 2 is further divided into sections which correspond to the fields from which the collected references were obtained.

The objectives of the dissertation are approached in the four chapters which follow. Chapter 3 addresses the reconciled top-down and bottom-up multiscale calibration of bcc Fe crystal plasticity. Chapter 4 contains work on the model form and SVE size effects of reduced order modeling of mesoscale variability in polycrystalline cartridge brass. Chapter 5 is directed towards the development of microindentation as a source of data for calibrating models of mesoscale variability. Chapter 6 documents the development of a systematic data collection procedure for the homogenization of texture effects in the deformation response of α-Ti. These chapters are internally structured with introductions, literature backgrounds, methodologies, and discussions. These case studies are organized in this manner to maintain consistency with journal articles that are or will be based on their content.

The conclusions and recommendations of the dissertation in general are collected in Chapter 7. As opposed to the discussions of the previous chapters, this discussion is targeted at the common themes which emerge from the dissertation.

CHAPTER 2. BACKGROUND - MULTISCALE METAL PLASTICITY MODELING

This reviews relevant background material. It is divided into sections to organize the content, as it spans many disciplines. These sections include plasticity models, microstructure, multiscale modeling, and uncertainty quantification. The topics are introduced and given context. Connections between sections are discussed.

2.1. Plasticity Models

The deformation of metals is complex and of widespread importance. Metal plasticity is a loading-path and history dependent phenomenon, and it occurs by mechanisms that exert themselves at a variety of length and time scales. A variety of constitutive models have been developed to make useful predictions at various levels of resolution and fidelity (Adams et al., 1989; Bammann, 1984; Barlat et al., 1991; Clayton et al., 2004; Clayton and McDowell, 2003; Edelman and Drucker, 1951; McDowell, 2010, 2008). The wide usage of metals gives rise to diversity in plasticity modeling needs, and many types of models are in widespread use. A discussion of the development of plasticity modeling is useful to navigate the different types of models which are featured in this dissertation. In addition, clarifying examples will be included.

Modern simulations of metal plasticity depend on certain mathematical foundations. In general, in continuum models a metal is simulated as a continuous deformable solid (Khan and Huang, 1995; Malvern, 1969). Continuum mechanics is used to establish a phenomenological framework for describing the deformation of materials.

The finite element method (FEM) (Reddy, 1993) allows numerical methods to be used to approximate analytical solutions for material response. With continuum descriptions, material deformation models such as plasticity and elasticity can be expressed in reproducible and comparable terms. By using FEM analysis, the predictions of these models can be compared to experiments conducted on laboratory specimens. These mathematical frameworks are important to the advancement of plasticity models.

Internal state variable (ISV) models of plasticity depart from classical thermodynamics (Horstemeyer and Bammann, 2010; McDowell, 2005). In classical formulations, the stress response of a deformed body is calculated from observable state variables. By including "hidden" ISVs, history dependence along non-equilibrium trajectories can be included in plasticity models. Numerous models which account for the accumulation of damage during deformation have been developed (Clayton and McDowell, 2004, 2003; Ghosh et al., 2001; Horstemeyer et al., 2000) using ISVs and evolution equations to embed models of damage within a phenomenological framework of material deformation kinematics.

Distinct differences exist between two popular categories of plasticity models: crystal plasticity (CP), and J2. In these models, tensor forms of stress and strain are related. As a displacement or force is applied to a simulated specimen, a mathematically defined relationship is used to calculate the resulting force or displacement, respectively. These relationships which constitute the simulation of material behavior are referred to as constitutive equations (Chaboche and Rousselier, 1983; Kothari and Anand, 1998; McDowell, 1985; Roters et al., 2010; Weber and Anand, 1990). Crystal plasticity is used to relate crystalline structure to the deformation kinematics of a material (Alharbi and

Kalidindi, 2015; Asaro, 1983; Buchheit et al., 2005; Patra and McDowell, 2012; Shahba and Ghosh, 2016). Crystal plasticity typically attributes plastic deformation to the glide of dislocations through the crystal lattice via constitutive equations. Notably, dislocations are not resolved discretely and are only sometimes included with ISV representations of local dislocation density (Arsenlis et al., 2004; Patra and McDowell, 2012). Engineering in practice often relies on continuum J2 plasticity and other "macroscopic" plasticity models (Bammann, 1984, p. 2; Barlat et al., 1991; Bassani, 1977). These models are much simpler to calibrate and use than CP. They are unable to predict the properties of related microstructures, however. The two models give an example of the trade-off between accuracy (J2 models) and predictive quality (CP models) which is frequently encountered in simulation.

CP models have been extended to include constitutive laws that propose to address physical mechanisms (Narayanan et al., 2014). In some atomistic simulations, dislocation movement is examined (Gordon et al., 2011; Gröger et al., 2008a), and the results of these simulations can be used to inform crystal plasticity models (Gröger et al., 2008b; Narayanan et al., 2014). These models build on the work of Kocks and others (Kocks, 1976) on constitutive relations which describe thermally activated migration of dislocations. Although constitutive laws allow for CP models to have increased fidelity at smaller length scales, there are limits to this refinement.

Material models involve distinct length and time scales. Models are selected according to application, based on the length scale of interest. Categorical length scales have emerged which reflect the most useful ranges of specific modeling approaches. These scales, as they will be referred to here on, are shown on a line in Figure 2.1. The

introduction of these length scales motivates multiscale methods, which are a central focus of this dissertation.

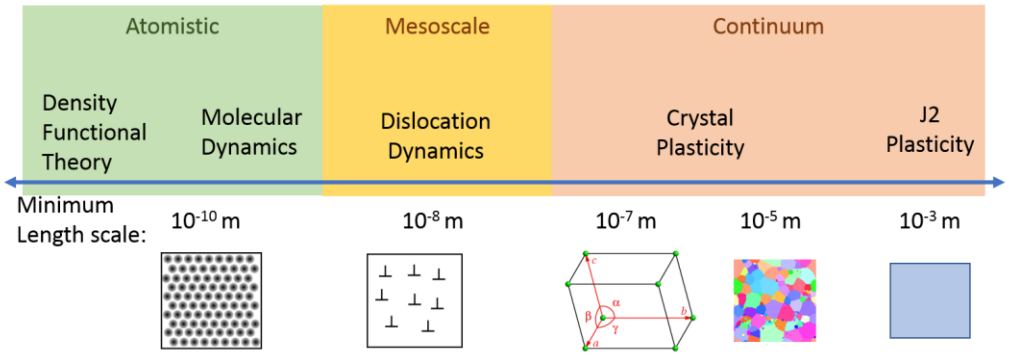

Figure 2.1. A depiction of the categorical length scales of metal plasticity modeling and simulation.

CP and macroplasticity are continuum models. Crystal plasticity models (Patra et al., 2014; Qin and Bassani, 1992; V. Vitek et al., 2004) and dislocation dynamics models (Li et al., 2014) have been used to capture the behavior of individual grains of a metal, which can measure from hundreds of nm to cm in size, although typical simulations are in μm. The time-scale of single crystal plasticity simulations is typically measured in s. Polycrystalline volumes are modeled with CP (or approximations) as well (Benedetti and Barbe, 2013; Buchheit et al., 2005; Paulson et al., 2017), with simulation sizes in the hundreds of μm to mm and time scales ranging to hundreds of s. Macroscopic elasto-viscoplasticity models (Bammann, 1984; Barlat et al., 1991; Bishop et al., 2015) can be used to simulate large volumes of material, from mm to m in size and in times from s to days or years.

Atomistic models are used to resolve mechanisms at much higher fidelity and resolution than is feasible with continuum models. Molecular dynamics (MD) models

(Narayanan et al., 2014; V Vitek et al., 2004) are fully discrete particle models and are used to track the motion of individual atoms in a crystal lattice over times measured in ps (10^{-12} s) and for volumes measured in nm. These simulations use approximations of the interatomic potential between atoms.

Mesoscale models are neither fully discrete nor continuous, and fall in-between the atomistic scale and the continuum scale. Discrete dislocation dynamics is a prominent example of a mesoscale model. In DDD, the dislocation line is the basis of the simulation. Dislocations are considered as discrete entities embedded within a continuum lattice (Arsenlis et al., 2012, 2004; Sobie et al., 2015). DDD can be used to study how dislocations form junctions (Capolungo, 2011), bypass obstacles which contribute to hardening (Sobie et al., 2015), and to model dislocation patterns as large as persistent slip bands (Amodeo and Ghoniem, 1990). Kinetic Monte Carlo (kMC) models are also used in the mesoscale. KMC addresses the complexity of dynamic kinematics at the mesoscale by reducing atomistic interactions to discrete states and the mechanisms by which those states are traversed by the simulated material (Plimpton et al., 2009; Voter, 2007). KMC can model discrete particles over increased time periods (~s) and thus is often used to describe the effects of radiation on materials (Domain et al., 2004; Monasterio et al., 2007). Mesoscale models address various problems which atomistic and continuum models cannot address efficiently.

The physical basis of each of these scale-specific models is important to consider when selecting a model. Atomistic models are defined using approximate interatomic potentials. These potentials are limited in their ability to replicate the range of defect structures and mechanisms at higher relevant scales which are predicted and observed in

a material. Often, these potentials are optimized for a specific application, such as the elastic moduli, vacancy formation, or surface energy. DDD models often do not resolve partial dislocations and atomic scale reactions at dislocation cores. CP models make predictions based on bulk material properties and largely neglect the details and influence of grain boundaries. In nanocrystalline materials, this limitation has an exaggerated effect on predictions. Macroplasticity models are unable to track the rotations of grains. This list of considerations is not exhaustive. As the length/time scales are traversed, the evolving structure of a material has various cumulative effects on predictions of material response, which must be considered in addition to the choice of a physical or phenomenological model.

2.2. Microstructure

Material microstructure has profound effects on the observed plasticity and other responses or properties of a material (McDowell et al., 2011; Paulson et al., 2017; van der Sluis et al., 2000). The characterization of microstructure has been of critical importance to the development of microstructure sensitive material models (Adams et al., 2001). Much work on the digital reconstruction of microstructures (Bostanabad et al., 2016; Chen et al., 2014; Fullwood et al., 2008) has employed high fidelity data for certain material systems. Direct numerical simulation (DNS) approaches have made use of this high fidelity information in predicting properties. In any modeling paradigm, there is a trade-off between fidelity and computational efficiency. As a result, much of the microstructure coupled data incorporated in materials models is of a statistical nature. In some cases, microstructures have been analyzed to extract the features most critical to the prediction of properties, to diminish the quantity of data needed as input (Acharjee and

Zabaras, 2003). This approach requires the user to specify criteria by which the data reduction is performed. In this section, research on microstructure representation is reviewed. Discussion is aimed at how uncertainty quantification and multiscale methods have been employed in using this information.

In crystal plasticity modeling, the quantifiable representation of microstructure is integral to reliable simulations across a material system. Some macroscopic plasticity models are informed by microstructure as well (Adams et al., 1989; Barlat et al., 2005; Yin et al., 2008). These models depend on the representation of microstructure to make predictions of properties. This work will include investigations of multiple approaches to microstructure-sensitive modeling. Some key aspects of microstructure representation are highlighted here.

Direct numerical simulation of microstructure is typically computationally intensive (Bishop et al., 2015; Kanit et al., 2003). It is an important approach, and is often used as a basis for comparison for new statistical approaches. Despite the common practice of using DNS as a ground truth during the development of more efficient methods, non-negligible discrepancy exists between CP models and the observed behavior of the materials they simulate. Chapter 3 investigates the limitations of accuracy in a single crystal application of a CP model. Chapter 4 employs DNS in comparison with statistical homogenization methods.

Microstructure can be represented statistically, and there exist numerous approaches to do so. Two-point and N-point correlation statistics can be used to recast observed arrangements of phases and misorientations of grain boundaries into a statistical

summary (Adams et al., 1989; Chen et al., 2014; Fullwood et al., 2008; Gokhale et al., 2005; Paulson et al., 2017). These statistics can be used to instantiate microstructures which are indistinguishable from a sample of the original observations (Chen et al., 2014; Fullwood et al., 2008). Two-point correlation statistics can be used to verify the representation of a material in a simulated volume (McDowell et al., 2011; Niezgoda et al., 2010). Computer vision can be used to identify microstructure images which contain dendritic formations (Chowdhury et al., 2016). Machine learning (Sundararaghavan and Zabaras, 2005) can be used to predictively determine a 3D reconstruction from limited statistical microstructure information from 2D images. Software such as Dream3D (Groeber and Jackson, 2014) has been developed to accelerate the reconstruction and instantiation of microstructure, and is used in Chapters 4, 5, and 6.

Texture approximation methods are useful in microstructure-sensitive modeling. Texture refers to the distribution of crystallographic orientations of grains and phases within a microstructure. Texture can be approximated by using generalized spherical harmonic (GSH) functions (Bunge, 2013) to transform a collection of orientations into a list of GSH coefficients. The GSH functions are an infinite series of orthogonal functions defined across orientation space in terms of Euler angles. By using a finite truncation of the infinite series of GSH functions, an orientation distribution function can be approximated to a tunable level of precision. Other methods exist for describing textures parametrically, such as Rodrigues orientation space (Kumar and Dawson, 2000; Morawiec and Field, 1996). Work in Chapter 6 will use GSH functions to approximate texture with a finite set of coefficients.

The impact of microstructure on material properties is scale-dependent. Different simulations focus on different length and time scales, and hence, different representations of microstructure. In some approaches, the description of local variations in material response to deformation is emphasized over high fidelity texture definition (Ostoja-Starzewski, 2006; Qidwai et al., 2012; Yin et al., 2008). The microstructure of a material may have a homogeneous texture, but smaller subvolumes of that material will exhibit deviations from that texture due to the finite sampling of grain orientations within a finite volume. In some applications, the variation in material response that results at these length scales is of interest. In DNS approaches (Bishop et al., 2015), these deformation response variations amount to uncertainties affecting macroscopic design. In the structure-property relations modeling of the materials knowledge system (Wheeler et al., 2014), relationships are extracted by correlating variations in localized response to deformation with the statistical descriptors of microstructure that accompany those responses. The work in Chapters 4 and 5 will focus on capturing localized variations in response to an applied deformation.

The use of models which are explicitly microstructure-sensitive in informing a higher length scale homogeneous model is referred to as homogenization. In classical homogenization approaches, a representative volume element (RVE) is used to determine the homogeneous properties of a material with a defined microstructure (van der Sluis et al., 2000). An RVE is large enough such that larger samples of the same material will predict the same response or properties. In some cases, the RVE approach is not appropriate because the statistical samples of volume are too large to simulate directly. These cases often require the material simulation volume to be smaller than the

characteristic length of the RVE. In some of these cases, an ensemble of statistical volume elements (SVE) is used (Yin et al., 2008) in place of an RVE. Smaller than an RVE, an SVE is only large enough to include lengths of all pertinent interactions. A single SVE is not representative of a microstructure, rather, it provides a statistical sample of that microstructure. In order to provide a statistical sample of the microstructure, an SVE must be at least large enough to contain the dominant correlation lengths of the microstructure. When this size requirement is met, as the number of SVEs increases in an ensemble, the statistics of the ensemble tend toward those of the microstructure.

A typical homogenization framework includes a crystal plasticity model, a homogenization scheme, and a macroplasticity model (Geers et al., 2010). These components fit the template of a hierarchical multiscale model (HMM): two distinct scales of models and a linking method. The work in this dissertation will include homogenization within investigations of HMMs in plasticity.

2.3. Multiscale Modeling

Multiscale modeling uses couplings of models, each of which describe problems at distinct length scales. Problems that necessitate multiscale modeling have mechanisms and processes occurring at distinct scales. These problems have dependence on both local and global conditions. Hydrological models have presented examples of advanced multiscale methodologies (Brunsell, 2010; Gupta et al., 1998; Khu et al., 2008). In hydrological modeling, local conditions and global conditions affect expected outcomes with complex interactions. Likewise, the inelastic deformation of metals depends on both

local structures and the collective behavior over a large volume of material. A successful multiscale model replicates observed phenomena at both local and global scales and captures the interactions between them. This section summarizes the research on multiscale modeling methods in metal plasticity.

Multiscale modeling of materials is increasingly commonplace, and diverse approaches have been explored (Chernatynskiy et al., 2013; McDowell, 2010). These approaches can be broadly classified as concurrent methods and hierarchical methods. Concurrent methods based on domain decomposition divide the modeling domain into regions, each region being resolved to a different scale (Curtin and Miller, 2003; Hao et al., 2004; Wagner and Liu, 2003). A boundary solution is forced, so that two adjacent regions do not suffer discontinuous solutions from one model to the other (Rudd and Broughton, 2000). This is often performed for continuum and atomistic simulations of solid state materials (Fish et al., 2007; Xiong et al., 2015). Concurrent methods may also be based on adaptive coarse-graining, an example of which is the Quasi-continuum method (Knap and Ortiz, 2001; Miller and Tadmor, 2002; Tadmor et al., 1996).

Hierarchical models typically connect information from one length scale to another via parameter sets, rather than solutions to critical boundary value problems. These parameters are often simply informed in a one-way fashion. This work includes new alternatives to those one-way approaches. To move beyond single-source informing of parameters, the uncertainty of each source must be quantified.

In the context of hierarchical multiscale modeling (HMM), information typically travels from bottom-up (BU) or from top-down (TD) (McDowell, 2010). The BU

information pathways take higher resolution (and lower length scale) simulations of postulated mechanisms to estimate parameters or quantities which are challenging to physically measure. These estimates then inform a higher length scale model. In a TD approach, experimental observations of material behavior across longer length and time scales are used to calibrate an intermediate length scale model that may also be built from ensembles of lower length scale simulations. The TD calibrated parameter values can then inform the selection of lower length scale models. For example, a crystal plasticity (CP) model for bcc Fe can be informed with TD and/or BU information (McDowell, 2012; Tallman et al., 2017). Molecular dynamics simulations (using the nudged elastic band method) of kink-pair nucleation on screw dislocation segments have been used to inform a CP model for bcc Fe from the BU (Narayanan et al., 2014). TD calibration of a CP model for bcc Fe has been performed using single-crystal uniaxial tension test data across multiple temperatures and crystallographic loading directions (Patra et al., 2014).

Both information pathways have limitations. TD pathways can suffer from non-uniqueness in the estimated parameter values, i.e., multiple unique combinations of parameter values can yield equivalently well-performing models. Moreover, by themselves, TD pathways are less sensitive to the form of constitutive models, whether at larger scales or lower mesoscales. BU models are often based on idealized unit-process cases with significant uncertainty in their mapping to the many-body effects that are present in experimental observations. When the uncertainty in a multiscale model is considered, the limitations here manifest as two iconic problems that are associated with uncertainty quantification in multiscale models: dimensionality and identifiability.

2.4. Uncertainty Quantification

Uncertainty Quantification (UQ) is the study and practice of accounting for the various sources of uncertainty in a scientific model (whether pertaining to theory or experiment), and the modeling of the effects of those uncertainties (R. C. Smith, 2013). Many problems are approached in UQ, including parameter estimation (Gaganis, 2009; Lacaze and Missoum, 2014; Rizzi et al., 2012a), uncertainty propagation (Acharjee and Zabaras, 2007; Rizzi et al., 2012b), and model discrepancy estimation (Arendt et al., 2012a; Brynjarsdóttir and O'Hagan, 2014; Ling et al., 2014; Pederson and Johnson, 1990). In multiscale models, the common application is uncertainty propagation (Coleman and Steele, 2009; Koslowski and Strachan, 2011; Rizzi et al., 2012b), a study of multiple effects. Often, a sensitivity analysis is a necessary prerequisite to UQ for a new model (Trucano et al., 2006). This section describes some established techniques in UQ, focusing on those used for multiscale models. Some characteristic issues in multiscale UQ will be addressed.

Different categories are defined to organize uncertainty into specific types. Where parameters are determined prior to model calibration (a priori) or as a part of calibration, the uncertainty in those estimates is known as parametric uncertainty. When multiple options of model form are reasonable for representing a material, perhaps either including or neglecting a secondary mechanism, the attribution of weight to either model's results is a problem known as model form uncertainty. In any case where an approximation is made in the method of calculations, the effect of those approximations is called numerical uncertainty. While many other forms of uncertainty exist and have been studied, the types named here are approached in the content of the dissertation.

A breakdown of uncertainty into aleatory and epistemic components is sometimes performed (Johnson et al., 2008). Aleatory uncertainty is also called irreducible uncertainty or variability. Epistemic uncertainty is also called reducible uncertainty or incertitude. The distinction made by this terminology is acknowledged, though it is not employed in this dissertation. A discussion of perspectives on the topic is included in Chapter 7.

Markov chain Monte Carlo (MCMC) methods are commonly used to explore the uncertainty characterization and propagation of multiscale models. MCMC uses a sampling of the stochastic parameters of a model to estimate the posterior probability distribution of the outcome, response, or quantity of interest (QoI) (Geyer, 1992). In applications to multiscale models (Beck and Au, 2002), these methods often become computationally expensive. Each sample in a MCMC study is accompanied by a run of the full-field model. The cost of this method can be avoided through the use of approximations and surrogate models.

Surrogate models are frequently used in multiscale UQ. A surrogate model is an approximation of the response of a model and is computationally cheaper than the model it approximates. A surrogate model is built on some designed sampling, or a quadrature of input space and resulting model response (Wilkinson, 2010). Polynomial chaos expansions (PCE) are a non-sampling method used to represent the effects of parameters using polynomials (Blatman and Sudret, 2010; Choi et al., 2003). PCE performs best with few input parameters and without sharp nonlinearities. Gaussian process (GP) models and their derivative forms are commonly used as surrogate models (Backlund et al., 2012; Brynjarsdóttir and O'Hagan, 2014; Gano et al., 2006; Dave Higdon et al., 2008; Jin et al.,

2001; Marc C. Kennedy and O'Hagan, 2001; Storlie et al., 2015; Wilkinson, 2010). GP models can be used in uncertainty propagation studies, and are more efficient than MCMC when fewer than twenty dimensions are considered at once (Chen et al., 2015). Regression models can be used as surrogate models and are simple and reliable to implement (Gano et al., 2006). Link functions can be used in regression to specify error distributions of non-Gaussian type (McCullagh, 1984). In Chapter 3, the regression surrogate modeling approach is used to approximate the likelihood function of the model in terms of the input parameters. In Chapter 4, a Gaussian process regression model is used as a surrogate for optimization between modeling scales. In Chapter 6, a surrogate model is built as a Gaussian process to systematically explore a parameter space through the reduction of uncertainty across a finite domain. GP modeling is introduced further in section 6.1.

Model form uncertainty is on the cutting edge of multiscale UQ. In multi-physics modelling, model form UQ has been performed (Riley and Grandhi, 2011). Multiscale and multi-physics modeling both require coordination of multiple models. Bayesian model averaging has been used to quantify model form uncertainty (Park et al., 2010). Few examples exist of multiscale modeling that consider model form uncertainty.

Model discrepancy methods are a suite of powerful UQ techniques. In a model discrepancy treatment, the original model is accompanied with a surrogate model-like layer which describes the discrepancy between the model response, Y^M, and the target data, Y^E, as a function of some alignment variables, $\mathbf{x}$, i.e.,

$$\delta(\mathbf{x}) = Y^E(\mathbf{x}) - Y^M(\mathbf{x}) \tag{1}$$

where alignment variables are known a priori (R. C. Smith, 2013). The use of discrepancy methods prior to calibration has been done (Brynjarsdóttir and O'Hagan, 2014). This work leaves the discrepancy methods for after calibration, to preserve the clarity of the physical interpretation of calibration parameters. For more discussion of this topic, see Chapter 3.

Some difficulties are shared by UQ and multiscale modeling. A scientific simulation can be expensive, and can involve many parameters to calibrate (Kennedy and O'Hagan, 2001). The introduction of UQ requirements on that simulation can exponentially increase the total computational cost of a problem. Similarly, multiscale methods lead to increasing numbers of parameters, the calibration of which can become increasingly costly. Additionally, in both UQ and multiscale modeling, the large number of parameters can cause difficulty when trying to assign effects to individual parameters. These two problems are known in each field as dimensionality and identifiability, and they deserve introduction.

The dimensionality problem refers to the cost explosion of quantifying uncertainty in problems with increasing numbers of dimensions to explore. Dimensionality problems also arise in microstructure representation problems (Paulson et al., 2017). Uncertainty propagation studies are clear examples of dimensionality costs in UQ. The established procedure for these studies is the MCMC method (Angelikopoulos et al., 2012; Beck and Au, 2002; Geyer, 1992), where the model is run many times to

explore the possible values of input parameters. MCMC methods are computationally intensive, sometimes requiring millions of runs of a model to converge to a posterior probability distribution. To manage the problem of dimensionality in scientific modeling, many techniques have been used.

Dimensionality reduction techniques are noteworthy in discussions of dimensionality. Principal component analysis (PCA) is a prominent technique (Jolliffe, 1986; Ma and Zabaras, 2011; Paulson et al., 2017). PCA describes the variation in response across a parameter space with new basis vectors, written in terms of the original parameters. By recombining the parameters into orthogonal vectors, PCA can reduce the number of independent dimensions of exploration. Parameter clustering (Song, 2010; Tong et al., 2004; Zhan and Tong, 2007) has been used to identify a model's parameters in stages, approaching the identification of parameters as multiple smaller problems. The problems within this dissertation are approached with necessary consideration for the dimensionality of any formulated design of experiments.

Materials simulations can be prohibitively expensive even after dimension reduction is performed. Surrogate modeling is one of the main strategies pursued to reduce this cost. Surrogate models have numerous formulations, as previously mentioned. Approximations are made to the calculations in this work where appropriate to better explore highly dimensional properties and responses.

The identifiability problem refers to when a model's output fails to indicate unique values for model input parameters. This non-uniqueness is often encountered in models with many calibration parameters. Many existing solutions make use of either

more detailed experimental data (Avril et al., 2008), or more types of experimental data (Arendt et al., 2012b). Work in this dissertation coordinates inputs from multiple length scales, and in doing so addresses this prevalent issue.

To reduce the impact of these limitations in multiscale approaches, combined TD, BU (TDBU) approaches have been proposed (McDowell, 2012). While concurrent methods exist which allow for two-way coupling (Ghosh, 2011; Ghosh et al., 2001), and both BU and TD data have been used in informing separate parameters of a HMM (Ghosh et al., 2016; Shahba and Ghosh, 2016), the reconciliation of, or resolution of disagreement between, TD and BU estimates of a single parameter set has not yet been established for a hierarchical approach. To address this lack, a TDBU calibration method is presented in Chapter 3. Information is used from TD and BU to optimize parameters of the homogenization of microstructure in Chapter 5.

CHAPTER 3. RECONCILED TOP-DOWN AND BOTTOM-UP HIERARCHICAL MULTISCALE CALIBRATION OF BCC FE CRYSTAL PLASTICITY

In this chapter, a test for connections between models via parameter sets is developed in the context of a HMM. A set of parameters from the slip system flow rule of a crystal plasticity model for bcc Fe is identified for connecting TD and BU information. The TD calibration is performed using experimental measurements of single crystal yield strength at multiple temperatures and crystallographic orientations, where a likelihood function in parameter space is informed using second order regression surrogate modelling. A BU calibration of the same model uses the parameter estimates from atomistic simulations to inform penalty functions. A constrained likelihood function incorporates the TD and BU information in one calibration of parameters. Decision making within HMM is approached. The benefit to calibration precision brought by incorporating additional data from BU is considered against the uncertainty in the requisite multiscale connection. This trade-off is formulated into an empirical test of the connection. Hypothetical decision making is demonstrated between multiple alternative BU estimates.

3.1. Introduction

Scientific model calibration is a rich field. Popular techniques for informing model parameters can accommodate the expense and complexity of materials models (Forrester et al., 2008; Gano et al., 2006; Salloum et al., 2015; Wilkinson, 2010).

Importantly, the uncertainty associated with a model can be incorporated in calibration approaches (Arendt et al., 2012a; Li et al., 2016; McFarland et al., 2008; McFarland and Mahadevan, 2008). These approaches are often used one at a time. To couple two sparse data sets (TD and BU), a calibration approach is used for each, and the two uncertain estimates are reconciled using a connection between models. The approach considers the connection between models to be an additional source of uncertainty. This consideration is new, and it supports decision making in the construction of hierarchical multiscale models. Addressing the implementation of this new consideration is the focus of this work.

The need for reconciliation of competing interests or estimates is encountered in many fields of study. Instances of reconciliation can be considered multiple-attribute decision making problems (Rao, 2008; Tzeng and Huang, 2011). Depending on the quantity of data available, different approaches to overcoming initial disagreement can be used. Multi-objective optimization requires data sufficient to inform functions for each goal and an expert decision maker to ascribe appropriate weights to each objective (Deb, 2014; Marler and Arora, 2004; Yapo et al., 1998). Robust optimization compromises an optimal solution to minimize the effect of expected inaccuracy (Allen et al., 2006; Bertsimas et al., 2011; Beyer and Sendhoff, 2007; Mulvey et al., 1995). The expected uncertainty of the model solution determines the extent to which the robust solution varies from the optimum. Work contained here treats the reconciliation of two sparse data sets as a constrained optimization, where the constraints are tied to expected uncertainty. This reconciliation has much in common with both categories of optimization mentioned above.

Data-scarce decision making is frequently encountered in real-world applications of simulation models. The scarcity of data in these scenarios renders big-data decision support techniques inviable. Rather, successful approaches are resourceful and incorporate information from multiple sources. Hydrological modeling of data scarce locations has been approached using predictions of local runoff from climate and or soil data--a multi model approach (Bangash et al., 2012; Dile and Srinivasan, 2014). In predictions of repair rates for marketed products (Fang and Huang, 2008) and service lives of water supply systems (Scholten et al., 2013), Bayesian methods have been used to incorporate expert opinion as informative priors to data scarce predictions. In an ecological study of brown bear habitats, a multiscale approach maximized the utility of scarce data (Martin et al., 2012). Imprecise information on seismic risk was incorporated with a traditional probability modeling approach to risk assessment using fuzzy intervals (Dong et al., 1987). In a landslide risk assessment, multiscale methods and fuzzy information were used in combination (Dragićević et al., 2015). Generally, these approaches adopt methods of combining information of different forms by appropriately translating between those forms (Hall, 2003). The work of this Chapter demonstrates this process by translating information from different sources and length scales into forms which may be combined.

The Chapter is outlined as follows. First, the goodness of fit between TD data and model response is measured. For each data point, a surrogate model is used to inform a likelihood function in input parameter space. Reference parameter estimates from BU simulations are used to formulate penalty functions, also in terms of input parameters. Likelihood functions and penalty functions are used in combination to find an integrated

TDBU estimate of parameters. A practical, empirical test of uncertain model-model connections is formulated. The utility of possible connections for reducing parametric uncertainty is evaluated. For this work, calibration is limited to the onset of slip.

3.2. Background

A strategy for reconciling TD and BU data to inform parameters of a CP model of bcc Fe is presented. Reconciliation is used here as a label for the process by which conflict between the parameter estimates determined by best fit to different data sets (or objectives) is resolved. A previously studied (Patra et al., 2014) physically-based model of the crystal plasticity of bcc Fe was selected, with a Kocks-type activation enthalpy driven flow rule (Kocks et al., 1975) governing the activity of slip systems. This model was informed along two previously defined pathways, one from BU and one from TD. The BU pathway is defined as established in work by Narayanan et al. (2014), by first identifying the thermal activation of a kink-pair on a screw dislocation segment to be the rate limiting step for dislocation motion (Seeger, 1956). Accordingly, the nudged elastic band (NEB) method (Jónsson et al., 1998) and molecular dynamics (MD) simulations of kink-pair nucleation are used to inform the CP model via transition state theory, resulting in estimates for five parameters of a flow rule with the same Kocks form. The TD pathway follows the work of Patra et al. (2014), and uses experimental data from the uniaxial tension tests of single crystal bcc Fe performed by Spitzig and Keh (1970a) and Keh (1965). The same five parameters in the flow rule were adjusted to bring the predicted yield strength in line with experimental data.

Much work has been done to understand the multiscale interrelations of non-Schmid stress effects, Peierls stress, and kink-pair activation enthalpy in bcc metals (Hale et al., 2015; Lim et al., 2015). The work of Lim et al. (2015) explores multiscale approaches to the same quantities of interest as this work. The parameters of the flow rule are informed from atomistics or from experiments, and the disparity of the two estimates is discussed. Notably, reconciliation of BU and TD estimates has not been attempted. Such a reconciliation is the focus of the current work.

A combined TDBU strategy to inform the CP model must overcome initial disagreement between data and dissimilarity in the form of data sources. These pathways have been shown to lead to CP model parameter values that are clearly different (Narayanan et al., 2014; Patra et al., 2014). For example, the thermal resistance to slip at 0K, also called the Peierls stress, is predicted by atomistic simulations to be around 1040 MPa for bcc Fe (Gordon et al., 2011, 2010). In contrast, empirically determined values cluster near 390 MPa (Kuramoto et al., 1979b, 1979a; Suzuki et al., 1995). The approach taken here seeks reconciliation of these contrasting estimates (Table 3-2).

Empirical TD calibration of computational materials models is widespread. The methods employed are typically optimizations of goodness of fit (Oskay and Fish, 2007; Yalcinkaya et al., 2008). Uncertainty Quantification methods often contribute estimates for the uncertainty associated with the results of these calibration methods (McFarland et al., 2008; McFarland and Mahadevan, 2008). Commonly, the uncertainty is expressed in terms of model output. In contrast, Bayesian methods apply Markov chain Monte Carlo sampling methods to establish uncertainty measurements in terms of model input parameters (Chkrebtii, 2013; Glimm et al., 2003; Higdon et al., 2004; Honarmandi and

Arroyave, 2017; Kennedy and O'Hagan, 2001; Rizzi et al., 2012a). While Bayesian methods can be too computationally expensive to carry out on already expensive computational materials models, surrogate modeling is often used to offset the additional costs.

The calibration approach described here does not use a model discrepancy term. The dominant approach to model calibration is to separately treat the measurement error and the model discrepancy (Brynjarsdóttir and O'Hagan, 2014; Marc C. Kennedy and O'Hagan, 2001; Wilkinson, 2010), i.e.,

$$Y^E = Y^M - \delta - \varepsilon \tag{2}$$

where Y^E is the experimental measurement, Y^M is the model prediction, δ is the model discrepancy, which is often defined functionally, and ε is the measurement error, which is defined as a random variable. This distinction requires defining the form of δ based on assumed prior information. The approach described here does not perform this decomposition. The connection between two models is to be evaluated, and model discrepancy methods may affect or confound that evaluation. After the degree of uncertainty of a connection has been established and a connection has been accepted, model discrepancy methods would be appropriate.

BU information is often expressed in terms of a resulting reference set of parameter estimates. These parameter estimates can be carried forward directly (Narayanan et al., 2014), or included in a study of uncertainty propagation (Koslowski and Strachan, 2011; Rizzi et al., 2012b; Tran and Wang, 2017), where parameter values

are taken as samples from a distribution or interval which reflects the uncertainty of each parameter. When constraints on parameters exist in an optimization setting, penalty methods are used (White and Anandalingam, 1993). The use of penalty methods in Chapter 3 allows the BU information to be included alongside the TD information in a calibration of an intermediate parameter set.

The methods here are distinct from model selection approaches (Beck and Yuen, 2004), such as Bayesian model averaging (Hoeting et al., 1999). Bayesian model averaging takes a class of models targeting the same subject (observations) and assigns them weights per their relative performance. To enable such comparisons, the target data are held fixed. In the TDBU context, the target data cannot be held fixed. Each information pathway reflects a unique data source. The connection cost method evaluates the connection between the different data sources. Subsequently, comparison of different possible connections is based on parametric uncertainty, rather than model fidelity.

In multi-fidelity modeling, discrepancy terms are used to relate a less-costly approximate model to the expensive full model to increase efficiency and improve predictions (Kennedy and O'Hagan, 2000). Like model selection techniques, the focus of multi-fidelity approaches is the response of the model. The TDBU work included is quite different from multi-fidelity modeling. In this approach, the TD and BU calibrations are not approximations of each other. Both pathways are considered valid and informative. Because of this, a different and entirely new approach is taken to incorporate both TD and BU in a reconciled calibration.

3.2.1. Material Constitutive Models

The crystal plasticity model used in this work is taken from the work of Patra et al. (2014) on constitutive equations to incorporate non-Schmid effects on yield strength in single crystal bcc Fe. The model is implemented using fully implicit integration in the finite element software Abaqus (Simulia, 2007). However, in this work it is executed via single material point simulations. This treatment, where a single integration point is simulated, assumes homogeneous deformation. The present work is only concerned with initial onset of slip, so this assumption is reasonable. A brief description of the crystal plasticity model is outlined next.

The crystal plasticity model uses a finite deformation assumption and multiplicatively decomposes the deformation gradient $\mathbf{F}$ into elastic and inelastic parts, $\mathbf{F}^e$ and $\mathbf{F}^{in}$, respectively (Asaro and Rice, 1977). The inelastic velocity gradient is given by $\mathbf{L}^{in} = \dot{\mathbf{F}}^{in} \cdot \mathbf{F}^{in-1}$. The sum of crystallographic shearing rates for all N_s slip systems comprises $\mathbf{L}^{in}$, i.e.,

$$\mathbf{L}^{in} = \sum_{\alpha=1}^{N_s} \dot{\gamma}^{\alpha} \mathbf{m}_0^{\alpha} \otimes \mathbf{n}_0^{\alpha} \quad . \tag{3}$$

Taken in the reference (or isoclinic intermediate) configuration, $\mathbf{m}_0^{\alpha}$ and $\mathbf{n}_0^{\alpha}$ are the unit vectors in the slip and slip plane normal directions for slip system α. Constitutive equations are used to define the slip system shearing rates $\dot{\gamma}^{\alpha}$ as a function of the resolved shear stress, τ^{α}, and the evolution of internal state variables (ISVs) on each slip

system. The material is assumed to have $N_s = 24$ $\{110\}\langle 111\rangle$ slip systems (Gröger et al., 2008b), considering both positive and negative shear directions. Dislocation density, ρ^α, is defined on a slip system basis and used as an ISV in the model. Dislocation density is considered as an additive sum of mobile, ρ_M^α, and immobile dislocation densities, ρ_I^α, i.e., $\rho^\alpha = \rho_M^\alpha + \rho_I^\alpha$.

In bcc metals at low to moderate homologous temperatures, inelastic deformation is rate limited by thermally activated glide of $\frac{1}{2}\langle 111\rangle$ screw dislocations, which occurs by kink-pair formation (Argon, 2008). As is generally done in continuum constitutive formulations of thermally activated dislocation glide, the crystallographic shearing rates are defined using a phenomenological Kocks-type activation enthalpy driven flow rule (Kocks et al., 1975), i.e.,

$$\dot{\gamma}^\alpha = \begin{cases} \dot{\gamma}_0 \exp\left(-\dfrac{\Delta F_g}{kT}\left(1 - \left(\dfrac{\tau_f^\alpha - s_a^\alpha}{s_t^\alpha} \right)^p \right)^q \right); \text{ for } \tau_f^\alpha > s_a^\alpha \\ 0; \text{ for } \tau_f^\alpha \le s_a^\alpha \end{cases} \tag{4}$$

Here, $\dot{\gamma}_0$ is the pre-exponential factor, ΔF_g is the activation energy barrier to dislocation glide (the rate limiting step of which being kink pair formation) in the absence of external stress, k is the Boltzmann constant, T is absolute temperature, τ_f^α is the driving stress for dislocation glide, s_a^α is the athermal slip resistance to dislocation glide, s_t^α is the thermal slip resistance, typically controlled by the characteristically high Peierls stress of bcc metals, and p and q are parameters that model the shape of the activation enthalpy

function. This flow rule is the primary subject of the TD and BU calibration in the present work.

The long range athermal slip resistance s_a^α is defined via a Taylor hardening model as a function of dislocation density, i.e.,

$$s_a^\alpha = Gb\sqrt{\sum_{\zeta=1}^{N_s} q_\rho A^{\alpha\zeta}\rho^\zeta} \tag{5}$$

where G is the shear modulus, b is the Burgers vector magnitude, q_ρ is the dislocation barrier strength, and $A^{\alpha\zeta}$ is the matrix of slip system dislocation interaction coefficients. The athermal slip resistance models the slip resistance from dislocation-dislocation interactions.

The model considers non-Schmid effects to contribute to the driving force for dislocation glide, τ_f^α, via a term that adds to the resolved shear stress, τ^α, and decays as an exponential function of the effective inelastic strain ε_{eff}^i, i.e.,

$$\tau_f^\alpha = \tau^\alpha + \sigma_{ns}^\alpha \exp\left(-\frac{\varepsilon_{eff}^i}{\varepsilon_0^i}\right) \tag{6}$$

Here, ε_0^i, the decay constant, is the value of effective inelastic strain which corresponds to a reduction to 37% of the contribution to the driving force at $\varepsilon_{eff}^i = 0$. Also, σ_{ns}^α is the

contribution of non-Schmid forces to the driving force for slip system α, (Gröger et al., 2008a; Patra et al., 2014) i.e.,

$$\sigma_{ns}^{\alpha} = a_1^T \mathbf{m}^{\alpha} \cdot \boldsymbol{\sigma} \cdot \mathbf{n}_{ns}^{\alpha} + a_2^T \left(\mathbf{n}^{\alpha} \times \mathbf{m}^{\alpha} \right) \cdot \boldsymbol{\sigma} \cdot \mathbf{n}^{\alpha} + a_3^T \left(\mathbf{n}_{ns}^{\alpha} \times \mathbf{m}^{\alpha} \right) \cdot \boldsymbol{\sigma} \cdot \mathbf{n}_{ns}^{\alpha} \tag{7}$$

where a_1^T, a_2^T, and a_3^T are atomistically or empirically determined coefficients, $\boldsymbol{\sigma}$ is the current stress state, and $\mathbf{n}_{ns}^{\alpha}$ is the unit vector normal to the 'non-slip' plane.

While the work in this study is focused on modeling the onset of slip, the crystal plasticity model contains constitutive equations regarding the evolution of defect densities. These evolution equations originate in earlier work (Patra and McDowell, 2012), and are briefly described here.

The evolution rates of mobile and immobile dislocation densities are defined as functions of the crystallographic shearing rate, $\dot{\gamma}^{\alpha}$, i.e.,

$$\dot{\rho}_M^{\alpha} = \frac{k_{mul}}{b} \sqrt{\sum_{\zeta} \rho^{\zeta}} \left| \dot{\gamma}^{\alpha} \right| - k_{cs} \exp\left(-\frac{\left(\tau^* - \left| \tau^{\chi} \right| \right) V_a}{kT} \right) \rho_M^{\alpha} \left| \dot{\gamma}^{\alpha} \right| - \frac{2R_c}{b} \rho_M^{\alpha} \left| \dot{\gamma}^{\alpha} \right| - \frac{1}{b\lambda^{\alpha}} \left| \dot{\gamma}^{\alpha} \right| \tag{8}$$

$$\dot{\rho}_I^{\alpha} = \frac{1}{b\lambda^{\alpha}} \left| \dot{\gamma}^{\alpha} \right| - k_{dyn} \rho_I^{\alpha} \left| \dot{\gamma}^{\alpha} \right| \ . \tag{9}$$

Each term on the RHS of Eq. (8) represents a different mechanism of dislocation interaction. The first term addresses the formation of new mobile dislocations by multiplication at existing segments, the second term is for cross-slip of dislocations

between slip systems (from slip plane α to slip plane χ), the third term regards the mutual annihilation of dislocations of opposite Burgers vector within a critical capture radius R_c, and the fourth term denotes the trapping of dislocations at barriers as a function of the mean free path for dislocation glide, $\lambda^{\alpha} = 1/\beta_{\rho}\sqrt{\rho^{\alpha}}$. In Eq. (9), the trapping of mobile dislocations reappears as the additive first term, and the annihilation of immobile dislocations via dynamic recovery is shown in the second term. Material constants k_{mul}, k_{cs}, and k_{dyn} correspond to the mobile dislocation multiplication, mobile dislocation cross-slip, and dynamic recovery of immobile dislocations. Also, τ^* is the activation stress for cross-slip corresponding to activation volume, V_a, and β_{ρ} is a constant related to dislocation trapping.

Model parameters other than those involved in the TDBU calibration are defined as follows in Table 3-1. The parameters in Table 3-1 are not included in the calibration parameters, $\boldsymbol{\theta}$, and are instead held fixed, because they are not addressed in both TD and BU information pathways. Additionally, they possess less uncertainty (e.g., elastic properties) or they have minimal relevance to the yield strength predictions of the model (e.g., dislocation evolution parameters that govern work hardening). These considerations are used to assert that a calibration of the five chosen parameters (taken from Eq. (4)), $\boldsymbol{\theta} = \left[\dot{\gamma}_0,\ \Delta F_g,\ p,\ q,\ s_t\right]$, is appropriate to the TDBU method pursued here.

Table 3-1. Crystal plasticity model parameters for bcc Fe held fixed during the calibration.

Parameter	**Value(s)**	**Meaning and source**
$C_{11}, C_{12}, C_{44}, \nu$	$239260 - 24520 / \left(\exp\left(\frac{392.03}{T(\mathrm{K})}\right) - 1\right)$ MPa, $135780 - 6550 / \left(\exp\left(\frac{469.65}{T(\mathrm{K})}\right) - 1\right)$ MPa, $120720 - 3500 / \left(\exp\left(\frac{162.9}{T(\mathrm{K})}\right) - 1\right)$ MPa, 0.29	Elastic constants (Adams et al., 2006)
a_1^T, a_2^T, a_3^T	$0.0106 + 2.3311\exp\left(-0.0162T\left(K\right)\right)$ $0.1727 + 108.9126\exp\left(-0.0496T\left(K\right)\right)$ $0.2699 + 3.5454\exp\left(-0.0160T\left(K\right)\right)$	Non-Schmid parameters (Patra et al., 2014)
G	$87600 - 17T\left(\mathrm{K}\right)$ MPa	Shear Modulus (Naamane et al., 2010)
a_0	0.2866 nm	Lattice parameter (Johnson and Oh, 1989)
$q^{\rho}, A^{\alpha\alpha}, A^{\alpha\zeta}\left(\zeta \neq \alpha\right)$	0.3, 1.0, 0.2	Hardening parameters (Patra et al., 2014)
$\rho_M^0 = \rho_I^0, \text{for all}\, \alpha$	4.0×10^4 mm^{-2}	Initial dislocation densities (Li et al., 2014; Patra et al., 2014)
$k_{mul}, k_{cs}, k_{dyn}, R_c, \beta_{\rho}$	$3.45 \times 10^{-2}, 0, 2.75 \times 10^2, 6b, 7.40 \times 10^{-2}$	Dislocation evolution parameters (Patra et al., 2014)

The flow rule of this crystal plasticity formulation can receive information from TD experiments (Patra et al., 2014) or from BU simulations (Narayanan et al., 2014). In order to connect the information from both pathways, some modifications to the previously used methods are necessary. The connections used previously will be outlined and the modifications explained.

The TD pathway uses experiments (Keh, 1965) on single crystals of pure bcc Fe to inform the values of four of the five parameters of interest: $\dot{\gamma}_0, \Delta F_g, p, \text{and}\, q$, as introduced with Eq. (4). The fitting procedure used the three uniaxial stress-strain curves

measured at 298 K for crystallographic loading directions $[001], [011]$, and $[\bar{1}11]$. The initial hardening response of the material shown in the curves (up to ~5% strain) was used in a goodness of fit based calibration of the four parameters. The thermal lattice resistance, $s_t^\alpha = s_t \text{ for all } \alpha$, was taken from the work of Suzuki et al. (1995). The value given is $s_t = 390\,\text{MPa}$. Other bcc Fe experiments on a wider range of orientations and temperatures were used as validation data (Spitzig and Keh, 1970a, 1970b, 1970c). The procedure resulted in the TD point estimates for the parameters, as shown in Table 3-2.

The BU route to inform the flow rule parameters takes a different approach. 3D nudged elastic band (NEB) method atomistic simulations (Narayanan et al., 2014) were performed to calculate the minimum energy pathway of a unit process of dislocation slip, via kink nucleation in single crystal bcc Fe. After using this method to determine the activation parameters of the rate limiting mechanism, transition state theory is applied in informing dislocation kinetics at the continuum scale. Their work employed the Proville embedded atom method interatomic potential for Fe (Proville et al., 2012). The stress-dependent function of kink nucleation is informed by these atomistic simulations and written in Kocks form (Kocks et al., 1975) as

$$H = H_0 \left(1 - \left(\frac{\tau_{\text{eff}}^\alpha}{s_{t0}} \right)^p \right)^q \tag{10}$$

where H is the stress-dependent activation energy for unit dislocation slip, H_0 is the activation energy for dislocation motion when the effective shear stress (τ_{eff}^α) on slip system α is zero. p and q are profiling parameters (called shape parameters in the TD

method) and s_{t0} is the thermal slip resistance at 0 K, (Peierls stress), for which the same value is assumed to apply for all slip systems. The parameter s_{t0} is treated as a constant. This formulation is placed into a flow rule (Eq. (12)) to describe the activity of dislocation slip systems in terms of the results of the atomistic simulations. The values for the parameters, H_0, p, q, and s_{t0} are determined as point estimates from a least-squares-based regression on the results of a series of atomistic simulations of kink nucleation. The parameter $\dot{\gamma}_0$ was estimated from BU calculations by assuming an approximation of the Debye frequency, υ_D, of Fe as the attempt frequency of the nucleation of thermal kinks. This was used with the approximate relation from work of (Gröger and Vitek, 2008), i.e.,

$$\dot{\gamma}_{0,\mathrm{BU}} = \frac{b^2 a \rho_M \upsilon_D}{l} \tag{11}$$

where b is the Burgers vector, l is the lateral extent of kinks at the saddle-point state, ρ is the dislocation density (estimated to be $10^{15}/\mathrm{m}^2$ in this calculation), and a is the distance moved by the dislocation in one activation step. The values of $\dot{\gamma}_{0,\mathrm{BU}}$, H_0, p, q, and s_{t0} are included as the BU reference set of estimates in Table 3-2.

The crystal plasticity model used in the work by Narayanan et al (2014) follows the same deformation kinematics as the model in this work. It has different hardening parameters, notably, a latent hardening coefficient of 1.4 (vs. 0.2 for the TD model). Where there are differences, the model used in this work more closely follows that pursued in the work of Patra et al. (2014).

The flow rule used in the BU model uses the stress dependent function of the energy of coordinated kink pair nucleation on screw dislocations to define the rate limiting step of dislocation glide as a thermally activated process. This formulation is shown (Eq. (13)) with similar formatting to the previously introduced TD phenomenological flow rule (Eq. (12)). The similarity of these formulations is used to explore the possibility of calibrating the same parameters on two sources of information.

$$\dot{\gamma}^{\alpha}_{\mathrm{TD}} = \begin{cases} \dot{\gamma}_0 \exp\left(-\dfrac{\Delta F_g}{kT} \left(1 - \left(\dfrac{\tau^{\alpha}_f - s^{\alpha}_a}{s^{\alpha}_t} \right)^p \right)^q \right); \text{ for } \tau^{\alpha}_f > s^{\alpha}_a \\ 0; \text{ for } \tau^{\alpha}_f \leq s^{\alpha}_a \end{cases} \tag{12}$$

$$\dot{\gamma}^{\alpha}_{\mathrm{BU}} = \begin{cases} \dot{\gamma}_{0,\mathrm{BU}} \exp\left(-\dfrac{H_0}{kT} \left(1 - \left(\dfrac{\tau^{\alpha} - s^{\alpha}_a}{s_t} \right)^p \right)^q \right); \text{ for } \tau^{\alpha}_f > s^{\alpha}_a \\ 0; \text{ for } \tau^{\alpha}_f \leq s^{\alpha}_a \end{cases} \tag{13}$$

These formulae have the same structure. They differ because the corresponding parameters within them are informed by different means. The TD version informs the parameters empirically whereas the BU flow rule informs them via simulations. The interpretations of the flow rule are necessarily different to reflect the interpretations made in their informing process. Specifically, the BU flow rule reflects characteristics of the unit process, whereas the TD flow rule reflects the effective multi-body interactions of the dislocation network. The TDBU treatment of these parameters is a reconciliation of these two different interpretations (and their parameter estimates).

3.3. Methodology:

An overview of the TDBU calibration method is presented. The details of the calibration method are described, such as how TD data is formulated in a likelihood function and how BU estimates are used to specify a penalty function. The use of parametric uncertainty to select between multiple uncertain multiscale connections is shown. The approximation of a cost to ascribe to the use of inexact model-model connections which is used in this process is also shown. The informing of the material models used in the HMM approach is also described in this section. The flowchart in Figure 3.1 outlines the process for reconciling the information from TD and BU for the purpose of informing the calibration parameters, $\boldsymbol{\theta}$, where $\boldsymbol{\theta} = \left[\dot{\gamma}_0, \Delta F_g, p, q, s_t\right]$. The flowchart in Figure 3.2 is an overview of the process for deciding between uncertain multiscale connections. The terms which appear in these flowcharts shall be introduced within this section.

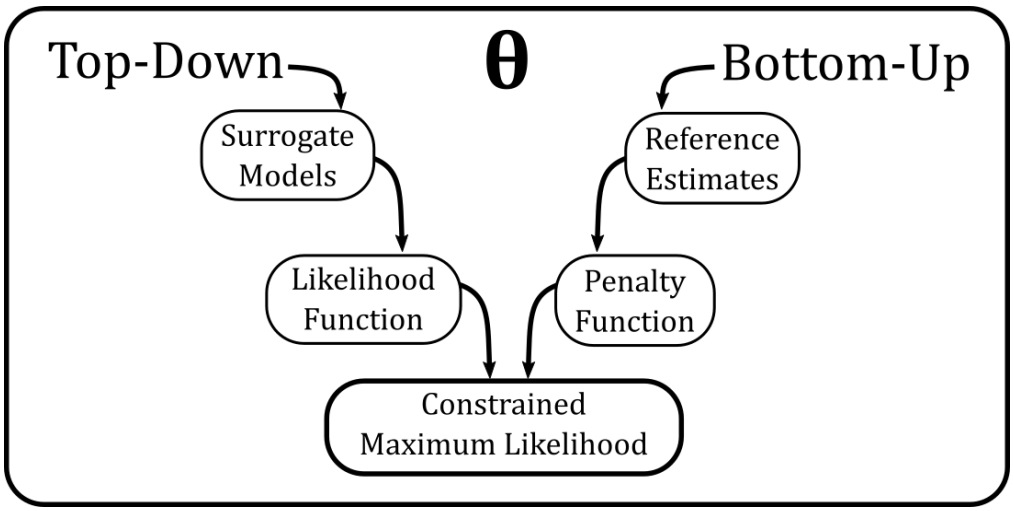

Figure 3.1. A flowchart of the calibration method for combining TD and BU data.

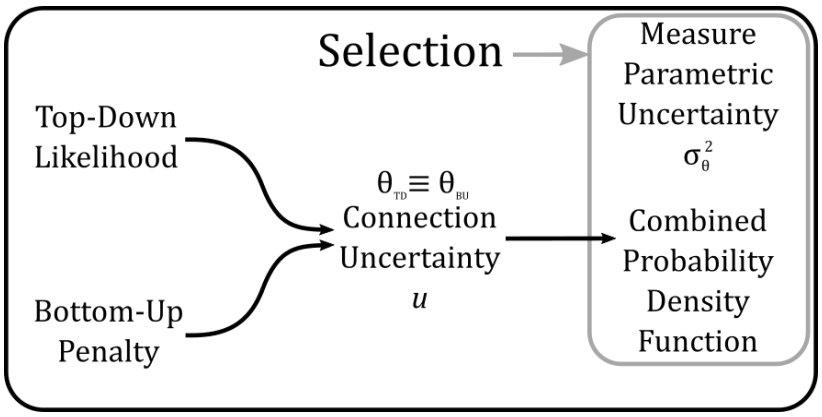

Figure 3.2. Flowchart of the method for the selection of uncertain connections.

Table 3-2. Reference estimates of the key flow rule parameters in the calibration ($\boldsymbol{\theta}$) from both TD and BU information pathways.

Parameter	$\dot{\gamma}_0$	ΔF_g *or* H_0	p	q	s_t
Top-down reference estimates $\hat{\boldsymbol{\theta}}_{\text{TD}}^{\text{ref}}$	$1.00\times10^{7}\ s^{-1}$	0.825 eV	0.47	1.0	390 MPa
Bottom-up reference estimates $\hat{\boldsymbol{\theta}}_{\text{BU}}^{\text{ref}}$	$3.19\times10^{7}\ s^{-1}$	0.57 eV	0.67	1.18	1040 MPa

The information sources of TD (Patra et al., 2014) and BU (Narayanan et al., 2014) do not have common ground--when they are different, there is no clear compromise. This is common in constitutive modeling responses of materials with hierarchical structure. Accordingly, we next outline a strategy to reconcile information from the TD and BU pathways.

An admissible parameter space is defined for the key calibration parameters, $\boldsymbol{\theta} = \left[\dot{\gamma}_0,\ \Delta F_g,\ p,\ q,\ s_t\right]$. The space is defined by simple bounds on each parameter. These bounds are chosen to reflect expert knowledge on the parameters. For the parameters

ΔF_g, p, q, and s_t, the estimates from TD and BU reflect the general range of estimates given by atomistic simulations and empirical measurements, respectively.

The parameter $\dot{\gamma}_0$ has been treated differently. In the case of $\dot{\gamma}_0$, values have been used as low as $4.0\times10^5 s^{-1}$ for bcc Fe (Patra and McDowell, 2012). With the other estimates, they present a range of two orders of magnitude. Accordingly, the parameter is examined. The model is only sensitive to proportionally large changes of $\dot{\gamma}_0$ (that is, changes in the value of $\dot{\gamma}_0$ which are near to the magnitude of $\dot{\gamma}_0$). This, combined with the large range of the estimated values, suggest that a transformation of $\dot{\gamma}_0$ could be a more informative predictor of model response. To weight values of $\dot{\gamma}_0$ in terms of proportional change in $\dot{\gamma}_0$, the parameter is transformed to $\ln(\dot{\gamma}_0)$ for the definition of the prior probability distribution function (PDF) for $\boldsymbol{\theta}$. This approach is reasonable in terms of the flow rule as well, as the flow rule can be equivalently restated as

$$\dot{\gamma}^{\alpha}_{\mathrm{TD}} = \begin{cases} \exp\left(\ln(\dot{\gamma}_0) - \dfrac{\Delta F_g}{kT}\left(1 - \left(\dfrac{\tau^{\alpha}_f - s^{\alpha}_a}{s^{\alpha}_t}\right)^p\right)^q\right); \text{ for } \tau^{\alpha}_f > s^{\alpha}_a \\ 0; \text{ for } \tau^{\alpha}_f \le s^{\alpha}_a \end{cases} \tag{14}$$

Here, the term $\ln(\dot{\gamma}_0)$ is inside the exponential function alongside the other parameters in $\boldsymbol{\theta}$. It is noted that this form obfuscates the units associated with $\dot{\gamma}_0$.

The chosen admissible parameter space contains both reference estimates (from TD and from BU). These bounding values are shown in Table 3-3. The admissible

parameter space is used for creating a uniform prior PDF for $\boldsymbol{\theta}$. In making the uniform prior, the values of calibration parameters within the bounds, $[\boldsymbol{\theta}_{\min}, \boldsymbol{\theta}_{\max}]$, are linearly mapped to intervals of $[0,1]$, thus removing the influence of units. This holds even in the case of $\ln(\dot{\gamma}_0)$, for which changes in units do not affect the result of mapping to $[0,1]$. Calculations are performed in these normalized ranges; however, results will be presented here in original units.

Table 3-3. Admissible parameter bounds for the calibration parameters $\boldsymbol{\theta}$.

Parameter	$\dot{\gamma}_0$	ΔF_g *or* H_0	p	q	s_t
$\boldsymbol{\theta}_{\min}$	$5.00\times10^{5}\,s^{-1}$	$0.55\,\mathrm{eV}$	0.4	1.0	$300\,\mathrm{MPa}$
$\boldsymbol{\theta}_{\max}$	$5.00\times10^{7}\,s^{-1}$	$0.95\,\mathrm{eV}$	0.8	1.5	$1100\,\mathrm{MPa}$

The TD experimental data set (Spitzig and Keh, 1970a) pertaining to the onset of slip in single crystals of bcc Fe is designated as the training data for the TD pathway. The TD data are expressed in model response space, i.e., stress and strain. Bringing that information into input (also parameter) space is a process that approximates an inverse relationship between model output and model input (Csiszar, 1991). The method adopted for this purpose in this work is referred to as second order regression (SOR) surrogate modeling (Gano et al., 2006). Whereas Bayesian MCMC methods derive parameter-value likelihood functions from a response-space comparison with training data (Honarmandi and Arroyave, 2017), the method used here merely approximates the likelihood functions from the training data. The relationship between model response and target datum i is defined as

$$Y^E(\mathbf{x}_i) = Y^M(\mathbf{x}_i, \boldsymbol{\theta}) + \varepsilon_i \ , \tag{15}$$

where $Y^E(\mathbf{x}_i)$ is the value of the experimental response (or datum, in this case yield strength) at the ith value of the physical parameter vector $\mathbf{x}$ (which here refers to temperature and crystallographic orientation). $Y^M(\mathbf{x}_i, \boldsymbol{\theta})$ is the model response at the ith set of values of the physical parameters and the calibration parameter vector $\boldsymbol{\theta}$. The strong assumption of this treatment is that the errors are independent and identically distributed (i.i.d.). This is only plausible for good estimates of $\boldsymbol{\theta}$. In this work, the error term, ε_i, is assumed to follow a Gaussian distribution with mean of zero and variance of σ_e^2 , i.e., $\varepsilon \sim N(0, \sigma_e^2)$. This variance is distinguished from others that appear later in this approach.

The statistical formulation above leads to a likelihood function of the form

$$\text{Likelihood}(\boldsymbol{\theta}) = \exp\left(-\frac{1}{2} \sum_{i=1}^{N_{data}} \frac{\left(Y^M(\mathbf{x}_i, \boldsymbol{\theta}) - Y^E(\mathbf{x}_i) \right)^2}{\sigma_{\text{exp},i}^2} \right), \tag{16}$$

where the number of data is N_{data} (here $N_{\text{data}} = 9$), and $\sigma_{\text{exp},i}^2$ is the expected variance of the ith datum, which may vary to reflect the different levels of precision associated with different data as well as to allow the likelihood to be based on relative error as opposed to absolute error. The values for these $\sigma_{\text{exp},i}^2$ are given by $\sigma_{\text{exp},i}^2 = \left(Y^E(\mathbf{x}_i) \sigma_e \right)^2$.

The values of Y^E and $\sigma^2_{\exp,i}$ are known a priori. To generate $Y^M(\mathbf{x}_i, \boldsymbol{\theta})$, the crystal plasticity model must be run (once for every value of $\mathbf{x}$ and $\boldsymbol{\theta}$ of interest). This approach uses SOR surrogate models to approximate $Y^M(\mathbf{x}_i, \boldsymbol{\theta})$ from a reduced number of crystal plasticity model runs. The SOR surrogate model is well documented (Gano et al., 2006); however, it is detailed here using different notation for clarity. The general form of a second order polynomial regression model is shown as

$$f = c_0 + \sum_{j=1}^{n_v} c_j \theta_j + \sum_{j=1}^{n_v} \sum_{k=j}^{n_v} c_{n_v - 1 + j + k} \theta_j \theta_k \tag{17}$$

where f is the predicted response, the crystal plasticity model calibration parameters $\boldsymbol{\theta} = [\theta_1 \ldots \theta_{n_v}]$ appear as variables (number of variables n_v), and coefficients $\mathbf{c} = [c_0 \ldots c_m]$ must be determined. The number of coefficients, m, is given by the triangular number $m = (n_v + 1)(n_v + 2)/2$. Using matrix notation, Eq. (17) becomes

$$f = \mathbf{c}^{\mathrm{T}} \overline{\boldsymbol{\theta}} \ , \tag{18}$$

where $\overline{\boldsymbol{\theta}}$ is the vector of terms

$$\overline{\boldsymbol{\theta}} = [1, \theta_1 \ldots \theta_{n_v}, \theta_1^2, \theta_1\theta_2, \theta_1\theta_3 \ldots \theta_{n_v}^2] \ . \tag{19}$$

To determine the coefficients, the surrogate must be trained on a sample of queries of the CP model response, across the values of calibration parameters within the

admissible parameter space, defined by $[\boldsymbol{\theta}_{\min}, \boldsymbol{\theta}_{\max}]$. The sample set is comprised of n_s queries and is organized in matrix form, i.e.,

$$\mathbf{A} = \begin{pmatrix} 1 & \theta_1^{(1)} & \cdots & \left(\theta_{n_v}^{(1)}\right)^2 \\ \vdots & \vdots & \ddots & \vdots \\ 1 & \theta_1^{(n_s)} & \cdots & \left(\theta_{n_v}^{(n_s)}\right)^2 \end{pmatrix} \in \mathbb{R}^{n_s \times m} \tag{20}$$

and

$$\mathbf{f} = [f^{(1)}, \ldots, f^{(n_s)}] \in \mathbb{R}^{n_s} \tag{21}$$

where $\mathbf{A}$ contains the values of the dependent variable terms corresponding to the crystal plasticity model responses (yield strength) contained in $\mathbf{f}$. The coefficients $\mathbf{c}$ can be solved using the set of linear equations formed from the queries, i.e.,

$$\mathbf{A}\mathbf{c} = \mathbf{f} \tag{22}$$

The system has a unique least squares solution, i.e.,

$$\mathbf{c} = \left(\mathbf{A}^{\mathrm{T}}\mathbf{A}\right)^{-1}\mathbf{A}^{\mathrm{T}}\mathbf{f} \tag{23}$$

only if the inverse, $\left(\mathbf{A}^{\mathrm{T}}\mathbf{A}\right)^{-1}$, exists. For this solution to exist, it is required that $n_s \geq m$. When $n_s > m$, the model becomes regressive, given that the coefficients become overdefined.

The response (predicted yield strength) of the crystal plasticity model $Y^M\left(\mathbf{x}_i, \boldsymbol{\theta}\right)$ is recorded for each of N_{data}, at multiple values across the previously defined admissible parameter space $\left[\boldsymbol{\theta}_{\min}, \boldsymbol{\theta}_{\max}\right]$. The admissible parameter space also establishes a uniform prior probability density for $\boldsymbol{\theta}$, in a Bayesian sense, i.e., $\text{Prior}\left(\boldsymbol{\theta}\right) = \textit{Uniform}\left(\boldsymbol{\theta}_{\min}, \boldsymbol{\theta}_{\max}\right)$. The values of Y^M as functions of $\boldsymbol{\theta}$ are interpolated using second order regression (SOR) surrogate models, per the relationship

$$f_i\left(\boldsymbol{\theta}\right) = Y^M\left(\mathbf{x}_i, \boldsymbol{\theta}\right) + \varepsilon_{\text{sur},i} \tag{24}$$

where each SOR surrogate $f_i\left(\boldsymbol{\theta}\right)$ depends only on $\boldsymbol{\theta}$, and mismatch between the crystal plasticity model and the surrogate is explained with the surrogate error term $\varepsilon_{\text{sur},i}$. Although $\varepsilon_{\text{sur},i}$ can be measured using a test set of crystal plasticity model runs, this approach approximates $\varepsilon_{\text{sur},i} \cong 0$. This approximation is supported by the R^2 values of the surrogate models (> 0.98). The linking function, which determines the distribution assumed for errors on the response, was chosen to be logarithmic. The lognormal error distribution matched the possible values for yield strength, given that the range of physical estimates yield strength, like the defined domain of the lognormal distribution, is non-negative.

Thus, the likelihood definition is rewritten in terms of the surrogate models, per

$$\text{Likelihood}\left(\boldsymbol{\theta}\right) \cong \exp\left(-\frac{1}{2} \sum_{i=1}^{N_{data}} \frac{\left(f_i\left(\boldsymbol{\theta}\right) - Y^E\left(\mathbf{x}_i\right)\right)^2}{\sigma_{\text{exp},i}^2} \right). \tag{25}$$

Finding the maximum of Eq. (25) will return a maximum likelihood estimate of the calibration parameters on the TD data, $\hat{\boldsymbol{\theta}}_{\text{TD}}$. This estimate is presented in Table 3-4. Note that the values of $\hat{\boldsymbol{\theta}}_{\text{TD}}$ and $\hat{\boldsymbol{\theta}}_{\text{TD}}^{ref}$ (from Table 3-2) do not match. The two estimates are produced by distinct calibration procedures carried out using different data. The values from $\hat{\boldsymbol{\theta}}_{\text{TD}}^{ref}$ are used here only for establishing the bounds for the prior, $\left[\boldsymbol{\theta}_{\min}, \boldsymbol{\theta}_{\max}\right]$.

It is noted that this approach uses a separate surrogate model to describe the model response that corresponds to each data point i of N_{data}. This is favored over the formulation of a single surrogate that interpolates across both calibration parameters and physical parameters, i.e., $f\left(\boldsymbol{\theta}, \mathbf{x}\right)$. While the preferred approach requires more CP model runs in total, it does not require the SOR model to emulate the relationships between temperature, orientation, and response.

The BU method used in previous work informed the crystal plasticity model parameters directly (Narayanan et al., 2014). In this work, the BU reference estimates are used to formulate penalty functions (Yeniay, 2005). The penalty functions used here treat the BU reference estimates from Table 3-2 as the constraint on $\boldsymbol{\theta}$, i.e.,

$$\boldsymbol{\theta} = \hat{\boldsymbol{\theta}}_{\mathrm{BU}}^{\mathrm{ref}} \tag{26}$$

The penalty is defined as a Gaussian error term, i.e.,

$$\mathrm{Penalty}\left(\boldsymbol{\theta}\right)_j = \exp\left(-\frac{1}{2}\frac{\left(\theta_j - \hat{\theta}_{\mathrm{BU},j}^{\mathrm{ref}}\right)^2}{\sigma_p^2} \right) \tag{27}$$

where σ_p^2 is the variance of the penalty, which controls the degree of influence of the BU information on the constrained likelihood. The penalty functions are imposed multiplicatively on the likelihood function, i.e.,

$$\text{Constrained Likelihood Function}\left(\boldsymbol{\theta}\right) = \text{Likelihood}\left(\boldsymbol{\theta}\right)\prod_{j=1}^{n_v}\mathrm{Penalty}\left(\boldsymbol{\theta}\right)_j \tag{28}$$

$$\mathrm{CLF}\left(\boldsymbol{\theta}\right) \cong \exp\left(-\frac{1}{2}\sum_{i=1}^{N_{data}}\frac{\left(f_i\left(\boldsymbol{\theta}\right) - Y^E\left(\mathbf{x}_i\right)\right)^2}{\sigma_{\exp,i}^2} \right)\prod_{j=1}^{n_v}\exp\left(-\frac{1}{2}\frac{\left(\theta_j - \hat{\theta}_{\mathrm{BU},j}^{\mathrm{ref}}\right)^2}{\sigma_p^2} \right) \tag{29}$$

or equivalently,

$$\mathrm{CLF}\left(\boldsymbol{\theta}\right) \cong \exp\left(-\frac{1}{2}\left(\sum_{i=1}^{N_{data}}\frac{\left(f_i\left(\boldsymbol{\theta}\right) - Y^E\left(\mathbf{x}_i\right)\right)^2}{\sigma_{\exp,i}^2} + \sum_{j=1}^{n_v}\frac{\left(\theta_j - \hat{\theta}_{\mathrm{BU},j}^{\mathrm{ref}}\right)^2}{\sigma_p^2} \right) \right) \tag{30}$$

Finding the maximum of the constrained likelihood function (CLF) returns the combined TDBU maximum likelihood (ML) estimate, $\hat{\boldsymbol{\theta}}_{\text{TDBU}}$.

Table 3-4. Maximum likelihood estimated values for the calibration parameters. TD corresponds to the unconstrained likelihood function, and TDBU corresponds to the likelihood function constrained by penalty terms. Values of $\sigma^2_{\text{exp},i} = \left(0.1Y^E\left(\mathbf{x}_i\right)\right)^2 \forall i$ were used.

Parameter	$\dot{\gamma}_0$	$\Delta F_g \text{ or } H_0$	p	q	s_t
$\hat{\boldsymbol{\theta}}_{\text{TD}}$	$5.00\times10^7\ s^{-1}$	0.79 eV	0.4	1.5	860 MPa
$\hat{\boldsymbol{\theta}}_{\text{TDBU}} \mid \sigma_p = 0.5$	$5.00\times10^7\ s^{-1}$	0.78 eV	0.4	1.38	796 MPa
$\hat{\boldsymbol{\theta}}_{\text{TDBU}} \mid \sigma_p = 0.2$	$3.93\times10^7\ s^{-1}$	0.75 eV	0.43	1.29	686 MPa
$\hat{\boldsymbol{\theta}}_{\text{TDBU}} \mid \sigma_p = 0.1$	$3.07\times10^7\ s^{-1}$	0.68 eV	0.52	1.28	652 MPa
$\hat{\boldsymbol{\theta}}_{\text{TDBU}} \mid \sigma_p = 0.05$	$3.12\times10^7\ s^{-1}$	0.60 eV	0.58	1.25	800 MPa
$\hat{\boldsymbol{\theta}}_{\text{TDBU}} \mid \sigma_p = 0.02$	$3.56\times10^7\ s^{-1}$	0.55 eV	0.63	1.21	972 MPa
$\hat{\boldsymbol{\theta}}_{\text{BU}}\left(=\hat{\boldsymbol{\theta}}^{ref}_{\text{BU}}\right)$	$3.19\times10^7\ s^{-1}$	0.57 eV	0.67	1.18	1040 MPa

3.3.1. Uncertainty Cost of Connections

To make an empirical comparison of multiple reasonable connection options, the quality of connections between models must be testable. If the TD-only approach is taken as the baseline, a TDBU connection can be qualified by its performance relative to the baseline case. If the CLF of Eq. (28) is used as the basis of a test, that test would suggest that the BU data should be included in all cases, due to the benefit of additional data in a data-scarce scenario. Indeed, such a test would be insensitive to the relationship between $\boldsymbol{\theta}_{\text{TD}}$ and $\boldsymbol{\theta}_{\text{BU}}$. Assume that data scarcity has led modelers to apply data of diminishing relevance. It is then reasonable to argue that using connections of this nature would incur some penalty or cost. That cost can be tied to the quality of the TDBU connection. The

trade-off between this connection cost and the benefit of additional data can become the basis of the TDBU connection test.

The meaning of connection quality must be defined. Let the connection between $\boldsymbol{\theta}_{\text{TD}}$ and $\boldsymbol{\theta}_{\text{BU}}$ be stronger when the two are similar, and let difference between $\boldsymbol{\theta}_{\text{TD}}$ and $\boldsymbol{\theta}_{\text{BU}}$ imply the connection between them is weaker. Let the connection quality be estimated by measurements on the CLF and the LF. The greater the difference between $\hat{\boldsymbol{\theta}}_{\text{TD}}$ and $\hat{\boldsymbol{\theta}}_{\text{BU}}$, the greater the difference will be between the sum of squared errors at $\hat{\boldsymbol{\theta}}_{\text{TDBU}}$, $\text{SSE}\left(\hat{\boldsymbol{\theta}}_{\text{TDBU}} \,|\, \text{TD, BU}\right)$, and at $\hat{\boldsymbol{\theta}}_{\text{TD}}$, $\text{SSE}\left(\hat{\boldsymbol{\theta}}_{\text{TD}} \,|\, \text{TD}\right)$. The comparison of these measurements becomes the basis of the cost imposed on the calibration on both TD and BU data.

The definition of the connection cost must satisfy some logical requirements. To construct a joint probability density function (PDF) of $\boldsymbol{\theta}$ using both TD and BU data, it must be assumed that a connection exists between data and models via the parameters, $\boldsymbol{\theta}$, i.e., $\boldsymbol{\theta}_{\text{TD}} \equiv \boldsymbol{\theta}_{\text{BU}}$. In other words, the parameters informed from TD and the parameters informed from BU are assumed to be equivalent (with equivalent interpretations), even if this may not be accurate. Equation (28) is a combination of TD and BU data that assumes the connection between TD and BU is valid. To impose a cost associated with the TDBU connection, that assumption of validity is relaxed. In constructing this new formulation, the following statements are upheld:

- Let the CLF as shown in equation (28) be the exact case, i.e., the case when the connection is certain and there is no cost.

- Let the cost be imposed consistently across the admissible parameter space for a given connection.
- Let increased cost of connection result in widened confidence intervals.

To abide by the above statements, cost of the connection is imposed on the CLF by including an exponent, i.e.,

$$CLF\left(\boldsymbol{\theta} \mid \text{Uncertainty}\right) = CLF\left(\boldsymbol{\theta}\right)^{u}, u \in \left(0,1\right] \tag{31}$$

where u is an exponent reflecting the cost of the uncertainty in the connection between the TD and BU data/models. A value of $u = 1$ reflects no connection cost and that no disagreement exists between TD and BU data, and a value of $u = 0$ reflects an infinite connection cost, where complete disagreement exists between the TD and BU data.

The quality of the connection must be estimated to inform u. As discussed with the definition of connection quality, take the sum of squared errors at $\hat{\boldsymbol{\theta}}_{\text{TDBU}}$ to inform u, per

$$u = \frac{1}{\max\left\{\text{SSE} + \text{Penalty}\left(\hat{\boldsymbol{\theta}}_{\text{TDBU}}\right), 1\right\}} = \frac{1}{\max\left\{-2\ln\left(CLF\left(\boldsymbol{\theta} \mid \boldsymbol{\theta} = \hat{\boldsymbol{\theta}}_{TDBU}\right)\right), 1\right\}} \tag{32}$$

for the TDBU case. The test of the connection requires a comparison with a baseline case. This case is given by $\hat{\boldsymbol{\theta}}_{\text{TD}}$ and the TD-only likelihood function. The TD-only likelihood function is taken as the null hypothesis, where the BU information is ignorance across the admissible space and u is informed per

$$u = \frac{1}{\max\left\{-2\ln\left(\text{Likelihood}\left(\boldsymbol{\theta} \mid \boldsymbol{\theta} = \hat{\boldsymbol{\theta}}_{\text{TD}}\right)\right), 1\right\}} \tag{33}$$

It is noted that the value of u for the BU penalty function alone can be estimated in this way, returning $u = 1$.

When multiscale modeling hierarchies are developed, multiple options may exist for connecting models. Not all multiscale connections are useful. To approach this, multiple connection options must be present and be evaluated. The application of this method to the CP modeling problem presented constitutes a single possible connection. Two alternate BU reference estimates are proposed. They represent two potential scenarios. The "cooperative" estimate agrees with the TD likelihood function. The "spurious" estimate strongly disagrees with the TD and leads to a poorly performing CP model when used directly. They are presented in Table 3-5 alongside the BU estimate from atomistic simulations. It is noted that these estimates are not used in any combination with each other. They are used as distinct alternative candidates. The TD data is used to connect with each case, forming the common basis for comparison.

Table 3-5. Contrived BU reference estimates shown alongside the estimates from the atomistic modeling of (Narayanan et al., 2014).

$\hat{\boldsymbol{\theta}}_{\text{BU}}^{\text{ref}}$	$\dot{\gamma}_0$	$\Delta F_g \text{ or } H_0$	p	q	s_t
Simulated	$3.19\times10^{7}\ s^{-1}$	$0.57\,\text{eV}$	0.67	1.18	$1040\,\text{MPa}$
"cooperative"	$1.58\times10^{7}\ s^{-1}$	$0.75\,\text{eV}$	0.48	1.3	$540\,\text{MPa}$
"spurious"	$5.00\times10^{5}\ s^{-1}$	$0.95\,\text{eV}$	0.8	1.5	$1100\,\text{MPa}$

The connections with each BU estimate are compared by examining their effects on the calibration of $\boldsymbol{\theta}$. Using the formulation in Eq. (31) for each estimate, posterior PDFs are informed using Bayes' rule, i.e.,

$$PDF\left(\boldsymbol{\theta}\right) = \frac{CLF\left(\boldsymbol{\theta}\right)^{u} \text{Prior}\left(\boldsymbol{\theta}\right)}{\text{Normalizing Const.}} \tag{34}$$

Here, the normalizing constant is found using the law of total probability.

The parametric uncertainty of $\boldsymbol{\theta}$ is estimated from the posterior PDF. The estimate used here is the variance of the joint posterior probability density function $PDF\left(\boldsymbol{\theta}\right)$, per

$$\sigma_{\boldsymbol{\theta}}^{2} = \int_{\boldsymbol{\theta}-\text{space}} PDF\left(\boldsymbol{\theta}\right) \sum_{j=1}^{n_v} \left(\theta_j - E\left[\theta_j\right]\right)^2 d\boldsymbol{\theta} \tag{35}$$

where $E\left[\theta_j\right]$ is the expected value, or mean, of parameter j, and $PDF\left(\boldsymbol{\theta}\right)$ is the posterior probability density function of $\boldsymbol{\theta}$.

3.4. Results:

The benefit of using BU data in addition to the default TD data is evaluated. Connection uncertainty is estimated and factored into the evaluation of parametric uncertainty. The CP model was run using the calibrated values of $\boldsymbol{\theta}$ returned by the calibrations on the TD data only and the TDBU combination. The model was also run using the BU reference values. The results of each calibration are compared to the

experimental TD data. The parametric uncertainty associated with the TD and TDBU calibrations are shown. The sum of the squared relative error of the response of the CP model is also shown, as well as the relative error plus the BU penalty. The performance and uncertainty measures are also shown for the hypothetical BU reference estimates. A parametric study of the variance of the penalty, σ_p^2, is performed.

The proportional limit from the experimental TD data (Spitzig and Keh, 1970a) and from the various calibrations of the CP model are shown for three temperatures and orientations in Figure 3.3. The angle χ is the misorientation between the maximum resolved shear stress plane of the loading and the reference (110) slip plane. The BU calibrated model returned yield strengths that greatly exceeded those from experimental data at lower temperatures. At 250 K, the BU had much more agreement with experimental data. The TDBU based calibration performed nearly as well as the purely TD based calibration.

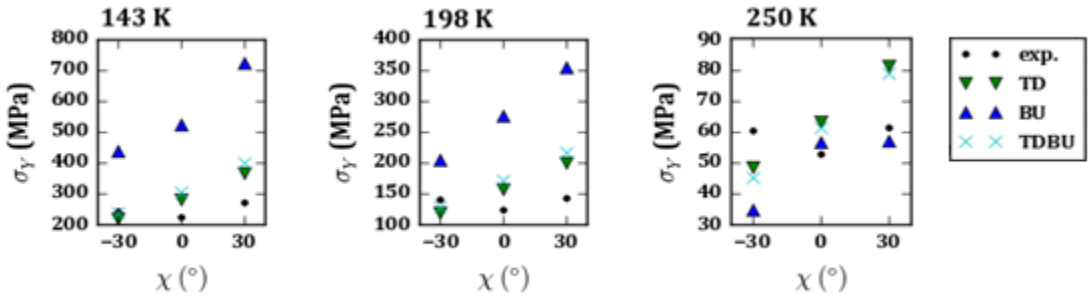

Figure 3.3. The proportional limit at three temperatures for loading on three crystallographic orientations. The BU used here is later referred to as Simulated BU.

The performance of each calibration was calculated by the sum of the squared errors (SSE) divided by the expected variances, $\sigma_{\exp,i}^2$, i.e.,

$$\text{SSE} = \sum_{i=1}^{N_{\text{data}}} \left(\frac{Y^M\left(\mathbf{x}_i, \hat{\boldsymbol{\theta}}\right) - Y^E\left(\mathbf{x}_i\right)}{\sigma_{\text{exp},i}} \right)^2 \tag{36}$$

Also, the BU penalty was calculated for each estimate, $\hat{\boldsymbol{\theta}}$, i.e.,

$$\text{Penalty} = \sum_{j=1}^{n_v} \left(\frac{\hat{\theta}_j - \hat{\theta}_{j,\text{BU}}^{ref}}{\sigma_p} \right)^2 \tag{37}$$

These performance measures are shown alongside the parametric uncertainty estimate $\sigma_{\boldsymbol{\theta}}^2$ for each calibration in Table 3-6. Across all shown BU reference estimates, the SSE is best for the TD-only calibrations. The SSE+Penalty is always minimized by the TDBU calibration. If the trend demonstrated by the examples holds for all BU reference estimates (and connections), the SSE and SSE+Penalty measures are insufficient as measures of empirical support for the TDBU connection. The parametric uncertainty estimate can increase or decrease with the addition of BU data, depending on the relationship between the TD likelihood function and the BU penalty function. This is shown in the change in the variance of the calibrated parameter values, $\sigma_{\boldsymbol{\theta}}^2$, also in Table 3-6.

Table 3-6. The relative performance of TD and TDBU calibrations of the CP model for $\sigma_p = 0.1$, based on different BU reference estimates of $\boldsymbol{\theta}$. For each BU reference estimate, the better performing calibration is underlined.

BU estimate $\hat{\boldsymbol{\theta}}_{\mathrm{BU}}^{\mathrm{ref}}$	**Calib.**	**SSE**	**SSE + Penalty**	u	$\sigma_{\boldsymbol{\theta}}^2$
Simulated	TD	37.7	161.7	5.98×10^{-2}	**0.296**
	TDBU	83.1	102.3	1.17×10^{-2}	**0.317**
"cooperative"	TD	37.7	81.0	5.98×10^{-2}	**0.296**
	TDBU	56.1	57.5	4.34×10^{-2}	**0.249**
"spurious"	TD	37.7	262.6	5.98×10^{-2}	**0.296**
	TDBU	78.0	224.4	5.69×10^{-3}	**0.340**

The results shown in Table 3-6 indicate that the "cooperative" $\hat{\boldsymbol{\theta}}_{\mathrm{BU}}^{\mathrm{ref}}$ values are the only case for which the TDBU connection is supported as implemented. The "cooperative" TDBU calibration exhibits a parametric uncertainty less than that of the TD-only calibration. Thus, this particular combination of TD and BU informed functions leads to a calibration where the benefit of additional data is more pronounced than the cost of using an additional, less relevant data set. Notably, the "cooperative" $\hat{\boldsymbol{\theta}}_{\mathrm{BU}}^{\mathrm{ref}}$ is not equal to $\hat{\boldsymbol{\theta}}_{\mathrm{TD}}$, implying that an effective connection between two uncertain sources need not be exact. u is shown to decrease from TD to each TDBU case, as is expected.

The parameter σ_p^2 controls the severity of the penalty function. In theory, it reflects the intrinsic uncertainty of the BU estimate in $\boldsymbol{\theta}-$space. In practice, it affects the degree of influence the BU reference has on the TDBU calibration result. If the value of σ_p^2 is too small, the TDBU calibration becomes insensitive to the TD data. Likewise, if the value of σ_p^2 is too large, the BU data have no effect on the TDBU estimate. To demonstrate this, the value of σ_p^2 is varied, and the results of the TDBU calibration are

shown, in Table 3-7. The values of $\hat{\boldsymbol{\theta}}_{\text{TDBU}}$ are shown in Table 3-4 for all the values of σ_p^2 explored in this parametric study. The value of $\sigma_{\boldsymbol{\theta}}^2$ returned for BU-only calibrations is largely a function of the value chosen for σ_p^2. This is also shown in Table 3-7. Given that the value of σ_p^2 was not empirically derived, the BU only calibrations cannot be easily compared with TD or TDBU in terms of $\sigma_{\boldsymbol{\theta}}^2$.

The results in Table 3-7 suggest that the TD calibration is the option with the least uncertainty. The value of $\sigma_{\boldsymbol{\theta}}^2$ is lower for the TDBU option where σ_p^2 is 0.02, however this case is considered inappropriate. As the value of σ_p^2 is decreased, the penalty functions contribute to increasingly narrow PDFs, as shown in the bottom row of Table 3-7. When two distributions are combined multiplicatively, a drastically narrower distribution will dominate the result. When the value of σ_p^2 is reduced to 0.02, the reduction of $\sigma_{\boldsymbol{\theta}}^2$ that occurs is an artifact of the TD likelihood function having a negligible effect on the CLF. This approach assumes that the empirically gathered TD information is the default information source for the CP model, so the $\sigma_p^2 = 0.02$ calibration, which doesn't effectively include the default information, is not an eligible option. Thus, the eligible option with the least uncertainty is identified to be the TD calibration.

Table 3-7. Parametric study of σ_p^2. The simulated $\hat{\boldsymbol{\theta}}_{\mathrm{BU}}^{\mathrm{ref}}$ is used for all cases. Penalty is 0 for BU only calibration. The values of $\sigma_{\boldsymbol{\theta}}^2$ for BU only calibrations are shown for the different values of σ_p^2.

σ_p	**Calib.**	**SSE**	**SSE + Penalty** for $\sigma_p^2 = \{0.5^2, 0.2^2, 0.1^2, 0.05^2, 0.02^2\}$					u	$\sigma_{\boldsymbol{\theta}}^2$
--	TD	37.7	42.6	68.4	160.5	529.2	3110	5.98×10^{-2}	**0.296**
0.5	TDBU	39.2	43.3	64.8	141.6	448.7	2598	4.70×10^{-2}	**0.301**
0.2	TDBU	52.7	55.9	72.5	131.9	369.5	2033	2.48×10^{-2}	**0.311**
0.1	TDBU	83.1	85.0	95.2	131.6	276.8	1294	1.17×10^{-2}	**0.317**
0.05	TDBU	130.6	131.3	134.9	147.9	199.6	561.7	5.79×10^{-3}	**0.312**
0.02	TDBU	213.2	213.3	213.8	215.7	223.1	274.9	3.53×10^{-3}	**0.222**
		SSE	$\sigma_{\boldsymbol{\theta}}^2$ for $\sigma_p^2 = \{0.5^2, 0.2^2, 0.1^2, 0.05^2, 0.02^2\}$						
--	BU	671.9	0.647	0.161	0.042	0.011	0.006	--	--

3.5. Conclusions

TD and BU calibrations of a scientific model and a novel treatment of connections between models were used to make decisions in the construction of a hierarchical multiscale model of single crystal bcc Fe with scarce input data (a typical condition for simulations of this type). A likelihood function was informed via SOR surrogate models for the TD calibration pathway. A penalty function was informed by the reference estimate of the BU simulation and an estimate of the associated uncertainty. The TDBU estimate was informed as a constrained optimization. The effectiveness of any pairing of TD and BU information was approached by estimating an uncertainty cost associated with each connection. This cost was an offset to the clear advantage of additional data in a sparse data setting. An empirical TDBU connection test was formulated using this tradeoff. This test was used to demonstrate the different possible effects of including BU data alongside TD data. This test showed that an increase in

uncertainty accompanied the inclusion of the BU simulation data in the calibration of the CP model used.

The TDBU estimates showed an increased level of parametric uncertainty, compared to the TD only estimate. The lowest value for σ_p^2 used, 0.02, showed a reduction in $\sigma_{\boldsymbol{\theta}}^2$ versus the TD. This is assumed to be due to the exaggerated precision of the penalty function. For the remaining TDBU formulations, the value of $\sigma_{\boldsymbol{\theta}}^2$ was greater than that of the TD calibration. From Table 3-6 we can gather that the reduction of $\sigma_{\boldsymbol{\theta}}^2$ in a TDBU calibration is possible. Thus, the failure of the BU data inclusion in reducing uncertainty in $\boldsymbol{\theta}$ is likely due to the difference in TD and BU being too large to easily reconcile. In this case, the connection may be improved by reexamining the choice of model form. Additionally, it may be necessary to use a mesoscale model as a translator, i.e., to adapt the BU estimates to include multi-process interactive effects. As an interesting note, there can be uncertainty that arises due to imposing a single value on a parameter that in truth varies. It has been suggested (Mori, 2017) that the Peierls stress is a function of temperature. Considerations of model-model connections may need to include such considerations of the underlying parameters.

This approach allows decision-makers to recognize the tradeoffs of imposing connections between models. In hierarchical multiscale models, parameters are often used to connect models between length-scales. The additional demands incurred by reconciliation between models might outweigh benefits in some cases, as is explored in Section 3.1. The connection between models may or may not be useful in approaching more detailed descriptions of a material, when uncertainty is considered. These

connections can be investigated with the method presented here, without the expense of gathering additional data. This provides needed decision support for the selection of connections in hierarchical multiscale models.

TDBU calibration can potentially alleviate issues of parameter non-uniqueness which often arise in TD-only calibrations. By applying data from multiple sources, TDBU calibration of parameters is less susceptible to non-uniqueness of parameters. The obstacle to broad applicability of such techniques is that in some cases, the combination of multiple sources of information will not be empirically sound, even if the connections are theoretically plausible. Once it is possible to empirically qualify connection strategies, such TDBU methods can be rigorously applied. Successful development of rigorous TDBU methodologies would thus benefit the calibration of a wide array of material models.

The method this work presents is not a search method. It assumes that new connections are between verified and validated models. The method examines the suitability of connecting these models, given that the validity of a connection does not necessarily follow from the validity of the comprising models. The models are each considered valid at individual length-scales; combined, they are operating beyond the scope of their initial validation. This method is a multiscale calibration process and preliminary to validation. Care must be taken to distinguish the failure of the connection from the failure of any component model.

The estimate of the connection cost, u, used in this work is straightforward to apply. It is based on a deterministic comparison of performance of ML estimates. This

approach may not be suitable for all calibration cases, and it is not rigorously derived here. The development of more comprehensive approaches to this step of the procedure will be the focus of future work.

The connection test is sensitive to the value of σ_p^2. An overly small value of σ_p^2 can coerce a reduction in $\sigma_{\boldsymbol{\theta}}^2$ by overwhelming the contribution of the TD data. Caution must be taken in selecting a value of σ_p^2 which allows both TD and BU data to influence the CLF. The relative influence of BU and TD can be monitored by comparing the variance of the TD-only Likelihood function and the variance of the product of the BU penalty functions.

CHAPTER 4. MODEL FORM AND SVE SIZE IN THE HOMOGENIZATION OF CRYSTAL PLASTICITY OF CARTRIDGE BRASS

In this chapter, an uncertainty propagation study of a statistical volume element (SVE) based homogenization is performed, focusing on model form and numerical uncertainties. A rate-dependent crystal plasticity (CP) model of cartridge brass is calibrated to room temperature uniaxial tension testing data of an annealed sample. Model forms are considered with and without the inclusion of back stress in the CP model. Three sizes of SVE are explored for numerical uncertainty effects. Effects are shown in a Bammann-Chiesa-Johnson (BCJ) macroscopic viscoplasticity model, calibrated element-wise to SVEs from an ensemble, in simulations of quasi-static uniaxial tension. The selection of model form is discussed. The numerical uncertainty of the homogenization process is quantified.

4.1. Introduction

Simulations of materials are limited in resolution and scope (Curtin and Miller, 2003). These limitations give rise to length and time scales pertaining to the basic physical regimes used for modelling materials and their behavior (Geers and Yvonnet, 2016). Despite advances in algorithmic efficiency and computational throughput, multiscale models often must be employed to resolve both the mechanism and the use-case of interest (Ellis and McDowell, 2017; McDowell, 2010). The homogenization of direct numerical simulation (DNS) is one such multiscale method, and it is used to connect microstructure-sensitive descriptions of deformation to continuum material

models (Geers et al., 2010). For a given response or property of interest (i.e., quantity of interest (QoI)), the Representative Volume Element (RVE) is sufficiently large to establish a homogeneous response or property for a given material and microstructure (Benedetti and Barbe, 2013), based on a crystal plasticity model, for example. A finite element model informed by RVE response can efficiently simulate a complex part geometry under loading. However, the homogeneous properties and responses based on the RVE only hold at sufficiently large volumes with limited or weak field gradients, limiting their applicability to cases involving geometric discontinuities (holes, fillets, etc.) that induce high local fields that spatially concentrate within volumes smaller than the RVE size, or strong stress-or strain field gradients over such scales.

Intrinsic variability will arise for samples of material volumes less than that corresponding to the RVE size, since such Statistical Volume Elements (SVE) do not capture all the necessary correlation lengths of microstructure (and corresponding statistical moments) under applied loading that give rise to homogeneous properties or responses. Therefore, ensembles of SVE simulations are necessary to characterize the statistical range of expected responses for a given sample (SVE) size. In other words, SVEs are employed as ensembles to represent statistical information about the microstructure-sensitive properties of a material (Qidwai et al., 2012). If the goal of simulating an ensemble of SVEs is to replicate (or at least approximate) RVE response, then the SVE size must be large enough to capture the dominant correlation lengths of the target microstructure for the given QoI, accepting some degree of approximation in neglecting higher order moments that are necessary to capture all statistical moments of QoI response as expressed by the RVE. In some cases, dominant correlation lengths can

be quite large (e.g., hundreds of microns in the case of microtextures of alloys), rendering the concept of RVE as difficult to access computationally for certain QoIs related to peak concentrated stresses or strains, for example. However, if the goal of SVE ensemble simulations is to capture variability associated with sampling size effects for sub-RVE volumes, then SVE-based ensemble simulations are necessary to characterize variability in material response as a function of size (e.g., at notches or stress-raisers). In this case, the number of SVEs necessary within the ensemble (ensemble size) must be large enough to capture the majority of the variability associated with random sampling with regard to the QoI. This ensemble size will depend on how large the SVE is relative to the dominant correlation lengths that affect QoIs; if the correlation lengths are large, then a very large number of SVEs must be employed in ensemble simulations to capture overall variability. If the correlation lengths are relatively limited in spatial extent, then far fewer SVEs are required.

Most engineering simulations are performed with homogeneous material models. QoIs such as "elastic stiffness" are not very stringent in their requirements on RVE size and many heterogeneous fine scale material models are feasible to estimate these. However, for many other QoIs, care is often not taken in addressing the "size effects" in variability of QoIs associated with sampling integration point volumes smaller than the RVE for a given microstructure. In other words, homogeneous material models are often applied to model material responses at length scales beneath the characteristic scale of the RVE for a given QoI. Despite this limitation, homogeneous models are widely preferred to CP for polycrystalline metals in engineering applications, due to their ease of use and simpler calibration requirements, which most often do not carefully consider RVE size.

The deployment of additively manufactured (AM) components in real-world applications challenges this longstanding approach (Bikas et al., 2016), given the increased uncertainty surrounding the process and the design of parts with finer and finer feature sizes (e.g., holes, fillets, etc.) that interplay with some of the larger characteristic microstructure length scales and gradients of structure. AM feature sizes will most often be much finer than the associated RVE scale for a given QoI.

Multiscale methods have been used to approach the design of AM components in the presence of a statistical approximation of uncertainty (Gorguluarslan et al., 2015). While the uncertainty in AM is in large part due to mismatch between the dimensions of the designed part and the manufactured result, improvements in process may reduce this component of uncertainty in overall performance. Moreover, the dependence of manufacturing process and scales of structure on properties or response QoIs will receive increasing attention. The accurate prediction of microstructure and the use of microstructure-sensitive models will become increasingly important to AM reliability predictions as the technology matures.

Multiscale methods add complication and calibration expense, even when they allow for more efficient computation (Fan, 2011; Tallman et al., 2017). This complication can arise as model form compatibility concerns or increases in the data requirements of cross-scale predictions. For example, the size and number of SVEs needed in an ensemble to be representative of the material globally (a higher length scale) far exceed the extent of local variability studies. The determination of these parameters is interdependent with the determination of model form (at all included length scales) and

the selection of calibration data, i.e., an adjustment in one of these may engender changes in the others.

In this work, SVE-based ensembles are pursued to characterize statistical variability as a function of sampling size of characteristic microstructure for cartridge brass. A hyperelastic crystal plasticity (CP) model of cartridge brass is used with Dream3D instantiations of microstructure and is calibrated to experimental measurements of the uniaxial monotonic stress-strain behavior of the material undergoing quasistatic deformation. The calibrated CP model is used to inform a Bammann-Chiesa-Johnson (BCJ) macro viscoplasticity model. The BCJ model is calibrated to each SVE response within an ensemble of SVEs generated from grain size statistics extracted from characterization of cartridge brass microstructure. The BCJ parameter values which represent the SVE responses are used to inform a larger-scale implementation of a BCJ model with local variations in material response. A design of experiments methodology explores two sizes of SVE and two forms of the CP model. The length scales for which an SVE-based sampling approach is supported by the results of this work are discussed.

4.2. Background

Cartridge Brass (C260) plasticity has been widely studied through simulations and experiments (Battaile et al., 2015; Buchheit et al., 2005; Carroll et al., 2012; Chiarodo et al., 1974; Schwartzbart et al., 1951). Room temperature uniaxial tensile tests of C260 can be found in the literature (Battaile et al., 2015; Buchheit et al., 2005; Carroll et al., 2012). Work on the hardening properties of C260 has demonstrated a distinction between kinematic and isotropic hardening (Krieg, 1975; Wagoner, 1982). This distinction can be

summarized as the exhibition of transient kinematic hardening, with large strains dominated by isotropic hardening (Wagoner, 1982). Accurate descriptions of hardening in C260 are relevant to the question of model form.

The crystal plasticity of cartridge brass has been modeled previously (Jia et al., 2012; Kuhlmann-Wilsdorf, 1999). In these models, the inelastic part of the deformation velocity gradient, $\mathbf{L}^{in}$, is given by the sum of the contributions of the crystallographic slip system shear rates, i.e.,

$$\mathbf{L}^{in} = \sum_{\alpha=1}^{N_s} \dot{\gamma}^{\alpha} \mathbf{m}_0^{\alpha} \otimes \mathbf{n}_0^{\alpha} \tag{38}$$

where, in the intermediate configuration, $\mathbf{m}_0^{\alpha}$ and $\mathbf{n}_0^{\alpha}$ are the unit vectors in the slip and slip plane normal directions for slip system α, with shearing rate $\dot{\gamma}^{\alpha}$. The 12 slip systems considered in the modeling of the fcc lattice of cartridge brass have slip planes in the $\{111\}$ family and slip directions in $\langle 110 \rangle$. The determination of the shear strain rates follows from the flow-rule of the CP model. The model of Jia et al. (2012) includes a dislocation density based activation enthalpy driven flow-rule. A much less detailed flow-rule is employed in this work.

The FEM software Abaqus (Simulia, 2007) is used to implement the material deformation models in this work. UMAT formulations of the CP model for C260, as well as the BCJ model introduced later on, are called by Abaqus as subroutines.

A CP model originally developed to describe OFHC Cu is adapted for cartridge brass. The model is based on the model documented in the work of Tanner et al. (1999). It uses a phenomenological slip system flow rule definition, i.e.,

$$\dot{\gamma}^{\alpha} = \dot{\gamma}_0 \left| \frac{\tau^{\alpha} - A^{\alpha}}{g^{\alpha}} \right|^{m} \operatorname{sgn}\left(\tau^{\alpha}\right) \tag{39}$$

where the reference shear rate is $\dot{\gamma}_0$, the strain rate-sensitivity exponent is m, and for slip system α the resolved shear stress is τ^{α} , the back stress is A^{α} , and the drag stress is g^{α}. The model form uncertainty study highlights the role of the back stress in simulating polycrystalline deformation response.

The CP formulation decomposes kinematic and isotropic hardening. The dynamic recovery of both hardening types is included in evolution equations, i.e.,

$$\dot{g}^{\alpha} = g_{dir}\left[\dot{\gamma}^{\alpha} + \sum_{\beta \neq \alpha}^{N_s} 1.4\dot{\gamma}^{\beta}\right] - g_{dyn} g^{\alpha} \sum_{\zeta=1}^{N_s} \dot{\gamma}^{\zeta} \tag{40}$$

where g^{α} is the drag stress value for slip system α, g_{dir} is the direct drag stress modulus, and g_{dyn} is the dynamic recovery coefficient for drag stress. β and ζ are used as summation indices for all N_s slip systems. A coefficient of latent hardening of slip systems is assumed to be 1.4. Similarly, the back stress evolves in self-hardening format, i.e.,

$$\dot{A}^{\alpha} = A_{dir}\dot{\gamma}^{\alpha} - A^{\alpha}A_{dyn}\left|\dot{\gamma}^{\alpha}\right| \tag{41}$$

where A^{α} is the back stress for slip system α, A_{dir} is the direct hardening modulus for back stress, and A_{dyn} is the dynamic recovery coefficient of back stress.

Back stress is not always included in CP models. For example, the discrete Fourier transform approach to accelerated CP calculations (Alharbi and Kalidindi, 2015; Knezevic et al., 2009) is often used with formulations of the flow rule that omit back stress, to allow hardening to be resolved as a tensor quantity and not in terms of slip systems. Various forms of kinematic hardening laws exist, with non-trivial differences (Hennessey et al., 2017). The selection of specific kinematic hardening model can be addressed if the necessity of back stress in the modeling of a material is established. The model in this work will exercise CP without back stress by setting hardening parameters A_{dir} and A_{dyn} to zero, with $A^{\alpha} = 0$.

The toolkit Dream3D has provided powerful microstructure instantiation methods to materials science research (Groeber and Jackson, 2014). The software package includes modular data-manipulation routines called *pipelines* which allow for microstructure data to be collected from images, or to be generated from statistics and distributions. In modeling polycrystalline plasticity, the instantiation of microstructure is a key step. The work in this Chapter uses Dream3D to generate SVE ensembles from generating statistics for grain size and texture.

SVE homogenization has been used to propagate variability in microstructure to the macroscale (Yin et al., 2008). Yin et al. studied the effective properties of porous steel. By using a variance based global sensitivity analysis, the most influential parameters of microstructure were identified. In a Markov chain Monte Carlo (MCMC) method, fluctuations of these most influential parameters (representing the variability of the microstructure) were propagated to inform statistically defined parameters of a 1-D BCJ macroplasticity model. In this chapter, a similar workflow will be assembled, with the main addition of an implementation of a 3-D BCJ model with local response variability.

Periodic boundary conditions are used in this work. The boundary conditions used in SVE simulations influence their solutions and size requirements (Ostoja-Starzewski, 2006). Periodic boundary conditions allow convergence to unbiased predictions of material response at smaller SVE sizes than do Dirichlet or Neumann boundary conditions (Kanit et al., 2003). More advanced boundary conditions have been developed. By incorporating a statistical microstructure description and Green's function in an interaction kernel, boundaries can be informed to reflect exterior statistics (Ghosh and Kubair, 2016). To some extent, the shape of the SVE, when combined with periodic boundaries, can impose bias in an anisotropic manner (Glüge et al., 2012). This work uses the more traditional periodic boundary conditions, taking up the limitations of the approach with multiscale methods.

Commonly in industry, a macroscopic plasticity model is used in lieu of more intensive alternatives. A model of this type is used in this work. Belonging to the category of J2 plasticity models, the Bammann-Chiesa-Johnson (BCJ) model is a widely

used internal state variable model for macroscopic viscoplasticity (Bammann, 1984). It specifies temperature effects, rate sensitivity, and includes parameters which control the contributions of isotropic and kinematic hardening. Hardening is formulated with both static and dynamic recovery. In this work, the BCJ model is used with the temperature dependence and static recovery removed, and focuses on matching properties at room temperature. The inelastic portion of the unrotated stretching tensor, $\mathbf{D}^{in}$, is written as

$$\mathbf{D}^{in} = \left\langle f \sinh\left(\frac{\left\| \boldsymbol{\sigma} - \boldsymbol{\alpha} \right\| - \left(R + Y \right)}{V} \right) \right\rangle \left(\frac{\boldsymbol{\sigma} - \boldsymbol{\alpha}}{\left\| \boldsymbol{\sigma} - \boldsymbol{\alpha} \right\|} \right) \tag{42}$$

where f and V are parameters which modify rate sensitivity, Y is a parameter for initial yield strength, R is the isotropic hardening internal state variable, and $\boldsymbol{\alpha}$ is the kinematic hardening tensor. R evolves accordingly, i.e.,

$$\dot{R} = \left[H\mathbf{D}^{in} - \left(\sqrt{\tfrac{2}{3}} R_d \left\| \mathbf{D}^{in} \right\| \right) R^2 \right] \tag{43}$$

where H is the direct isotropic hardening coefficient and R_d is the dynamic recovery coefficient of isotropic hardening. Static recovery of isotropic hardening is omitted for this room-temperature application. The kinematic hardening tensor evolves as a co-rotational rate, i.e.,

$$\overset{\circ}{\boldsymbol{\alpha}} = \left[h\mathbf{D}^{in} - \left(\sqrt{\tfrac{2}{3}} r_d \left\| \mathbf{D}^{in} \right\| \right) \|\boldsymbol{\alpha}\| \boldsymbol{\alpha} \right] \tag{44}$$

where h is the direct kinematic hardening coefficient and r_d is the dynamic recovery coefficient of kinematic hardening. Static recovery is also omitted for kinematic hardening at room temperature. Here, this macroscopic plasticity model is made responsive to microstructurally dependent property variations through the statistical homogenization of CP-SVE simulations of $\sigma - \varepsilon$ response. A regression model is used to make efficient the repetitive fitting of the BCJ model to CP-SVE results.

A Gaussian process (GP) regression model is used to accelerate the fitting between plasticity models. This procedure uses a kernel function to predict a mean function across the parameter space from the values of prior observations, i.e.,

$$k\left(\mathbf{x}_i, \mathbf{x}_j\right) = h^2 \exp\left(-\frac{\operatorname{dist}\left(\mathbf{x}_i, \mathbf{x}_j\right)^2}{2l^2} \right) + \alpha\delta_{ij} \tag{45}$$

where h and l are hyperparameters controlling the scale and length of the squared exponential kernel function, and α is the hyperparameter controlling the noise in the GP, and δ_{ij} is the Kronecker delta. The Euclidian distance in parameter space between observations $\mathbf{x}_i$ and $\mathbf{x}_j$ is shown as $\operatorname{dist}\left(\mathbf{x}_i, \mathbf{x}_j\right)$. The GP was used to select the next parameter combination to execute to match to the CP-SVE results.

Numerical uncertainty is a prevalent issue in multiscale modeling (Kanit et al., 2003; McFarland and Mahadevan, 2008). The effects of numerical truncation, the simplification of problems to their first order terms, and the substitution of a finite sample for a large population are common instances where numerical uncertainty arises in materials models. In this work, the numerical uncertainty of the SVE based coarse graining of mesoscale polycrystalline plasticity will be quantified using an empirical test of two samples known as the Kolmogorov-Smirnov test.

Empirical cumulative distribution functions (ECDF) will be constructed from the simulation results. This method for describing statistical samples does not assume any form for the underlying distribution (Birnbaum, 1952). It is a step-function defined as a function of the variable x, i.e.,

$$F_N(x) = \frac{n}{N}, n = \#\text{of samples } X_i > x \tag{46}$$

where N is the total number of samples, X_i. It approximates the cumulative distribution function $F(x) = \text{Prob}[X \leq x]$.

The Kolmogorov-Smirnov (K-S) 2-sample test is based on the ECDF, and is used to test if two samples are taken from the same underlying distribution. The K-S statistic is determined from the maximal value of the absolute difference in the respective ECDFs, i.e.,

$$D_{N,M} = Max\left[\left|F_N\left(x\right) - F_M\left(x\right)\right|, \text{for all } x\right] \tag{47}$$

where $D_{N,M}$ is the K-S statistic between the first sample and second sample, whose ECDFs are $F_N\left(x\right)$ and $F_M\left(x\right)$, respectively. The K-S test assumes that the samples of each distribution are taken from a continuously defined variable, and that the samples are independent. The K-S test will be used in this work to quantify differences in the microstructure based response variability predictions made with each modeling approach.

4.3. Methodology

The methodology consists of a calibration of the CP parameters in two model forms, a design of experiments to generate SVE ensembles, a calibration of the BCJ model to individual SVEs, accelerated by the use of a Gaussian process regression model, and the simulation of larger volumes of the material with statistically informed elements. The steps of this method are elaborated here and are summarized in Figure 4.1.

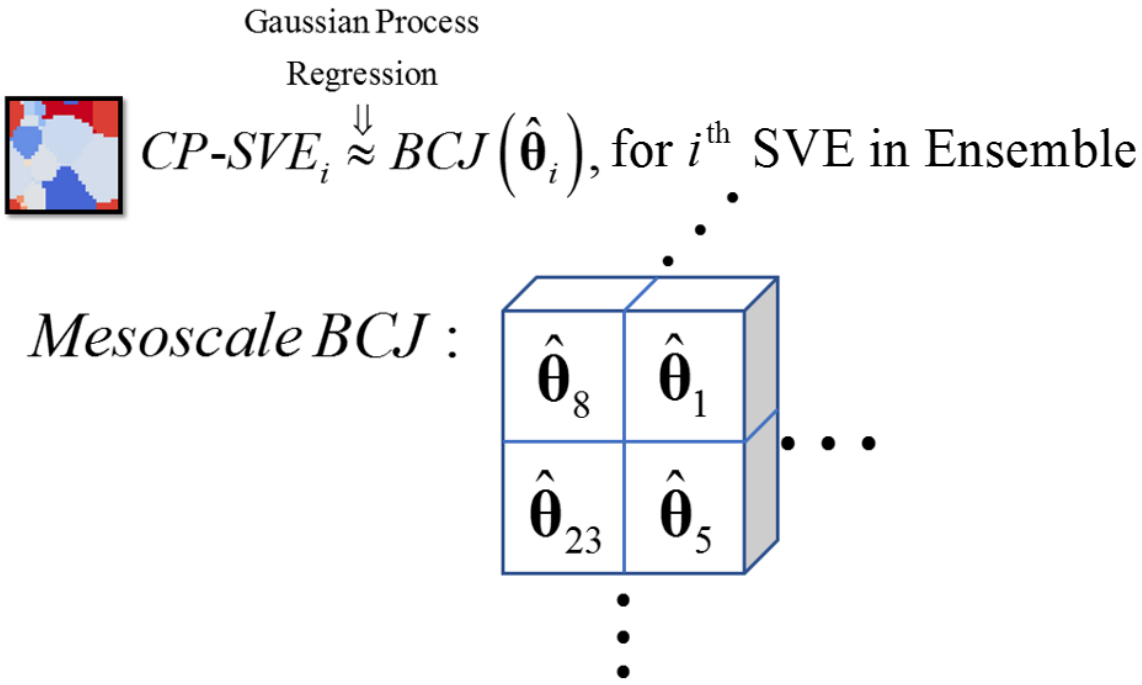

Figure 4.1. A schematic of the models and linking methods used in this chapter.

Design of Exp.	*CP with Back Stress*	*Back Stress* $= 0$
SVE Size $= 200\,\mu m$	$Ens\left(100\,SVEs\right)$	$Ens\left(100\,SVEs\right)$
SVE Size $= 300\,\mu m$	$Ens\left(30\,SVEs\right)$	$Ens\left(30\,SVEs\right)$

Figure 4.2. The design of experiments for the crystal plasticity simulations of polycrystalline volumes.

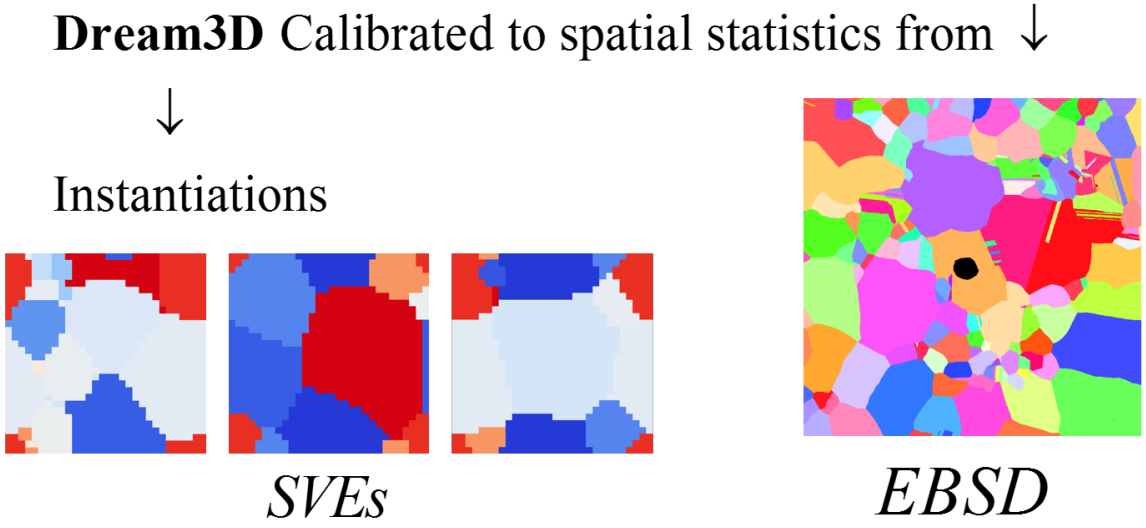

Figure 4.3. A schematic summarizing the generation of microstructures to be used in this chapter.

The same experimental data were used to calibrate the parameters of the CP for each model form. The experimental data were taken from Carroll et al. (2012) for the room temperature uniaxial tension testing of an annealed sample of C260. The sample, annealed at 600°C for 8 hours, included a laser etched hole of 100 μm diameter, positioned centrally through the thickness of 1.02mm. The calibration parameter sets are shown in Table 4-1. The calibrations were performed using ensembles of 10 polycrystalline simulations, each of 20 elements per side. Notably, these ensembles were smaller in number than those used in the coarse-graining work which follows.

The ensemble mean response was compared to the experimental $\sigma - \varepsilon$ curve for the material at room temperature under uniaxial tension. The material specimen was tested at an applied strain rate of $0.0012 \cdot s^{-1}$. The sum of squared errors (SSE) of stress as a function of axial strain was minimized. The model form excluding back stress was

calibrated in the same manner as the previous form; however, the parameters A_{dir} and A_{dyn} were both held fixed at 0.

Model form variations influence the calibration of the model. In the back stress inclusive case, large values were predicted for the back stress parameters, indicating a significant contribution to the simulated material response. In the case where these back stress parameters were set to zero a priori, other parameters in the calibration set were emphasized, i.e., g_0, g_{dir}, and g_{dyn}.

Table 4-1. Crystal plasticity calibration parameters given the same experimental data values, reflecting the model form choices often taken in the literature.

Parameter	**Parameter name**	**Value A (With back stress)**	**Value B (No back stress)**
g_0	Initial drag stress	11.31 MPa	34.51 MPa
g_{dir}	Direct hardening modulus for drag stress	193.51 MPa	379.95 MPa
g_{dyn}	Dynamic recovery coefficient for drag stress	3.685	5.751
$A(t=0)$	Initial value of back stress	0	0
A_{dir}	Direct hardening modulus for back stress	42.67 GPa	0 MPa
A_{dyn}	Dynamic recovery coefficient for back stress	1540	0

Microstructure used in the CP calibration was calibrated to electron back-scattering diffractometry (EBSD) data. The EBSD data was originally gathered alongside the tensile testing data (Carroll et al., 2012). 2D grain size statistics were gathered from the EBSD image provided by the authors of that work. The data was filtered to reject grains smaller than 10 microns in diameter as noise. An RVE-sized microstructure was

generated using Dream 3D (Groeber and Jackson, 2014). The microstructure was assigned initially random texture and equiaxed grain shapes. A lognormal distribution was used to model grain sizes. A 2D section was taken from that instantiated volume. By comparing the mean and standard deviation of effective grain diameter, the parameters of the log-normal distribution were calibrated. The 2D calibration results are shown in Table 4-2. The lognormal distribution was defined as,

$$d \sim Lognormal\left(\mu = 2.2, \sigma = 1.6\right) \tag{48}$$

$$P\left[d = x\right] = \frac{1}{x}\frac{1}{\sigma\sqrt{2\pi}}\exp\left(-\frac{\left(\ln x - \mu\right)^2}{2\sigma^2}\right), \quad x \in \left[4\mu\text{m},\ 304\mu\text{m}\right] \tag{49}$$

where d is the equivalent sphere diameter of grains, μ is the mean of the $\log\left(d\right)$ and σ is the standard deviation of the $\log\left(d\right)$. The tails of the distribution were cut off, limiting the grain size to lie in the range 4 to $304\,\mu\text{m}$.

Table 4-2. The 2D grain size statistics used to calibrate the distribution used in microstructure instantiation.

$\left(\text{2D Stats}\right)$	$E\left[d \mid \text{Section}\right], \left(\mu\text{m}\right)$	$\sigma\left[d \mid \text{Section}\right], \left(\mu\text{m}\right)$
EBSD Section	65.1	55.7
RVE Section	66.7	54.1

Once the CP parameters were calibrated, the CP simulations of SVE ensembles were performed. Ensembles of SVEs were generated using Dream 3D (Groeber and Jackson, 2014). The generating statistics for grain size were gathered from an EBSD image published in the work by Carroll et al. (2012). The material selected was annealed

at 600°C for 8 hours. SVE ensemble members were constructed using 20 or 30 hexahedral elements in each dimension for a total of 20^3 or 30^3 elements, as seen in Figure 4.4.

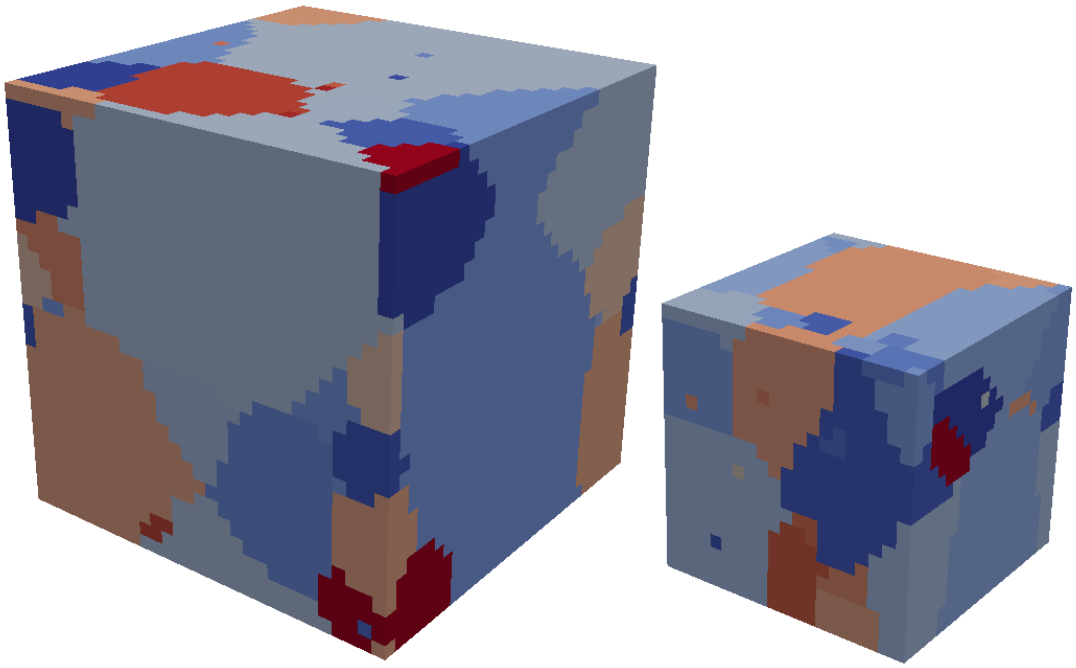

Figure 4.4. The two sizes of SVE used for calibration in the work are shown. The large SVE is 300 microns per side, the small SVE is 200 microns per side.

Due to the grain size distribution, the smaller SVEs each contained an average of 38 grains. A large variation existed in grain count between SVEs. The microstructures used in model form A correspond one-to-one with those used with model form B. SVE ensembles contained either 100 smaller SVEs or 30 larger SVEs. In all SVEs, elements measured $10\,\mu\text{m}$ in each direction. The microstructure statistics are shown in Table 4-3. Here, $E[d\,|\,\text{ens.}]$ is the expected value of the effective diameter of a grain in either ensemble, and $\sigma[d\,|\,\text{ens.}]$ is the standard deviation of the grain diameters within either ensemble.

Larger polycrystalline volumes were simulated with CP to investigate the effects of SVE size. Simulations were carried out for ten separate 60 elements per direction instantiations of the same microstructure statistics. A set of ten simulations was performed using each form of the CP model.

Table 4-3. 3D statistics of the number and equivalent diameter of the grains in the microstructure instantiations of each SVE ensemble in the study.

SVE size	**SVEs in ensemble**	**Total Grains**	**Grains per SVE**	$E[d \mid \text{ens.}]$	$\sigma[d \mid \text{ens.}]$
$(200\mu m)^3$	100	3777	38	35.25	40.75
$(300\mu m)^3$	30	2983	99	37.18	44.99
$(600\mu m)^3$	10	9018	902	37.5	41.29

Abaqus Standard (implicit) was used to simulate the polycrystals (Simulia, 2007). Periodic boundary conditions were used in each direction. In one direction, displacement was imposed on the boundary, simulating uniaxial strain at a constant rate of $0.0012\,\text{s}^{-1}$ at room temperature. To simulate the crystal plasticity of C260, a UMAT subroutine was called to define the stress-strain response. This UMAT was adapted for use on C260 from the model used by Tanner et al. on OHFC Cu (1999). The ensemble-averaged results of these simulations were compared to the experimental $\sigma - \varepsilon$ data for Cartridge Brass, shown in Figure 4.5. To compare with the data, a tensile monotonic load was simulated. An additional loading path which applied compression, followed by tensile loading, was used to distinctly inform the kinematic and isotropic hardening parameters of the BCJ model. The ensemble average results of these simulations are shown below, in Figure 4.6.

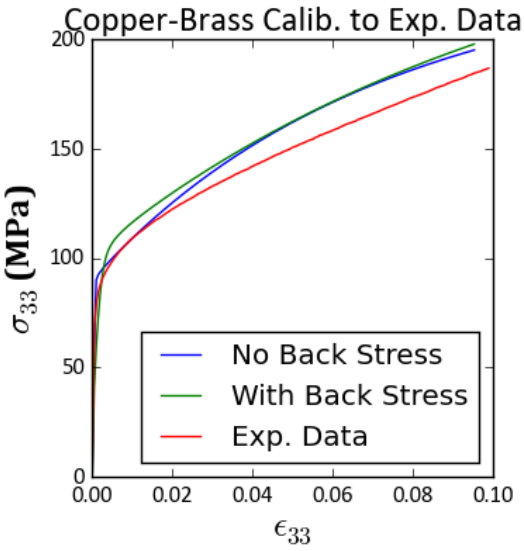

Figure 4.5. The comparison of the crystal plasticity results for both model forms with the experimental data previously obtained (Carroll et al., 2012).

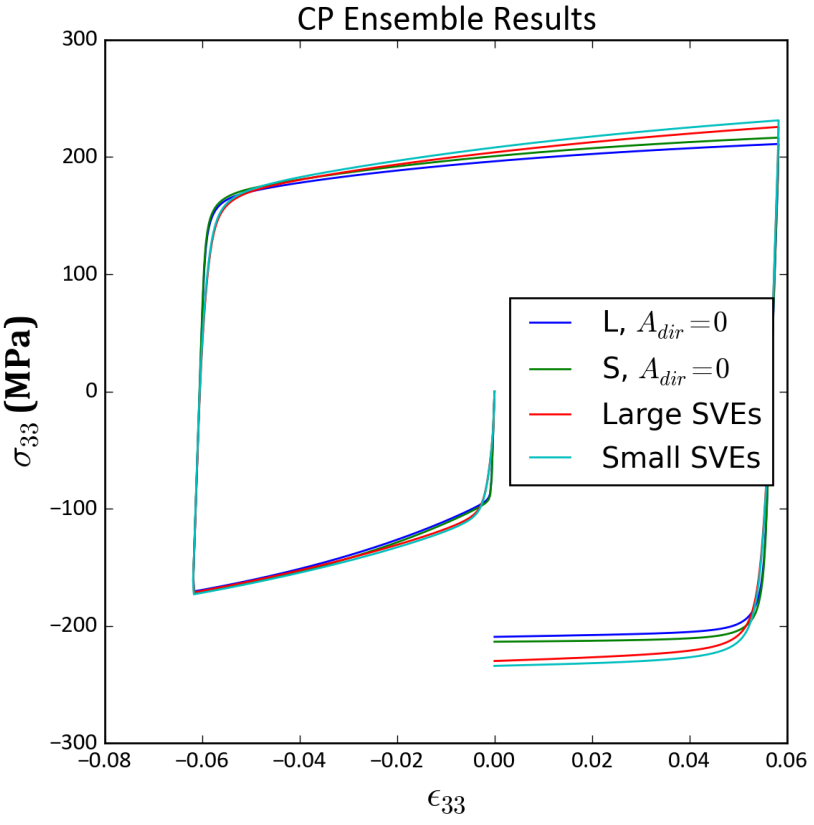

Figure 4.6. The SVE ensemble means for the CP simulations used to calibrate the BCJ parameters.

The BCJ model parameters were informed by calibrating the model to the results of each individual CP-SVE simulation. The rate sensitivity parameters, V and f, were determined by calibrating the BCJ model to CPSVE results taken at a series of simulated strain rates. The values of the rate sensitivity BCJ parameters are shown in Table 4-4. The remaining calibration parameters, $\boldsymbol{\theta}_{BCJ} = [E, Y, H, R_d, h, r_d]$, are estimated to fit to every SVE in an ensemble individually. This calibration procedure was accelerated by the use of a partially automated calibration routine. This routine is referred to as Autocal, and was developed alongside the work of this chapter. A detailed description of the package is left to Appendix A. The calibration was used to minimize the difference in the axial stress between CP-SVE and BCJ models, as a function of axial strain. This procedure is detailed below.

Table 4-4. The calibrated values of the rate sensitivity parameters of the BCJ model.

Parameter	Value
V	2.2
f	5×10^{-6}

An initial, one-at-a-time sensitivity study of parameters was first performed. Linear extrapolation, based on the sensitivity analysis, was used to make inductive guesses for the parameter values which fit to each SVE result. The BCJ model was run at each of these guesses. A GP regression model was constructed to interpolate between simulations to link BCJ parameter values to the prediction of $\sigma - \varepsilon$ behavior, using these inductive estimates as an initial dataset. Using the predictions of the GP model to adjust the parameter value estimates, the sum of squared errors (SSE) between the target (referring to the stress-strain response of a SVE plasticity simulation) and the prediction

of the GP model on the BCJ parameters was minimized. The GP model is formulated as follows:

$$\begin{aligned} Obj &= \sum_{timestep=1}^{800} \left(\sigma_{BCJ,timestep} - \sigma_{CP,timestep} \right)^2 \\ \hat{\sigma}_{BCJ,i} &\sim GP\left(\boldsymbol{\theta}_{BCJ} \right), \text{for } i \text{ in} \left(1,800\right) \end{aligned} \tag{50}$$

where the objective (Obj) is the sum of squared errors between the axial stress of BCJ and CP, measured at 800 linearly spaced time-intervals. A linear interpolation of the simulations is used as needed to inform the GP on this basis. Iteratively, the GP was trained on an accumulation of new BCJ results three times. Further optimization of BCJ parameters (until the predicted optimal BCJ parameter values ceased to change) was also attempted, but resulted in BCJ parameter values that led to unstable error accumulation in the plasticity simulation. The values of the BCJ parameters which corresponded to the smallest SSE, as predicted by the GP after three learning iterations, were then used in a subsequent batch of BCJ model runs. These estimated values were entered into a database for future use.

Autocal is a python package which builds on many other packages. The optimization was performed using scipy (Millman and Aivazis, 2011), the initial linear effects model was built using statsmodels (*statsmodels*, 2018), and the GP regression model was built using scikit-learn (Pedregosa et al., 2011), all of which are python packages. The Matern kernel function was used for the GP approach, and the hyperparameters were tuned to maximize the log likelihood of the model. The

hyperparameter optimization was repeated with randomly chosen starting conditions for every iteration, to avoid local maxima in the likelihood function.

The BCJ parameter estimates from the calibration were stored as libraries of local representations. Each CP-SVE simulation corresponded to an estimate for each BCJ parameter. As a result, these estimated parameters were not considered independent. The covariance and correlation of the parameters was set to reflect the variability of the material response to which those parameters were fitted. The analysis of the parameter estimates is included in the results section.

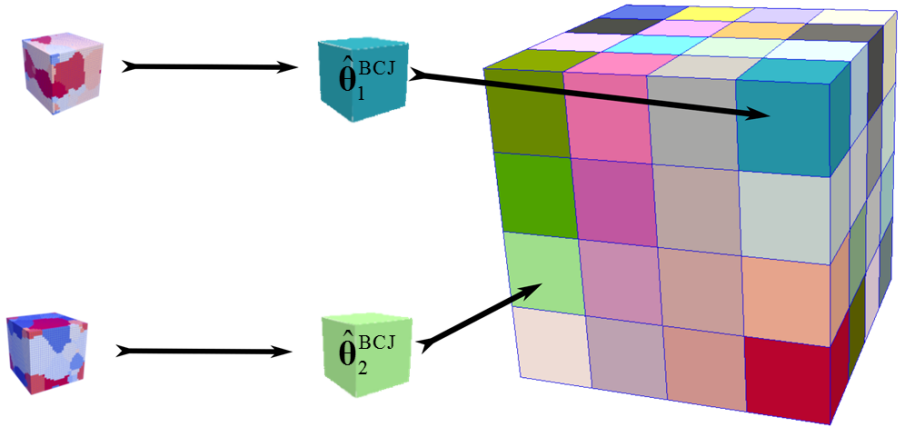

Figure 4.7. A schematic showing the BCJ parameter estimates, sourced from individual SVEs, informing the mesoscale model's individual single-integration-point elements.

Mesoscale models were constructed from the BCJ models by populating elements of a hexahedral mesh. Linear brick elements with reduced integration were used consisting of eight nodes and one integration point. The values of the six BCJ parameters passed into the UMAT subroutine were passed with unique values for each element. The values were drawn from a library of parameter estimates containing one estimation for each SVE in the ensemble. Thus, the BCJ parameters varied in value from element to element within the mesoscale mesh, as shown in Figure 4.7. The element size

corresponded to the size of the SVE which informed the parameter estimates used in that mesoscale model, e.g., when the 300 microns per side SVEs informed the parameters, the mesoscale mesh resolved elements of 300 microns per side. The mesoscale models were used to simulate two hexahedral volumes, of either 0.6mm or 1.2mm in size per direction.

4.4. Results

The variability and mean predictions of the $\sigma - \varepsilon$ behavior of polycrystalline cartridge brass are explored with two CP model forms and two characteristic SVE sizes. Uncertainty is attributed to numerical imprecision in homogenization and variability in microstructure.

The SVE instantiations from Dream3D contain variability. Grain shape and texture were not varied. The size of grains and the number of grains per SVE were highly variable. The statistics of the grain size distributions of each SVE are shown in Figure 4.8 and Figure 4.9. A cluster of SVEs with much lower than average grain number are present in the smaller sized SVE ensemble.

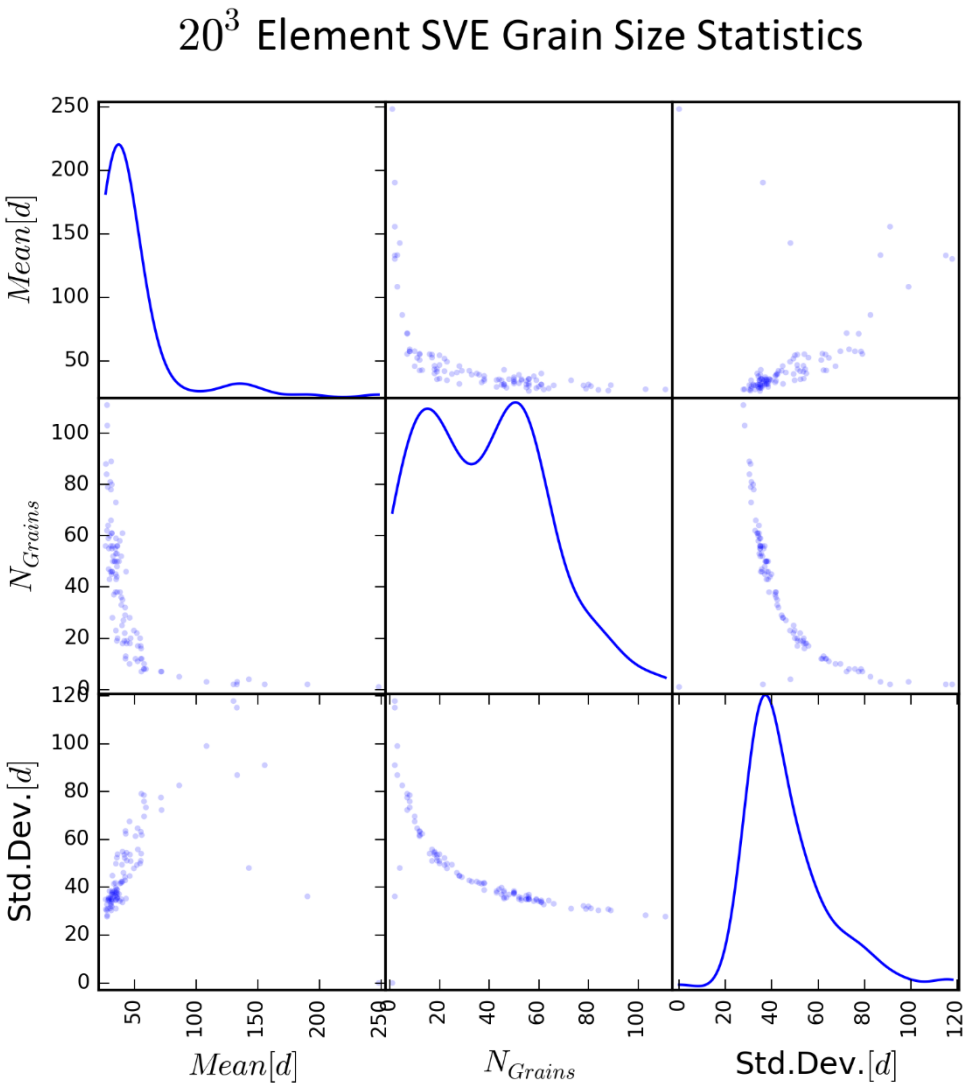

Figure 4.8. Pairwise scatter plots of the grain size statistics which belong to each SVE in the ensemble of 100 smaller polycrystalline volumes. Kernel density estimates (kde) of individual statistics are shown on the diagonal subplots. The y-axis of the kdes show probability density and have minima of zero.

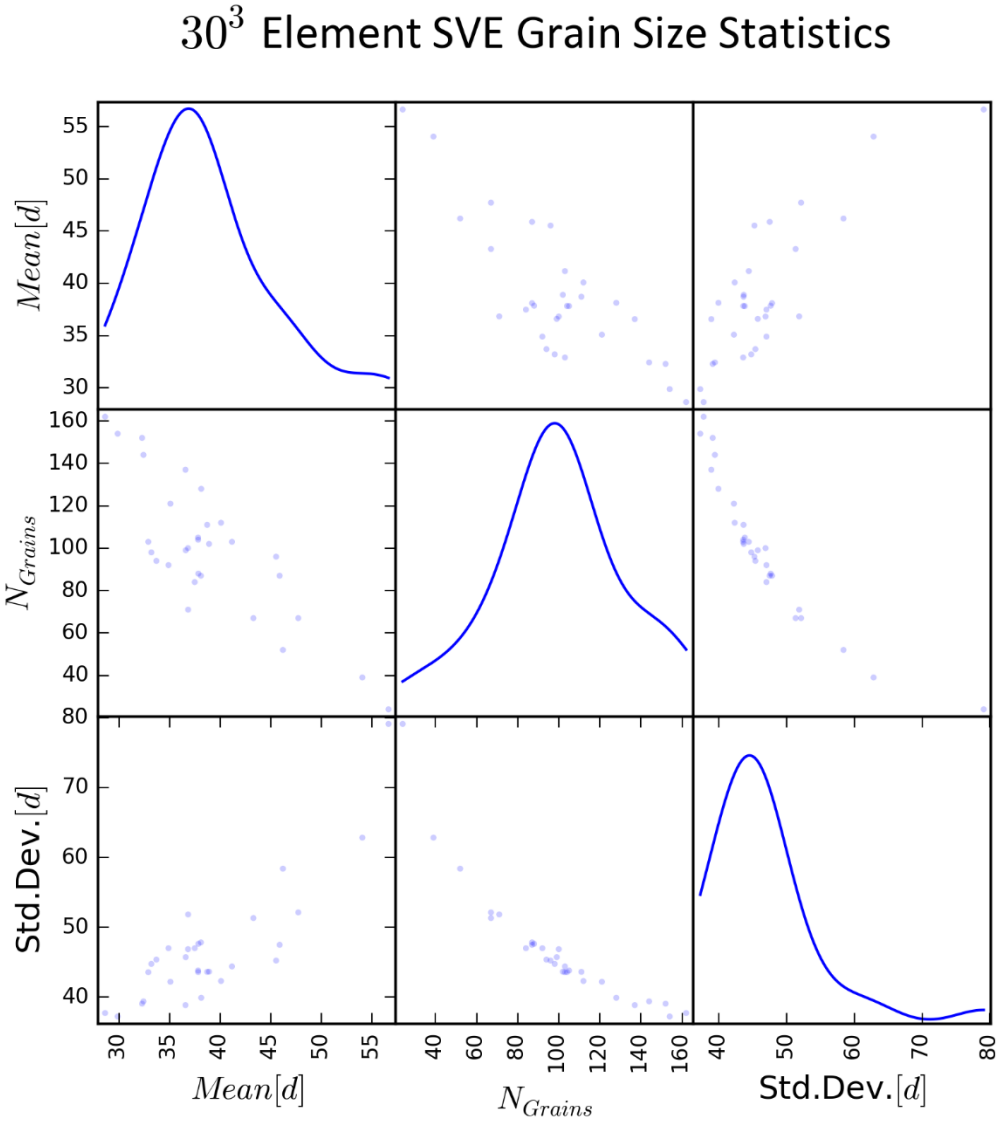

Figure 4.9. Pairwise scatter plots of the grain size statistics which belong to each SVE in the ensemble of 30 larger polycrystalline volumes. Kernel density estimates (kde) of individual statistics are shown on the diagonal subplots. The y-axis of the kdes show probability density and have minima of zero.

The CP simulations present variability in stress response to deformation. This variability is apparent in the results shown in Figure 4.10.

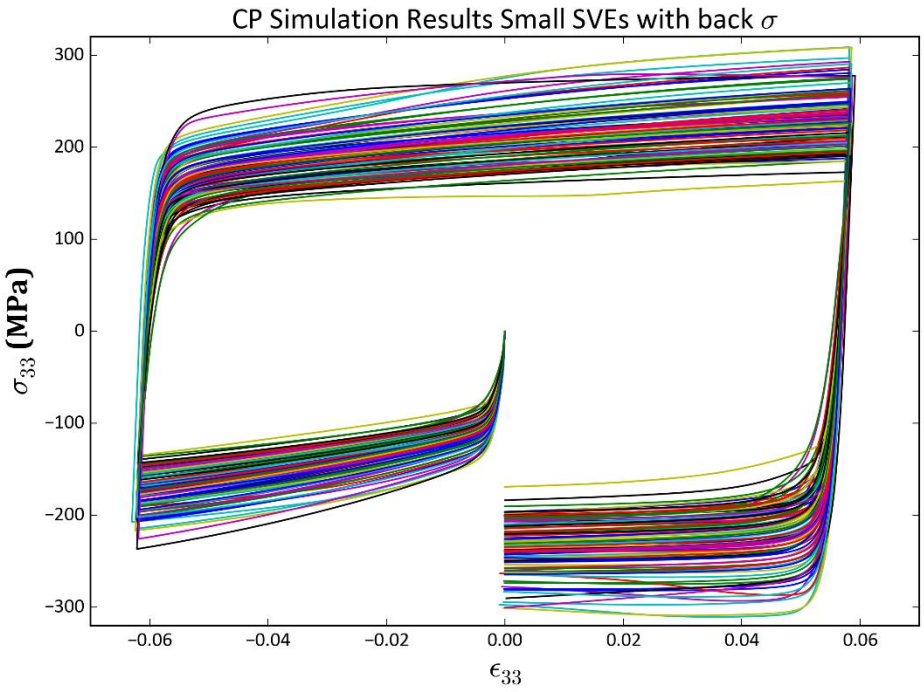
CP Simulation Results Small SVEs with back σ
300
200
100
0
−100
−200
−300
σ_{33} (MPa)
−0.06
−0.04
−0.02
0.00
0.02
0.04
0.06
ϵ_{33}

a)

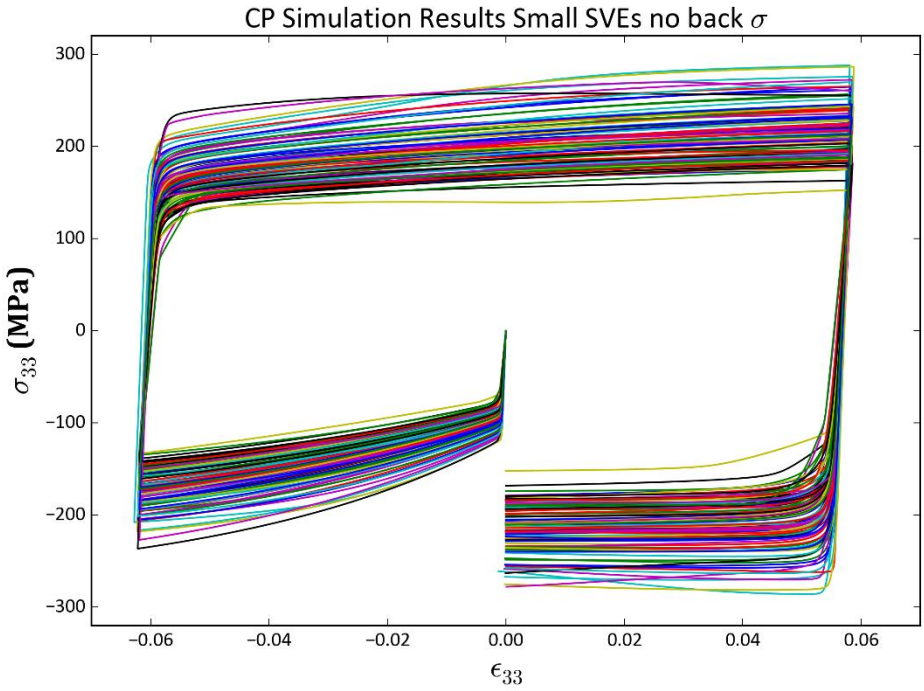
CP Simulation Results Small SVEs no back σ
300
200
100
0
−100
−200
−300
σ_{33} (MPa)
−0.06
−0.04
−0.02
0.00
0.02
0.04
0.06
ϵ_{33}

b)

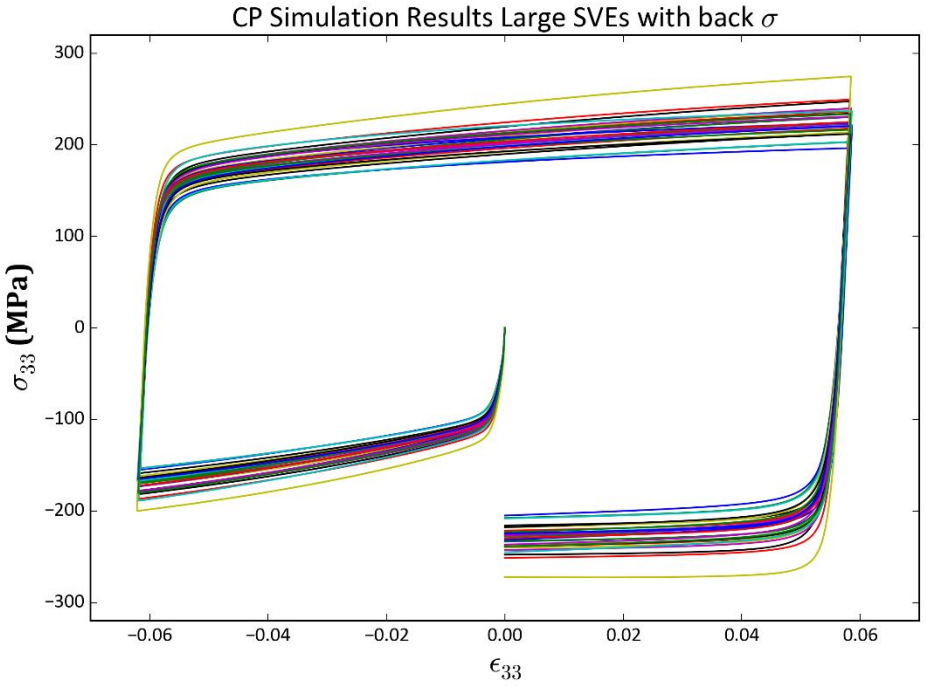

c)

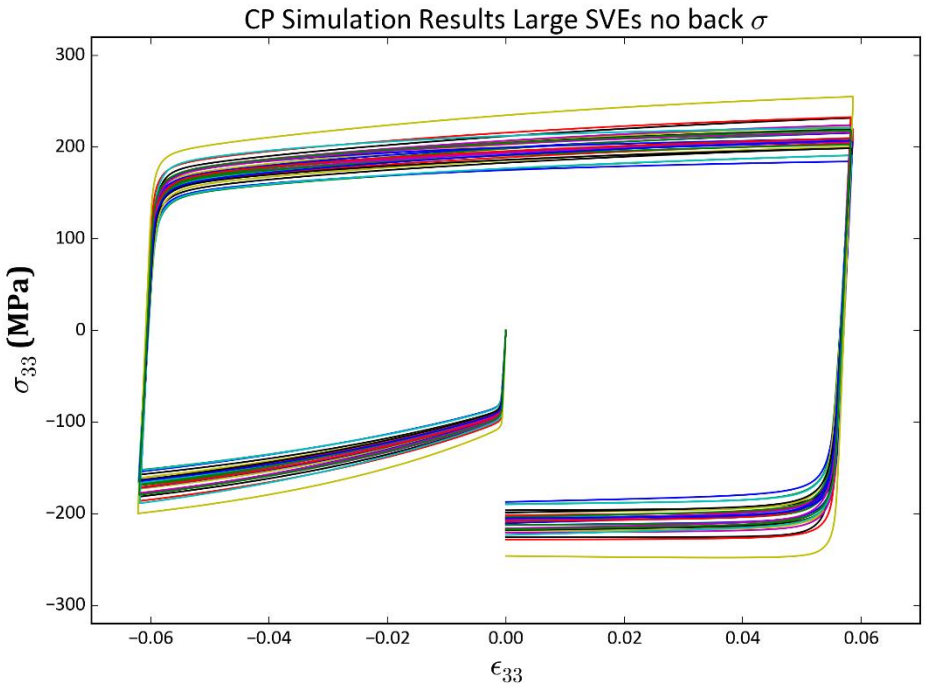

d)

Figure 4.10 a, b, c, d. The results of the CP-SVE simulations for both SVE sizes and CP model forms.

This variability reflects the microstructure variations present in the SVE ensembles. The approximation of the SVE results using the BCJ model largely captures this variability.

The discrepancy between the CP-SVE results and the BCJ approximations is formulated as

$$Y_{CP}^{M}\left(SVE_i, \text{strain}\right) = Y_{BCJ}^{M}\left(\hat{\boldsymbol{\theta}}_i, \text{strain}\right) + \delta\left(\text{strain}\right) + Error \tag{51}$$

where $Y_{CP}^{M}\left(SVE_i, \text{strain}\right)$ is the CP model response (axial stress) of the i-th SVE and as a function of axial strain, $Y_{BCJ}^{M}\left(\hat{\boldsymbol{\theta}}_i, \text{strain}\right)$ is the BCJ model response given the i-th calibration parameter estimate $\hat{\boldsymbol{\theta}}_i$ as a function of axial strain, and $\delta\left(\text{strain}\right)$ is the bias of the BCJ approximations as a function of axial strain. This formulation is applied to each combination of CP model form and SVE size included in the study. The bias of the BCJ approximation is shown in Figure 4.11. The bias is larger for the homogenizations based on the smaller SVEs.

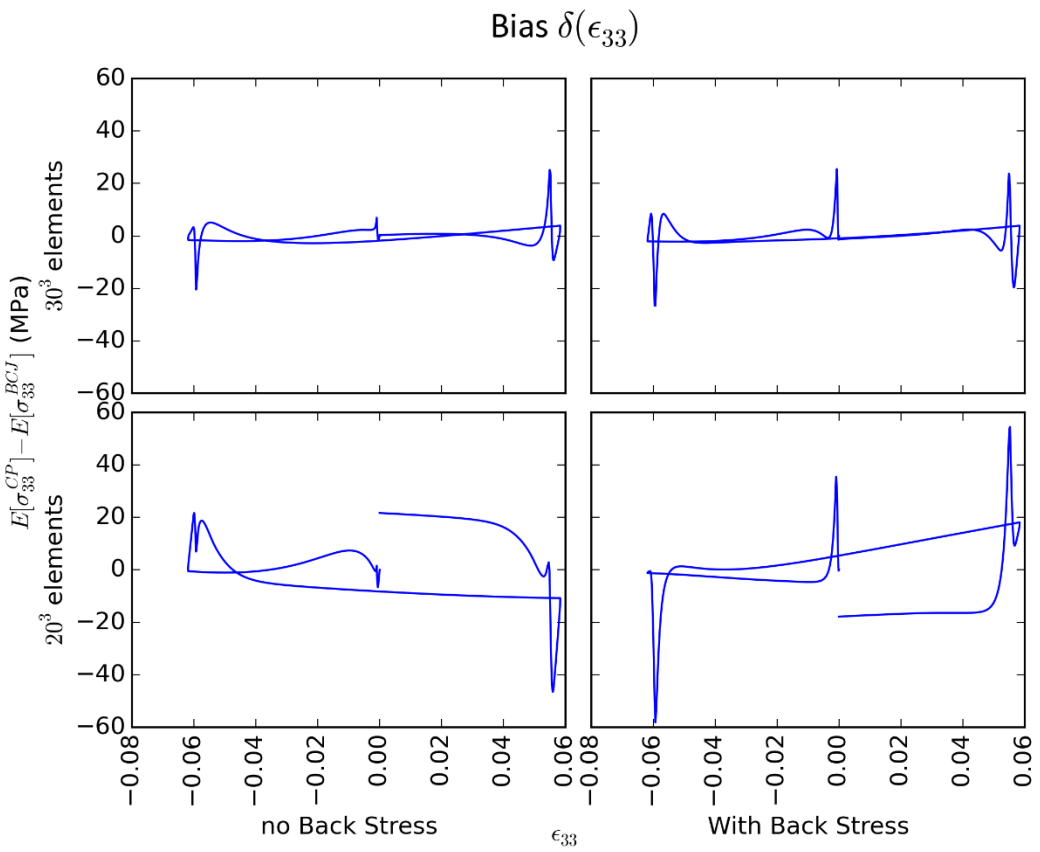

Figure 4.11. The bias as a function of the applied axial strain history for each combination of SVE size and CP model form.

The error term is treated as a random variable. The variation of the residual between the target (CP) and the approximation (BCJ) is affected by numerous factors. The calibration algorithm, the limitations of the reduced order model, and the variations contained in the SVE ensemble all influence this mismatch. There is a complicated covariance between different parts of the residuals as functions of axial strain. The details of this covariance left to later discussion. Without involving the covariance of the error, the error can be described as a normally distributed random variable whose variance is a function of the deformation history. This variance is shown in Figure 4.12.

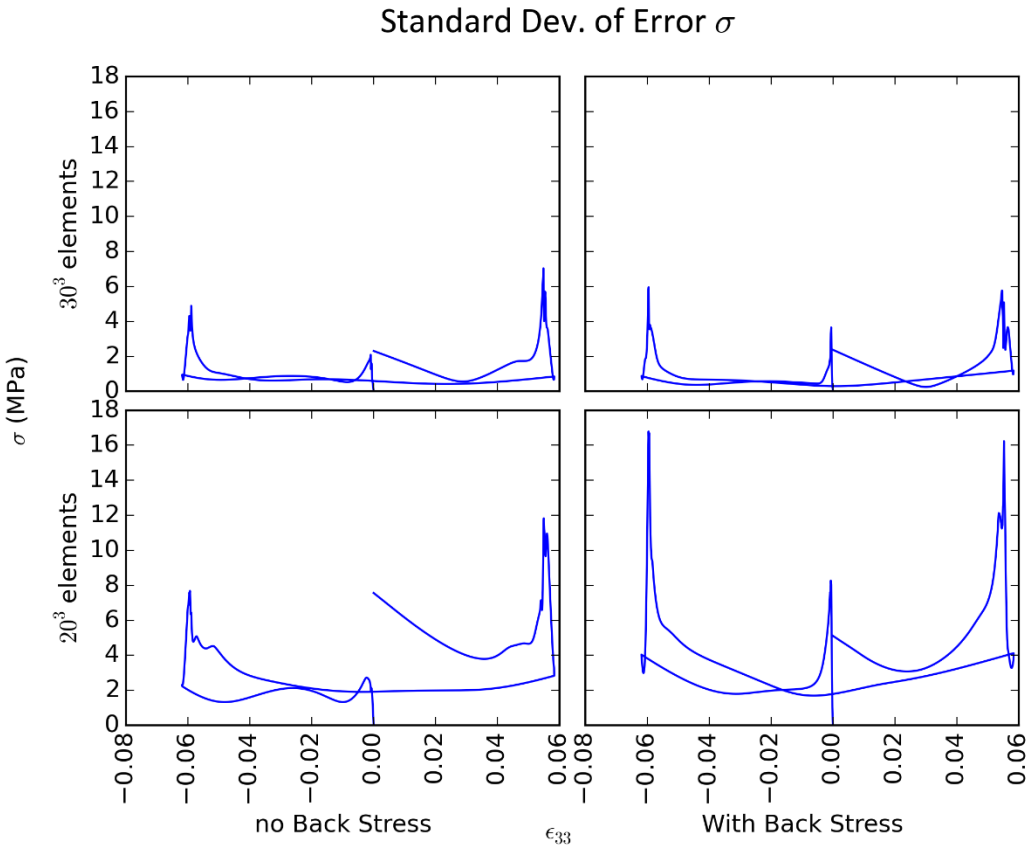

Figure 4.12. The standard deviation of the error between the BCJ model and the target CP-SVE results as a function of the applied axial strain path.

The error of the approximation was small relative to the variation captured by the approximation. This is measured by the coefficient of determination, R^2. For each ensemble, the R^2 was taken for each SVE. The compiled values are shown in Table 4-5. The minimum value of R^2 for each ensemble is the worst case of the approximation procedure.

Table 4-5. The coefficient of determination of the different homogenizations as averaged over each ensemble and as minima of each ensemble.

R^2	20^3el with A_{dir}	20^3el $A_{dir}=0$	30^3el with A_{dir}	30^3el $A_{dir}=0$
Average	0.999417	0.999587	0.999656	0.999734
Minimum	0.998129	0.997812	0.999515	0.99954

The BCJ approximations reflect all the microstructure dependent variability in the values given to the six calibration parameters. To show the relationships between the many parameters, which are implied by the fitting procedure, a correlation scatter-plot is included for each pair of calibration parameters. Each point in each of these plots represents the BCJ parameter values corresponding to a single SVE simulation. These scatter-plots are organized into a matrix layout, with each calibration parameter in turn appearing on the y and x axes. Along the diagonal of this matrix layout, KDEs are used to show the distribution of the values for each parameter individually. A matrix layout of scatter-plots is shown for each homogenization (Figure 4.13, Figure 4.14, Figure 4.15, and Figure 4.16). The correlation of the elastic stiffness via Young's modulus, E, and the initial yield strength, Y, is strongly positive in all four cases. This is quantified in each correlation matrix shown in Table 4-6. Parameter value means and standard deviations are also shown in Table 4-6. Model form and microstructure influence the BCJ estimates.

In the case of the kinematic hardening modulus, r_d, the kinematic hardening from the CP model back stress is captured along with the inter-granular kinematic hardening which occurs in polycrystalline metals. The difference in r_d between the two CP model forms is large and is present in all SVEs nearly equally. The effect of the microstructure instantiation variability on inter-granular kinematic hardening is inherently variable. By inspecting the ratio of $\frac{\text{St.D.}}{\text{Mean}}$ of r_d, evidence supporting this breakdown of the inter- and intra-granular kinematic hardening can be found. In the small SVE case without back stress, the ratio is 0.6. When back stress is excluded from CP, inter-granular kinematic hardening mechanisms dominate kinematic hardening behavior at higher length scales.

Table 4-6. Correlation coefficients between the BCJ parameters calibrated to individual SVEs. Mean values, standard deviations, and the standard deviation relative to the mean of each parameter is also shown.

30, w	E	H	R_d	Y	h	r_d	Mean	St.D.	$\frac{\text{St.D.}}{\text{Mean}}$
E	1.00	0.90	-0.51	0.95	0.45	0.56	112883	10950	0.097
H	0.90	1.00	-0.22	0.85	0.52	0.44	1032	97	0.094
R_d	-0.51	-0.22	1.00	-0.53	-0.28	-0.44	0.0708	0.0087	0.123
Y	0.95	0.85	-0.53	1.00	0.24	0.47	71.13	5.03	0.071
h	0.45	0.52	-0.28	0.24	1.00	0.62	14264	1506	0.106
r_d	0.56	0.44	-0.44	0.47	0.62	1.00	120.1	5.72	0.048
20, w	E	H	R_d	Y	h	r_d	Mean	St.D.	$\frac{\text{St.D.}}{\text{Mean}}$
E	1.00	0.87	-0.59	0.98	-0.19	0.10	113021	21241	0.188
H	0.87	1.00	-0.33	0.88	0.09	0.08	1039	190	0.183
R_d	-0.59	-0.33	1.00	-0.57	0.04	0.04	0.0670	0.0151	0.225
Y	0.98	0.88	-0.57	1.00	-0.21	0.07	81.02	12.36	0.153
h	-0.19	0.09	0.04	-0.21	1.00	0.41	6838	1544	0.226
r_d	0.10	0.08	0.04	0.07	0.41	1.00	84.1	11.06	0.131
30, no	E	H	R_d	Y	h	r_d	Mean	St.D.	$\frac{\text{St.D.}}{\text{Mean}}$
E	1.00	0.80	-0.49	0.88	-0.02	0.11	121041	11841	0.098
H	0.80	1.00	-0.02	0.63	0.23	0.27	1248	124	0.099
R_d	-0.49	-0.02	1.00	-0.72	0.55	0.51	0.1112	0.0136	0.122
Y	0.88	0.63	-0.72	1.00	-0.40	-0.28	85.67	6.14	0.072
h	-0.02	0.23	0.55	-0.40	1.00	0.90	1689	737	0.436
r_d	0.11	0.27	0.51	-0.28	0.90	1.00	57.7	14.75	0.255
20, no	E	H	R_d	Y	h	r_d	Mean	St.D.	$\frac{\text{St.D.}}{\text{Mean}}$
E	1.00	0.77	-0.56	0.93	-0.71	-0.43	122974	24033	0.195
H	0.77	1.00	-0.18	0.78	-0.34	-0.26	1247	221	0.178
R_d	-0.56	-0.18	1.00	-0.62	0.43	0.14	0.1047	0.0229	0.219
Y	0.93	0.78	-0.62	1.00	-0.58	-0.34	87.63	14.74	0.168
h	-0.71	-0.34	0.43	-0.58	1.00	0.64	1684	1010	0.600
r_d	-0.43	-0.26	0.14	-0.34	0.64	1.00	58.6	15.58	0.266

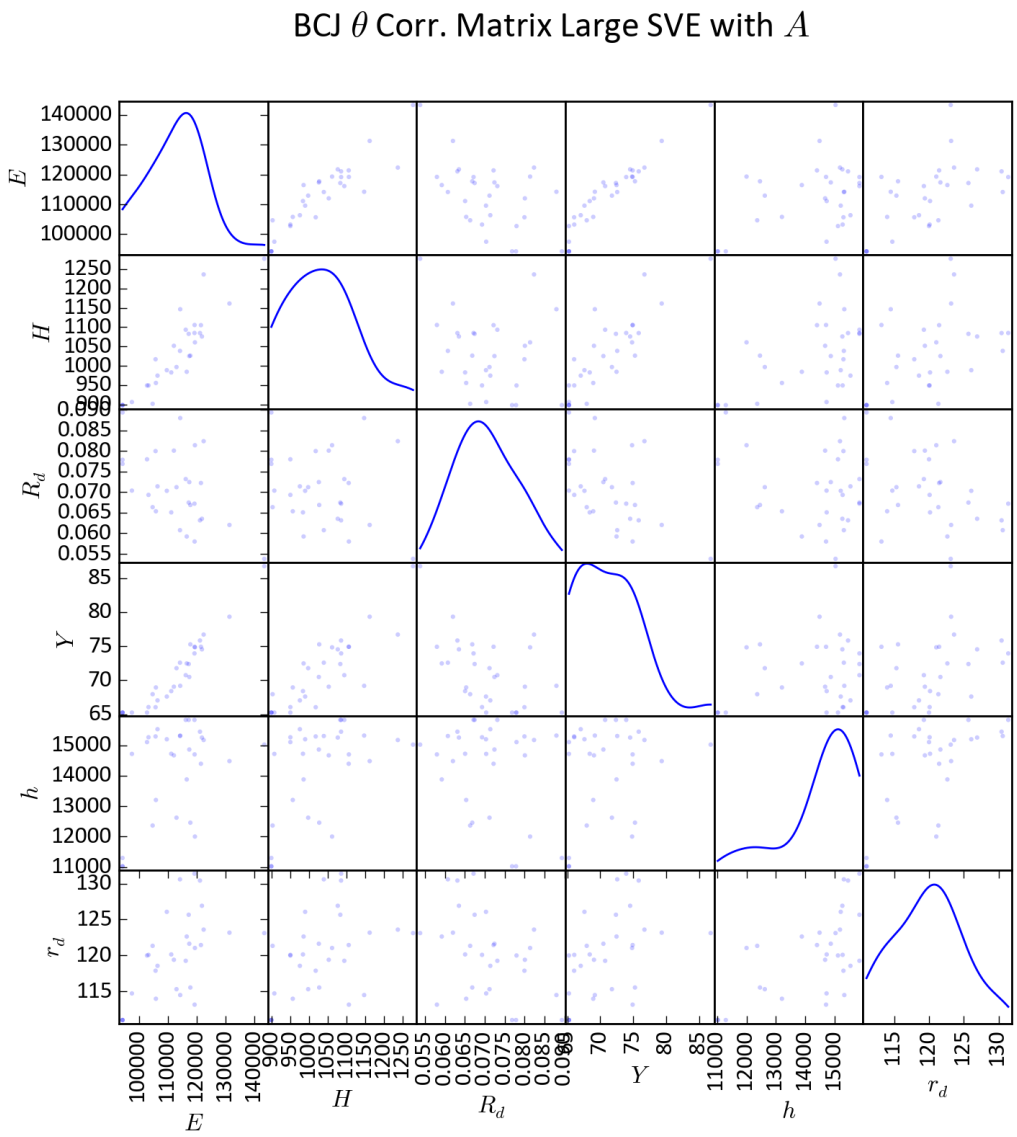

Figure 4.13. All calibration parameters used to fit the BCJ model to individual SVE simulations in scatter-plots, in a matrix layout. Kernel density estimates of each parameter are shown along the diagonal of the matrix layout. This figure contains the data from the homogenization of the larger SVEs simulated with back stress.

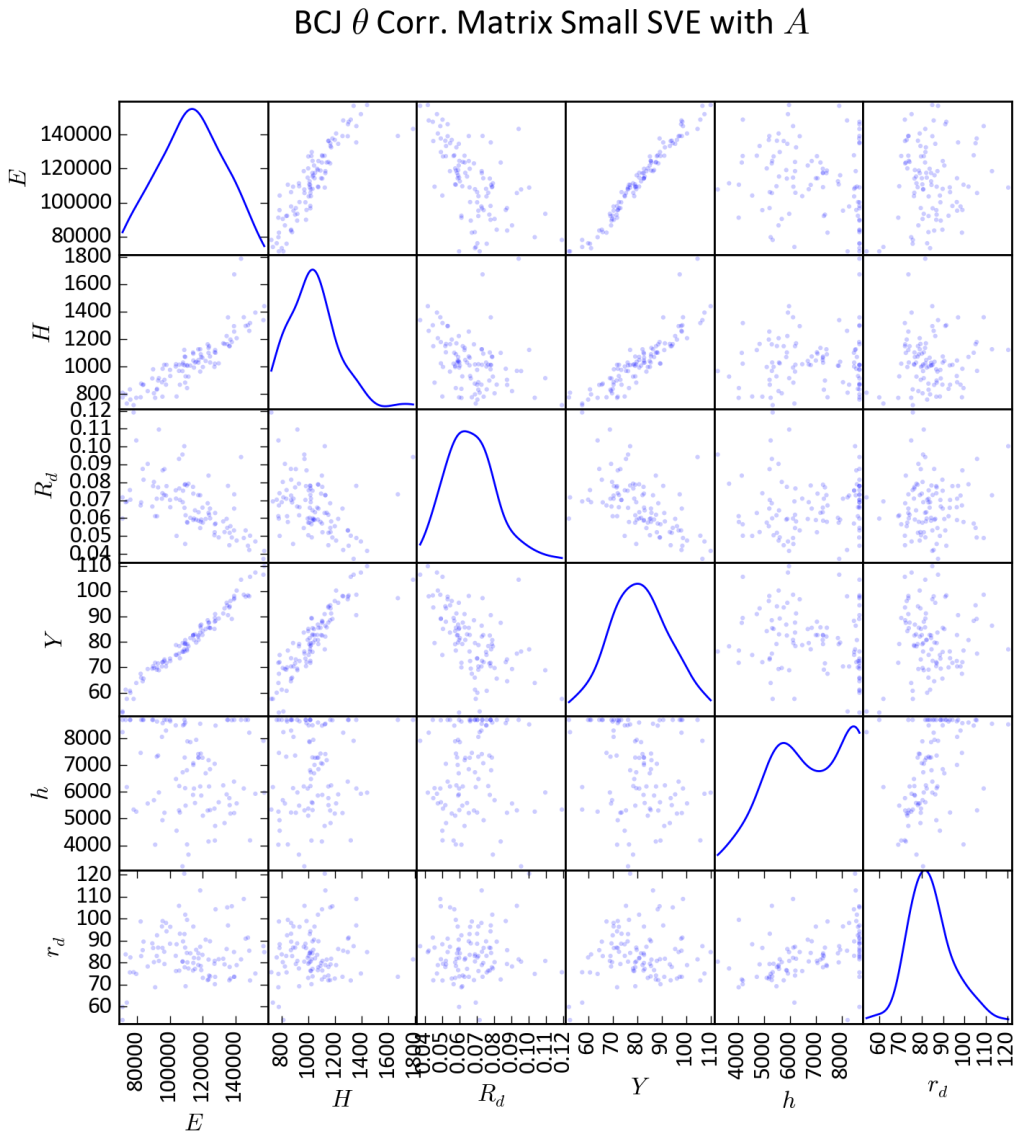

Figure 4.14. All calibration parameters used to fit the BCJ model to individual SVE simulations in scatter-plots, in a matrix layout. Kernel density estimates of each parameter are shown along the diagonal of the matrix layout. This figure contains the data from the homogenization of the smaller SVEs simulated with back stress.

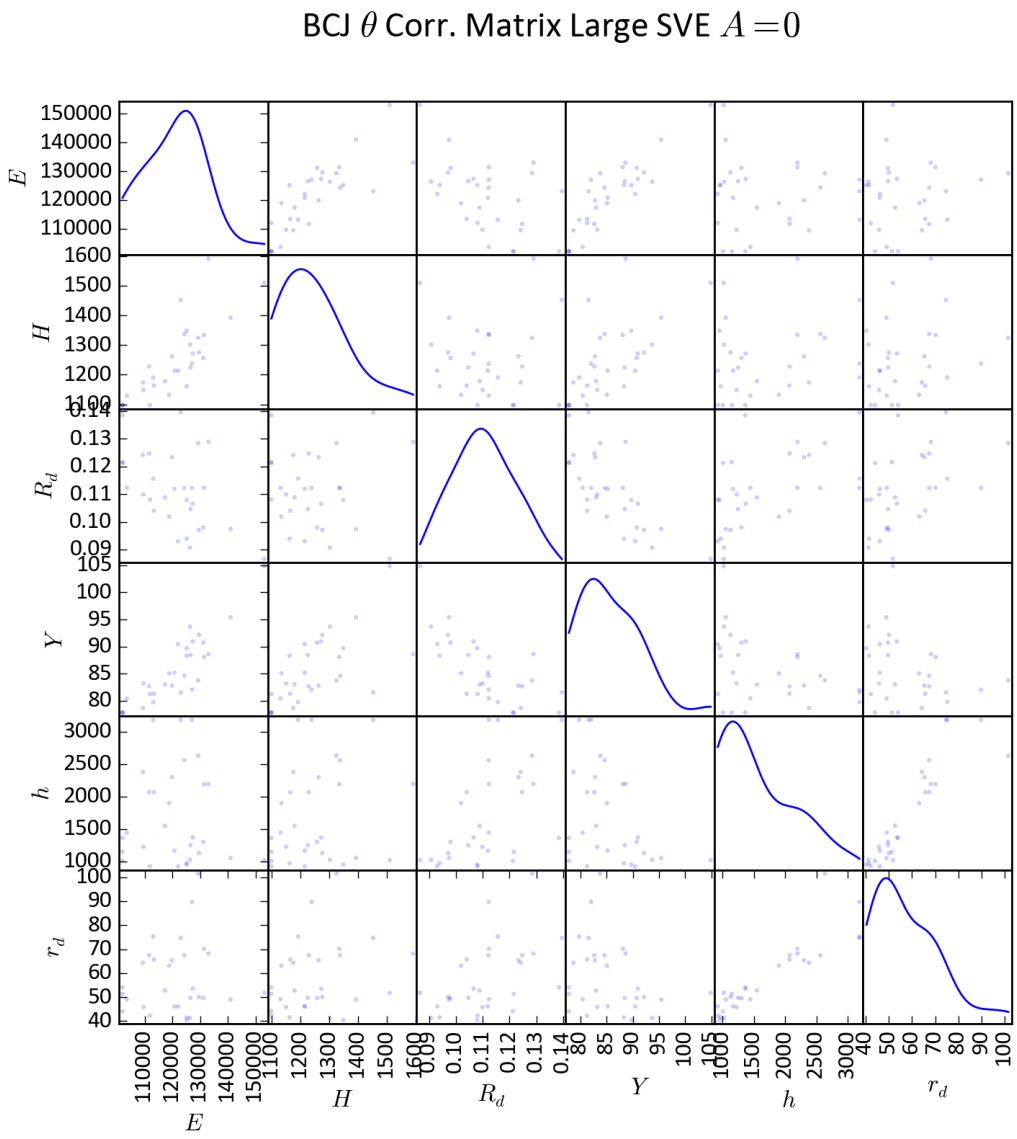

Figure 4.15. All calibration parameters used to fit the BCJ model to individual SVE simulations in scatter-plots, in a matrix layout. Kernel density estimates of each parameter are shown along the diagonal of the matrix layout. This figure contains the data from the homogenization of the larger SVEs simulated without back stress.

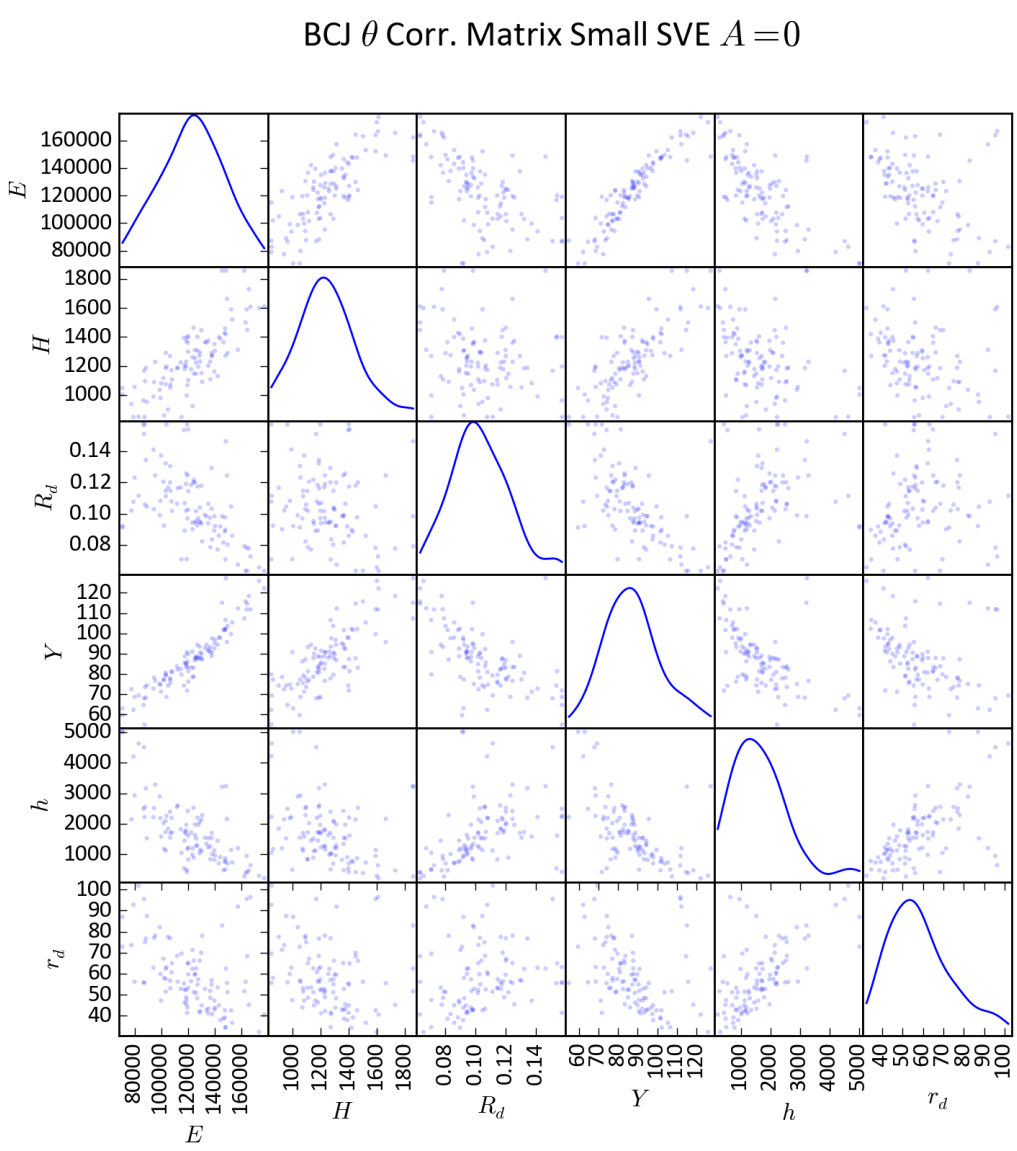

Figure 4.16. All calibration parameters used to fit the BCJ model to individual SVE simulations in scatter-plots, in a matrix layout. Kernel density estimates of each parameter are shown along the diagonal of the matrix layout. This figure contains the data from the homogenization of the smaller SVEs simulated without back stress.

The libraries of $\hat{\boldsymbol{\theta}}_{BCJ}$ were used to inform the modeling of local variations in a larger-scale simulation. The finite elements of the larger-scale mesh were informed with individual estimates of $\boldsymbol{\theta} = \left[E, Y, H, R_d, h, r_d\right]$, using random selection with replacement.

The variability in the response of the elements of the larger-scale BCJ model is compared with the variability of the SVEs, the BCJ estimates of the SVEs, and the variability of SVE-sized sections of some larger CP simulations. This comparison is shown in Figure 4.17. The variability of results is lower for the simulations using SVEs with larger volumes. The difference in variability between the SVE ensemble results and the dissected larger CP simulation results could indicate the influence of longer range interactions on the local observed variability. This difference in variability also appears between the results of the BCJ approximations and the results of including those approximations in a larger scale FE mesh, suggesting that non-negligible longer-range interactions have effects on the local variability observed, despite the reduction in model fidelity. The CP results for the model without back stress exhibit increased variability at the onset of plastic deformation relative to the results of the model form which includes back stress.

Assuming that interactions are simulated between sub-volumes of the full field simulations, the sub-volume responses would be subject to spatial covariances. As a result, they would not represent independent samples of a random variable. In the following material, these sub-volume responses are treated as if they are independent. This is a useful simplification, given that the dominant effect in the variation between the sub-volumes is that of the randomly sampled differences in microstructure, which are ostensibly independent.

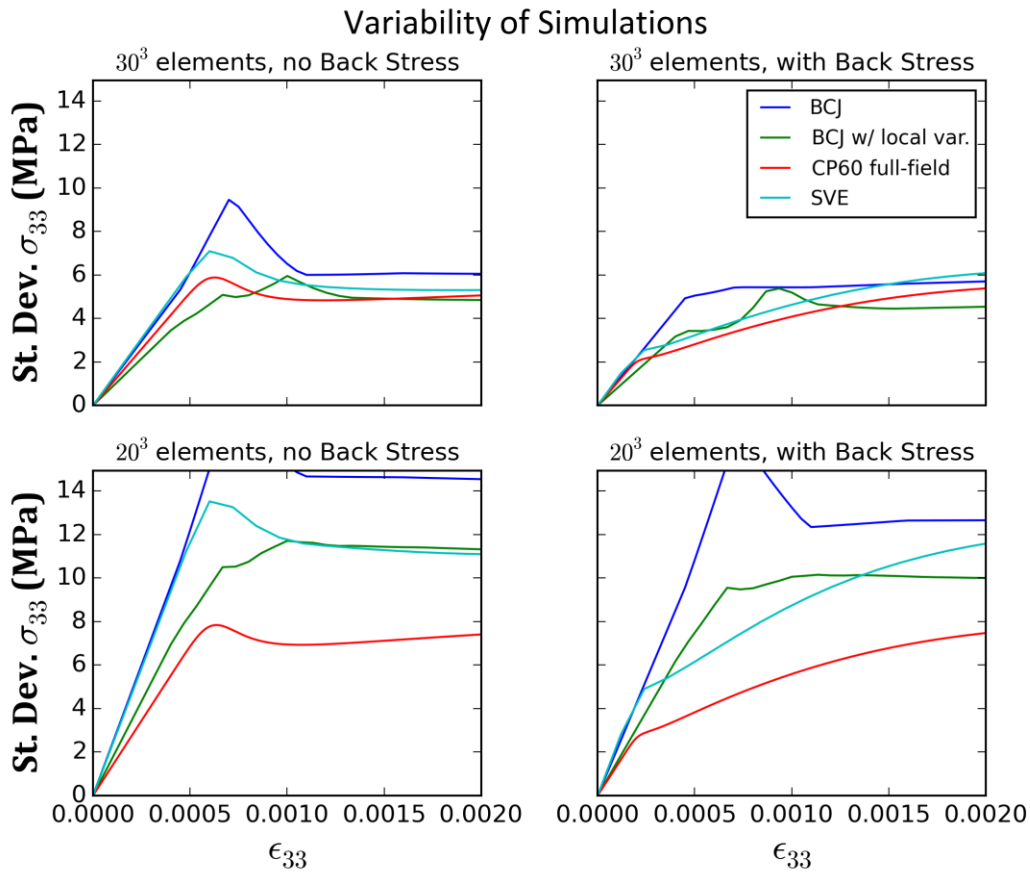

Figure 4.17. The standard deviation of axial stress (in MPa) as a function of mean axial strain, presented as a comparison of variability between modelling strategies.

The variability of the behavior of a 0.6 mm hexahedral volume of polycrystalline material is predicted by the mesoscale implementation of the BCJ model, and those predictions are compared to the variability of full-field CP simulations. Additionally, the SVE results and BCJ approximations are used to approach a prediction of the response of the same material and volume by using a naïve volume average of the appropriate number of simulations to equal the mesoscale volume. The standard deviation of these calculations is shown as a function of mean axial strain in Figure 4.18. The full field DNS present a large variation in relation to the other results. The remaining simulations present very similar levels of variability to one another. This marked underprediction of

variability is likely a result of long range interactions within the full field CP model that are omitted in the other simulations. Material response is correlated between adjacent volumes of material. In a statistical sense, this mimics a reduction in the number of independent samples of material response which are present in the overall response measurement. Notably, the BCJ model with local variations did not reproduce the larger variability observed in the full field CP results. The agreement between the full field models and the simulations based on the 20^3 element SVEs arises due to a canceling out of the local variation overprediction of the simulations of that SVE size (see Figure 4.17) with the mesoscale variation underprediction. This agreement is likely coincidental.

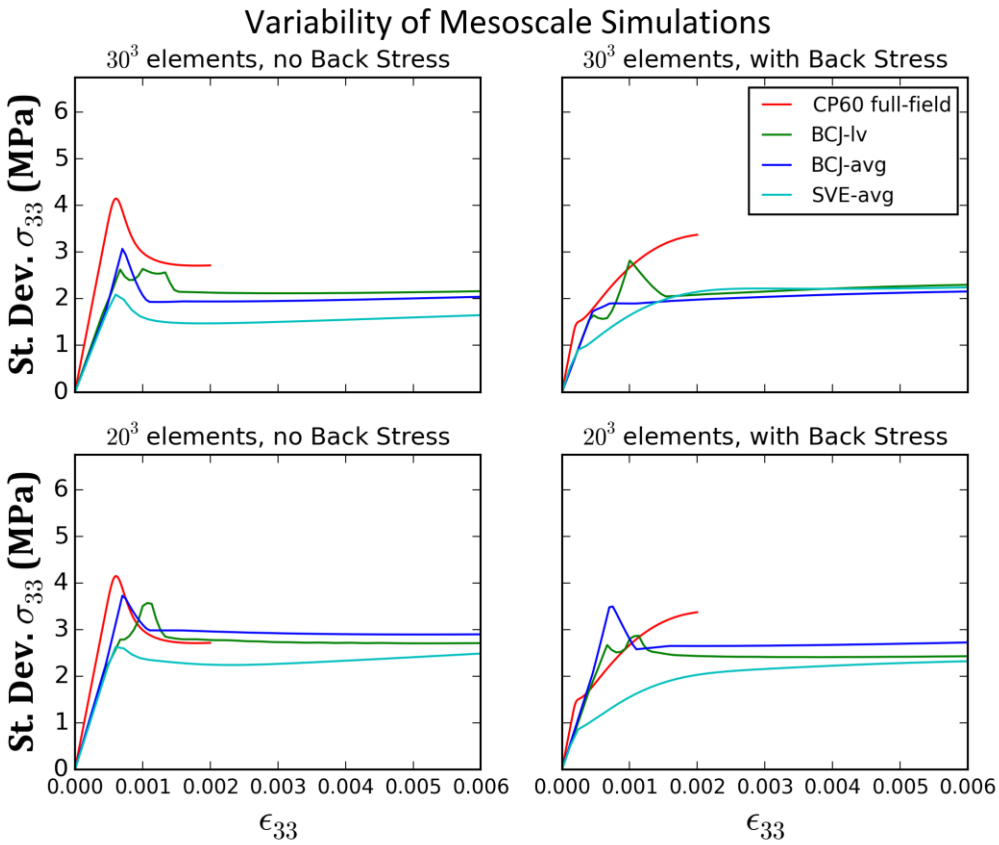

Figure 4.18. The standard deviation of the axial stress response of mesoscale volumes predicted with the various modeling approaches. For completeness, naïve volume averaging of the smaller simulations is included as a point of comparison.

An ECDF is generated for the axial stress at each value of mean axial strain. As an example, the distribution of BCJ approximations at $\varepsilon_{33} = 0.04$ is shown for two different CP model forms in Figure 4.19. To calculate the K-S statistic, the absolute difference between the two ECDFs is taken at all values of x, or σ_{33}, in this case. The maximum of this difference becomes the K-S statistic. For the ECDFs shown in Figure 4.19, the K-S statistic is 0.09.

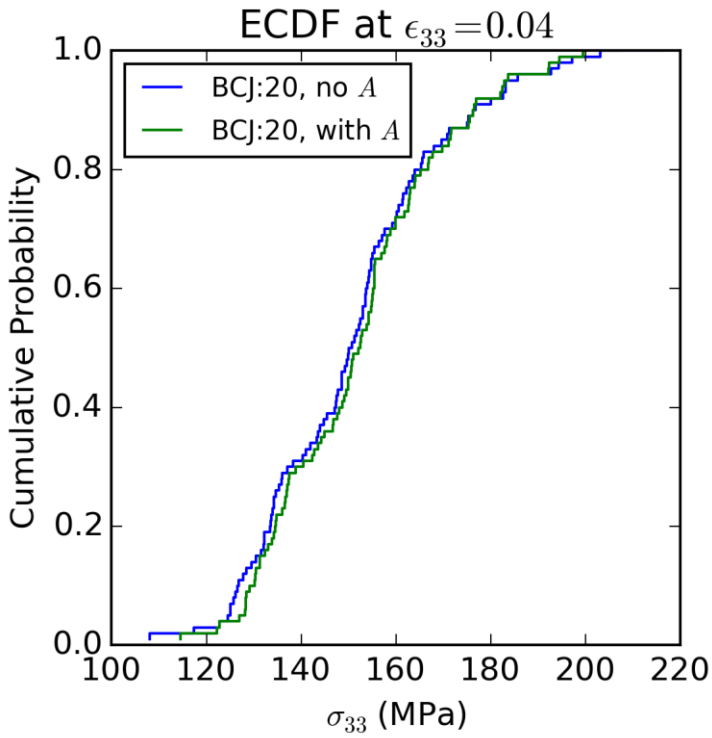

Figure 4.19. An example showing the ECDF of BCJ results at 0.04 axial strain, based on the two different CP model forms.

The K-S test is used to determine the probability that the two samples are taken from the same distribution. For a sample size and a K-S statistic, a probability is determined using the two-sided asymptotic Kolmogorov-Smirnov distribution. This

application uses this probability to indicate the information loss between the target sample and the approximation sample.

The information loss of the coarse-graining is quantified using the K-S test. The DNS of ten 0.6 mm sized-hexahedral polycrystalline volumes are used a target sample of the material response of C260 at 0.2 and 0.3 mm-sized hexahedral sub-volumes. Empirical cumulative distribution functions are calculated from the sets of results. The SVE ensembles, the BCJ approximations, and the elements of the mesoscale BCJ simulations are compared to the reference distribution of stress response to mean axial strain. The comparisons are made using the samples of stress responses in each at a specified applied strain, as seen in Figure 4.20. The two samples of results are considered to be from different distributions if the probability value drops below the significance level of 0.01. The approximations are successful if the probability value is high. This indicates the probability of the null hypothesis of the two sample K-S test: the two samples are drawn from the same distribution.

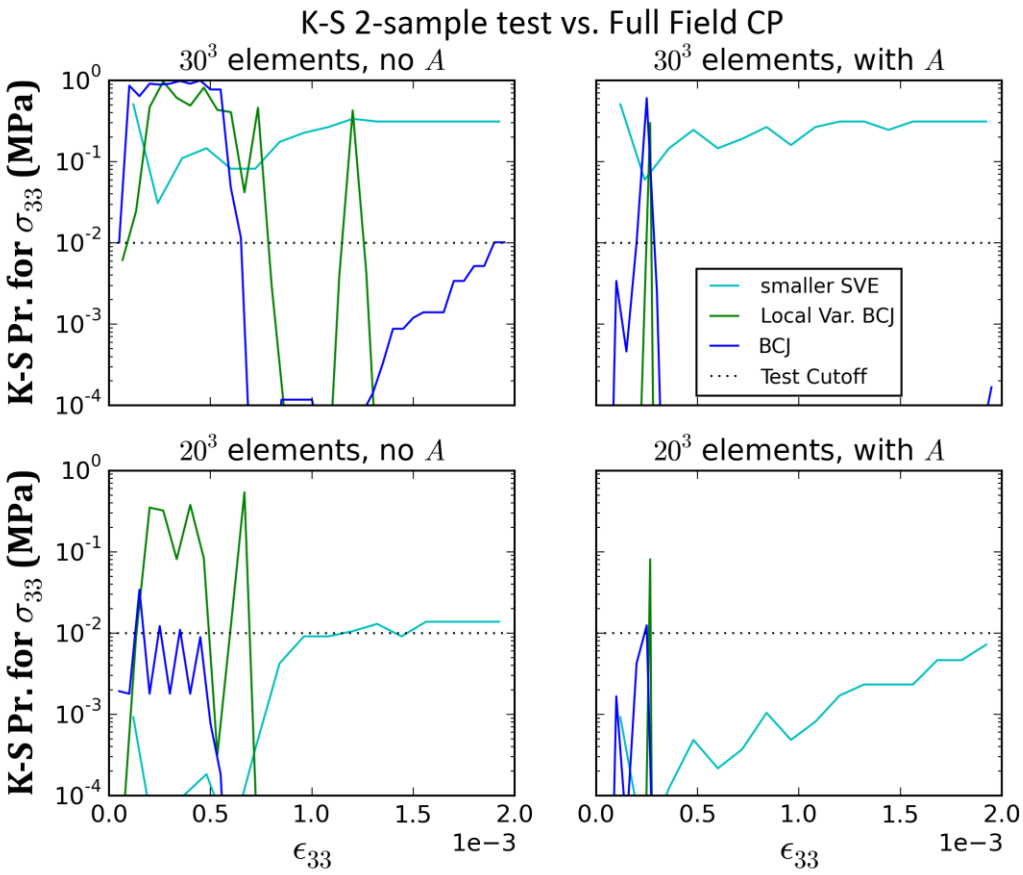

Figure 4.20. The K-S test of each set of simulation in comparison to the reference of the full field CP simulations of the polycrystalline material. The significance level used in this test is 0.01.

To isolate the variation of simulated response in a K-S test, the bias of the simulation methods was identified and removed. Bias was estimated by comparing the ensemble average response between the different approaches, the results of which are shown in Figure 4.21. The bias of the BCJ-based methods is more pronounced in the approximation of the CP model with back stress. The BCJ model is known to predict elastic-plastic transitions to be sharper than the predictions of a CP model. This is a result of the presence of material heterogeneity in the polycrystal plasticity simulation, as well as differences in the form of the flow rule. In the results from the CP model form with back stress, the elastic-plastic transition is more gradual, and less suited to being

approximated by this formulation of the BCJ model. The K-S test repeated for the model results, after compensating for the estimated bias, is shown in Figure 4.22.

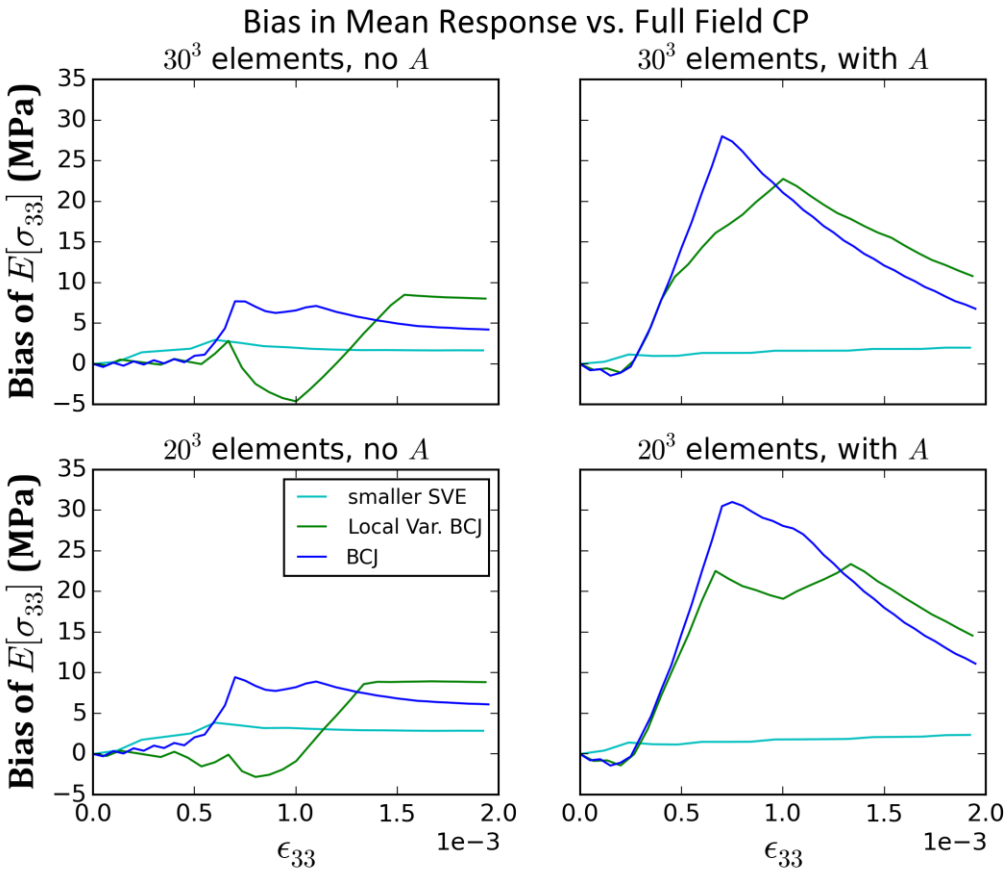

Figure 4.21. The estimates of bias in axial stress (MPa) as a function of mean axial strain. Bias is measured in comparison with the full field CP simulations, using the difference between the ensemble mean of response of each simulation approach.

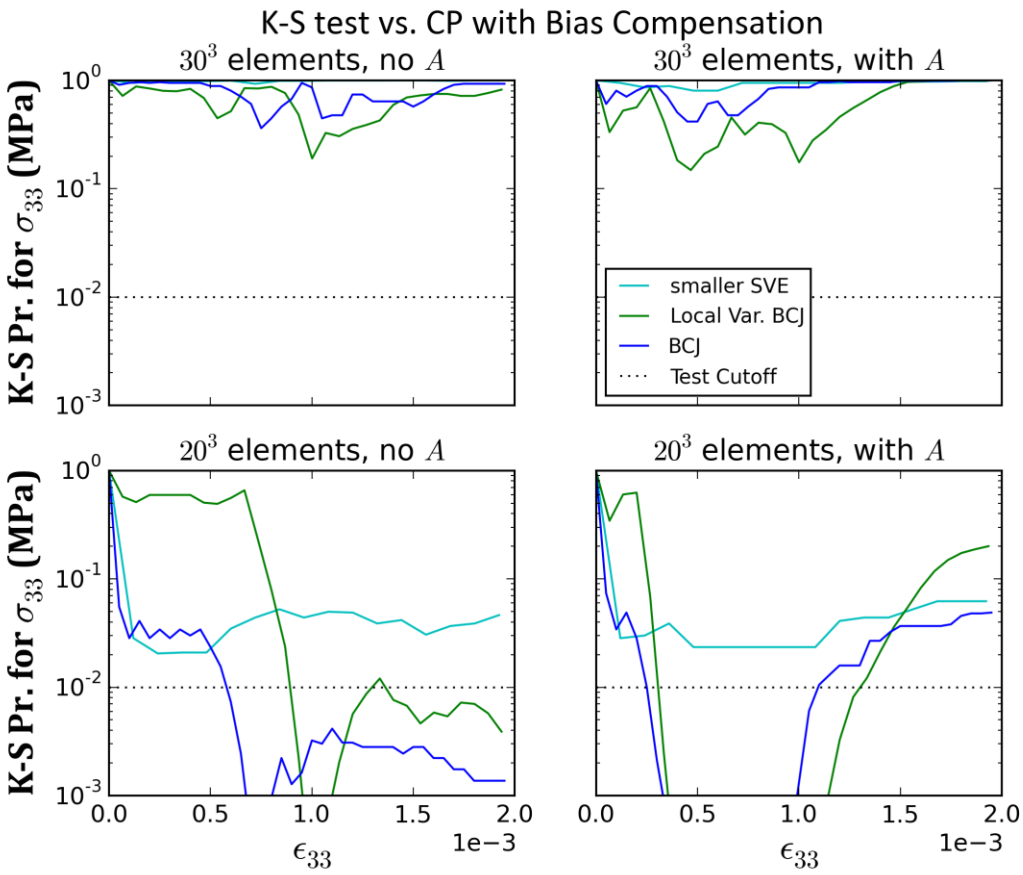

Figure 4.22. K-S 2-sample test results for each simulation approach in comparison to the full field CP simulations. The test is performed using the bias corrected distributions of axial stress response as functions of mean axial strain. A significance level of 0.01 was used for this test.

4.5. Conclusions

The analysis of the results is organized into main topics. The CP model form study showed that the inclusion of back stress has effects on the predicted response at higher length scales. The results of the SVE size study shows that the 200 μm SVEs have larger numerical uncertainty than the 300 μm SVE ensemble. The correlations in BCJ parameter estimates are discussed. The capability of the BCJ model in describing plasticity at the mesoscale is found to require covariance information between adjacent coarse grain elements. A prediction of the coarse-grained covariance is formulated, based

on quantitative characterization of simulated microstructure. The value of correlation enforced local response measurements is discussed.

4.5.1. Back Stress in Crystal Plasticity

The inclusion of back stress in the simulation of material response at the mesoscale allows for the meta-elastic behavior observed in C260 to be included in the CP model. This study had limitations with respect to data availability. As a result, experimental data of a cyclic loading of C260 could not be used to specify the ratio of kinematic and isotropic hardening in the calibrated model. This work relies on the observations of Wagoner (1982) to assert that the hardening behavior in the material is primarily kinematic up to strains of 0.04, after which the saturation of kinematic hardening leaves isotropic mechanisms as the dominant influence on response. Thus, the calibration of kinematic and isotropic hardening could be identified from the limited data.

As seen in Figure 4.13 through Figure 4.16, the exclusion of back stress in the CP model leads to coarse grained representations whose kinematic hardening is dominated by inter-granular kinematic hardening. When the microstructure is varied from simulation to simulation, the predictions of kinematic hardening are more variable for the back stress exclusive calibration (relative to the magnitude of the expected mean kinematic hardening, which is lower), as shown in Table 4-6. This effect clarifies the importance of choosing appropriate models in microstructure-sensitive approaches. The consequences of choosing a lower fidelity alternative may persist into coarse-grained predictions.

The BCJ model struggled to replicate the gradual elastic plastic transition shown in the CP simulations. The inclusion of back stress in the CP model led to an even more

gradual transition between elastic and plastic response as a function of applied strain. To mimic this feature of the simulated response, the BCJ model requires extreme values of hardening parameters which lead to algorithmic instability. This limitation affects the fidelity of the coarse-grained model, as can be seen in Figure 4.21. Future work may benefit from using models and approaches which can overcome this numerical limitation.

4.5.2. SVE Size Effects

Both SVE ensembles used in this study (hexahedra of 200 μm and 300 μm) were too small to capture some interactions. From a homogenization of microstructure perspective, neither was sufficient in size or number. Rather than focusing on performance of homogenization, the focus of this work is to articulate the challenges to the coarse-graining of polycrystalline response at length scales at which inhomogeneity in response is present.

The K-S test suggested that the 300 μm SVE ensemble performed better than the 200 μm SVE ensemble. A clear difference in information loss existed between the two sizes of approach, as compared to the 600 μm simulations. This information loss was observed prior to the BCJ approximation (see Figure 4.20) as well as after the bias compensation (see Figure 4.22). The smaller SVE size ensemble overestimated local variability. In situations where coarse graining at scales near the maximum grain size is needed, some method other than the SVE ensemble approach may be necessary.

4.5.3. Correlations Between BCJ Parameters in the Calibration Set

The predictions of the BCJ parameters exhibited covariations between E, Y, and H. This covariation is a topic of interest to surrogate model development. In this work, the GP model was used as a calibration aid, and not in place of the BCJ simulations (as would be the case in a surrogate modeling approach). Nevertheless, an identification of the origin of these correlations is of interest.

If the parameters of the BCJ model are identifiable given the calibration data used, the covariation in the parameters reflects a covariation of behaviors present in the data. Commonly, parameters of a material model are treated as random variables, and analyzed as if they exhibit independence. In this work, care was taken to avoid this. BCJ parameter estimates were considered as vectors of six associated quantities as opposed to samples from six independent random variables. In future work with GP models on this material, the type of approach shown may be warranted unless some stronger basis for independent parametric variation can be made.

4.5.4. Spatial Correlation of Coarse-Grained Elements

Properties have spatial correlations in microstructure-sensitive simulations. These correlations have consequences when making predictions of the variability of properties while traversing length scales. At the length scales simulated in this work, a proportion of the correlations are not enforced in a naïve coarse-graining approach, i.e., an approach which does not consider the expected correlation between the simulated response of an SVE and the response of a neighboring volume.

The BCJ local variations model underpredicted the variance of response in 600 μm SVEs. The coarse-grained BCJ model with local variations was populated with parameter values without enforcing correlations between adjacent elements. The severity of the variance underprediction suggests that these correlations have significant effects on the variability of mean response as a function of SVE and coarse-graining element size.

The variances predicted by each model were compared to estimate the number of independently sampled calibrations whose average would vary in keeping with the full-field simulations. The predictions are shown in Figure 4.23. The mean of four BCJ approximations of SVEs of 300 μm in length had the most similar variance of response to that of the 600 μm length CP simulations. If the full field volume is composed of 300 μm in length sub-volumes and the response of each sub-volume is assumed to be independent of nearest neighbors, the mean of eight BCJ approximations would be needed to match variances. Such a significant difference (four instead of eight) suggests that the use of fully independent results in the informing of the coarse-grained model is not a viable approach for making predictions at the mesoscale for this material.

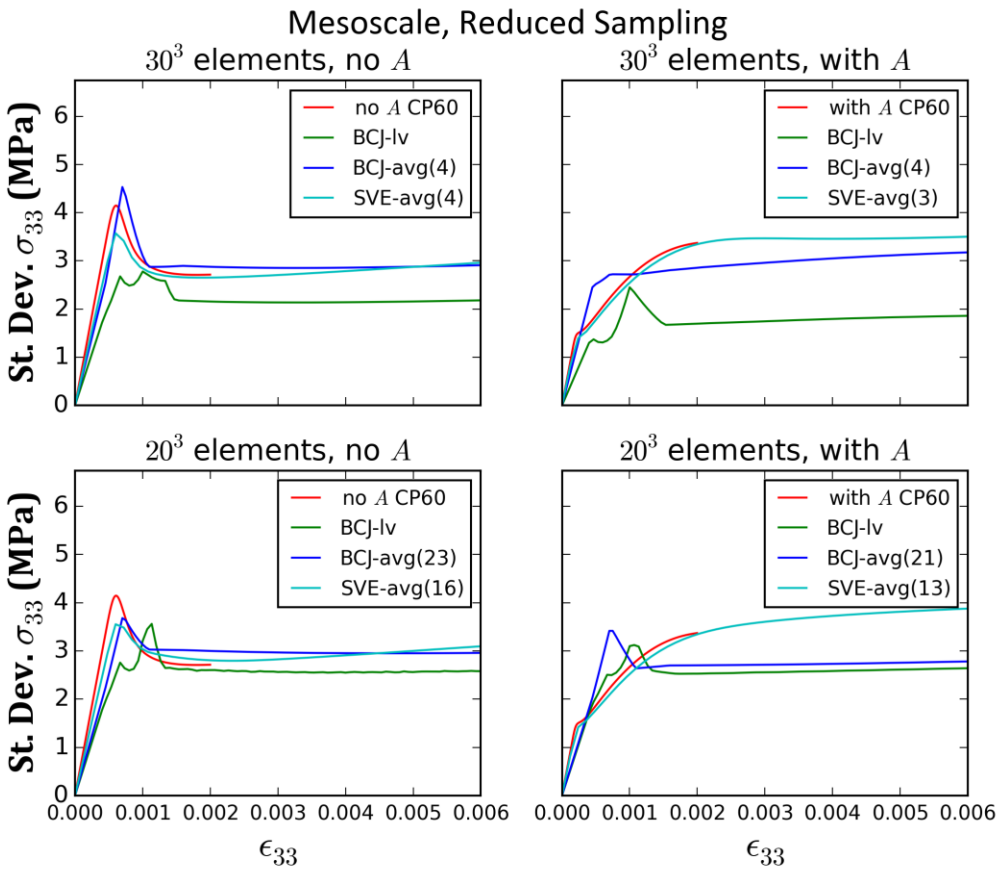

Figure 4.23. The variability predictions based on a reduced number of independent sub-volumes which correspond to the full-field variability. The number of samples used is shown in parenthesis in the legend.

4.5.5. Microstructure Quantification Based Prediction of Coarse-Grained Correlations

Microstructure determines the correlation between the responses of adjacent volumes. Grains which occupy multiple adjacent coarse-grained elements lead to covariance of the mean responses of those coarse-grained volumes. A simple algorithm is used to calculate the proportion of volume in SVEs of a given size which is occupied by these "boundary-split" grains. A 2d section is taken from each SVE, and two perpendicular lines are drawn on the section. The grain containing the intersection is counted three times, the grains intersected by either line are counted twice, and the other

grains appearing in the section are counted once. This frame is shown in Figure 4.24. The volumes of the grains V_i are multiplied by the counting multipliers m_i, and the sum is divided by 6 times the total SVE volume, i.e.,

$$\mathrm{Corr}\left(\mathrm{SVENN}\right) \approx \mathrm{E}\left[\frac{\sum_{grains=i} m_i V_i}{6V_{SVE}}\right], \text{ for an SVE ensemble} \tag{52}$$

where E[x] is the expected value of x, here for the ensemble of SVEs, and $\mathrm{Corr}\left(\mathrm{SVENN}\right)$ is the estimated correlation between nearest neighbor SVEs in a coarse-grained model. The counting multipliers, along with the division factor (6) are included to account for the dependence of the covariance of regions which split a homogenous volume on the proportion of that shared volume in either region. The covariance is highest when the volume is split evenly. When counting grains on a planar section, lines and points have increasing preference for grains which are (A) larger and (B) bisected at a plane nearer to the grain's centroid, assuming equiaxed spheroidal grains. The formulation is left as simple as possible, while reflecting the conditions imposed by periodic boundaries.

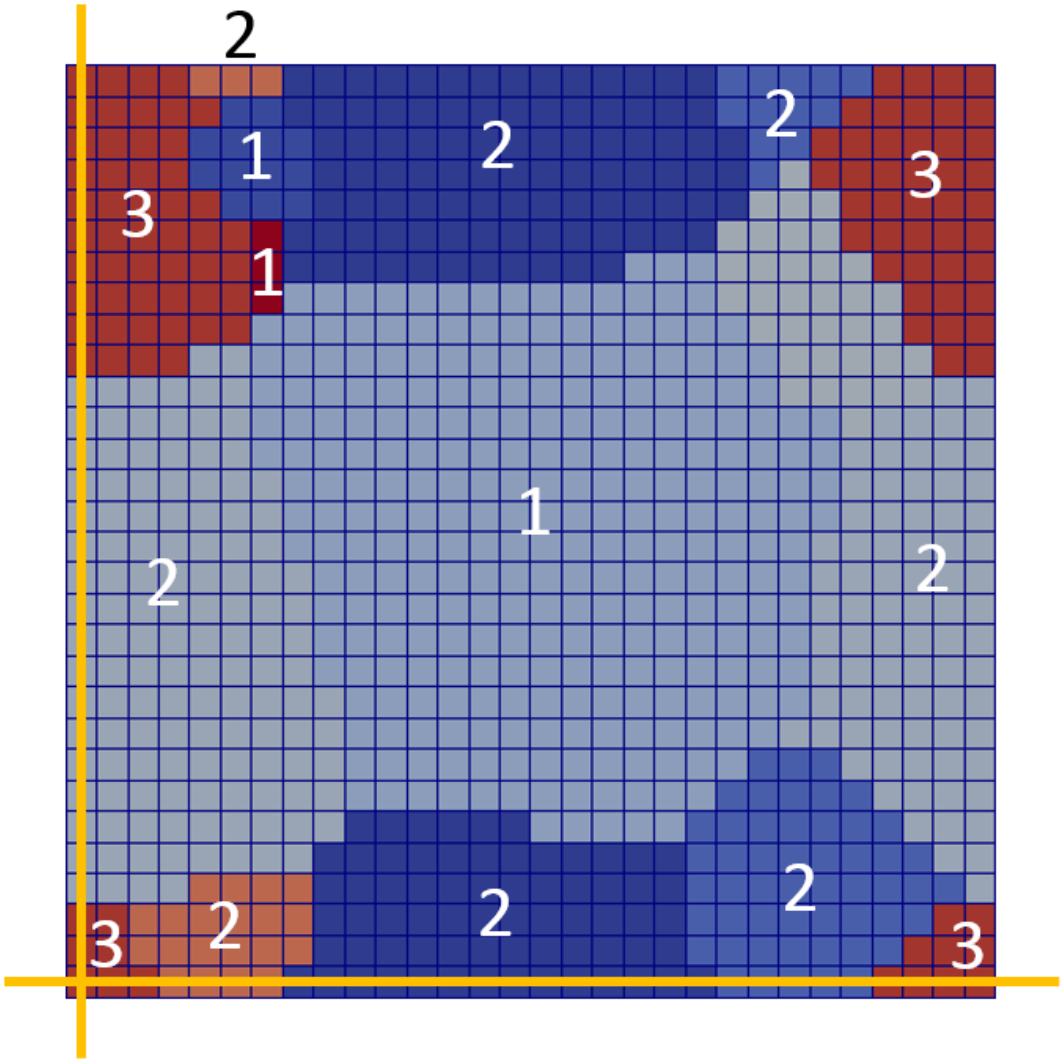

Figure 4.24. The counting frame used to estimate the shared volume for an SVE of a specific size. Numbers represent m_i for each grain shown. Periodic boundaries are imposed.

The correlation of adjacent SVE sized volumes in the full-field simulations was calculated to compare with the above microstructure characterization base approach. The statistically measured full-field correlations were taken only in-plane, for the plane normal to the loading direction. This was done to avoid including the micromechanical covariation of stress along the loading direction in the estimate of microstructure-specific covariation in stress response. The correlation was averaged in an equal weighting of

stress values as a function of strain. These results are shown alongside the results of estimates of the shared volume correlation in Table 4-7. The precision of the match is considered coincidental, as many influential factors were not included, and the correlations change as a function of applied strain.

Table 4-7. The estimates of the correlation which applies when embedding the properties of SVE results adjacently in a coarse-grained mesh.

Coarse-Grained Nearest Neighbor Correlation Coefficient Estimates			
SVE Size	Full-Field Statistics with A	Full-Field Statistics without A	MS-Characterization Based Estimates
200μm	0.340	0.299	0.342
300μm	0.212	0.186	0.218

4.5.6. The Scale-Separation of Interaction Lengths

Coarse-graining of polycrystalline plasticity at the sub-RVE scale requires a separation of interactive and covariance effects by length scale. Localized simulations are needed to inform the material response at the length scales between single crystal and RVE. These local simulations do not contain all essential correlation lengths that influence the spatial covariance of microstructure and response. These additional covariances must be included as an additional "layer". When informing a coarse-grained mesh, the local measurements must be used in conjunction with a correlation enforcing algorithm. This algorithm may need to be designed with the consideration that the parameters of the coarse graining (CG) model (BCJ in this work) and the response of the material may not have a linear relationship. As a result, interpolations in the CG parameter space may not suffice as a means of interpolating response. If interpolation is

used to enforce correlations in the CG mesh, it will depend on a detailed model of parameter effects. The development of such an approach is left to future work

4.5.7. Summary

The conclusions of the work are summarized. SVEs which are too small will over-estimate variability specific to their length scale, as was observed with SVEs of 20^3 elements. The exclusion of back stress from a CP model will result in kinematic hardening predictions of purely inter-granular character. Parameters which describe related behaviors are subject to covariation. Spatial correlations omitted from a local coarse-grained approximation are necessary to include in predictions of variability at length-scales larger than the SVE length of the approximation.

CHAPTER 5. MULTISCALE MODEL DEVELOPMENT: MICROINDENTATION AND MESOSCALE VARIABILITY IN POLYCRYSTALLINE CARTRIDGE BRASS

In this chapter, a multiscale model development strategy is proposed for a reduced-order mesoscale model for a polycrystalline ductile metal. Data is gathered on the deformation response to load of cartridge brass at two separate length scales. Uniaxial tensile test data, paired with EBSD image data, is used in calibrating a crystal plasticity (CP) model of polycrystalline cartridge brass. Microindentation data is gathered using cartridge brass specimens with matching microstructure statistics. A bottom-up pathway is established using Dream3D and the CP model to simulate statistical volume elements (SVE). A top-down pathway is outlined using the microindentation data and FEM simulations of microindentation. A multi-objective calibration is proposed to identify the reduced-order model designs to be used in a multiscale application.

5.1. Introduction

The maturation of additive manufacturing (AM) is leading to the rise of increasingly intricate components in demanding applications (Bikas et al., 2016; Frazier, 2014). The features of these parts will soon exist at the same length scales as features of the microstructure (Hirt et al., 2017). For these components, the influence of material response variability and feature geometry will likely interact in determining the reliability of a specific design. To optimize feature geometry and microstructure, a model may be needed which can capture the influence of both.

Engineering models cannot yet capture the interactions of microstructure and geometry which influence performance (Francois et al., 2017; Hirt et al., 2017). Designing a new modeling tool will require a consideration of both cost and fidelity. Homogeneous treatments are unsuited to capturing microstructure-sensitive response. The expense of full field resolution of microstructures may make CP modeling cost-prohibitive to engineering applications. A reduced-order model of ductile metal plasticity which can approximate mesoscale response variability may be appropriate as a compromise of cost and fidelity.

To avoid bias in the model, the bottom-up CP-SVE simulations are used in conjunction with top-down observations of mesoscale variability. Microindentation has been historically used as a non-destructive test of material properties (Bishop et al., 1945; Blau, 1986). Recently, nanoindentation has been proposed as a method for gathering high throughput observations of local materials properties (Weaver et al., 2016). In this work, microindentation is used as a top-down data source for variability in the mesoscale response of polycrystalline cartridge brass.

To develop a computational engineering tool for mesoscale polycrystalline ductile metals, a reduced-order modeling approach is proposed along with a multiscale approach to the calibration and design of that model. Microindentation measurements, microstructure statistics, and uniaxial tensile tests are used to develop a multiscale calibration dataset. Discussion is focused towards the obstacles to model development and model formulations which may lead to improved multiscale performance.

5.2. Methodology

The proposed multiscale model development framework is described in detail in this section. The content is divided into three subsections: the bottom-up pathway, the top-down pathway, and the multiscale development criteria formulation.

5.2.1. Bottom-Up Pathway: CP-SVE

This section describes the steps involved in connecting crystal plasticity to mesoscale response variability predictions. A previously calibrated CP model is identified. The microstructure statistics of the material are used with Dream3D to generate finite element mesh instantiations of the material. A sufficient size is identified for the SVEs to capture variation in mesoscale response. An ensemble of SVEs is used to comprise a BU prediction of mesoscale response and variation.

The initial work for the BU pathway is taken from the work of Chapter 4. The 300 μm SVE ensemble is chosen to investigate variability in the material response at the mesoscale.

5.2.2. Top-Down Pathway: Spherical Microindentation

This section contains a stepwise description of the methods used to establish a top-down connection pathway from spherical microindentation to the mesoscale variability of material response to loading. These steps are outlined here, and details are provided in the remainder of the section. Brass sheet is cut into samples, characterized by visual microscopy, and compared to the BU statistics. Microindentation experiments are carried out on samples of annealed rolled cartridge brass plate at room temperature.

Variations in deformation response to two different indentation loads is measured within each set of 50 tests per load. FEM simulations of microindentation is used to relate measurements to material variability.

5.2.2.1. Specimen Preparation and Characterization

The Cartridge brass samples are taken from plate procured from McMaster-Carr. The specimen from McMaster-Carr is to specifications of ASTM standard B36. The plate measured $0.125" \pm 0.007"$ thick and 6" square. The material is ½ hard, with a heat treatment H02. The plate is cut into small samples of roughly 0.5 in^2 in area using a waterjet cutter (Maxiem 1515 manufactured by Omax) operated by the Georgia Tech Invention Studio.

The material samples are prepared for characterization and testing. Sample preparation was performed by Theodore Zirkle. The samples are mounted in Bakelite, forming cylindrical mounted samples with circular top surfaces of 3 cm in diameter. The mounted samples are polished under 5-10 lbs force per sample at 100 rpm for 1 minute using ALO paper for each at three grit levels, P220, P500, and P1200 with water as a lubricant. Polishing is continued with 1 μm DIAMAT diamond abrasive grit on an ATLANTIS polishing pad with DIALUBE Purple Extender lubricant for an additional two minutes. Polishing is concluded with 0.05 μm alumina grit on a NAPPAD polishing pad at 100 rpm for one minute. The details of polishing are summarized in Table 5-1.

Table 5-1. The stepwise details of the polishing procedure followed in preparing the C260 samples.

Abrasive	**Surface**	**Lubricant**	**Force per sample**	**Speed**	**Duration**
P220 grit	ALO paper	Water	5-10 lbs	100 rpm	Until planar
P500 grit	ALO paper	Water	5-10 lbs	100 rpm	1 min
P1200 grit	ALO paper	Water	5-10 lbs	100 rpm	1 min
1 μm DIAMAT diamond	ATLANTIS polishing pad	DIALUBE Purple Extender	5-10 lbs	100 rpm	2 min
0.05 μm Nanometer alumina	NAPPAD polishing pad	None	5-10 lbs	100 rpm	1 min

A sample is etched to characterize microstructure. Etching was performed by Theodore Zirkle. The etching is completed in three steps. The first step consists of an immersion of the polished sample in dilute ammonium hydroxide. Pace Technologies pre-mixed etchants, Copper No. 1 and Copper No. 2 are used by swabbing the sample with the etchant. The details of the etching procedure are summarized in Table 5-2.

Table 5-2. A stepwise summary of the etching procedure used in this work.

Etchant	**Concentration**	**Application**
Dilute NH_4OH/H_2O	Dilute Aqueous	Immersion
Pace Technologies Copper No. 1	50% (v/v) DI Water 50% (v/v) Nitric Acid	Swabbing
Pace Technologies Copper No. 2	80% (v/v) DI Water 20% (v/v) HCl 40g/L $FeCl_3$	Swabbing

Microstructure statistics are gathered from micrographs of the etched specimen. Micrographs were taken by Theodore Zirkle. The optical microscopy is performed using

a Leica DM IRM microscope, and the sample is placed on a Prior Proscan electronic stage. Micrographs are taken at 2.5X and 10X magnification. Micrographs are obtained using a Photometrics RS CCD camera operated using Imagepro MC imaging software. An example micrograph is shown in Figure 5.1. Analysis of the micrographs (performed by Theodore Zirkle) provided grain size statistics of a lognormally distributed type, with a mean apparent grain size of 71 μm.

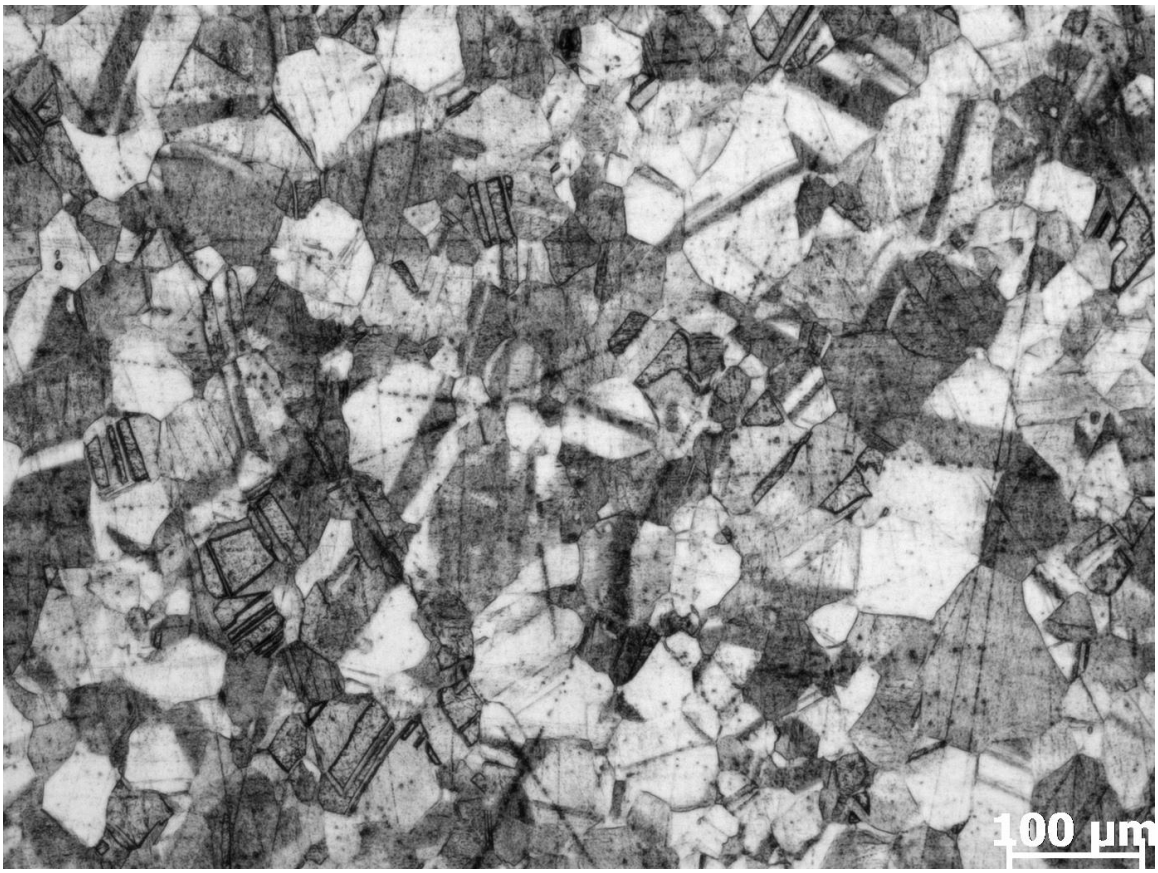

Figure 5.1. A 10X magnification micrograph taken of the etched and polished sample of the C260 H02 plate obtained from McMaster-Carr.

5.2.2.2. Microindentation Procedure

Proprietary microindentation equipment is used to perform testing. Spherical microindentation testing was performed by Theodore Zirkle, using a Futuretech FR-e

indenter. The indentation tip is a Leco 1/16” (1.58mm) ball indenter, which meets the ASTM E-18 standard. The Futuretech indenter can only apply specific magnitude loads. The loads used in this study are 60 kg and 100 kg. Each load is applied to points on the surface of the sample, with a 3 mm separation between points. A total of 50 tests are performed at each of the two specified loads. Measurements of the radius of each indentation are gathered by using imaging software to analyze micrographs taken after testing.

5.2.2.3. FEM Simulation

To relate the testing results to material response, a FEM simulation was performed. The FEM simulation was performed using ABAQUS (Simulia, 2007)The details of the simulation are summarized in this section, with specific attention given to the mesh construction and the material model used. Theodore Zirkle performed the simulations described in this section.

A mesh was created to accommodate the loading conditions of spherical microindentation in an efficient simulation. The mesh is based on work of a previous student on FEM simulations of spherical nanoindentation (Priddy, 2016). The simulation mesh is a 2D axisymmetric formulation, with the axis of symmetry at the point of initial contact of the indenter and the sample. The mesh has a free surface at the top and outer boundaries. The bottom boundary is displacement controlled in the z-direction (parallel to indentation direction). The mesh density is varied linearly to maximize resolution at the critically stressed region. An image of the mesh is included in Figure 5.2.

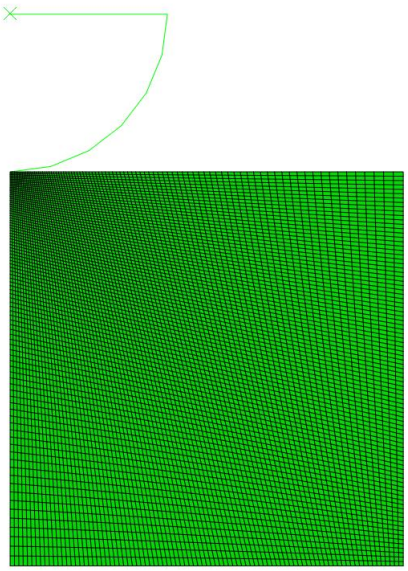

Figure 5.2. The axisymmetric mesh used in initial simulations of microindentation.

A material model was created by fitting tensile test data. The tensile data was taken from published work on cartridge brass with matching microstructure statistics (Carroll et al., 2012). Abaqus's built in piecewise linear model was fitted to the tensile response corresponding to the mean grain size of 71 μm. The model is isotropic and rate insensitive. The indentation is performed in simulation until a target applied load is reached.

The material model is varied linearly to investigate the sensitivity of microindentation radius to material response. A response coefficient is used to multiplicatively modify the material response to a given stress, i.e.,

$$\sigma = [\text{Coef.}]\, f(\varepsilon) \tag{53}$$

where σ is stress, $f(\varepsilon)$ is the modeled strain response to stress, and $[\text{Coef.}]$ is the response coefficient. Microindentation simulations are performed using a range of values for the response coefficient between 0.88 and 1.12.

The influence of the response of spatially distinguished volumes on the variation of indentation radius is investigated. The variability of the indent radius at fixed load is compared for a range of response coefficient values, applied to the entire simulation volume. An additional comparison is made, only modifying the response of the material within the critically stressed volume (defined at maximum indent depth).

5.3. Initial Results

Microindentation data is presented. Initial FEM simulations are used to investigate the volumetric domain of the material response which influences the variations found in the microindentation data.

Two loads are investigated. The 60 kg load indentations are observed with a mean indentation radius of 388.1 μm and a standard deviation of 3.13 μm. The 100 kg load indentations are observed with a mean indentation radius of 490.9 μm and a standard deviation of 3.85 μm. The data are shown in histograms in Figure 5.3 and Figure 5.4.

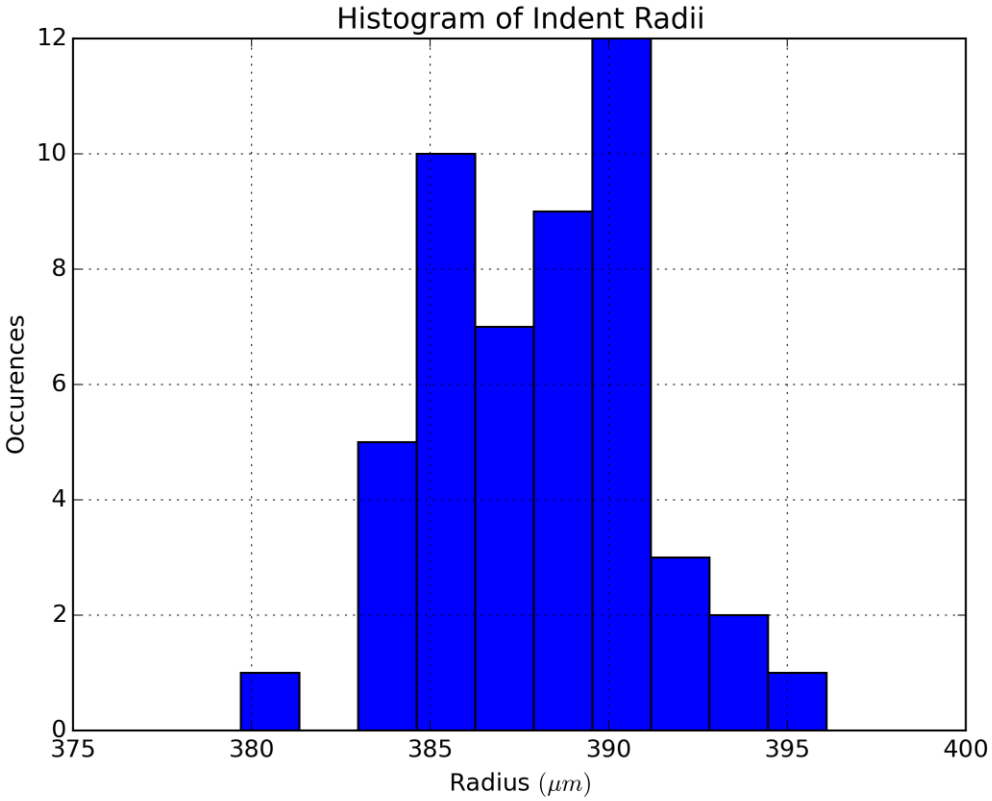

Figure 5.3. A histogram of the 60-kg load spherical microindentation measured radii.

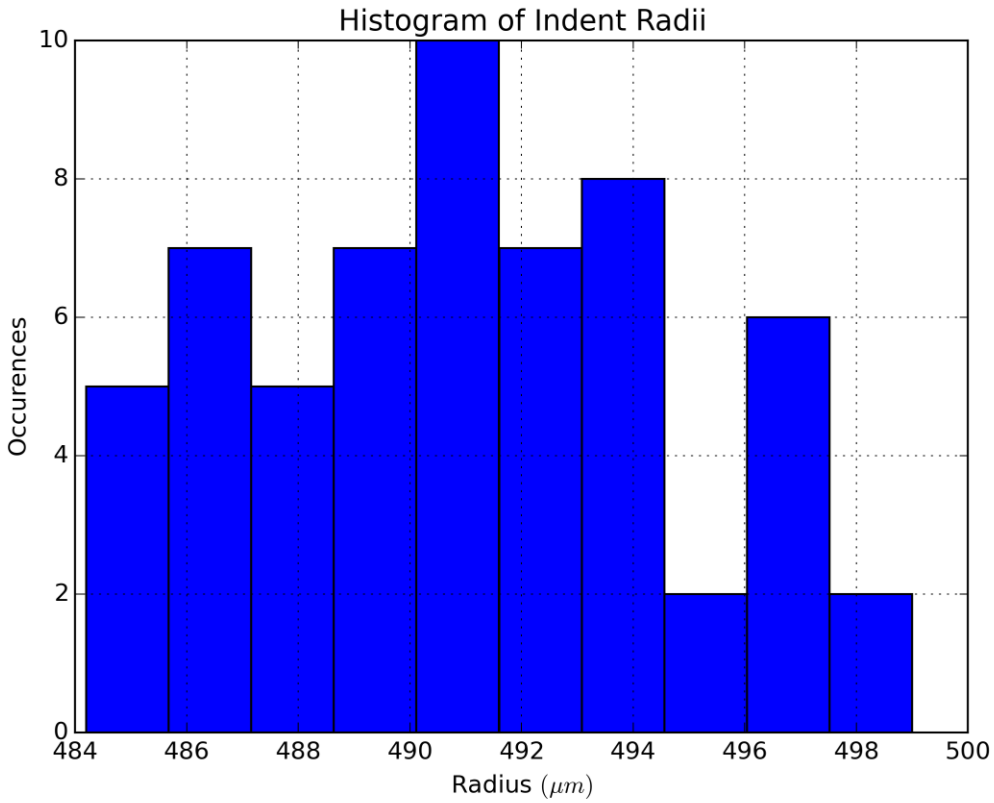

Figure 5.4. A histogram of the 100-kg load spherical microindentation measured radii.

Initial FEM simulations are used to explore the relation of the measured quantity to material response. A 60-kg load is used in the initial simulations. The indentation radii are shown in Figure 5.6. The volume of material critically stressed (>90% of maximum stress) is measured and shown in. The critically stressed volume only contributes 12.1% of the variation in measured indentation radius, relative to the variation from modifying the response of the entire simulated material volume homogenously. It is noted that the simulations predict indentation radii which are larger than the experimentally observed values by a factor of two.

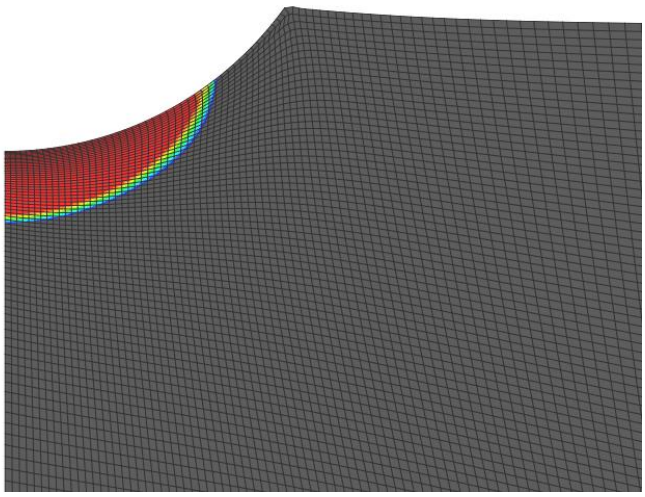

Figure 5.5. The critically (>90% of max) stressed volume in microindentation as simulated.

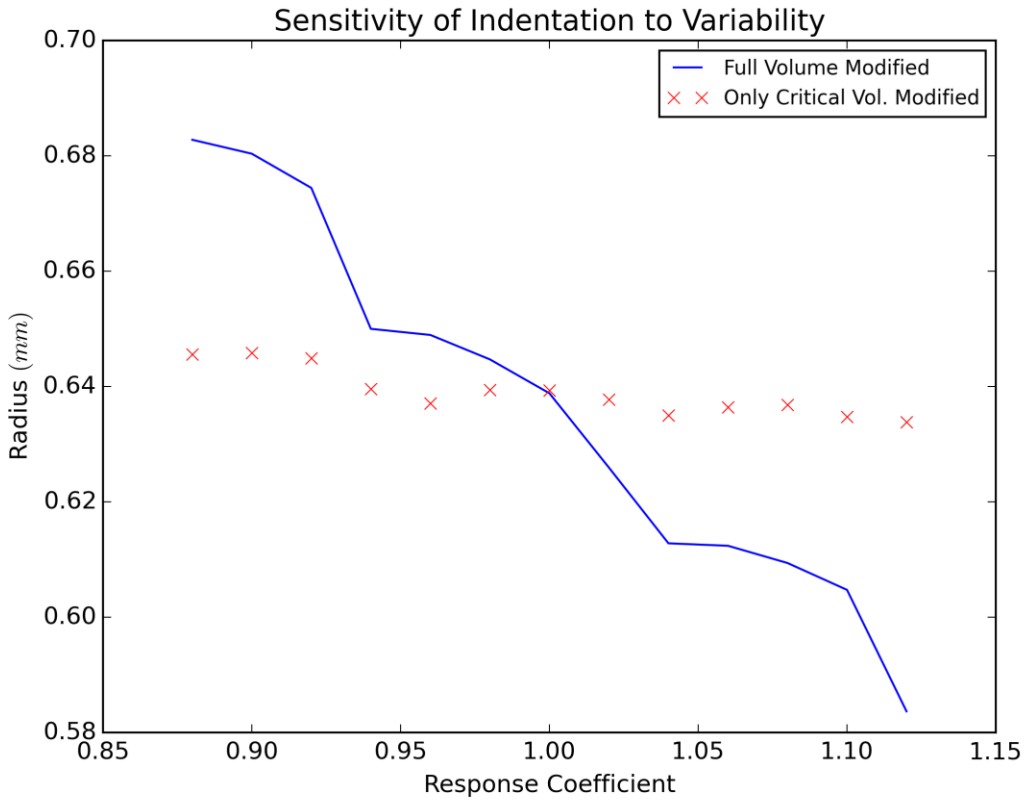

Figure 5.6. Initial simulated indentation radii sensitivity to modification of material response in entire material homogenously, and in only a critically stressed volume of the material.

5.4. Discussion

The remaining challenges of informing polycrystalline response variability from microindentation data are discussed. The use of a set of CP-SVE microindentation simulations may be needed to explore interactions between microstructure and microindentation. The coordination of TD and BU information in reduced-order model development is outlined.

Microindentation variability and microstructure variability are not well linked. This connection requires a simulation of microindentation in order to relate the measured quantity (indentation radius) to an indication of material response as well as a volume of material associated with the measurement. Typically, this volume is estimated in an equally weighted sampling of grains, according to a relation of grain size and indentation stress zone size. It is yet to be determined if the dependence of the measured response is equally dependent on each of the grains in the affected zone. The model used to make this connection is a biasing influence on any subsequent connections between length scales. Additionally, the differences between the simulated indentation and the indentation-as-measured experimentally can have profound influence on the interpretation of the data. For example, the elastic deformation of the indenter tip may affect the observed indentation radius. An optimization of the TD pathway may be critical to the full development of a reduced-order multiscale model.

A fully resolved CP-SVE study of microindentation may be needed to explore the interactions of microstructure variability and the deformation of microindentation. Initial simulations suggest that material response outside the critically stressed volume has

greater influence on the observed indentation radius than the material response within the critically stressed volume. The extent to which material surrounding the plastically deformed region is included in the determination of the microindentation radius has not been fully explored. Such an exploration is needed to aid in developing a reduced-order model of the deformation response.

A reduced order model which can be fitted to data from TD and BU will likely include certain capabilities. At the mesoscale lengths of interest, the response of an SVE is anisotropic. Given that the loading conditions of the BU (uniaxial tension) and the TD (spherical microindentation) are different, a reduced order model which fits both datasets will likely need to reflect anisotropy in coarse-grained response. Given that the mesoscale lengths of interest are likely smaller than the largest lengths of measurable microstructure correlation, correlations between coarse-grained elements may be necessary to appropriately populate larger simulation volumes.

To summarize, an initial exploration of a multiscale development framework for modeling the mesoscale variability of deformation response in cartridge brass is performed. More work is needed to use microindentation to quantify microstructure response variability from TD. A full CP-SVE testing may be needed to explore the interactions of deformation and microstructure at the mesoscale. Coarse-grained models with support for anisotropic response may be necessary in candidate reduced-order models.

CHAPTER 6. α -TI TEXTURE EFFECT CALIBRATION IN THE MATERIALS KNOWLEDGE SYSTEM

Microstructure-sensitive modeling of materials is an expensive part of the ICME paradigm. Data-driven structure-property relation discovery algorithms, such as those based on the Materials Knowledge System (MKS) (Fast and Kalidindi, 2011; Kalidindi et al., 2010) accelerate microstructure-sensitive modeling, making it applicable to time-sensitive use cases. The calibration of MKS to a new material system can be a time-consuming procedure, and it requires the user to understand texture analysis, the crystal plasticity (CP) model used in the calibration, and the manner by which the MKS constructs a model for a material. Exercising the CP model is also the largest computational expense associated with the use of MKS. Optimization of the calibration procedure for MKS would both further accelerate the use of MKS and simplify the process for developing MKS for new materials. In this work, a typical approach to calibration of MKS is compared with a calibration method which uses Gaussian process (GP) based adaptive sampling in an application to α -Ti. The typical approach uses both known textures and hypothetical textures in a statistical volume element (SVE) ensemble approach to calibrate the MKS model for the predefined textures. The adaptive sampling method uses a systematic "binning of textures" procedure to generalize the MKS calibration across the range of feasible textures. The finite set of textures obtained with the binning procedure is indexed for use with the GP model using generalized spherical harmonic (GSH) functions, which constitute an orthonormal, primitive basis of texture. The number of SVEs in each ensemble is studied to assess effects on the efficiency of

exploring textures. The predicted variance of the GP at randomly selected textures is correlated with the validation uncertainty of the MKS model calibrated on the set of SVE ensembles which inform the GP. The validation of the MKS model is used as a measure of calibration success and is used to determine the relative merit of the different calibration approaches considered. The results of the approach indicate the influence of misorientation in polycrystalline response. Improvements supporting the use of MKS as a predictive tool are discussed.

6.1. Introduction

The Materials Knowledge System is a collection of structure-property relationship discovery tools (Kalidindi et al., 2016; Paulson et al., 2017; Wheeler et al., 2014) and is implemented in python as PyMKS (Wheeler et al., 2014). The homogenization model of MKS links microstructure to properties with sophisticated regression methods. The properties are interpolated from results of CP simulation of SVEs. Microstructure is parameterized using two-point correlations between the crystallographic orientations of the material at each element in the SVE. Principal component analysis (PCA) is used to extract the most important correlations. A polynomial regression is used to explain the variation in CP results with differences in the microstructure. Once calibrated, the MKS homogenization method offers profound efficiency increases over CP simulations alone (Paulson et al., 2017). The design of the calibration dataset is the most computationally expensive and analytically intensive step for applying MKS to a new material. In order to expand on the advantages offered by MKS, this work uses a Gaussian process model to direct CP simulations in the exploration of a material system across texture. The challenges to this work are the high dimensionality of texture and the expense of high

precision simulations. Strategies are employed to make efficient use of computational time in the exploration of texture effects on properties. A systematic binning of texture is explored on a parametric basis.

When texture is part of the design space for a material, the definition of a hull (Adams et al., 2013a, 2013b) is needed. The microstructure hull is a convex set of texture definitions which contain all possible microstructures for the material system. Without this hull, the design space is incompletely defined, and unphysical microstructures might be preferred by optimization of the design parameters. The work in this chapter is a preliminary step in the design process. To simplify the calibration, the incorporation of a complete microstructure hull is left to subsequent work.

Data selection is a bottle-neck for algorithmic pattern-recognition. Differing notably from the scientific approach to data collection, data-driven applications require algorithms to work in an a priori use-case, i.e., the data needed to inform the algorithm must be collectible without expert knowledge guiding that collection procedure. To specify what this means in a material modeling context, the calibration of MKS for a newer material system is described. Assuming a CP model of this material is calibrated to experimental specimen testing such that it is considered accurate across all textures, an MKS model can be calibrated using the CP model. A scientific approach to the data selection for the CP to MKS calibration would explore the microstructure hull for this material. In a data-driven paradigm, the microstructure hull may or may not be available. The data-driven calibration of MKS for this new material could be used to investigate its potential design performance. This approach could motivate research investment in the material system. The data-driven data selection requires a generalizable procedure which

considers computational budgetary constraints. The data selection methods which abide by these requirements are significantly different from the traditional scientific approaches. Such differences are discussed in this work.

Generalized spherical harmonic (GSH) functions are used to provide reduced-order representations of texture (Adams et al., 2013c, 2013d; Bunge, 2013). The GSH functions, T_l^{mn} , form an approximate basis for all definitions of textures, $f(g)$, in a crystallographic system, i.e.,

$$f(g) = \sum_{l=0}^{\infty} \sum_{m=-l}^{+l} \sum_{n=-l}^{+l} C_l^{mn} T_l^{mn}(g) \tag{54}$$

where g represents an orientation in Euler angle form, $(\varphi_1, \phi, \varphi_2)$. This basis is navigated using coefficients C_l^{mn}. While the GSH functions are an infinite series, they are truncated for use. The truncation leads to an approximate representation of texture space within a finite parameter space. The GSH coefficients are used to index the textures generated with a binning procedure such that they can be explored parametrically.

Gaussian Process (GP) models are used for regression, classification and as surrogates for more expensive models (Forrester et al., 2008; McHutchon and Rasmussen, 2011; Rasmussen and Williams, 2006). These GP models use kernel functions, whose hyperparameters are informed using observations over some specified input basis. The hyperparameters are tuned to maximize the conditional likelihood of the model, given the observations. The definition of the kernel function allows the GP to define predictions over the basis in terms of a mean function and a covariance function. A

Gaussian process model is used to monitor the exploration of texture space in the calibration simulation set. The GP model gives predictions of response as well as the predicted standard deviation from the mean at any point in the input space. Combining these predictions with an incremental data collection approach allows the design of experiments to adapt to the responses as they are measured.

Adaptive sampling has been used in materials design (Dehghannasiri et al., 2017; Gopakumar et al., 2018). Adaptive sampling methods depend on a feedback loop between observations and subsequent experiments. This feedback loop can be crafted with a surrogate model and an objective criterion. The surrogate model presents 'best guesses' of properties and uncertainty across the design space, based on collected measurements or simulations. In design problems, adaptive data collection is often approached as a two-phase procedure, composed of exploration and exploitation. In the exploration phase, new experiments are selected to maximize reduction to uncertainty. In the exploitation phase, experiments are chosen which are likely to improve upon the best possible observed design properties. The adaptive sampling application in this work uses an uncertainty reduction objective, i.e., it is exclusively employed in the exploration phase. In this work, a calibration of a MKS model for all textures is the desired outcome, as opposed to an optimization of a set of design properties. It is also noted that for this work, the CP-FEM simulations replace the laboratory experiments in the feedback loops of the examples referenced.

The use of GP surrogate models in high dimensional adaptive sampling has notable limitations. The GP model, under an uncertainty reduction sampling criterion, will tend to prefer the exploration of the "corners" of a parameter space, i.e., the

combinations of parameter values near to the maximum and minimum of a space. This tendency can be problematic for the case of GSH coefficients, for which the "corners" indicate aphysical combinations of GSH coefficients. Additionally, the exploration of these "corners" can be expensive in high-dimensional spaces. The work in this chapter efficiently avoids these issues by limiting the exploration to an independently defined data frame. The GSH functions and GP model are used to select from a limited set of textures by developing covariances in terms of a GSH space.

α-Ti is the material modeled in this work. Ti-6Al-4V, also known as Ti64, is an important alloy in aerospace applications (Boyer, 1996). The two-phase alloy consists of the hexagonal α phase and the cubic β phase (Donachie, 2000). The alloy has useful fatigue and creep resistance, as well as the characteristically high specific strength of titanium. While the two phases appear as a mixture in Ti64, the work in this chapter models the texture of the α component alone, as a simplification of the full problem of texture and phase fraction. Krzysztof Stopka et al. approach the two-phase Ti64 problem in recent work (n.d.). Krzysztof Stopka implemented the crystal plasticity modeling and MKS work which is documented in this chapter. The crystal plasticity model used for α-Ti in this work is taken from previous work (B. D. Smith, 2013; Zhang et al., 2007). The quantities of interest in this work are the texture dependence of the yield strength, σ_Y, (measured as the 0.2% offset yield, $\sigma_{Y,0.2\%}$) and the uniaxial elastic stiffness modulus, E_{11}.

6.2. Methodology

The systematic exploration of textures was approached as follows. Multiple calibrations were designed to explore the effect of binning textures and the use of the GP model. The design scheme is summarized in a flowchart in Figure 6.1.

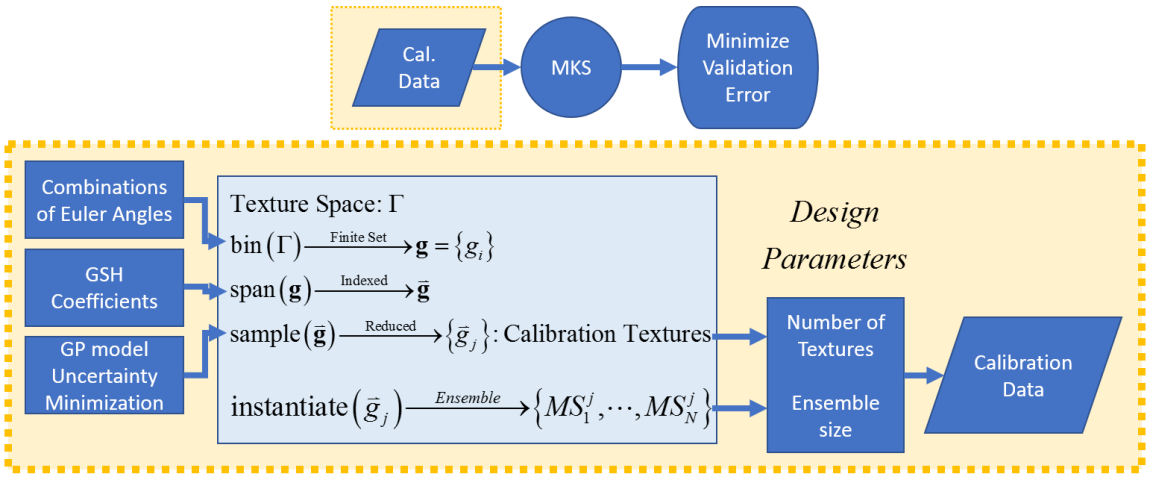

Figure 6.1. A flowchart of the calibration dataset design.

The number of total simulations is held constant between calibrations to reflect computational budget constraints. Two control calibrations were designed which do not use a GP model: one which uses texture targets belonging to the binned procedurally generated set, the other using textures from previous MKS calibration work and are not contained by the binned set. Three calibrations are formulated to use GP-driven adaptive sampling with differently sized SVE ensembles. A set of textures chosen to maximize coverage in the calibration space are used to initialize the GP model. Batches of SVE ensembles are run at textures which have maximum predicted potential to reduce the GP prediction uncertainty. Validation sets are designed to test the performance of the calibrations in different situations. The validation sets are either selected from the binning

procedure or originate external to the binning procedure. The MKS models, calibrated on each calibration design, are compared in terms of mean relative error in predicting the results of the validation simulations.

6.2.1. Data Selection: Texture Binning Procedure

A texture binning procedure was used to define a limited set of textures for use in the calibration of an MKS model. The section of Euler angle space which describes all hcp crystals is discretized by taking eight values of the first two Euler angles, $\{\varphi_1, \phi, \varphi_2\}$. The third Euler angle, φ_2, was not explored, given that the GSH indexing method used did not distinguish between different values of φ_2. The 64 combinations of the discrete values are used in addition to random texture as a fundamental set of orientations. These orientations are used individually to establish the basic 65 textures. The texture set is expanded by including binary combinations of all 65 preferred orientations in ratios of 0.25-0.75, 0.5-0.5, and 0.75-0.25. The total set of textures has 6,305 specific orientation distributions.

Random noise is added to sharp texture components when informing the SVE instantiations. The CP model depends on crystallographic differences between grains, rather than grain boundaries, to simulate a polycrystal. If sharp textures were imposed, the CP simulation would effectively combine grains of the same orientation into a single crystal. To reflect the grain size statistics used in the instantiation of the microstructures used in this work, random noise is added to the sharp textures when informing the grains of a SVE, prior to simulation. Noise is applied in a Euclidean space which is

subsequently mapped onto the Euler angle space. The mapping is performed for the hcp crystal system of α-Ti as follows:

$$\begin{aligned} e\left[e_1, e_2, e_3\right]_{0 \le e_i \le 1} &\rightarrow g\left[\varphi_1, \phi, \varphi_2\right]_{hcp} \\ \varphi_1 = 2\pi e_1,\ \phi = \cos^{-1}\left(1 - e_2\right),\ \varphi_2 &= \frac{\pi}{3} e_3 \end{aligned} \tag{55}$$

Noise is added to the Euclidean coordinate for the sharp texture as a sample from a Gaussian distribution of mean 0 and variance 0.025, i.e., $N\left(0, 0.025\right)$. Random texture is drawn from the Euclidean space using a uniform distribution for each component. Each grain in an instantiation is assigned an orientation in this manner.

This binning procedure does not approach misorientation in any systematic way. It is expected that misorientation statistics have important effects on the homogenized stress response of a polycrystal to strain. The potential for these misorientation effects to be missing from the binned set of textures is acknowledged. The results of this study are used to suggest whether a larger, more sophisticated binning procedure which considers misorientation is necessary to generalize MKS across texture space.

6.2.2. Calibration Design

The proposed calibration design contains a data-driven sampling loop. The components of this loop include GSH functions, a set of binned textures, an initialization dataset selection, the instantiation of microstructure volumes for simulation, the extraction of data from simulations, a sampling criterion, a stopping criterion, and a parametric exploration of the data collection approach. To provide context for the many

components described in this section, a flowchart of the sampling loop is shown in Figure 6.2.

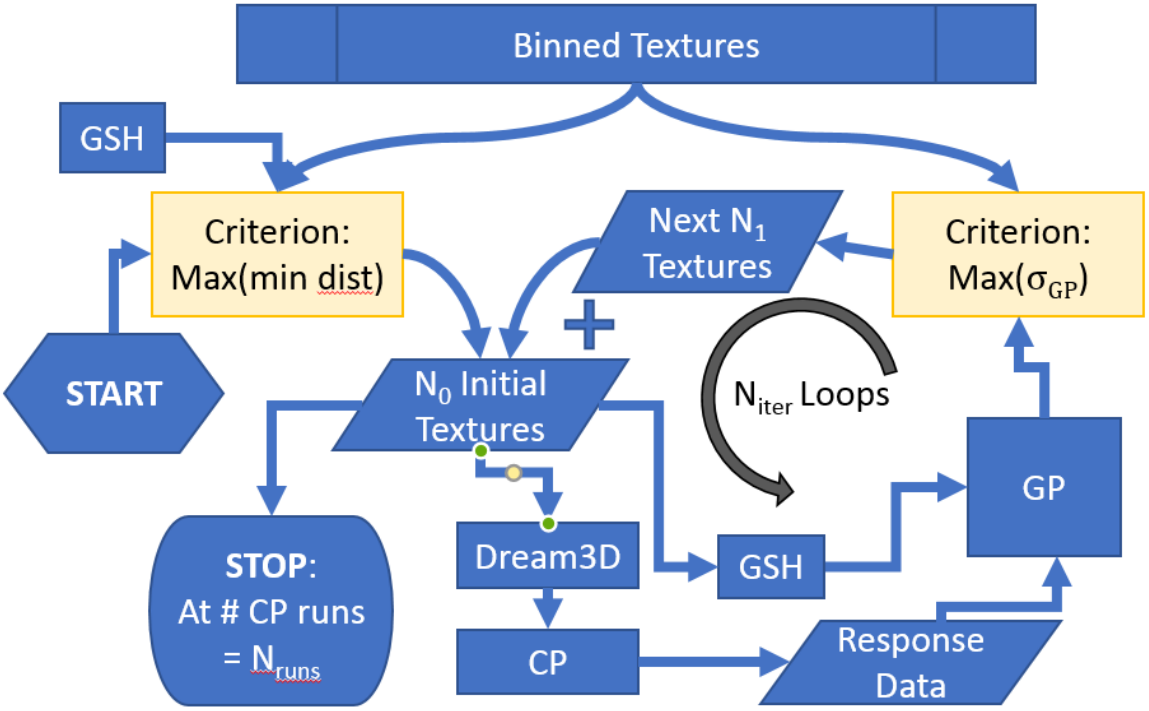

Figure 6.2. A flowchart of the initialization and adaptive sampling loop employed in this work.

To initialize the GP calibration, an initialization dataset is selected. A set of SVE ensembles are selected to initialize a GP model which relates GSH coefficients to simulated yield strength and elastic stiffness of polycrystalline α-Ti. These initial data are expected to influence the results of the calibrations. To compare the approaches with consistency in starting conditions, the textures selected for the initialization set are chosen once and used for all the calibrations. The initialization set of textures contains N_0 textures selected from the 6,305 combinations of the binning procedure. The selection of these textures depends on an indexing of the texture options using GSH coefficients.

Four calibration datasets were used as controls to the GP based methods. The first control was made from the initial set of textures which were used to initialize the GP model in the other calibrations. In this control approach, the number of SVEs simulated at each initial texture was higher, totaling to the entire simulation budget. A random sampling of 240 textures in the binned set were simulated as an alternative strategy to the GP approach. These controls allow the effect of the GP model to be distinguished from the effect of the binning procedure and from the effect of different SVE ensemble size. The other control calibrations used previously specified textures as targets. These textures were taken from previous work on MKS for Ti64 (Paulson et al., 2017). These external textures were included to investigate limitations in the binned dataset.

The computational cost of the calibration is held fixed in comparing multiple approaches. The purpose of this constraint is to test these calibration approaches in terms of efficacy at a fixed cost. The cost of all CP-FEM simulations is calculated as

$$N_{runs} = N_{SVE}\left(N_0 + N_{iter}N_1\right), \tag{56}$$

where N_{runs} is the total number of CP-SVE simulations in the calibration design, N_{SVE} is the number of SVEs in each ensemble, N_0 is the number of ensembles in the initialization batch, N_1 is the number of ensembles in each adaptive batch, and N_{iter} is the number of adaptive steps in the calibration. The parameter values are described for the different calibration designs in this work in Table 6-1.

Table 6-1. The design parameters for the calibrations which use the GP model and which use pre-selected textures*.

Calibration Design	N_{runs}	N_{SVE}	N_0	N_1	N_{iter}	**Total Textures**
GP-3	240	3	8	4	18	80
GP-5	240	5	8	4	10	48
GP-10	240	10	8	4	4	24
Control-Binned	240	30	8	–	–	8
Control-External 1	240	30	8	–	–	8*
Control-External 2	240	30	8	–	–	8*
Random Binned	240	1	240	–	–	240

The GSH functions are used to index the texture combinations generated in the binning procedure. The formula which calculates the GSH coefficients can be simplified for the summation of equally weighted orientations, i.e.,

$$C_l^{mn} = \frac{2l+1}{J}\sum_{j=1}^{J} T_l^{mn*}\left(g_j\right) \tag{57}$$

where C_l^{mn} are the coefficients for the GSH functions T_l^{mn}, l is the degree of the function, J is the total number of orientations, g, indexed by j, and the asterisk denotes the complex conjugate. The 6305 textures are indexed by the first 15 GSH functions so that the textures can be located in a consistent parametric space. This parametric definition is a requirement for the exploration of these textures in a GP regression.

The 15 GSH coefficients $\mathbf{C} = \left[C_l^{mn} \right]$ are mapped to equally sized intervals of uniform density, $\mathbf{p}$. GSH coefficients can have complex values. The values for coefficients in the texture set may have ranges which differ from coefficient to coefficient. To avoid complications which could arise from using a GP model on a complex and anisotropic parameter space, a mapping is applied to $\mathbf{C}$. Symmetry of the crystal system allows the separation of the real and imaginary components of the complex valued coefficients. $C_0^{0,0}$ is not included in $\mathbf{p}$, as it is not variable. The values of each component of $\mathbf{C}$ for each included texture are mapped to the interval $[0,1]$ and given uniform spacings. The values of $\mathbf{p}$ are used in the GP model.

The initialization texture set is chosen according to an algorithm to fill the GSH-space. N_0 textures are selected from the 6,503 procedurally generated textures by identifying the N_0 points in GSH-space which refer to those textures. The first point is selected from the binning procedure set at random. The subsequent points are chosen such that the minimum of the Euclidean distances between the new point and all previously identified points is maximized. Due to the randomness of the first selection, this method can be repeated to investigate the effects of the initialization on the calibration performance.

Dream3D is used to generate the microstructure instantiations used in the CP simulations (Groeber and Jackson, 2014). The grain size distribution is defined using a discretized lognormal distribution with 10 equally spaced bins, defined according to

$$P\left[d = x\right] = \frac{1}{x}\frac{1}{\sigma\sqrt{2\pi}}\exp\left(-\frac{\left(\ln x - \mu\right)^2}{2\sigma^2}\right), \quad x \in \left[36\mu\text{m},\ 96\mu\text{m}\right] \tag{58}$$

where the parameter μ is equal to 4.064 and σ is equal to 0.264. The grain shapes are assumed to be equiaxed. The microstructures are generated prior to the calibrations. The orientation of each grain is overwritten to reflect the selected texture. As a result, for those calibrations which use the binning procedure, the influence of the inherently variable procedure of microstructure instantiation on the difference in the calibrations is minimized. A notable exception to this procedure is the second control calibration, whose SVE instantiations are generated using Dream3D and orientation distribution data.

The initialized GP model is used to select textures for subsequent simulations. Points in GSH-space which correspond to procedurally generated textures are selected which have the highest predicted variance. The GP model is used to predict the standard deviation from the mean predicted response, i.e.,

$$E\left[\sigma_{GP}\left(\mathbf{p}\right)\right],\ \mathbf{p} = \left[p_1, p_2, \ldots, p_{14}\right] \tag{59}$$

where $E\left[w\right]$ denotes the expected value of some quantity w, $\mathbf{p}$ is the vector of parameters p_i which correspond to the GSH coefficients, C_l^{mn}, each mapped to the closed interval, $\left[0,1\right]$, and σ_{GP} is the estimated standard deviation of the GP, defined as a function of $\mathbf{p}$. For each subsequent batch of N_1 SVE ensembles used in the calibration,

$\mathbf{p}$ values are chosen according to an algorithm. For all textures in the binned set, σ_{GP} is predicted. The textures whose σ_{GP} values are above the cutoff criterion, i.e.,

$$\sigma_{GP} > \max\left(\sigma_{GP}\left(\mathbf{p}\right)\right) - tol \times \left(\max\left(\sigma_{GP}\left(\mathbf{p}\right)\right) - \min\left(\sigma_{GP}\left(\mathbf{p}\right)\right)\right) \tag{60}$$

where the maximum and minimum refer only to the values for the binned textures. The value used for tol is set to select the top 50 to 100 values. Of those selected textures, the maximal value is taken as the first point of the next batch. Each subsequent point is taken by searching the selected samples for the point with the maximal minimum distance to the already selected new points.

The number of SVEs per ensemble used for the GP calibrations, N_{SVE}, is smaller than typical of SVE ensembles. This N_{SVE} is a parameter of the calibration and is large enough to provide a reasonable estimate of the variance of the SVE results within each ensemble. Due to the interpolation from the GP model, multiple small ensembles can be used to explore more of the parametric space at a lower precision. The work in this chapter explores whether this strategy can give more efficient reductions in the expected deviation from the predicted mean than can fewer, larger ensembles.

Smaller ensembles of SVEs are used in informing the GP model. The cost of the calibration is fixed, as is the total number of simulations. To explore texture more broadly in a calibration of the MKS model, smaller ensembles of SVEs must be used. The properties determined by small SVE ensemble are inherently noisy. To accommodate that noise in the GP, the kernel of the model is built with a noise parameter. This parameter is

estimated from results of simulations on a larger ensemble of SVEs. The unbiased predictor for the variance of the SVE response for σ_Y, written here as x_i, is given as

$$\hat{\sigma}^2 = \frac{1}{N_{SVE} - 1} \sum_{i=1}^{N} \left(x_i - m \right)^2 \tag{61}$$

where N_{SVE} is the number of SVEs in the ensemble, m is the mean of the ensemble of responses, and $\hat{\sigma}^2$ is the unbiased estimate of population variance, σ^2. This informs the GP via a hyperparameter α, which determines the level of noise to expect in the data. Without an appropriate level of noise, the solution of the covariance equations would become singular for any points that are close together in GSH-space.

6.2.3. Gaussian Process Regression Model

The texture space was adaptively sampled using the GP model. The expected value of the standard deviation σ_{GP} of the GP model was maximized to find the next texture to explore. By investigating the texture defined by the maximum of σ_{GP}, the expected reduction in uncertainty of the GP is maximized. The use of this $\max(\sigma_{GP})$ criteria replaces the need for a list of expert-designed texture classes to generate a design of experiments for the calibration of the MKS model.

The GP formulation used predicts the ensemble average elastic stiffness and offset yield strength from the GSH approximation of the texture bin which corresponds to the SVE ensemble simulated. I.e.,

$$E[E], E[\sigma_y] \sim GP(\mathbf{p}) \tag{62}$$

where $E[E]$ is the ensemble average of the elastic stiffness, $E[\sigma_y]$ is the expected value of the 0.2% offset yield strength, and $\mathbf{p}$ is the linear mapping onto $[0,1]$ intervals of the 14 GSH coefficients used to parameterize the texture bins.

The adaptive sampling is performed on 1-point statistics. As a result, the adaptive sampling can only include 1-point statistics in its coverage of the binned dataset. In other words, the variation of misorientations (a 2-point statistic) present in a binned dataset would not be explored by this GP model as formulated. The current binning procedure was not made to survey misorentations. However, should future work include misorientation in the binned data, the GP model would need to be made sensitive to those misorientations in order to adaptively sample that variation.

The python package scikit-learn (Pedregosa et al., 2011) was used to generate the GP model which relates the SVE ensemble-mean yield strength to texture. The Gaussian process regression module was used. The kernel function was constructed as a product of the squared exponential kernel and a constant kernel, with the white noise kernel function, i.e.,

$$k(\mathbf{x}_i, \mathbf{x}_j) = h^2 \exp\left(-\frac{dist(\mathbf{x}_i, \mathbf{x}_j)^2}{2l^2}\right) + \alpha\delta_{ij} \tag{63}$$

where h and l are hyperparameters controlling the scale and length of the squared exponential kernel function, α is the hyperparameter controlling the noise in the GP, and δ_{ij} is the Kronecker delta. The value of α varied with each SVE ensemble, as estimated from the response of the constituent SVEs. For more detail on kernel functions and GP models like the one used here, see the book by Rasmussen and Williams (2006).

6.2.4. Crystal Plasticity Model and Simulations

The CP model of α-Ti was adapted from previous work (B. D. Smith, 2013; Zhang et al., 2007). The formulation is phenomenological and rate sensitive, and plastic deformation is calculated in the intermediate kinematic configuration. The kinematic treatment and the constitutive equations are outlined.

The deformation gradient of the material is decomposed multiplicatively into elastic (stretch and rigid rotation) and inelastic (dislocation motion) parts, i.e.,

$$\mathbf{F} = \mathbf{F}^{e} \cdot \mathbf{F}^{in} \tag{64}$$

where $\mathbf{F}^{e}$ is the deformation gradient contribution of the elastic stretching of the lattice and the rigid rotation of the lattice, and $\mathbf{F}^{in}$ is the deformation gradient contribution which arises from dislocation motion. The Asaro equation (Asaro, 1983) is used to express the inelastic velocity gradient $\mathbf{L}^{in}$ in terms of the activities of the crystallographic slip systems, i.e.,

$$\mathbf{L}^{in} = \sum_{\alpha=1}^{N_s} \dot{\gamma}^{\alpha} \mathbf{m}_0^{\alpha} \otimes \mathbf{n}_0^{\alpha} \tag{65}$$

where $\mathbf{m}_0^{\alpha}$ and $\mathbf{n}_0^{\alpha}$ are the unit vectors in the slip and slip plane normal directions for slip system α, and $\dot{\gamma}^{\alpha}$ are the crystallographic shearing rates. For α-Ti, the number of slip systems, N_s, is 24 (Mayeur, 2004), including 3 basal, 3 prismatic, 6 first-order pyramidal, and 12 second-order pyramidal systems. Slip system details are compiled in Table 6-2.

Table 6-2. The slip systems of α-Ti considered in the CP model.

Name	**Number**	**Family**
Basal	3	$\langle 11\bar{2}0 \rangle \{0001\}$
Prismatic	3	$\langle 11\bar{2}0 \rangle \{10\bar{1}0\}$
1st order Pyramidal	6	$\langle 11\bar{2}0 \rangle \{10\bar{1}1\}$
2nd order Pyramidal	12	$\langle 11\bar{2}3 \rangle \{10\bar{1}1\}$

A power-law hardening model is used for the shearing rate relation. The constitutive shearing rate is given by

$$\dot{\gamma}^{\alpha} = \dot{\gamma}_0 \left\langle \frac{\left|\tau^{\alpha} - \chi^{\alpha}\right| - \kappa^{\alpha}}{D^{\alpha}} \right\rangle^{M} \operatorname{sgn}\left(\tau^{\alpha} - \chi^{\alpha}\right) \tag{66}$$

where $\dot{\gamma}_0$ is the reference shearing rate, τ^{α} is the resolved shear stress on slip system α, χ^{α} is the back stress, κ^{α} is the threshold stress, D^{α} is the drag stress, and M is the

strain-rate sensitivity exponent. Here, κ^{α} includes a Hall-Petch term and a softening term κ_s^{α}, i.e.,

$$\kappa^{\alpha} = \frac{\kappa_y}{\sqrt{d}} + \kappa_s^{\alpha} \tag{67}$$

where κ_y is the Hall-Petch slope and d is the mean slip distance. κ^{α} evolves with the dynamic recovery of κ_s^{α}, i.e.,

$$\dot{\kappa}^{\alpha} = \dot{\kappa}_s^{\alpha} = -\mu\kappa_s^{\alpha}\left|\dot{\gamma}^{\alpha}\right| \tag{68}$$

where μ is the softening rate coefficient. The drag stress does not evolve, and is defined as,

$$D^{\alpha} = \tau_{CRSS}^{\alpha} - \frac{\kappa_y}{\sqrt{d}} - \left(\kappa_s^{\alpha}\right)_{t=0} \tag{69}$$

where τ_{CRSS}^{α} is the critical resolved shear stress for slip system α, and $\left(\kappa_s^{\alpha}\right)_{t=0}$ is given as a constant. Back stress evolves with direct hardening and dynamic recovery, i.e.,

$$\dot{\chi}^{\alpha} = h\dot{\gamma}^{\alpha} - h_D\chi^{\alpha}\left|\dot{\gamma}^{\alpha}\right| \tag{70}$$

where h is the direct hardening coefficient and h_D is the dynamic recovery coefficient.

The model is used to simulate the response of α-Ti at room temperature. The values of the parameters used in the CP model are contained in Table 6-3. More detailed explanation can be found in Smith (2013).

Table 6-3. The parameters of the CP model for α-Ti (B. D. Smith, 2013).

Name	Value	Name	Value	Name	Value (MPa)	Name τ_{CRSS}^{α}	Value (MPa)
d	5 μm	h	8000 MPa	$C11$	172,832	*prism*	275
$\dot{\gamma}_0$	$0.001\,\mathrm{s}^{-1}$	h_D	8000	$C12$	97,910	*basal*	350
M	15	μ	2	$C13$	73,432	$pyr\langle a\rangle$	470
κ_y	$12.7\ \mathrm{MPa\ mm}^{0.5}$	$\chi_{t=0}$	0 MPa	$C33$	192,308	$pyr\langle a+c\rangle$	570
$\left(\kappa_s^{\alpha}\right)_{t=0}$	50 MPa			$C44$	49,700		

CPFEM simulations were performed to gather the elastic stiffness and offset yield strength of each cube-shaped SVE. The simulations were run using periodic boundary conditions and hexahedral elements of 10 μm in size, with eight nodes and one integration point per element. The initial SVE size measured 290 μm in each direction. Along one axial direction, the simulation boundary was displaced at a constant rate to impose an effective strain rate of $0.0012\ \mathrm{s}^{-1}$ in uniaxial tension at room temperature. Abaqus Standard (Simulia, 2007) is used, and the model is contained in a UMAT.

6.2.5. Calibrations of MKS

Each set of calibration simulations is used to calibrate an MKS model of the homogenized response of α-Ti as a function of texture. The MKS calibration procedure includes the determination of certain parameters which influence the numerical uncertainty of the resulting model. The methods used in this work in evaluating these

parameters are detailed. The parameter values taken in this work are summarized in Table 6-4.

Table 6-4. MKS homogenization parameter values selected to compare calibration data selection approaches. LOOCV stands for leave one out cross validation.

Parameter	**Value or Criterion**
$\tilde{L}$	15, (lowest calibration error)
S-P Regression Order	1
$\tilde{R}$	$\min(LOOCV)$, *a posteriori:* $\min(\%MRE, validation)$

The number of GSH coefficients, $\tilde{L}$, to use in characterizing the microstructures must be chosen. Before MKS identifies the most important PCs from the 2-point correlation statistics, the number of GSH coefficients to consider is selected. The number of coefficients is typically 6, 15, or 41, reflecting the number of coefficients included when the maximum degree, l, is 2, 4, or 6. For the work here, 15 GSH coefficients were used. The relative performance of MKS models formulated with different numbers of coefficients was explored. The calibration error was used to select the best performing $\tilde{L}$ value.

The maximum order of the regression terms is 1 for this work. The terms in the S-P linkage equations are regressions of the PCs. The inclusion of linear terms in the consideration can allow linear patterns to be captured by MKS. The most appropriate value for the regression order depends not only on the expected underlying dependence of properties to structure but also on the degree to which the calibration data collected can inform these higher order regressive coefficients. All calibration datasets in this work contained 240 simulations. For these datasets, first order regressions were the most able

to capture the S-P linkages, as indicated by the mean relative error for the calibration data.

The number of PCs to be included in the regression model, $\tilde{R}$, is selected using leave one out cross-validation (LOOCV). This measure is used in previous work with MKS. LOOCV is used as a measure to prevent overfitting of the calibration data. The choices for $\tilde{R}$ are specific to each calibration and to each QoI (modulus or strength). The specific $\tilde{R}$ values chosen for each calibration are used to compare the various calibrations, and are shown in Table 6-5. In addition, the performance when $\tilde{R}$ is chosen *a posteriori* is considered. This selection procedure demonstrates possible performance gains. Achieving such performance using *a priori* methods is considered in the discussion.

Table 6-5. The values of $\tilde{R}$, selected to minimize LOOCV errors for each calibration design.

Calibration Design Name	**Best $\tilde{R}$ Value for Modulus, Strength**
Control-External 1	14, 14
Control-External 2	13, 2
Control-Initial Binned	29, 7
Control-Random Binned	17, 18
GP- $N_{SVE} = 10$	26, 27
GP- $N_{SVE} = 5$	24, 26
GP- $N_{SVE} = 3$	23, 36

6.2.6. Validation Data

The validation of the MKS model was performed with data withheld during each calibration. Four validation sets of simulations were defined. A validation set was made

from the textures of each external set (1 and 2). A validation set was made from the texture bins used as the initialization data for the GP model. A validation set was made from single SVEs from 240 of the bins randomly selected without replacement from the 6,305 texture bins. These validation sets are named and detailed in Table 6-6.

Table 6-6. The validation simulation sets by name and description.

Validation Set	**Description**
Same texture-External 1	Eight textures defined without binning, taken from previous work (Paulson et al., 2017) same as those used in Control-External 1 but with new microstructure instantiations
Same texture-Initial Binned	The eight initial textures used in all the GP-informed calibrations, as well as Control-Initial Binned, with new instantiations
New texture-External 2	Same eight textures as those used in Control-External 2 but with new microstructure instantiations
New texture-Random Binned	240 textures taken from the binning procedure at random

The externally defined textures were determined by expert selection. Two sets were specified to demonstrate the performance of the expert decision calibration in both an interpolative validation and an extrapolative validation. For reference, orientation distribution functions (ODFs) of these external texture sets are included in Figure 6.3 (for External 1) and Figure 6.4 (for External 2).

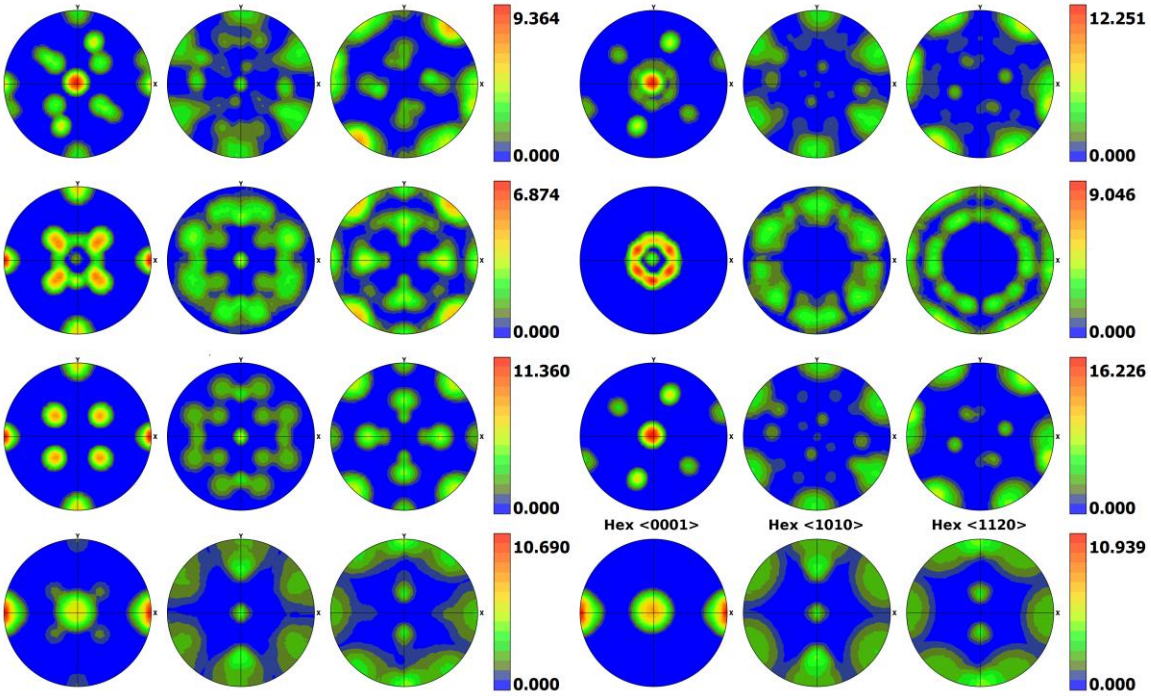

Figure 6.3. ODFs which describe the simulated textures included in the validation set External 1.

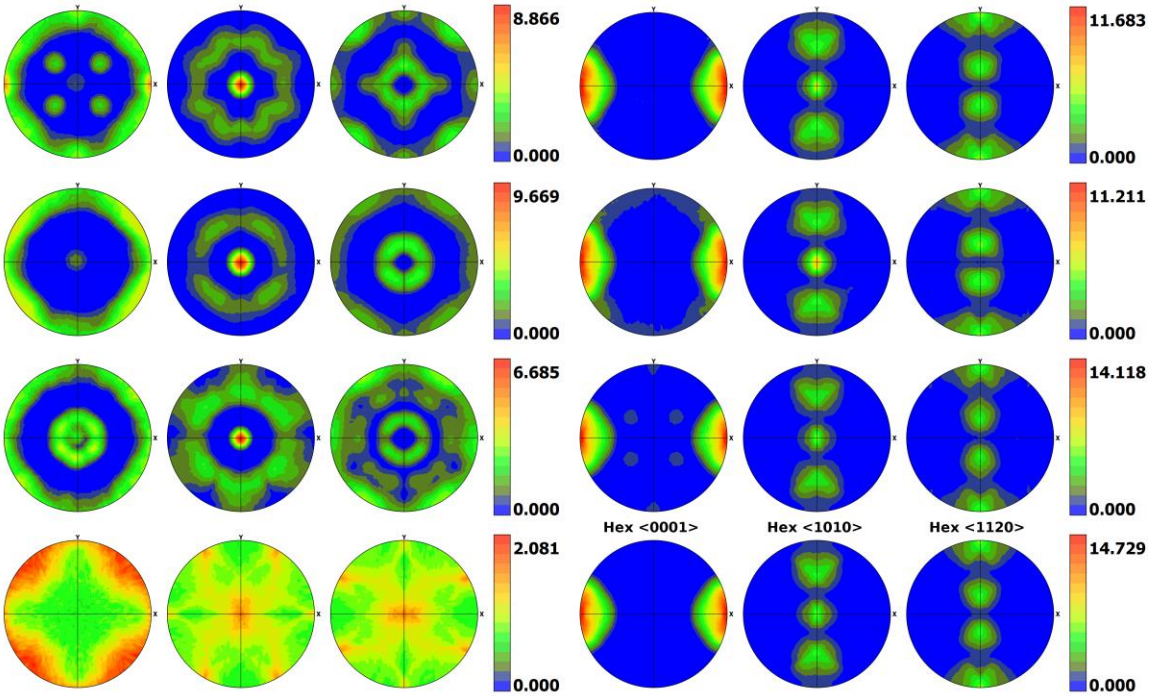

Figure 6.4. ODFs which describe the simulated textures included in the validation set External 2.

6.3. Results

The calibration designs are compared in this section. The PC representation of the different designs are explored. The percent mean relative error (%MRE) in validation of each calibration design is measured for each combination of data sets. The %MRE is also recorded for each combination when $\tilde{R}$ is chosen *a posteriori* to minimize validation error. The GP designs performed as well as the external designs using preselected $\tilde{R}$ values and better than the external designs when using ideal $\tilde{R}$ values.

PC space is used to inspect the calibration designs. The data from every calibration is included in a single PC space and plotted in terms of the first two shared PCs in Figure 6.5. The variations in 2-point correlation statistics within the calibration sets are described in terms of the PCs which are derived for each calibration set separately. The calibration sets are plotted in terms of the values of the first two PCs for each SVE in Figure 6.6. In the externally defined calibration sets, the colors indicate different texture ensembles. In the binned sets, the colors indicate the iteration in which the textures were selected. It should be noted that multiple textures were included in each iteration for the GP and binned calibrations. In interpreting these figures, it should be noted that the first two PCs amount to different levels of explained variance with respect to the different sets of calibration data. More than 80% of the variance of the external sets is explained in the first two PCs. Less than 50% of the variance of the binned sets is explained by the first two PCs. These statistics are shown in Figure 6.7.

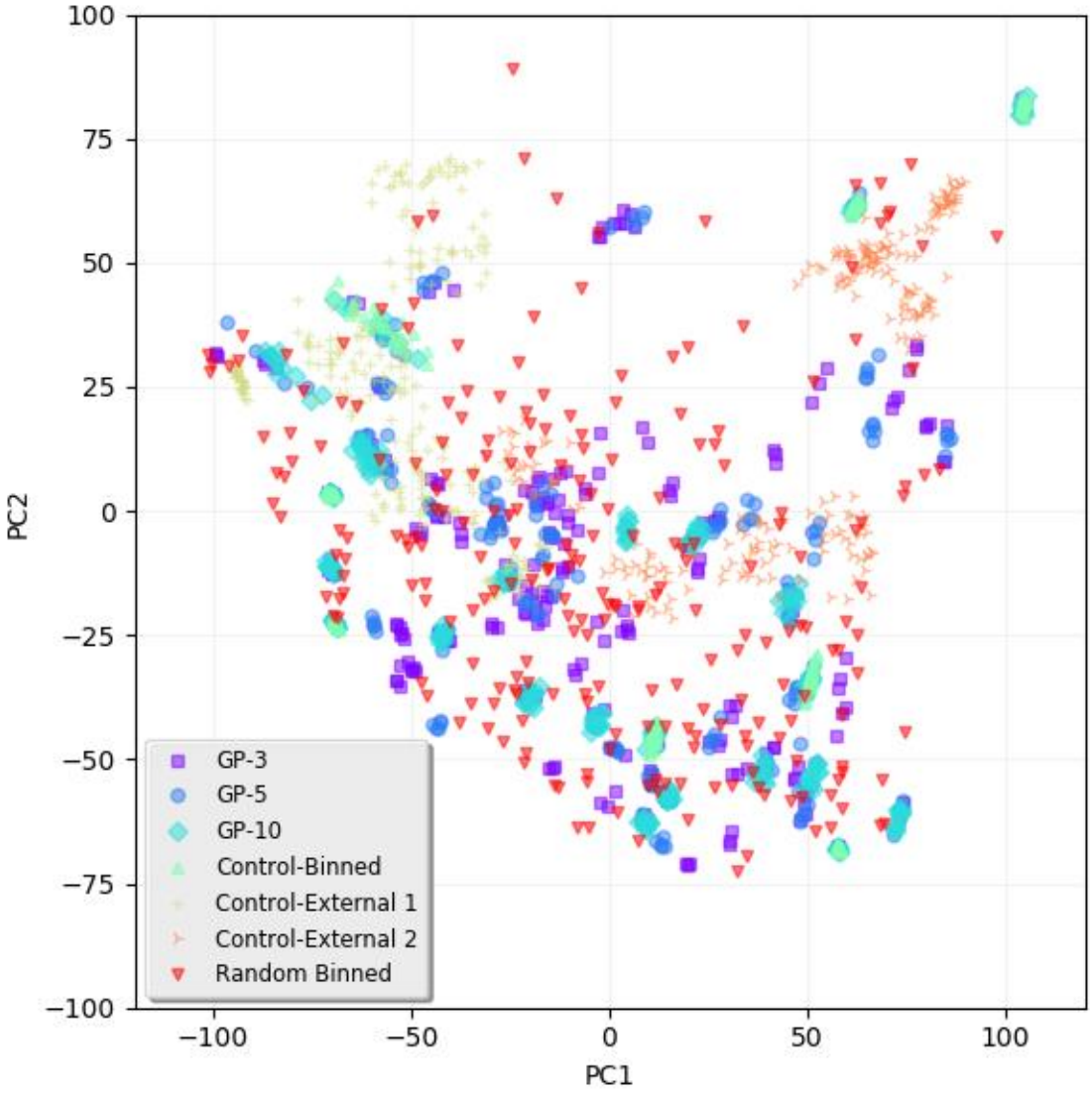

Figure 6.5. All calibrations plotted in terms of two principal components, derived from a calibration of MKS including all data shown.

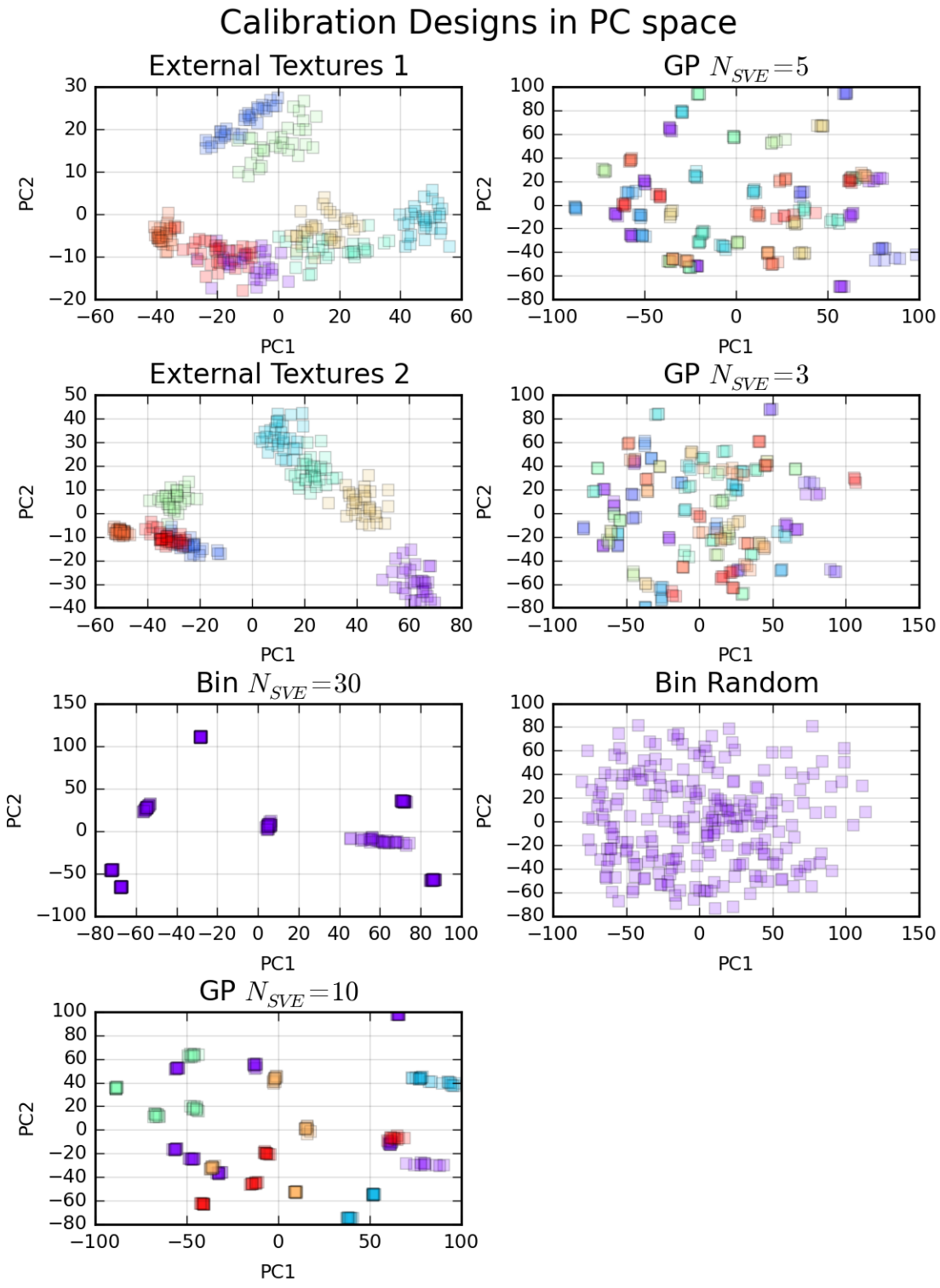

Figure 6.6. The different calibration sets shown in terms of the top two PCs which explain the variation in their microstructure instantiations.

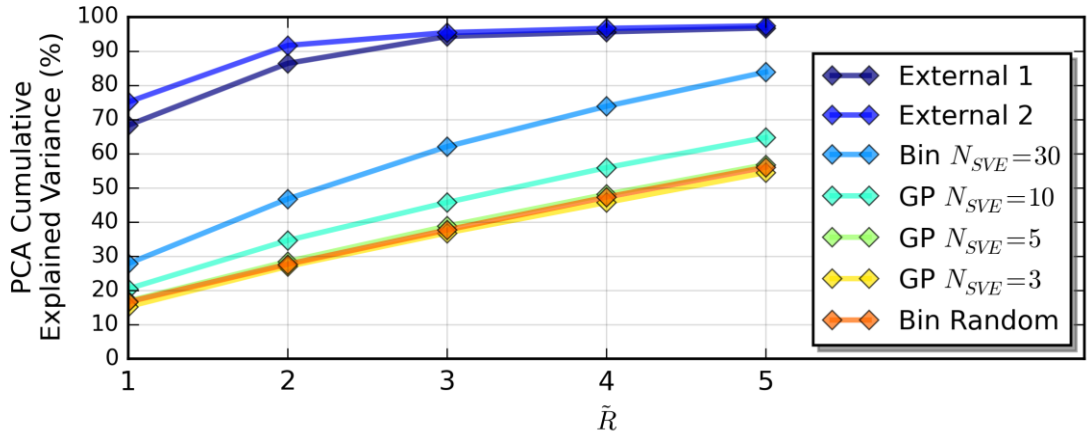

Figure 6.7. The percent cumulative explained variance for the first five PCs for each calibration design used in this work.

The performance of the calibration designs was compared based on *a priori* selections of the MKS parameter $\tilde{R}$. The values of $\tilde{R}$ used to predict elastic modulus and yield strength are shown in Table 6-7 and Table 6-8, respectively. The %MRE was measured for the validation sets for elastic modulus and for yield strength, as shown in Table 6-7 and Table 6-8, respectively, and plotted in Figure 6.8 and Figure 6.9, respectively. The best performances were observed for cases where the validation set and the calibration set were most similar.

Table 6-7. The mean relative percent error of MKS elastic modulus predictions based on each calibration design, measured on each validation set, where $\tilde{R}$ is determined by minimizing LOOCV.

Elastic Modulus		**Validation Set**			
Calibration Set	$\tilde{R}$	Bin $N_{SVE}=30$	Bin Random	External 1	External 2
Bin $N_{SVE}=30$	29	0.017	0.448	0.288	0.231
GP $N_{SVE}=10$	26	0.054	0.914	0.339	0.224
GP $N_{SVE}=5$	24	0.299	0.231	0.357	0.145
GP $N_{SVE}=3$	23	0.423	0.206	0.403	0.149
Bin Random	17	0.479	0.208	0.397	0.172
External Textures 1	14	0.955	0.494	0.052	0.554
External Textures 2	13	0.237	0.319	0.276	0.063

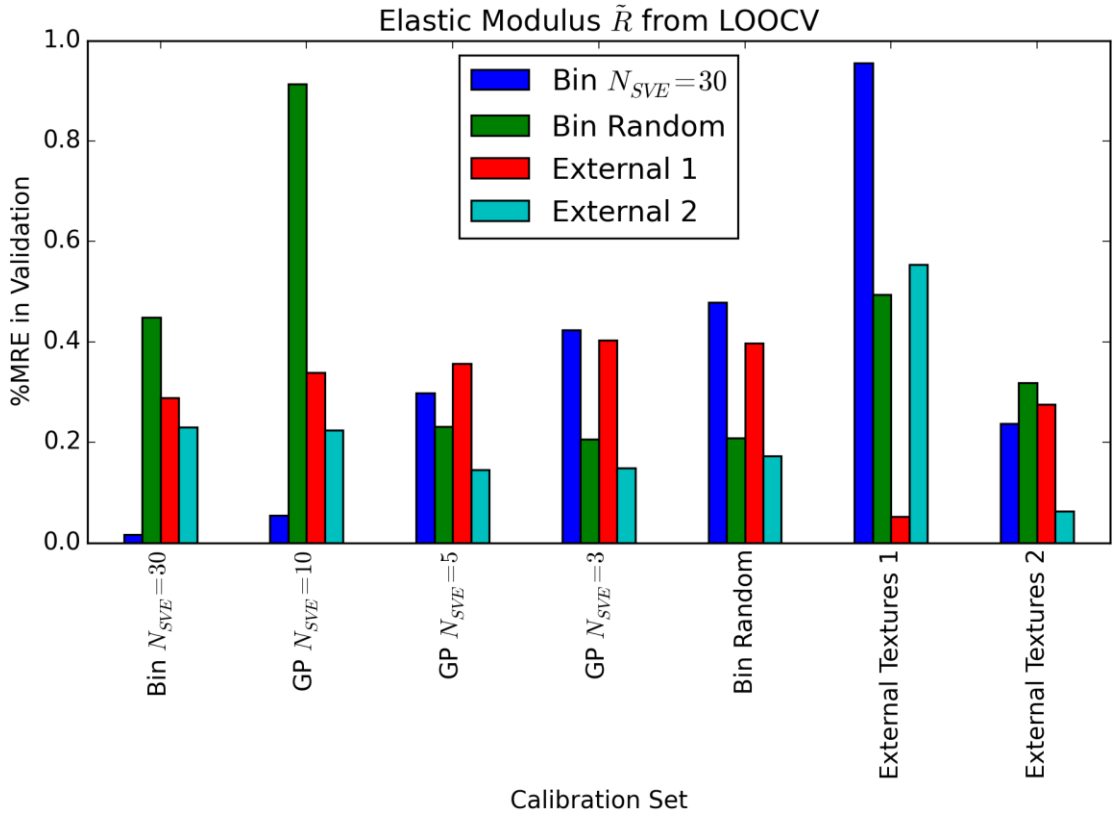

Figure 6.8. The mean relative percent error of MKS elastic modulus predictions based on each calibration design, measured on each validation set (see legend), where $\tilde{R}$ is determined by minimizing LOOCV.

Table 6-8. The mean relative percent error of MKS yield strength predictions based on each calibration design, measured on each validation set, where $\tilde{R}$ is determined by minimizing LOOCV.

Yield Strength		**Validation Set**			
Calibration Set	$\tilde{R}$	Bin $N_{SVE}=30$	Bin Random	External 1	External 2
Bin $N_{SVE}=30$	7	0.32	4.46	3.54	1.29
GP $N_{SVE}=10$	27	0.76	12.25	4.95	1.67
GP $N_{SVE}=5$	26	3.31	2.85	4.91	0.91
GP $N_{SVE}=3$	36	4.02	2.82	4.98	1.27
Bin Random	18	5.10	2.41	2.85	3.16
External Textures 1	14	6.62	5.58	0.72	4.63
External Textures 2	2	3.45	2.59	2.24	0.48

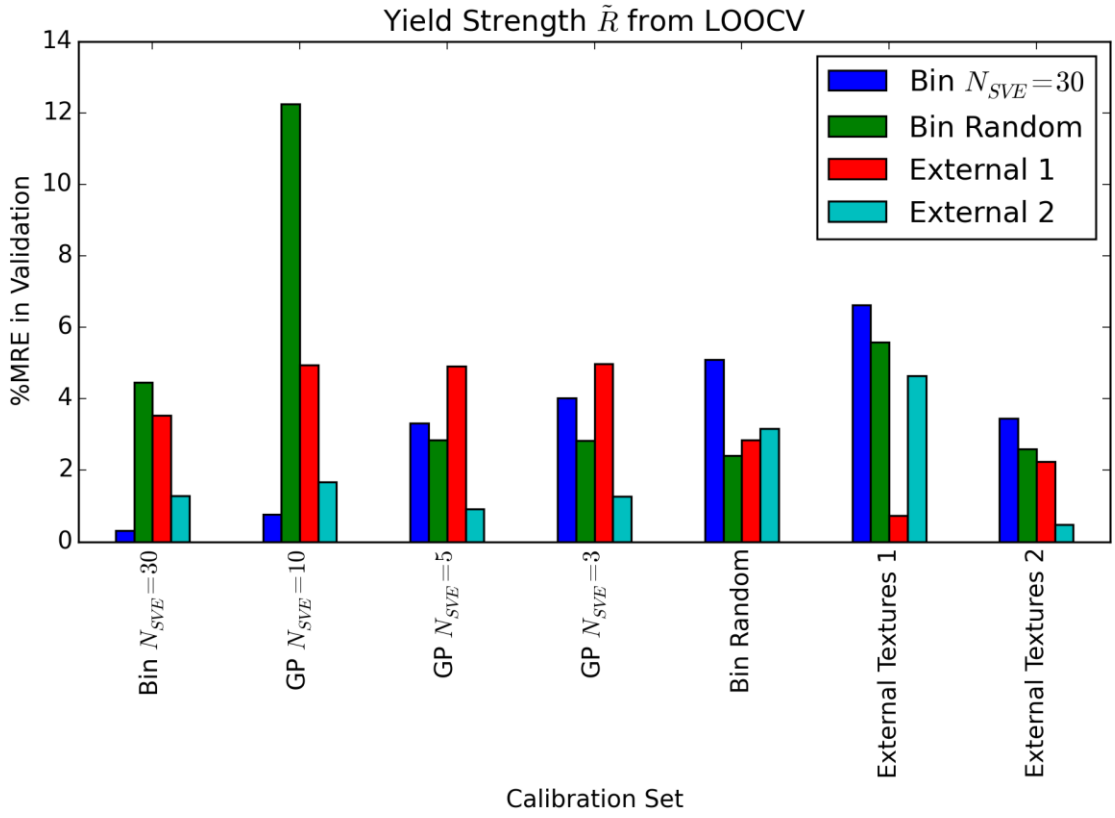

Figure 6.9. The mean relative percent error of MKS yield strength predictions based on each calibration design, measured on each validation set (see legend), where $\tilde{R}$ is determined by minimizing LOOCV.

The MKS calibrations were also compared on the basis of ideal choices for $\tilde{R}$. For a given calibration and validation pairing, including some number of PCs ($\tilde{R}$) resulted in the least %MRE on the validation set. This value was often different from that value of $\tilde{R}$ predicted by finding the minimum LOOCV error. This evaluation of $\tilde{R}$ is based on analysis of validation data, and hence is referred to as an *a posteriori* approach to the selection of $\tilde{R}$. It is included in this work as an indication of the best possible configuration of MKS, under the assumption that the favorable $\tilde{R}$ values could be predicted from data available *a priori*, using a criterion other than the minimum LOOCV error. The best performing values for $\tilde{R}$ were specific to each calibration validation pair, and are shown in Table 6-9 for elastic modulus and Table 6-10 for yield strength. The %MRE in validation is shown for elastic modulus in Table 6-9 and in Figure 6.10; yield strength is shown in Table 6-10 and in Figure 6.11.

Table 6-9. The mean relative percent error of MKS elastic modulus predictions based on each calibration design, measured on each validation set, where $\tilde{R}$ is chosen *a posteriori* based on mean validation error. The $\tilde{R}$ values are specific to each calibration-validation pair.

Elastic Modulus	Bin $N_{SVE}=30$		Bin Random		External 1		External 2	
Calibration Set	$\tilde{R}$	%Error	$\tilde{R}$	%Error	$\tilde{R}$	%Error	$\tilde{R}$	%Error
Bin $N_{SVE}=30$	60	0.013	16	0.422	13	0.266	12	0.219
GP $N_{SVE}=10$	26	0.053	16	0.267	9	0.159	9	0.205
GP $N_{SVE}=5$	30	0.295	19	0.205	9	0.206	21	0.139
GP $N_{SVE}=3$	39	0.400	16	0.202	11	0.232	26	0.143
Bin Random	19	0.479	14	0.208	60	0.363	44	0.172
External Textures 1	53	0.929	59	0.480	14	0.052	60	0.550
External Textures 2	31	0.228	33	0.267	6	0.269	58	0.059

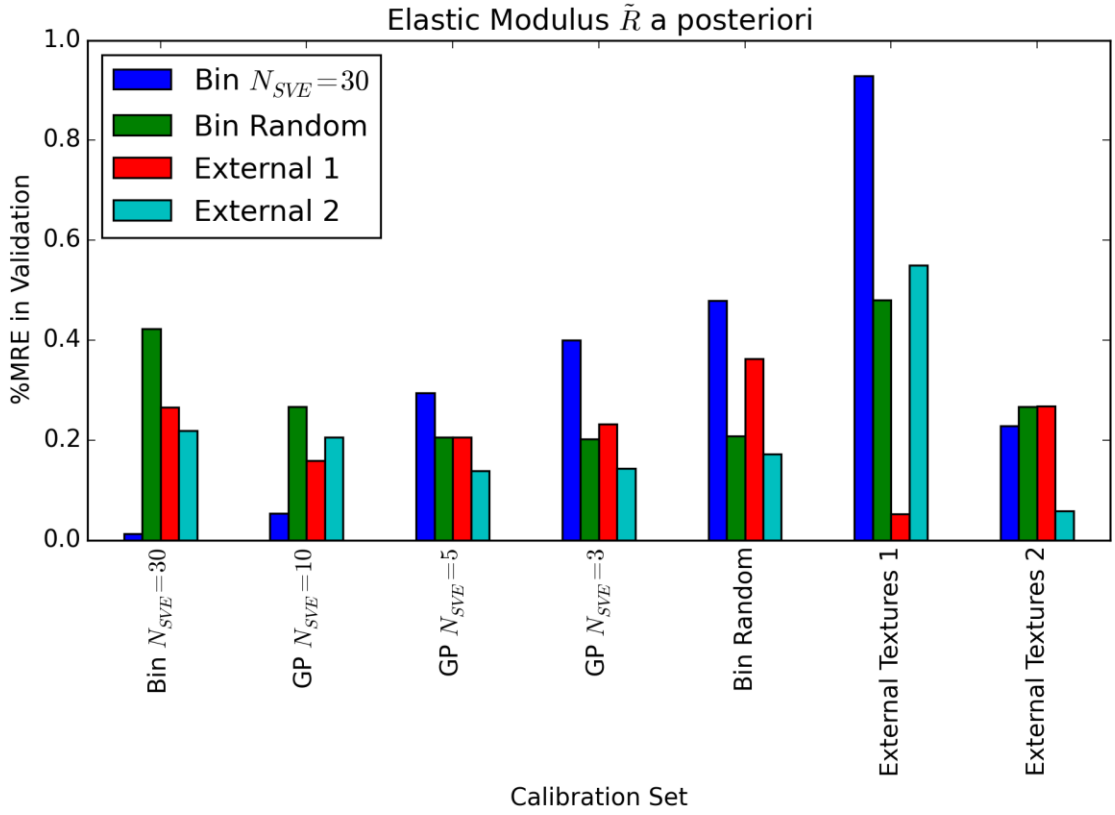

Figure 6.10. The mean relative percent error of MKS elastic modulus predictions based on each calibration design, measured on each validation set, where $\tilde{R}$ is chosen *a posteriori* based on mean validation error.

Table 6-10. The mean relative percent error of MKS yield strength predictions based on each calibration design, measured on each validation set, where $\tilde{R}$ is chosen *a posteriori* based on mean validation error.

Yield Strength	Bin $N_{SVE}=30$		Bin Random		External 1		External 2	
Calibration Set	$\tilde{R}$	%Error	$\tilde{R}$	%Error	$\tilde{R}$	%Error	$\tilde{R}$	%Error
Bin $N_{SVE}=30$	60	0.24	4	4.02	2	2.99	2	0.95
GP $N_{SVE}=10$	26	0.75	16	3.03	5	1.24	14	0.73
GP $N_{SVE}=5$	17	3.24	17	2.66	7	1.57	17	0.82
GP $N_{SVE}=3$	37	4.02	13	2.75	9	2.62	44	1.21
Bin Random	45	4.65	48	2.29	8	1.92	14	3.06
External Textures 1	59	6.23	7	4.37	24	0.72	41	4.49
External Textures 2	10	3.18	8	2.58	7	2.19	60	0.41

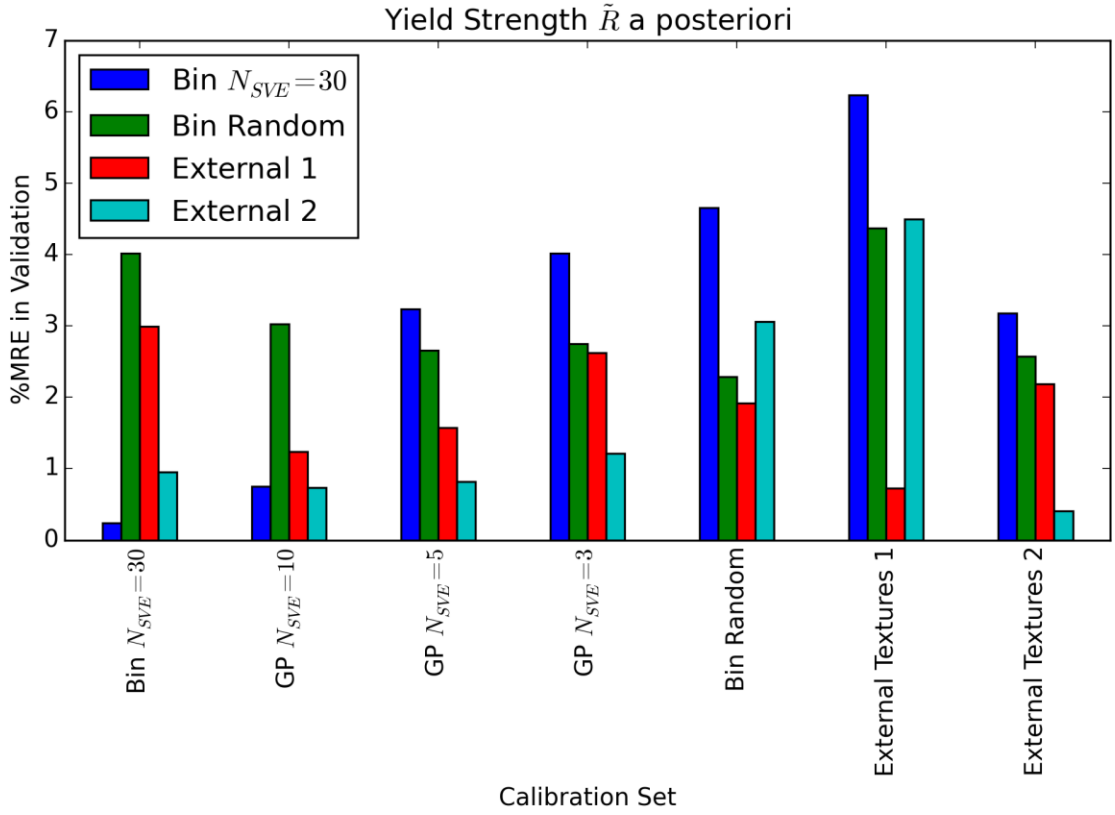

Figure 6.11. The mean relative percent error of MKS yield strength predictions based on each calibration design, measured on each validation set, where $\tilde{R}$ is chosen *a posteriori* based on mean validation error.

6.4. Discussion

This work demonstrates the use of MKS to extrapolate across textures based on a systematic calibration. MKS has been calibrated to specific textures in previous work. The current work is unique in attempting to make predictions beyond the specific textures contained in the calibration set. Predictions of this type are more demanding with respect to a calibration. The discussion is focused on the proof of concept this work provides, the limitations encountered in extrapolation, and suggestions for future improvements to MKS for the sake of reliability in predictions.

6.4.1. Proof of Concept

A systematic binning of texture was used to calibrate MKS in homogenization of α-Ti deformation response with respect to variations in texture. The binning method, when paired with a GP adaptive sampling method, led to results competitive with expert selection of texture-based calibration methods. In establishing this new approach as viable, the contributions of this work include developmental advantages which allow for incremental improvements to the method over time.

Systematic approaches to calibration are easier to improve upon incrementally. The performance of the expert selection calibrations was highly variable. The binning/GP method also exhibited some variability in performance. Whereas expert selection provides no suggestions for improvement, the systematic approach can be parametrically optimized without additional expert guidance. This work did not explore varying parameters of the binning procedure. By adjusting the numbers of bins for each Euler angle, the variation simulated in grains of each orientation, the number of weightings to include for each combination of orientations, and the maximum number of orientations in a combination to explore, shortcomings of this version of the binning method can be addressed.

The simulation of SVEs in ensembles in MKS calibration allows for the capture of effects of microstructure not explicitly explored in the calibration design. SVE ensemble size was investigated as a parameter of calibration design. If texture was the only influential design variable, the GP $N_{SVE} = 3$ would have outperformed the other GP methods instead of exhibiting a trade-off between validation sets, as was observed. By

simulating multiple microstructure volumes of the same texture, MKS can be trained to include the effects of misorientation and other higher-order correlation statistics. This suggests that the efficiency and reliability of future calibration designs could be improved by including a systematic exploration of misorientation, in addition to texture.

6.4.2. "Edge Cases" in Data-Driven Predictions

Using MKS to represent a specific texture set is much simpler than generalizing predictions to all textures of a material. Addressing this additional complexity exposes new failure mechanisms or 'edge cases' for the MKS model. The character of these 'edge cases' is valuable information to the advancement of MKS as a data-driven tool. These cases are documented here.

Dissimilarity between validation data and calibration data can lead to unreliable extrapolation on PCs as $\tilde{R}$ increases. The variance of the calibration set, with respect to each PC, decreases with each subsequent PC. This trend follows from the method by which the PCs are derived. If the validation data is dissimilar to the calibration data, the trend may not hold for the validation data. As $\tilde{R}$ increases, it becomes increasingly likely that the next additional PC would lead to extrapolation in the MKS predictions corresponding to the validation data. Extrapolation is unreliable in regression models such as MKS. One case from the study is shown as an example in Figure 6.12. The %MRE for the calibration, LOOCV, and validation data is plotted for the elastic modulus and yield strength predictions for the MKS model calibrated on the GP $N_{SVE} = 10$ design and validated on the Binned Random set. At PCs 18, 23, and 24, notable increases in validation %MRE are present. In the lower portion of Figure 6.12, the values of the PC

corresponding to the calibration and validation data are shown in a histogram heatmap, shown in blue and red respectively. At these PCs (18, 23, and 24) the validation (red) data extends far beyond the calibration data (blue). Improved robustness in these applications could be found by using an estimate of the extrapolation in each PC from the calibration to the validation data in PC selection for a validation domain-specific prediction model.

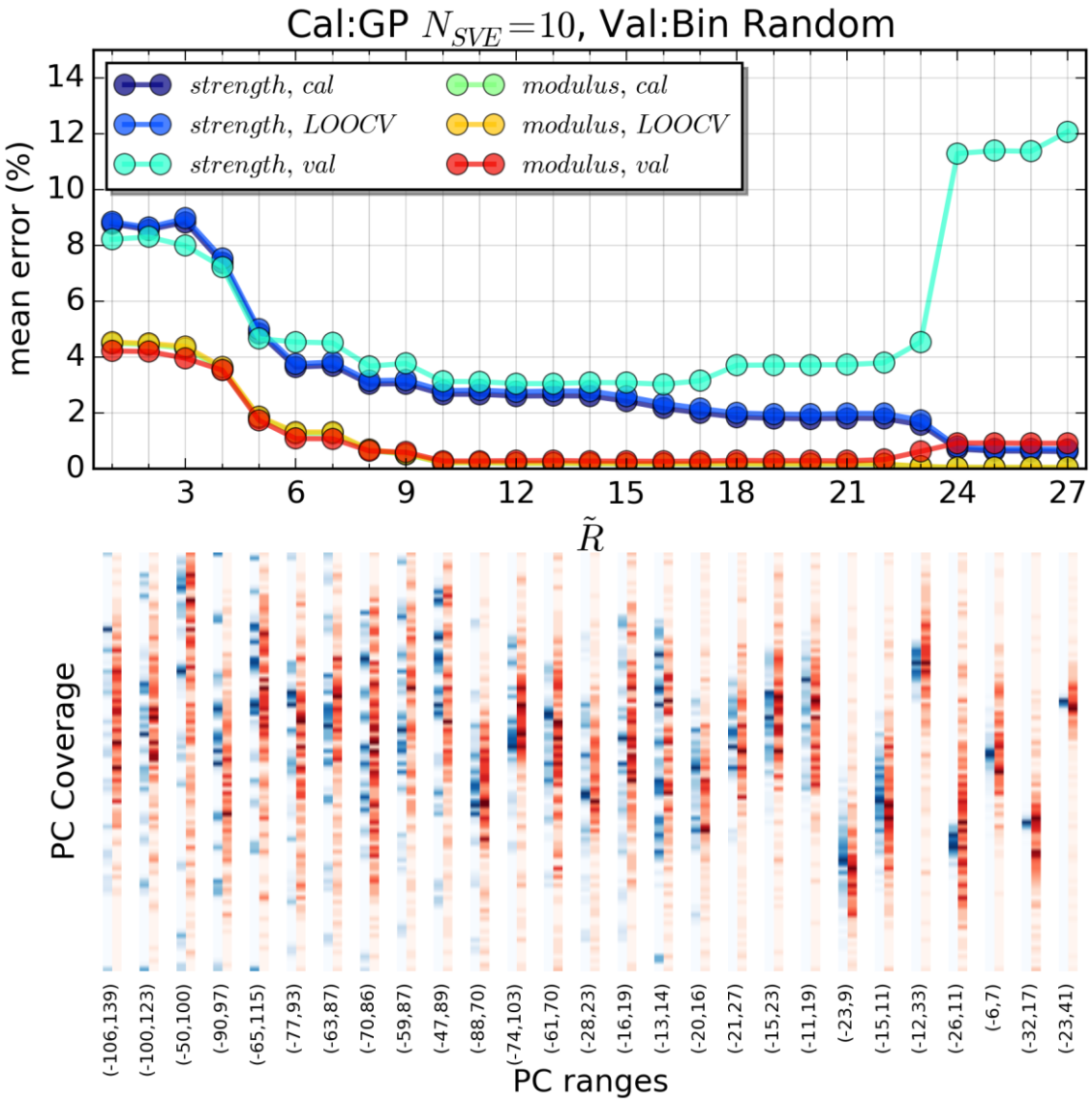

Figure 6.12. The %MRE scores for each QoI for a single calibration-validation pair, plotted above heatmap histograms of the calibration (blue) and validation (red) microstructure statistics with respect to each PC.

Misorientation was found to be influential with respect to yield strength predictions. The GP and binned calibrations had some limitations which did not appear in the traditional expert selection calibration approaches. These limitations can be linked to the formulation of the binning procedure, which did not explicitly track misorientations between grains. In the texture bins which included a combination of two orientations of

grains, misorientation statistics were sampled within an SVE ensemble. The misorientation distributions present in the expert selected textures were more complicated and diverse than those found in the binned textures. This is evident, given the expert selected textures often included more than two (up to 12) preferred orientations. Without calibration data which represents diverse misorientation distributions, the effects of misorientation will not be captured by the MKS model.

6.4.3. Future Work

The findings of this work support development of new functionality for MKS. To support MKS as a predictive tool, new prediction confidence estimation techniques will be needed, and the development of a systematic sampling of misorientations will be useful to improve the robustness of predictions across textures.

LOOCV minimization resulted in less-than-ideal performing choices for $\tilde{R}$. LOOCV, as a parameter selection method, only performs optimally when the validation data and the calibration data belong to the same distribution. I.e., when validation data includes new textures, LOOCV does not operate as intended. More appropriate for this application of MKS would be a version of LOOCV where an entire SVE ensemble is left out of the calibration at a time. The comparison of calibration and validation data in PC space could be used to reject PCs which would lead to extrapolation. This approach would be purely *a priori*, and could increase the reliability of the MKS model in predictive applications such as the case shown in this work.

An efficient sampling procedure for misorientation would improve the calibration of MKS. The data binning used in this work was intended to explore texture space with a

finite set of simulations. The GP model was selected as a method for systematically selecting data from that finite set. By training MKS on smaller ensembles of SVEs, more textures could be represented in the calibration set. Misorientation effects were not captured as effectively. To incorporate misorientation alongside texture in a calibration data binning procedure, two components will be needed: (1) a systematic approach to discretely binning the influential variations in misorientation distributions and (2) an approximate basis of misorientation which is independent of texture for indexing the bins for GP-driven bin selection. A sensitivity study on the effect of the number of bins dedicated to either design variable (texture and misorientation), may be necessary.

CHAPTER 7. CONCLUSIONS AND RECOMMENDATIONS

This chapter provides a new context to the work developed in each of the main topics of the dissertation. The contributions of each section are summarized with respect to the overall goals of this work. Perspectives gained from this work, which do not pertain to a single section alone are compiled here.

7.1. Overview of Contributions

The work contained in this dissertation has identified obstacles to the widespread application of scientific multiscale material models and contributed to the resolution of those obstacles. The following individual topics are reintroduced alongside their respective obstacles.

In Chapter 3, the coordination of information across length-scales was formulated in a TDBU approach to calibrate a CP model of bcc Fe. The reconciliation of parameter estimates introduced in this chapter is a necessary ingredient in the development of multiscale models. Models require calibration; multiscale models often lack multiscale calibration. Comprehensive multiscale development of material models will require accounting for how much the information from each scale is included in calibration and application. The constrained likelihood methods developed in Chapter 3 allow for this accounting. Data-driven selection of model-model connections will depend on formulations of a connection cost, a concept established in Chapter 3.

Chapter 4 contains an investigation of reduced-order approximations of polycrystal plasticity with respect to SVE size and model form. Reliable design of

additively manufactured components will require a modeling paradigm which can simultaneously consider microstructure statistics and a complex geometry in a robust and time-efficient approach. The work in Chapter 4 demonstrates the need for a multiscale treatment of this approach, which includes both reduced-order local response approximations and longer-range correlations.

In Chapter 5, the implementation of microindentation as the TD component of a TDBU mesoscale variability estimate is outlined. The variability of microstructures will be a critical factor in designing components at the mesoscale. TDBU inclusion of experimental measurements of that variability will be needed to avoid the potential bias that relying solely on CP variability estimates may impose. The descriptions in this chapter indicate the problems to be considered while developing such a TDBU approach.

In Chapter 6, the calibration of the MKS homogenization model of α-Ti in the prediction of texture effects is formulated in a systematic binning and adaptive sampling method. The predictive ability of data-driven tools such as MKS depends upon those tools being sufficiently calibrated. Currently, the user must determine the calibration quality of the MKS model, limiting the number of qualified users. The systematic definition of the calibration of MKS, as was performed in Chapter 6, is a prerequisite for developing MKS into a self-calibrating approach to the efficient prediction of microstructure-sensitive material response.

In brief, the contributions are as such. Chapter 3 developed a TDBU reconciliation of parameters and an empirical TDBU connection test. Chapter 4 investigates the CG description of variability in polycrystals. Chapter 5 identifies the

challenges to using microindentation variability to inform microstructure response variability. Chapter 6 formulates an automated generator of calibration data for a data-driven S-P relation model.

7.2. Perspectives on Difficulties in ICME

Prevailing challenges exist in the pursuit of ICME, and the perspectives on those challenges gleaned from the work of this dissertation are mentioned here. This dissertation is organized around the efforts of ICME. Progress in specific cases is essential to these efforts. Additionally, some details of those specific cases are consequences of unifying difficulties which are endemic to the multiscale problems of ICME. Commentary on the nature of those difficulties is offered along with recommendations.

The goals of ICME include developing the capability of engineering design tools to include the processing-structure-property linkages established by scientific computational models and experimental data. Remaining obstacles to the achievement of this goal are consequences of the unique conditions in which knowledge is gathered in materials science; these obstacles are not observed in simply any massive collection of data. Descriptions of nature which are not scale-specific defy even physicists their discovery--there is no Theory of Everything. Nevertheless, ICME has need of a holistic perspective of materials across length and time scales. The barriers to assembling this perspective are numerous, though they may include the following: material models are predominantly developed with a single length-scale in mind, scale linking between models is not yet accountable to differences in predictions based at constituent scales,

there is a lack of uncertainty estimation in engineering toolkits, and source criticism is required for data-driven multiscale modeling. Each of these is discussed here.

7.2.1. Over-specification of Models at a Length-Scale

Models which are conceptualized and calibrated at a single length scale are unreliable in making predictions at different length scales. Cutting-edge material models are often very specific in terms of material and QoI. These trends reflect the scarcity of high quality data on these materials and responses. Models are also typically defined based on physical assumptions which are length and time scale-specific. The data selected to calibrate the models is often restricted to that physically defined length scale. While data collection is often restricted by data scarcity, the barriers to using data from other length scales arise from the difficulty of the analysis involved--not scarcity. These single-scale models are numerous, yet there are few models which are specified to incorporate the scale-dependence of material response.

ICME has been predicated on the coordination of multiple single-scale models in a multiscale hierarchy. This formulation leads to a critical issue: the relative influence of competing mechanisms across length-scales does not “drop out” from an ideal arrangement of scale-specific treatments. Connections between scales are not trivial additions to the existing models. In order to apply the rigor necessary to construct useful connections between scales, those connections must be included in the development of the models themselves.

Multiscale models can be calibrated with data which is gathered at multiple scales. A multiscale calibration of this description constitutes a multi-objective

optimization. In other words, a model developed around observations at a single scale would suffer in that single-scale performance in the course of being calibrated to data from multiple scales. The connections between these observations, should they be captured by any model, would likely be found in a model whose performance is less diminished by the inclusion of multiple scales of calibration data. It is therefore worthwhile to develop multiscale models with multiscale data and by extension, worthwhile to gather data at multiple scales in concurrence.

7.2.2. Accountability in Linking Length-Scales

Hierarchical multiscale models are often built using parametric connections between scales which are examined for theoretical soundness but which are untested on an empirical basis. In the eventuality of multiple theoretically sound alternatives for a given connection, the de facto selection strategy is based in the preferences of the researcher. Where there is disagreement among researchers in this process, no resolution of that disagreement can be supported by such a selection process. As is the case with models in general, the prevailing connection between models must be the candidate which best suits the appropriate data. In the multiscale case, the appropriate data must belong to two separate categories (each scale is a category of data) which are only relatable if a connection of some sort is assumed. The development of a widely acceptable standard of practice is needed to make routine the testing of new model-model connections in the field of multiscale material modeling

The development of a multiscale model is built on the supposition that a single-scale treatment is insufficient to accurately describe the behavior of interest. This

assumption is a foundation for the criterion on which model-model connections can be empirically tested. A connection between scales which is a component of a successful multiscale model must allow the following requirements to be met:

5. The model must be able to fit calibration data at each length-scale included in consideration of the multiscale approach. The model and the data must be compatible.
6. The predictions at each scale must be sensitive to the calibration data at each other scale (in addition to that of the same scale), that is, an appreciable change in the calibration data at one scale must in general produce a change in the predictions at another scale. The scales must not be independent in the multiscale approach.

It is notable that the second requirement is not relevant to single-scale models. Additionally, this test of multiscale model connections is incompatible with the BU-only approach to multiscale modeling.

The work in Chapter 3 comprises a single example of the testing of TDBU model connections. The approach considered a cost associated with the use of data across an imperfect model-model connection. In introducing such a cost, the connection could be evaluated based on an apparent trade-off between the benefit of additional data and the cost of including multiscale data. The approach used likelihood based methods for analyzing the influence of additional data in terms of the model's sensitivity. The approach used reconciliation methods to impose the compatibility of the model with both length scales of data. The criterion developed in Chapter 3 was useful in testing the multiscale approach used. Other conditions may necessitate the development of other

multiscale criteria. In such cases, the compatibility and sensitivity requirements mentioned here may still be useful.

7.2.3. Uncertainty Estimation is Needed in Engineering Modeling Tools

Material modelers employ specific expertise to interpret models appropriately. When materials science is used to inform performance predictions, models of some sort are often developed. When these models are physically informed, the developers of that model gather an understanding of the limitations associated with the predictions of that model. When a physically derived model is too costly to be employed in engineering workflows, a surrogate modeling approach is often developed. The development of a surrogate model involves the careful selection of surrogate modeling approach, often providing the developer with a sense of the limitations associated with any application of that surrogate. In either case, the expertise accumulated during the development of these sophisticated models is essential to the responsible interpretation of the predictions which the model provides.

Without the expertise of a material modeler, models can be prone to improper use. In any case where predictions are made by a model, those predictions may become invalid. If the model is applied in a domain for which it is not validated (or at least considered valid) the predictions it provides may be subject to catastrophic errors. When a model is used in an appropriate domain, the predictions may become erroneous if they are interpreted to be more precise or more accurate than they are in fact. Most advanced material models are not formulated to indicate if either of these cases is present when a prediction is given.

Material modeling tools can be used responsibly when uncertainty estimates accompany predictions. The precision and accuracy of a model can be modeled alongside predictions of material response. The development of such uncertainty models is needed to improve the suitability of materials models for widespread deployment. For cases of invalid application of a model, more sophisticated approaches to uncertainty estimation may be necessary to provide appropriate guidance. Domain-sensitive uncertainty modeling requires all inputs to be parameterized or embedded in a model (in the case of categorical inputs).

Uncertainty estimation for ICME modeling tools can benefit from the combination of surrogate modeling and UQ techniques. UQ is inherently costly, much more so than the models on which it is performed. For the sake of providing user guidance in modeling tools, the precision of many UQ techniques is unnecessary. It is likely that the uncertainty of a material model may be sufficiently captured using a surrogate model trained on a selection of UQ tests of the material model. The development of such uncertainty surrogate models will demand expertise on the part of the developer, however the results will reduce the expertise requirements on the end user of the modeling tool.

7.2.3.1. Epistemic and Aleatory Uncertainty and their Use in an ICME Context

Epistemic and aleatory uncertainty are concepts which add value in specific applications. In reliability and risk assessment, the distinction of uncertainty into aleatory and epistemic components is valuable for decision making. Often, policy demands that risk is fully mitigated by a final design (consider the example of nuclear waste storage).

The additional cost of a design which can withstand the 99th percentile of predicted outcomes may be considerable. If an agency could expect the uncertainty of the prediction to diminish under continued study (and funding), the potential cost savings could motivate continuing research efforts. This is precisely the benefit of quantifying the epistemic component of uncertainty in such a design case. Many of the components of the uncertainty are tied to the goal of the design problem, and these contribute to the aleatory uncertainty. Where more knowledge might reveal more precise estimates, the epistemic uncertainty is the quantity which will be impacted. Broadly, these cases are well-defined applications accompanied by funding decisions which are sensitive to uncertainty.

Computational model design in ICME related problems requires decision making that does not extract much benefit from the epistemic and aleatory distinction. In ICME, the design problem often includes the design or selection of the model to be used. Often, the choice of one model over another will require uncertainty estimation, however the proportions of aleatory and epistemic components do not influence the decision making. To substantiate this assertion, each category of uncertainty will be described in the context of an ICME model design problem.

Aleatory uncertainty is not useful when comparing modeling approaches. When the chosen model is not fixed, the definition of aleatory uncertainty becomes more complicated in practice. Aleatory uncertainty is defined as the irreducible component of uncertainty, or variability. This definition is incomplete, as the variability and irreducibility are features of the answer given to *a specific question*. In many approaches to modeling materials (and especially with multiscale modeling), each potential approach

may include variations in foundational assumptions in approaching the estimation of roughly the same QoI. *By modifying the question, the aleatory component of uncertainty is susceptible to change*. In model design, it is very possible that the uncertainty in an answer is a result of asking an ill-posed question. To researchers of model design, the maintenance of flexibility in question formulation can be a powerful asset. At the same time, this flexibility renders aleatory uncertainty quantification unhelpful within the model design procedure.

Epistemic uncertainty in a model design problem is only ever partially quantifiable, and is only helpful in specific cases. Epistemic uncertainty is defined as the reducible component of uncertainty or the incertitude of a statement. In materials modeling, epistemic uncertainty is often quantified by exploring possible values of model inputs which cannot be precisely informed. This approach is common in part due to the data scarcity which often occurs in material modeling. In practice, this accomplishes little more than a sensitivity analysis. Additionally, this procedure cannot approach the quantification of the uncertainty caused by model discrepancy. Model discrepancy is the primary cause of epistemic uncertainty in modeling problems where sufficient appropriate calibration data is available. To quantify model discrepancy, a higher fidelity model must be available for comparison. The highest fidelity model available becomes the de facto ground truth, and the discrepancy of this "best" model is unquantifiable and unknown. These limitations inhibit the use of aleatory and epistemic uncertainty in the typical manner.

There do exist some examples in ICME where the distinction between aleatory and epistemic uncertainty is clearly useful. The uncertainty categories are useful in

technical criticism of problematic modeling approaches. The argument for replacing a method is strengthened if the model owes uncertainty to a large epistemic contribution. In surrogate modeling, uncertainty can be broken down into the component from the surrogate model and the component carried over from the full-fidelity model. In describing the uncertainty of the surrogate model relative to the existing uncertainty, the benefits of efficient alternatives can be more readily interpreted. Additionally, once a model and application have been identified, the distinction of uncertainty is critical to reliability modeling and process design.

Material modeling also presents unique conceptual challenges which are similar to those for which the disambiguation of uncertainty components is used. In the polycrystalline length scale, the effects of microstructure are often modelled deterministically by CP or an alternative, whereas the microstructure itself is instantiated statistically and contains variability. At the scale of homogeneous response, the influence of microstructure is characterized as an uncertainty. In development of mesoscale modeling approaches, the approximation of material response will require a clear definition of the difference between the variability inherent to the material at a given scale and the uncertainty which arises in the course of model order-reductions, approximations, and regressions. Quantities such as variability and conditional probabilities may become QoIs in addition to the typical mean-value estimates of response. Care is required to distinguish approximation error from variability.

7.2.4. Source Criticism is Needed for Data-Driven Multiscale Methods

In the informing of multiscale, multi-attribute, and multi-objective models, an equal weighting of all available data is not likely the ideal strategy. In a single scale model, not all data is useful. In statistical models, outliers are often rejected in order to draw clear conclusions from a dataset. In material models, calibration data is often processed in some way, e.g., a stress-strain curve returned from testing of an experimental specimen may be modified to account for machine compliance. The concept of informed decision making with regard to the inclusion and exclusion of available data is not new. In multiscale models, new considerations must be made which arise due to the consequences of modeling in multiple scales.

Data can be rejected on grounds of inaccuracy or irrelevance. In the case where a machine compliance adjustment is made to a raw tensile test result, the apparent elastic modulus of the raw test data is too inaccurate to be used in the modeling of the material in the absence of the tensile testing equipment. It is rejected in calibration of a material model in preference of a literature value of the elastic properties of the material, derived with a different method. The effect of machine compliance is often considered an error in the measurement of the elastic modulus. As an alternative interpretation, the measurement made by the test could be aimed at capturing the effective combination of the sample elastic properties and the machine compliance of the testing rig. The raw data is not necessarily inaccurate in this case--it may be an exact reflection of the elastic properties and machine compliance in combination. It is that the magnitude of that measurement is not relevant to a model of the material alone.

The distinction between these data rejection criteria is important in a multiscale context. The accuracy of data is not intrinsic to the measurements which were made to provide it, rather, the accuracy of data is a property derived from the combination of the source and the use. In this, the concept of relevance is more indicative of this application-specificity.

Multiscale models allow data to be included from one length scale in predictions made at another length scale. In a hierarchical multiscale model, a model is used at each length scale included in the hierarchy. Each model inevitably suffers imperfect accuracy due to neglected mechanisms, effects, etc. As more length scales are spanned from data to prediction, the more these inaccuracies accumulate. As a result, a HMM is disadvantaged in making predictions in this BU manner in comparison to a single-scale method. Additionally, when data are included from multiple scales, the accuracy of those data with respect to the prediction will vary as a function of scale.

For multiscale models to be most advantageous, they must incorporate data of different levels of accuracy/relevance at weights which reflect that difference. Additionally, any experimental observation is made with limited precision. A comprehensive approach to these demands may take benefit from the field of source criticism, information evaluation, or credibility (Rieh and Danielson, 2008). To advance the state of the art in multiscale modeling, multiscale source criticism will likely be a critical component.

If the methods of multiscale modeling of materials are to be implemented in data-driven approaches, source criticism will become increasingly important. Data-driven

methods depend on intensive data curation. The complications which arise in multiscale modeling applications are not common in applications of data-driven algorithms at large. Therefore, the mainstream machine learning community is unlikely to address these challenges which are unique to multiscale materials models. The development of source criticism for multiscale models will likely fall to computational materials modelers.

APPENDIX A. AUTOCAL MANUAL

A.1. What is Autocal?

Autocal is a python package which provides a systematic calibration approach that builds on a python "pipeline" used in the McDowell research group to submit HPC cluster simulations (Kern, 2016). An overview of the calibration procedure is given here. The procedure implemented in Autocal for calibrating a model consists of three steps. (1) The user selects a set of calibration parameters and offers an estimate of their ranges. (2) Autocal studies the primary effects of each parameter and suggests revised parameter ranges by making comparisons to a target. (3) Autocal iteratively informs a Gaussian process model with the results of model runs across the revised parameter ranges until an acceptable calibration is reached. The procedure is summarized in a flowchart in Figure A-0.1.

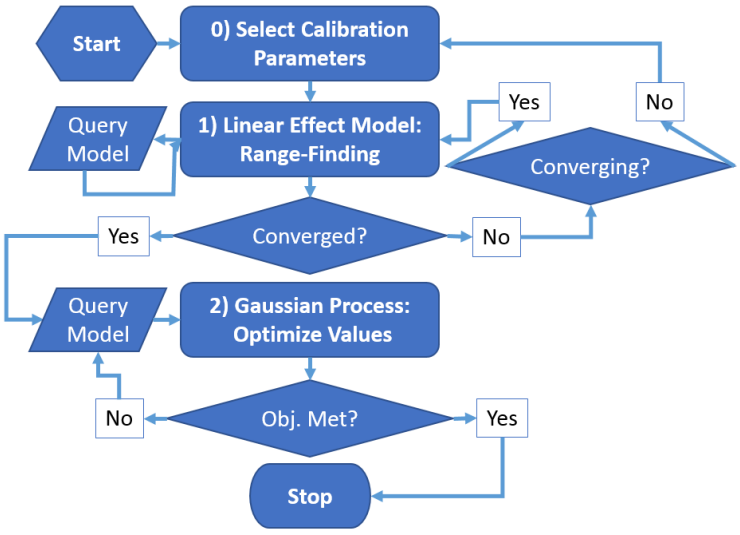

Figure A-0.1. A flowchart which shows the steps of the Autocal procedure.

Autocal attempts to find appropriate ranges for the calibration parameters of a model. A linear effects model is built from a one at a time sensitivity test. This linear model is used to interpolate (or extrapolate) from the initial sensitivity ranges to match model response with a target (experimental) response. As extrapolation is a likely and necessary occurrence for range-finding, a linear model is the most stable and appropriate formulation of effects model to use in this application. In the case of nonlinear parameter dependence and strong interactions in parameters, this initial step may require iteration until convergence in range predictions has been reached. This initial step can save time by increasing the chances that the optimal calibration parameter values exist within chosen limits.

Once parameter ranges are established, Autocal optimizes the calibration of parameters. The optimization makes use of a Gaussian process model to (strictly) interpolate between model results. The GP model can support the time-interpolation of a time-series (such as a $\sigma - \varepsilon$ curve) into equidistant samples, such that the response is considered as a vector of measurements. This equidistant sampling allows for equal weighting of the response as a function of time. The objective function is currently defined in terms of absolute squared error, i.e.,

$$Obj\left(\boldsymbol{\theta}\right) = -\sum_{t=0}^{\max(t)} \left(Y_t^M\left(\boldsymbol{\theta}\right) - Y_t^E\right)^2 \tag{71}$$

where $Obj(\boldsymbol{\theta})$ is the objective function of calibration parameters, $\boldsymbol{\theta}$, from time $t = 0$ to $\max(t)$, and $Y_t^M(\boldsymbol{\theta})$ is the model response or QoI at time t and calibration parameter values, $\boldsymbol{\theta}$. Y_t^E is the experimental target response or QoI at time t.

An adaptive sampling is used to efficiently arrive at the optimal calibration. The GP model requires an initial set of results to predict response. Subsequent calibration values are selected by investigating the model response at the maximum of the objective function as predicted by the GP. The GP can accommodate non-linear relationships between parameters and QoIs.

Autocal is designed to handle interdependence (or interactions) in the effects of parameters in the calibration set. The range finding step can be repeated from different initial ranges to test for the existence of local minima in the response surface. The GP model, being a kernel method, is especially suited to follow variations which are analytically complicated. As a result, if a calibration set fails to lead to a consistent prediction, the problem may reside in the relationship between the measurement data and the parameter set.

The use of a GP in extrapolation is not recommended. When the optimal solution lies outside the range of the GP, it can be necessary to search solutions in an extrapolative manner or to rebuild the GP over different parameter ranges. The process of training a GP model is more expensive than the linear effects model. Autocal is designed to avoid building the GP more than once or using the GP in extrapolation. The two-step procedure is an important feature of Autocal.

Autocal is a python package which builds on other common scientific packages. The optimization was performed using scipy (Millman and Aivazis, 2011), the initial linear effects model was built using statsmodels (*statsmodels*, 2018), and the GP regression model was built using scikit-learn (Pedregosa et al., 2011), all of which are python packages.

Autocal is built to be compatible with the McDowell Research Group job submission pipeline, developed by Paul Kern and maintained by Adrienne Muth. The code for Autocal, the pipeline, and the material models mentioned in this guide are all maintained on the McDowell Research Group Enterprise Github.

A.2. Getting Started

Prerequisites for the use of Autocal are Python 2.7.x, access to the McDowell Group's Georgia Tech enterprise github, an operational implementation of the Autocal branch of the PythonScripting repository, and the installation of a number of python packages (many of which may be included in a distribution of python, such as Anaconda). To use the pipeline, other open-sourced software is required. These prerequisites are shown in Table A-1.

Table A-1. The prerequisite software, packages, and repositories which must be installed prior to testing Autocal. This list may change as features are added. Check the Autocal repository or contact Gary Whelan for help.

Prerequisite	**Source**	**Notes**
Python 2.7	www.python.org	
Ipython, Numpy, Scipy, Pandas, Matplotlib, Crypto, Scikit-learn, statsmodels, subprocess, pickle	PIP	Doesn't include packages required by pipeline. Check version dependencies.
Dream.3D	dream3d.bluequartz.net	Need to link in config.txt
Gmsh	gmsh.info	Need to link in config.txt
PythonScripting-Autocal	https://github.gatech.edu/McDowell-Lab/PythonScripting/tree/Autocal	Clone repo to local system
Autocal	https://github.gatech.edu/McDowell-Lab/Autocal	Clone repo to local system
Copper-Brass	https://github.gatech.edu/McDowell-Lab/Copper-Brass	Clone repo to local system
Other material folders	https://github.gatech.edu/McDowell-Lab/*	As needed
Access to Granulous	Ask lab manager	

Once prerequisites are operational, the installation can be tested. Using an interactive python session in the directory containing the cloned github repositories (type ipython in command prompt), import autocal, then run autocal.test_1(<your username>) once autocal finishes initializing. Your username is the username for accessing Granulous. Test results should be compared to the guide in the Autocal repository for troubleshooting and further help.

A.3. Pitfalls and Precautions

Autocal is a specialized application of a number of powerful techniques. The limitations of those techniques must be understood and respected, as potentially

undesirable and even disastrous consequences await those who put blind faith in a calibration result.

A.3.1. Scenario Descriptor Inputs Must Match Target

Models can have many inputs. Some of these inputs have external definitions, for example the temperature of a material or the applied rate of strain. These inputs, which are known prior to calibration, are referred to as scenario descriptor inputs.

Descriptor inputs must correspond between simulations and the data which are used to calibrate those simulations. This requirement is not automatically ensured, and it is up to the user to locate the metadata needed to ensure this requirement is met.

A.3.2. Calibration Parameters Must Be Identifiable by Quantity of Interest (QoI)

Calibration parameters are distinct from the previously mentioned scenario descriptor inputs, in that they adopt values as needed to fit a model to a target. Complications arise in this process when the relationship between a parameter and a QoI is tenuous.

Identifiability refers to the precision with which a parameter can be evaluated through comparisons in terms of a given QoI. In order to be identifiable by a QoI, a parameter must (1) have a significant effect on the value of the QoI predicted by the model, that is, a change in the value of the parameter results in a significant change in the QoI, and (2) that effect must be distinguishable from the effect of each other parameter in the active calibration set.

Autocal does not currently specify the identifiability of parameters. Autocal can be used to investigate the relationships between calibration parameters. When the nature of the relationships between a calibration parameter set and a QoI is not established, it may be necessary to investigate different combinations of parameters and QoIs in order to find a workable set.

A.3.3. Calibration Parameter Set Should be Made Smaller if Possible

The efficiency and reliability of Autocal drop off dramatically as more calibration parameters are considered at once. Specific relationships between a QoI and a specific subset of the calibration parameters in a material model should be used to guide calibrations, in multi-stage calibration approaches, if needed. By no means should every possible calibration parameter be included in a single calibration with Autocal. To determine if a chosen set of parameters is small enough, examine the identifiability of each parameter. If all parameter effects are distinct and simple, the largest number of parameters that Autocal can handle is perhaps two dozen, though algorithmic efficiency issues will accumulate at numbers any higher than ten parameters.

A.4. Developing a New Material for Use with Autocal

Autocal is designed to be adaptable to new material systems operating with the pipeline. Once the user has tested the installation and successfully run Autocal, they can begin developing a new material for use with Autocal. Assuming the new material folderis compatible with the pipeline, only three files need to be edited: in the material folder the user must make edits to material.py (e.g. Ti64.py, Al7075.py) and in the Autocal folder the user must make additions to autocal.py and _init_.py.

A.4.1 Material/Material.py

First, in the material folder, once the user has determined which parameters could be subject to calibration, material.py should be edited to take values from Autocal.py and assign them via the input file (and input file writer). (As needed, the UMAT should be altered to read in these parameters from the input file.) Under write_mat_defs, where the values assigned to these parameters are defined, the user should replace the hard-coded values with string variables passed in from the pipeline (using the DoE header 'calib'). For more guidance in how to properly edit this section of the code the user can look to the differences between Ti64.py in the Autocal branch and master branch of Ti64 in the McDowell Group's Georgia Tech enterprise github. Next, two files in the Autocal folder must be edited.

A.4.2 Autocal/__init__.py

init.py can be quickly edited using the template already existing in the code to add initialization for the new material.

A.4.3 Autocal/autocal.py

In autocal,py 3 sections, all near the top of the code above the "Make no changes below here" comment block, must be edited.

A new local directory should be defined to hold the results of the calibration. In the initial block of code, define this directory as a global variable following the example of the existing "LOCAL#" directory definitions. The location of the target dataset being used to compare to QoIs to determine the quality of the calibration should be defined following

the example of the existing "EXP_Material_#". The Dream.3D file being used to instantiate microstructures should be located and defined following the example of the existing "MaterialD3" lines in autocal.py.

A.4.4 Testing a new material

Testing the new material in autocal can be built using the "test_2" function as a template. For simplicity, rewrite test_2 to call a new material (or copy it and rename it test_3 if needed). Here the user must add their calibration parameter set and the respective initial range for each parameter (corresponding to the changes made in material.py). As appropriate given the user's target data, specify changes to the parameters, options and features shown in Table A-2 below.

Table A-2. User defined parameters for test_2.

hmode1	-deprecated-
cpus2	Number of cores per simulation
ortho2	-deprecated-
nsteps2	Approximate number of time-steps to specify
n_el2	Number of elements per side of SVE
ensemble1	Number of SVEs per ensemble
iterations	Number of times to perform range-finding step
preserveMS	If =1, microstructure instantiations are held fixed through subsequent iterations. if =0, new instantiations are used for each simulation
its3	Number of iterations for GPM
bm2	Experimental set up (see "get_load")
passkey	-change this to a private pin to increase security-

A.4.5 Putting the new material into production

Lastly the user must append the "material_selector" function to include their material. In this section a new elseif (elif) statement must be added following the

example of the existing elseif statements. A screenshot of this function is included for reference in Figure A-0.2.

```
def material_selector(mat='',param={}):
    """ADD YOUR MATERIAL DEFINITIONS HERE!
    template:
        elif mat == <'matfol name'>:
            mat_vars['order']=<list of the strings, in order, of the calibration
                parameters passed in to the input file via matfol/matfol.py>
            mat_vars['tag']=<short string to identify runs other than by a number>
            mat_vars['bpath']=<path to existing folder to contain calibration runs>
            mat_vars['d3d_file']=<path to dream3d file for MS instantiation>
    """
    home=os.getcwd()
    mat_vars={}
    if mat == 'BCJ':
        mat_vars['order']=['E','Y','V','f','h','rd','H','RD']
        mat_vars['tag']='bcj'
        mat_vars['bpath']=LOCAL2
        mat_vars['d3d_file']=r'%s\%s\BCJ25.dream3d'%(LOCAL1,mat)
        mat_vars['EXP']=LOCAL1+r"\Copper-Brass\exp600C.csv"
        mat_vars['ver']='6.10-1'
        if len(param.keys())==0: #pass in default params for BCJ model (assuming params
            param={'E':[110000],'Y':[52.33],'V':[2.2],'f':[5e-6],'h':[50.],'H':[800.],'rd':[8.26E-2],'RD':[2.55E
    elif mat == 'BCJ_stochastic':
        mat_vars['order']=['E','Y','V','f','h','rd','H','RD']
        mat_vars['tag']='bcjs'
        mat_vars['bpath']=LOCAL1 +r"\BCJScalib"
        mat_vars['d3d_file']=r'%s\BCJ25.dream3d'%(LOCAL1)#,mat)
        mat_vars['EXP']=LOCAL1+r"\Copper-Brass\exp600C.csv"
        mat_vars['ver']='6.10-1'#'6.10-1'
        mat_vars['increment_sf']=100.
        mat_vars['wtx']=0.3
        #mat_vars['reporting']='interval'
        #mat_vars['interval']='4'
```

Figure A-0.2. The material_selector function, which allows quick, persistent changes to the options which can be material-specific.

In addition to these required changes to develop a new material for use with autocal, the user may find it necessary to add a new loading schedule to autocal.py to match their dataset. To do this the user should add a new elif statement in the "get_load" function of autocal.py, name their loading schedule appropriately and define the strain amplitude, number of loading cycles (0 delimited), load ratio for cyclic loading, and strain rate. A screenshot of this function is included for reference in Figure A-0.3.

```
151 def get_load(lname):
152     """Add your loading schedule here.
153     """
154     lp={}
155     if lname=='hard':
156         strain = 0.04
157         nloadings=0
158         ratio = 0
159         gdot=[0.0012]
160     elif lname=='rev':
161         strain = 0.06
162         nloadings=1
163         ratio = -1
164         gdot=[0.0012]
165     elif lname=='long':
166         strain = 0.1
167         nloadings=0
168         ratio = 0
169         gdot=[0.0012]
170     elif lname=='yield':
171         strain = 0.002
172         nloadings=0
173         ratio = 0
174         gdot=[0.0012]
175     elif lname=='fatigue':
176         strain = 0.008
177         nloadings=5
178         ratio = -1
179         gdot=[0.001]
```

Figure A-0.3. The get_load function, which allows persistent definition of loading paths.

REFERENCES

Acharjee, S., Zabaras, N., 2007. A non-intrusive stochastic Galerkin approach for modeling uncertainty propagation in deformation processes. Comput. Struct., Computational Stochastic Mechanics 85, 244–254. https://doi.org/10.1016/j.compstruc.2006.10.004

Acharjee, S., Zabaras, N., 2003. A proper orthogonal decomposition approach to microstructure model reduction in Rodrigues space with applications to optimal control of microstructure-sensitive properties. Acta Mater. 51, 5627–5646. https://doi.org/10.1016/S1359-6454(03)00427-0

Adams, B.L., Canova, G.R., Molinari, A., 1989. A Statistical Formulation of Viscoplastic Behavior in Heterogeneous Polycrystals [WWW Document]. Texture Stress Microstruct. https://doi.org/10.1155/TSM.11.57

Adams, B.L., Henrie, A., Henrie, B., Lyon, M., Kalidindi, S.R., Garmestani, H., 2001. Microstructure-sensitive design of a compliant beam. J. Mech. Phys. Solids 49, 1639–1663. https://doi.org/10.1016/S0022-5096(01)00016-3

Adams, B.L., Kalidindi, S.R., Fullwood, D.T., 2013a. Chapter 9 - Microstructure Hull and Closures, in: Microstructure Sensitive Design for Performance Optimization. Butterworth-Heinemann, Boston, pp. 183–194. https://doi.org/10.1016/B978-0-12-396989-7.00009-5

Adams, B.L., Kalidindi, S.R., Fullwood, D.T., 2013b. Chapter 14 - Second-Order Hull, Property Closure, and Design, in: Microstructure Sensitive Design for Performance Optimization. Butterworth-Heinemann, Boston, pp. 303–330. https://doi.org/10.1016/B978-0-12-396989-7.00014-9

Adams, B.L., Kalidindi, S.R., Fullwood, D.T., 2013c. Chapter 5 - Spectral Representation of Microstructure, in: Microstructure Sensitive Design for Performance Optimization. Butterworth-Heinemann, Boston, pp. 89–109. https://doi.org/10.1016/B978-0-12-396989-7.00005-8

Adams, B.L., Kalidindi, S.R., Fullwood, D.T., 2013d. Chapter 3 - Spectral Representation: Generalized Fourier Series, in: Microstructure Sensitive Design for Performance Optimization. Butterworth-Heinemann, Boston, pp. 45–65. https://doi.org/10.1016/B978-0-12-396989-7.00003-4

Adams, J.J., Agosta, D.S., Leisure, R.G., Ledbetter, H., 2006. Elastic constants of monocrystal iron from 3 to 500 K. J. Appl. Phys. 100, 113530. https://doi.org/10.1063/1.2365714

Adler, R.J., Casey, B., Jacob, O.C., 1995. Vacuum catastrophe: An elementary exposition of the cosmological constant problem. Am. J. Phys. 63, 620–626. https://doi.org/10.1119/1.17850

Alharbi, H.F., Kalidindi, S.R., 2015. Crystal plasticity finite element simulations using a database of discrete Fourier transforms. Int. J. Plast., Plasticity of Textured Polycrystals In Honor of Prof. Paul Van Houtte 66, 71–84. https://doi.org/10.1016/j.ijplas.2014.04.006

Allen, J.K., Seepersad, C., Choi, H., Mistree, F., 2006. Robust Design for Multiscale and Multidisciplinary Applications. J. Mech. Des. 128, 832–843. https://doi.org/10.1115/1.2202880

Amodeo, R.J., Ghoniem, N.M., 1990. Dislocation dynamics. II. Applications to the formation of persistent slip bands, planar arrays, and dislocation cells. Phys. Rev. B 41, 6968–6976. https://doi.org/10.1103/PhysRevB.41.6968

Andersson, J.-O., Helander, T., Höglund, L., Shi, P., Sundman, B., 2002. Thermo-Calc & DICTRA, computational tools for materials science. Calphad 26, 273–312. https://doi.org/10.1016/S0364-5916(02)00037-8

Angelikopoulos, P., Papadimitriou, C., Koumoutsakos, P., 2012. Bayesian uncertainty quantification and propagation in molecular dynamics simulations: A high performance computing framework. J. Chem. Phys. 137, 144103. https://doi.org/10.1063/1.4757266

Arendt, P.D., Apley, D.W., Chen, W., 2012a. Quantification of Model Uncertainty: Calibration, Model Discrepancy, and Identifiability. J. Mech. Des. 134, 100908. https://doi.org/10.1115/1.4007390

Arendt, P.D., Apley, D.W., Chen, W., Lamb, D., Gorsich, D., 2012b. Improving Identifiability in Model Calibration Using Multiple Responses. J. Mech. Des. 134, 100909–100909. https://doi.org/10.1115/1.4007573

Argon, A., 2008. Strengthening Mechanisms in Crystal Plasticity. OUP Oxford, Oxford.

Arsenlis, A., Rhee, M., Hommes, G., Cook, R., Marian, J., 2012. A dislocation dynamics study of the transition from homogeneous to heterogeneous deformation in irradiated body-centered cubic iron. Acta Mater. 60, 3748–3757. https://doi.org/10.1016/j.actamat.2012.03.041

Arsenlis, A., Wirth, B.D., Rhee, M., 2004. Dislocation density-based constitutive model for the mechanical behaviour of irradiated Cu. Philos. Mag. 84, 3617–3635. https://doi.org/10.1080/14786430412331293531

Asaro, R.J., 1983. Micromechanics of Crystals and Polycrystals. Adv. Appl. Mech. 23, 1–115. https://doi.org/10.1016/S0065-2156(08)70242-4

Asaro, R.J., Rice, J.R., 1977. Strain localization in ductile single crystals. J. Mech. Phys. Solids 25, 309–338. https://doi.org/10.1016/0022-5096(77)90001-1

Avril, S., Bonnet, M., Bretelle, A.-S., Grédiac, M., Hild, F., Ienny, P., Latourte, F., Lemosse, D., Pagano, S., Pagnacco, E., Pierron, F., 2008. Overview of Identification Methods of Mechanical Parameters Based on Full-field Measurements. Exp. Mech. 48, 381. https://doi.org/10.1007/s11340-008-9148-y

Backlund, P.B., Shahan, D.W., Seepersad, C.C., 2012. A comparative study of the scalability of alternative metamodelling techniques. Eng. Optim. 44, 767–786. https://doi.org/10.1080/0305215X.2011.607817

Bammann, D.J., 1984. An internal variable model of viscoplasticity. Int. J. Eng. Sci. 22, 1041–1053. https://doi.org/10.1016/0020-7225(84)90105-8

Bangash, R.F., Passuello, A., Hammond, M., Schuhmacher, M., 2012. Water allocation assessment in low flow river under data scarce conditions: A study of hydrological simulation in Mediterranean basin. Sci. Total Environ., Integrated modelling and monitoring at different river basin scales under global change 440, 60–71. https://doi.org/10.1016/j.scitotenv.2012.08.031

Barlat, F., Aretz, H., Yoon, J.W., Karabin, M.E., Brem, J.C., Dick, R.E., 2005. Linear transfomation-based anisotropic yield functions. Int. J. Plast. 21, 1009–1039. https://doi.org/10.1016/j.ijplas.2004.06.004

Barlat, F., Lege, D.J., Brem, J.C., 1991. A six-component yield function for anisotropic materials. Int. J. Plast. 7, 693–712. https://doi.org/10.1016/0749-6419(91)90052-Z

Bassani, J.L., 1977. Yield characterization of metals with transversely isotropic plastic properties. Int. J. Mech. Sci. 19, 651–660. https://doi.org/10.1016/0020-7403(77)90070-4

Battaile, C.C., Emery, J.M., Brewer, L.N., Boyce, B.L., 2015. Crystal plasticity simulations of microstructure-induced uncertainty in strain concentration near voids in brass. Philos. Mag. 95, 1069–1079. https://doi.org/10.1080/14786435.2015.1009958

Beck, J.L., Au, S.-K., 2002. Bayesian Updating of Structural Models and Reliability using Markov Chain Monte Carlo Simulation. J. Eng. Mech. 128, 380–391. https://doi.org/10.1061/(ASCE)0733-9399(2002)128:4(380)

Beck, J.L., Yuen, K.-V., 2004. Model Selection Using Response Measurements: Bayesian Probabilistic Approach. J. Eng. Mech. 130, 192–203. https://doi.org/10.1061/(ASCE)0733-9399(2004)130:2(192)

Benedetti, I., Barbe, F., 2013. Modelling Polycrystalline Materials: An Overview of Three-Dimensional Grain-Scale Mechanical Models. J. Multiscale Model. 05, 1350002. https://doi.org/10.1142/S1756973713500029

Bertsimas, D., Brown, D., Caramanis, C., 2011. Theory and Applications of Robust Optimization. SIAM Rev. 53, 464–501. https://doi.org/10.1137/080734510

Beyer, H.-G., Sendhoff, B., 2007. Robust optimization – A comprehensive survey. Comput. Methods Appl. Mech. Eng. 196, 3190–3218. https://doi.org/10.1016/j.cma.2007.03.003

Bikas, H., Stavropoulos, P., Chryssolouris, G., 2016. Additive manufacturing methods and modelling approaches: a critical review. Int. J. Adv. Manuf. Technol. 83, 389–405. https://doi.org/10.1007/s00170-015-7576-2

Birnbaum, Z.W., 1952. Numerical Tabulation of the Distribution of Kolmogorov's Statistic for Finite Sample Size. J. Am. Stat. Assoc. 47, 425–441. https://doi.org/10.1080/01621459.1952.10501182

Bishop, J.E., Emery, J.M., Field, R.V., Weinberger, C.R., Littlewood, D.J., 2015. Direct numerical simulations in solid mechanics for understanding the macroscale effects of microscale material variability. Comput. Methods Appl. Mech. Eng. 287, 262–289. https://doi.org/10.1016/j.cma.2015.01.017

Bishop, R.F., Hill, R., Mott, N.F., 1945. The theory of indentation and hardness tests. Proc. Phys. Soc. 57, 147. https://doi.org/10.1088/0959-5309/57/3/301

Blatman, G., Sudret, B., 2010. An adaptive algorithm to build up sparse polynomial chaos expansions for stochastic finite element analysis. Probabilistic Eng. Mech. 25, 183–197. https://doi.org/10.1016/j.probengmech.2009.10.003

Blau, P.J., 1986. Microindentation Techniques in Materials Science and Engineering: A Symposium Sponsored by ASTM Committee E-4 on Metallography and by the International Metallographic Society, Philadelphia, PA, 15-18 July 1984. ASTM International.

Bostanabad, R., Bui, A.T., Xie, W., Apley, D.W., Chen, W., 2016. Stochastic microstructure characterization and reconstruction via supervised learning. Acta Mater. 103, 89–102. https://doi.org/10.1016/j.actamat.2015.09.044

Boyer, R.R., 1996. An overview on the use of titanium in the aerospace industry. Mater. Sci. Eng. A, International Symposium on Metallurgy and Technology of Titanium Alloys 213, 103–114. https://doi.org/10.1016/0921-5093(96)10233-1

Brunsell, N.A., 2010. A multiscale information theory approach to assess spatial–temporal variability of daily precipitation. J. Hydrol. 385, 165–172. https://doi.org/10.1016/j.jhydrol.2010.02.016

Brynjarsdóttir, J., O'Hagan, A., 2014. Learning about physical parameters: the importance of model discrepancy. Inverse Probl. 30, 114007. https://doi.org/10.1088/0266-5611/30/11/114007

Buchheit, T.E., Wellman, G.W., Battaile, C.C., 2005. Investigating the limits of polycrystal plasticity modeling. Int. J. Plast. 21, 221–249. https://doi.org/10.1016/j.ijplas.2003.10.009

Bunge, H.-J., 2013. Texture Analysis in Materials Science: Mathematical Methods. Elsevier.

Capolungo, L., 2011. Dislocation junction formation and strength in magnesium. Acta Mater. 59, 2909–2917. https://doi.org/10.1016/j.actamat.2011.01.026

Carroll, J.D., Brewer, L.N., Battaile, C.C., Boyce, B.L., Emery, J.M., 2012. The effect of grain size on local deformation near a void-like stress concentration. Int. J. Plast. 39, 46–60. https://doi.org/10.1016/j.ijplas.2012.06.002

Chaboche, J.L., Rousselier, G., 1983. On the Plastic and Viscoplastic Constitutive Equations—Part I: Rules Developed With Internal Variable Concept. J. Press. Vessel Technol. 105, 153–158. https://doi.org/10.1115/1.3264257

Chen, D., He, X., Teng, Q., Xu, Z., Li, Z., 2014. Reconstruction of multiphase microstructure based on statistical descriptors. Phys. Stat. Mech. Its Appl. 415, 240–250. https://doi.org/10.1016/j.physa.2014.07.066

Chen, P., Zabaras, N., Bilionis, I., 2015. Uncertainty propagation using infinite mixture of Gaussian processes and variational Bayesian inference. J. Comput. Phys. 284, 291–333. https://doi.org/10.1016/j.jcp.2014.12.028

Chernatynskiy, A., Phillpot, S.R., LeSar, R., 2013. Uncertainty Quantification in Multiscale Simulation of Materials: A Prospective. Annu. Rev. Mater. Res. 43, 157–182. https://doi.org/10.1146/annurev-matsci-071312-121708

Chiarodo, R.A., Spain, I.L., Bolsaitis, P., 1974. Elastic constants and their pressure derivatives of α-brass single crystals. J. Phys. Chem. Solids 35, 762–764. https://doi.org/10.1016/S0022-3697(74)80234-9

Chkrebtii, O.A., 2013. Probabilistic solution of differential equations for Bayesian uncertainty quantification and inference (Thesis). Simon Fraser University.

Choi, S.-K., Grandhi, R., Canfield, R., Pettit, C., 2003. Polynomial Chaos Expansion with Latin Hypercube Sampling for Predicting Response Variability, in: 44th AIAA/ASME/ASCE/AHS/ASC Structures, Structural Dynamics, and Materials Conference, Structures, Structural Dynamics, and Materials and Co-Located Conferences. American Institute of Aeronautics and Astronautics. https://doi.org/10.2514/6.2003-1749

Chowdhury, A., Kautz, E., Yener, B., Lewis, D., 2016. Image driven machine learning methods for microstructure recognition. Comput. Mater. Sci. 123, 176–187. https://doi.org/10.1016/j.commatsci.2016.05.034

Clayton, J.D., McDowell, D.L., 2004. Homogenized finite elastoplasticity and damage: theory and computations. Mech. Mater. 36, 799–824. https://doi.org/10.1016/j.mechmat.2003.08.001

Clayton, J.D., McDowell, D.L., 2003. Finite polycrystalline elastoplasticity and damage: multiscale kinematics. Int. J. Solids Struct. 40, 5669–5688. https://doi.org/10.1016/S0020-7683(03)00317-2

Clayton, J.D., McDowell, D.L., Bammann, D.J., 2004. A multiscale gradient theory for single crystalline elastoviscoplasticity. Int. J. Eng. Sci. 42, 427–457. https://doi.org/10.1016/j.ijengsci.2003.08.001

Coleman, H.W., Steele, W.G., 2009. Appendix B: Taylor Series Method (TSM) for Uncertainty Propagation, in: Experimentation, Validation, and Uncertainty Analysis for Engineers. John Wiley & Sons, Inc., pp. 257–269. https://doi.org/10.1002/9780470485682.app2

Csiszar, I., 1991. Why Least Squares and Maximum Entropy? An Axiomatic Approach to Inference for Linear Inverse Problems. Ann. Stat. 19, 2032–2066. https://doi.org/10.1214/aos/1176348385

Curtin, W.A., Miller, R.E., 2003. Atomistic/continuum coupling in computational materials science. Model. Simul. Mater. Sci. Eng. 11, R33. https://doi.org/10.1088/0965-0393/11/3/201

Deb, K., 2014. Multi-objective Optimization, in: Burke, E.K., Kendall, G. (Eds.), Search Methodologies: Introductory Tutorials in Optimization and Decision Support Techniques. Springer Science & Business Media, New York, pp. 403–449. https://doi.org/10.1007/978-1-4614-6940-7_15

Dehghannasiri, R., Xue, D., Balachandran, P.V., Yousefi, M.R., Dalton, L.A., Lookman, T., Dougherty, E.R., 2017. Optimal experimental design for materials discovery. Comput. Mater. Sci. 129, 311–322. https://doi.org/10.1016/j.commatsci.2016.11.041

Dile, Y.T., Srinivasan, R., 2014. Evaluation of CFSR climate data for hydrologic prediction in data-scarce watersheds: an application in the Blue Nile River Basin. JAWRA J. Am. Water Resour. Assoc. 50, 1226–1241. https://doi.org/10.1111/jawr.12182

Domain, C., Becquart, C.S., Malerba, L., 2004. Simulation of radiation damage in Fe alloys: an object kinetic Monte Carlo approach. J. Nucl. Mater. 335, 121–145. https://doi.org/10.1016/j.jnucmat.2004.07.037

Donachie, M.J., 2000. Titanium: A Technical Guide, 2nd Edition. ASM International.

Dong, W.M., Chiang, W.L., Shah, H.C., 1987. Fuzzy information processing in seismic hazard analysis and decision making. Soil Dyn. Earthq. Eng. 6, 220–226. https://doi.org/10.1016/0267-7261(87)90003-0

Dragićević, S., Lai, T., Balram, S., 2015. GIS-based multicriteria evaluation with multiscale analysis to characterize urban landslide susceptibility in data-scarce environments. Habitat Int., Special Issue: Exploratory Spatial Analysis of Urban Habitats 45, 114–125. https://doi.org/10.1016/j.habitatint.2014.06.031

Edelman, F., Drucker, D.C., 1951. Some extensions of elementary plasticity theory. J. Frankl. Inst. 251, 581–605.

Ellis, B.D., McDowell, D.L., 2017. Application-Specific Computational Materials Design via Multiscale Modeling and the Inductive Design Exploration Method (IDEM). Integrating Mater. Manuf. Innov. 6, 9–35. https://doi.org/10.1007/s40192-017-0086-3

Fan, J., 2011. Multiscale Analysis of Deformation and Failure of Materials. John Wiley & Sons.

Fang, C.-C., Huang, Y.-S., 2008. A Bayesian decision analysis in determining the optimal policy for pricing, production, and warranty of repairable products. Expert Syst. Appl. 35, 1858–1872. https://doi.org/10.1016/j.eswa.2007.08.075

Fast, T., Kalidindi, S.R., 2011. Formulation and calibration of higher-order elastic localization relationships using the MKS approach. Acta Mater. 59, 4595–4605. https://doi.org/10.1016/j.actamat.2011.04.005

Fish, J., Nuggehally, M.A., Shephard, M.S., Picu, C.R., Badia, S., Parks, M.L., Gunzburger, M., 2007. Concurrent AtC coupling based on a blend of the continuum stress and the atomistic force. Comput. Methods Appl. Mech. Eng. 196, 4548–4560. https://doi.org/10.1016/j.cma.2007.05.020

Forrester, A., Sobester, A., Keane, A., 2008. Engineering Design Via Surrogate Modelling: A Practical Guide. Wiley-Blackwell, Chichester, West Sussex, England.

Francois, M.M., Sun, A., King, W.E., Henson, N.J., Tourret, D., Bronkhorst, C.A., Carlson, N.N., Newman, C.K., Haut, T., Bakosi, J., Gibbs, J.W., Livescu, V., Vander Wiel, S.A., Clarke, A.J., Schraad, M.W., Blacker, T., Lim, H., Rodgers, T., Owen, S., Abdeljawad, F., Madison, J., Anderson, A.T., Fattebert, J.-L., Ferencz, R.M., Hodge, N.E., Khairallah, S.A., Walton, O., 2017. Modeling of additive manufacturing processes for metals: Challenges and opportunities. Curr. Opin. Solid State Mater. Sci. 21, 198–206. https://doi.org/10.1016/j.cossms.2016.12.001

Frazier, W.E., 2014. Metal Additive Manufacturing: A Review. J. Mater. Eng. Perform. 23, 1917–1928. https://doi.org/10.1007/s11665-014-0958-z

Fullwood, D.T., Niezgoda, S.R., Kalidindi, S.R., 2008. Microstructure reconstructions from 2-point statistics using phase-recovery algorithms. Acta Mater. 56, 942–948. https://doi.org/10.1016/j.actamat.2007.10.044

Gaganis, P., 2009. Model calibration/parameter estimation techniques and conceptual model error, in: Baveye, P.C., Laba, M., Mysiak, J. (Eds.), Uncertainties in Environmental Modelling and Consequences for Policy Making, NATO Science for Peace and Security Series C: Environmental Security. Springer Netherlands, pp. 129–154.

Gano, S.E., Kim, H., Brown II, D.E., 2006. Comparison of Three Surrogate Modeling Techniques: Datascape, Kriging, and Second Order Regression, in: Proceedings of the 11th AIAA/ISSMO Multidisciplinary Analysis and Optimization Conference. Presented at the 11th AIAA/ISSMO Multidisciplinary Analysis and Optimization Conference, American Institute of Aeronautics and Astronautics, Portsmouth, VA, p. 7048. https://doi.org/10.2514/6.2006-7048

Geers, M.G.D., Kouznetsova, V.G., Brekelmans, W.A.M., 2010. Multi-scale computational homogenization: Trends and challenges. J. Comput. Appl. Math., Fourth International Conference on Advanced COmputational Methods in ENgineering (ACOMEN 2008) 234, 2175–2182. https://doi.org/10.1016/j.cam.2009.08.077

Geers, M.G.D., Yvonnet, J., 2016. Multiscale modeling of microstructure–property relations. MRS Bull. 41, 610–616. https://doi.org/10.1557/mrs.2016.165

Geyer, C.J., 1992. Practical Markov Chain Monte Carlo. Stat. Sci. 7, 473–483.

Ghosh, S., 2011. Micromechanical Analysis and Multi-Scale Modeling Using the Voronoi Cell Finite Element Method. CRC Press.

Ghosh, S., Kubair, D.V., 2016. Exterior statistics based boundary conditions for representative volume elements of elastic composites. J. Mech. Phys. Solids 95, 1–24. https://doi.org/10.1016/j.jmps.2016.05.022

Ghosh, S., Lee, K., Raghavan, P., 2001. A multi-level computational model for multi-scale damage analysis in composite and porous materials. Int. J. Solids Struct. 38, 2335–2385. https://doi.org/10.1016/S0020-7683(00)00167-0

Ghosh, S., Shahba, A., Tu, X., Huskins, E.L., Schuster, B.E., 2016. Crystal plasticity FE modeling of Ti alloys for a range of strain-rates. Part II: Image-based model with experimental validation. Int. J. Plast. 87, 69–85. https://doi.org/10.1016/j.ijplas.2016.09.003

Glimm, J., Lee, Y., Ye, K.Q., Sharp, D.H., 2003. Prediction using numerical simulations, a Bayesian framework for uncertainty quantification and its statistical challenge, in: Proceedings of the Fourth International Symposium on Uncertainty Modeling and Analysis (ISUMA '03). Presented at the Fourth International Symposium on Uncertainty Modeling and Analysis, IEEE, College Park, MD, pp. 380–385. https://doi.org/10.1109/ISUMA.2003.1236189

Glüge, R., Weber, M., Bertram, A., 2012. Comparison of spherical and cubical statistical volume elements with respect to convergence, anisotropy, and localization behavior. Comput. Mater. Sci. 63, 91–104. https://doi.org/10.1016/j.commatsci.2012.05.063

Gokhale, A.M., Tewari, A., Garmestani, H., 2005. Constraints on microstructural two-point correlation functions. Scr. Mater. 53, 989–993. https://doi.org/10.1016/j.scriptamat.2005.06.013

Gopakumar, A.M., Balachandran, P.V., Xue, D., Gubernatis, J.E., Lookman, T., 2018. Multi-objective Optimization for Materials Discovery via Adaptive Design. Sci. Rep. 8, 3738. https://doi.org/10.1038/s41598-018-21936-3

Gordon, P.A., Neeraj, T., Li, Y., Li, J., 2010. Screw dislocation mobility in BCC metals: the role of the compact core on double-kink nucleation. Model. Simul. Mater. Sci. Eng. 18, 085008. https://doi.org/10.1088/0965-0393/18/8/085008

Gordon, P.A., Neeraj, T., Mendelev, M.I., 2011. Screw dislocation mobility in BCC Metals: a refined potential description for α-Fe. Philos. Mag. 91, 3931–3945. https://doi.org/10.1080/14786435.2011.597947

Gorguluarslan, R.M., Park, S.-I., Rosen, D.W., Choi, S.-K., 2015. A Multilevel Upscaling Method for Material Characterization of Additively Manufactured Part Under Uncertainties. J. Mech. Des. 137, 111408-111408–12. https://doi.org/10.1115/1.4031012

Groeber, M.A., Jackson, M.A., 2014. DREAM.3D: A Digital Representation Environment for the Analysis of Microstructure in 3D. Integrating Mater. Manuf. Innov. 3, 5. https://doi.org/10.1186/2193-9772-3-5

Gröger, R., Bailey, A.G., Vitek, V., 2008a. Multiscale modeling of plastic deformation of molybdenum and tungsten: I. Atomistic studies of the core structure and glide of 1/2〈1 1 1〉 screw dislocations at 0 K. Acta Mater. 56, 5401–5411. https://doi.org/10.1016/j.actamat.2008.07.018

Gröger, R., Racherla, V., Bassani, J.L., Vitek, V., 2008b. Multiscale modeling of plastic deformation of molybdenum and tungsten: II. Yield criterion for single crystals based on atomistic studies of glide of screw dislocations. Acta Mater. 56, 5412–5425. https://doi.org/10.1016/j.actamat.2008.07.037

Gröger, R., Vitek, V., 2008. Multiscale modeling of plastic deformation of molybdenum and tungsten. III. Effects of temperature and plastic strain rate. Acta Mater. 56, 5426–5439. https://doi.org/10.1016/j.actamat.2008.07.027

Gupta, H.V., Sorooshian, S., Yapo, P.O., 1998. Toward improved calibration of hydrologic models: Multiple and noncommensurable measures of information. Water Resour. Res. 34, 751–763. https://doi.org/10.1029/97WR03495

Hale, L.M., Lim, H., Zimmerman, J.A., Battaile, C.C., Weinberger, C.R., 2015. Insights on activation enthalpy for non-Schmid slip in body-centered cubic metals. Scr. Mater. 99, 89–92. https://doi.org/10.1016/j.scriptamat.2014.11.035

Hall, J.W., 2003. Handling uncertainty in the hydroinformatic process. J. Hydroinformatics 5, 215–232.

Hao, S., Liu, W.K., Moran, B., Vernerey, F., Olson, G.B., 2004. Multi-scale constitutive model and computational framework for the design of ultra-high strength, high toughness steels. Comput. Methods Appl. Mech. Eng., Multiple Scale Methods for Nanoscale Mechanics and Materials 193, 1865–1908. https://doi.org/10.1016/j.cma.2003.12.026

Hennessey, C., Castelluccio, G.M., McDowell, D.L., 2017. Sensitivity of polycrystal plasticity to slip system kinematic hardening laws for Al 7075-T6. Mater. Sci. Eng. A 687, 241–248. https://doi.org/10.1016/j.msea.2017.01.070

Higdon, D., Gattiker, J., Williams, B., Rightley, M., 2008. Computer Model Calibration Using High-Dimensional Output. J. Am. Stat. Assoc. 103, 570–583. https://doi.org/10.1198/016214507000000888

Higdon, D., Kennedy, M., Cavendish, J., Cafeo, J., Ryne, R., 2004. Combining Field Data and Computer Simulations for Calibration and Prediction. SIAM J. Sci. Comput. 26, 448–466. https://doi.org/10.1137/S1064827503426693

Hirt, L., Reiser, A., Spolenak, R., Zambelli, T., 2017. Additive Manufacturing of Metal Structures at the Micrometer Scale. Adv. Mater. 29, 1604211. https://doi.org/10.1002/adma.201604211

Hoeting, J.A., Madigan, D., Raftery, A.E., Volinsky, C.T., 1999. Bayesian model averaging: a tutorial (with comments by M. Clyde, David Draper and E. I. George, and a rejoinder by the authors. Stat. Sci. 14, 382–417. https://doi.org/10.1214/ss/1009212519

Honarmandi, P., Arroyave, R., 2017. Using Bayesian framework to calibrate a physically based model describing strain-stress behavior of TRIP steels. Comput. Mater. Sci. 129, 66–81. https://doi.org/10.1016/j.commatsci.2016.12.015

Horstemeyer, M.F., Bammann, D.J., 2010. Historical review of internal state variable theory for inelasticity. Int. J. Plast., Special Issue In Honor of David L. McDowell 26, 1310–1334. https://doi.org/10.1016/j.ijplas.2010.06.005

Horstemeyer, M.F., Lathrop, J., Gokhale, A.M., Dighe, M., 2000. Modeling stress state dependent damage evolution in a cast Al–Si–Mg aluminum alloy. Theor. Appl. Fract. Mech. 33, 31–47. https://doi.org/10.1016/S0167-8442(99)00049-X

Jia, N., Roters, F., Eisenlohr, P., Kords, C., Raabe, D., 2012. Non-crystallographic shear banding in crystal plasticity FEM simulations: Example of texture evolution in α-brass. Acta Mater. 60, 1099–1115. https://doi.org/10.1016/j.actamat.2011.10.047

Jin, R., Chen, W., Simpson, T.W., 2001. Comparative studies of metamodelling techniques under multiple modelling criteria. Struct. Multidiscip. Optim. 23, 1–13. https://doi.org/10.1007/s00158-001-0160-4

Johnson, J.D. (ProStat, Helton, J.C. (Arizona S.U., Oberkampf, W.L., Sallaberry, C.J., 2008. Representation of Analysis Results Involving Aleatory and Epistemic Uncertainty. (No. SAND2008-4379). Sandia National Laboratories.

Johnson, R.A., Oh, D.J., 1989. Analytic embedded atom method model for bcc metals. J. Mater. Res. 4, 1195–1201. https://doi.org/10.1557/JMR.1989.1195

Jolliffe, I.T., 1986. Principal component analysis and factor analysis, in: Principal Component Analysis. Springer, pp. 115–128.

Jónsson, H., Mills, G., Jacobsen, K.W., 1998. Nudged elastic band method for finding minimum energy paths of transitions, in: Proceedings of the International School of Physics. Presented at the Classical and Quantum Dynamics in Condensed Phase Simulations, LERICI, Villa Marigola, pp. 385–404. https://doi.org/10.1142/9789812839664_0016

Kalidindi, S.R., Medford, A.J., McDowell, D.L., 2016. Vision for Data and Informatics in the Future Materials Innovation Ecosystem. JOM 68, 2126–2137. https://doi.org/10.1007/s11837-016-2036-5

Kalidindi, S.R., Niezgoda, S.R., Landi, G., Vachhani, S., Fast, T., 2010. A Novel Framework for Building Materials Knowledge Systems. CMC Comput. Mater. Contin. 17, 103–126. https://doi.org/10.3970/cmc.2010.017.103

Kanit, T., Forest, S., Galliet, I., Mounoury, V., Jeulin, D., 2003. Determination of the size of the representative volume element for random composites: statistical and numerical approach. Int. J. Solids Struct. 40, 3647–3679. https://doi.org/10.1016/S0020-7683(03)00143-4

Keh, A.S., 1965. Work hardening and deformation sub-structure in iron single crystals deformed in tension at 298°k. Philos. Mag. 12, 9–30. https://doi.org/10.1080/14786436508224942

Kennedy, M.C., O'Hagan, A., 2001. Bayesian calibration of computer models. J. R. Stat. Soc. Ser. B Stat. Methodol. 63, 425–464. https://doi.org/10.1111/1467-9868.00294

Kennedy, M.C., O'Hagan, A., 2000. Predicting the Output from a Complex Computer Code When Fast Approximations Are Available. Biometrika 87, 1–13.

Kern, P.C., 2016. Improvements to the computational pipeline in crystal plasticity estimates of high cycle fatigue of microstructures (Thesis). Georgia Institute of Technology.

Khan, A.S., Huang, S., 1995. Continuum theory of plasticity. John Wiley & Sons.

Khu, S.-T., Madsen, H., di Pierro, F., 2008. Incorporating multiple observations for distributed hydrologic model calibration: An approach using a multi-objective evolutionary algorithm and clustering. Adv. Water Resour. 31, 1387–1398. https://doi.org/10.1016/j.advwatres.2008.07.011

Knap, J., Ortiz, M., 2001. An analysis of the quasicontinuum method. J. Mech. Phys. Solids, The JW Hutchinson and JR Rice 60th Anniversary Issue 49, 1899–1923. https://doi.org/10.1016/S0022-5096(01)00034-5

Knezevic, M., Al-Harbi, H.F., Kalidindi, S.R., 2009. Crystal plasticity simulations using discrete Fourier transforms. Acta Mater. 57, 1777–1784. https://doi.org/10.1016/j.actamat.2008.12.017

Kocks, U.F., 1976. Laws for Work-Hardening and Low-Temperature Creep. J. Eng. Mater. Technol. 98, 76–85. https://doi.org/10.1115/1.3443340

Kocks, U.F., Argon, A.S., Ashby, M.F., 1975. Thermodynamics and Kinetics of Slip. Pergamon Press.

Koslowski, M., Strachan, A., 2011. Uncertainty propagation in a multiscale model of nanocrystalline plasticity. Reliab. Eng. Syst. Saf. 96, 1161–1170. https://doi.org/10.1016/j.ress.2010.11.011

Kothari, M., Anand, L., 1998. Elasto-viscoplastic constitutive equations for polycrystalline metals: Application to tantalum. J. Mech. Phys. Solids 46, 51–83. https://doi.org/10.1016/S0022-5096(97)00037-9

Krieg, R.D., 1975. A practical two surface plasticity theory. J. Appl. Mech. 42, 641–646.

Kuehmann, C.J., Olson, G.B., 2009. Computational materials design and engineering. Mater. Sci. Technol. 25, 472–478. https://doi.org/10.1179/174328408X371967

Kuhlmann-Wilsdorf, D., 1999. The theory of dislocation-based crystal plasticity. Philos. Mag. A 79, 955–1008. https://doi.org/10.1080/01418619908210342

Kumar, A., Dawson, P.R., 2000. Computational modeling of f.c.c. deformation textures over Rodrigues' space. Acta Mater. 48, 2719–2736. https://doi.org/10.1016/S1359-6454(00)00044-6

Kuramoto, E., Aono, Y., Kitajima, K., 1979a. Thermally activated slip deformation of high purity iron single crystals between 4.2 K and 300 K. Scr. Metall. 13, 1039–1042. https://doi.org/10.1016/0036-9748(79)90199-6

Kuramoto, E., Aono, Y., Kitajima, K., Maeda, K., Takeuchi, S., 1979b. Thermally activated slip deformation between 0·7 and 77 K in high-purity iron single crystals. Philos. Mag. A 39, 717–724. https://doi.org/10.1080/01418617908239302

Lacaze, S., Missoum, S., 2014. Parameter estimation with correlated outputs using fidelity maps. Probabilistic Eng. Mech. 38, 13–21. https://doi.org/10.1016/j.probengmech.2014.08.002

Li, D., Zbib, H., Sun, X., Khaleel, M., 2014. Predicting plastic flow and irradiation hardening of iron single crystal with mechanism-based continuum dislocation dynamics. Int. J. Plast. 52, 3–17. https://doi.org/10.1016/j.ijplas.2013.01.015

Li, W., Lin, G., Li, B., 2016. Inverse regression-based uncertainty quantification algorithms for high-dimensional models: Theory and practice. J. Comput. Phys. 321, 259–278. https://doi.org/10.1016/j.jcp.2016.05.040

Lim, H., Hale, L.M., Zimmerman, J.A., Battaile, C.C., Weinberger, C.R., 2015. A multi-scale model of dislocation plasticity in α-Fe: Incorporating temperature, strain rate

and non-Schmid effects. Int. J. Plast., Special Issue on Constitutive Modeling from Micro-Scale to Continuum in Honor of Prof. Frédéric Barlat 73, 100–118. https://doi.org/10.1016/j.ijplas.2014.12.005

Ling, Y., Mullins, J., Mahadevan, S., 2014. Selection of model discrepancy priors in Bayesian calibration. J. Comput. Phys. 276, 665–680. https://doi.org/10.1016/j.jcp.2014.08.005

Ma, X., Zabaras, N., 2011. Kernel principal component analysis for stochastic input model generation. J. Comput. Phys. 230, 7311–7331. https://doi.org/10.1016/j.jcp.2011.05.037

Malvern, L.E., 1969. Introduction to Continuum Mechanics. Prentice Hall Inc Engle Cliffs NJ 1696, 301–320.

Marler, R.T., Arora, J.S., 2004. Survey of multi-objective optimization methods for engineering. Struct. Multidiscip. Optim. 26, 369–395. https://doi.org/10.1007/s00158-003-0368-6

Martin, J., Revilla, E., Quenette, P.-Y., Naves, J., Allainé, D., Swenson, J.E., 2012. Brown bear habitat suitability in the Pyrenees: transferability across sites and linking scales to make the most of scarce data. J. Appl. Ecol. 49, 621–631. https://doi.org/10.1111/j.1365-2664.2012.02139.x

Mayeur, J.R., 2004. Three Dimensional Modeling of Ti-Al Alloys with Application to Attachment Fatigue (Thesis). Georgia Institute of Technology.

McCullagh, P., 1984. Generalized linear models. Eur. J. Oper. Res. 16, 285–292. https://doi.org/10.1016/0377-2217(84)90282-0

McDowell, D.L., 2012. Multiscale Modeling and Microstructure-Sensitive Materials Design.

McDowell, D.L., 2010. A perspective on trends in multiscale plasticity. Int. J. Plast., Special Issue In Honor of David L. McDowell 26, 1280–1309. https://doi.org/10.1016/j.ijplas.2010.02.008

McDowell, D.L., 2008. Viscoplasticity of heterogeneous metallic materials. Mater. Sci. Eng. R Rep. 62, 67–123. https://doi.org/10.1016/j.mser.2008.04.003

McDowell, D.L., 2005. Internal State Variable Theory, in: Yip, S. (Ed.), Handbook of Materials Modeling. Springer Netherlands, pp. 1151–1169. https://doi.org/10.1007/978-1-4020-3286-8_58

McDowell, D.L., 1985. An Experimental Study of the Structure of Constitutive Equations for Nonproportional Cyclic Plasticity. J. Eng. Mater. Technol. 107, 307–315. https://doi.org/10.1115/1.3225824

McDowell, D.L., Ghosh, S., Kalidindi, S.R., 2011. Representation and computational structure-property relations of random media. JOM 63, 45–51. https://doi.org/10.1007/s11837-011-0045-y

McFarland, J., Mahadevan, S., 2008. Multivariate significance testing and model calibration under uncertainty. Comput. Methods Appl. Mech. Eng., Validation Challenge Workshop 197, 2467–2479. https://doi.org/10.1016/j.cma.2007.05.030

McFarland, J., Mahadevan, S., Romero, V., Swiler, L., 2008. Calibration and Uncertainty Analysis for Computer Simulations with Multivariate Output. AIAA J. 46, 1253–1265. https://doi.org/10.2514/1.35288

McHutchon, A., Rasmussen, C.E., 2011. Gaussian Process Training with Input Noise, in: Shawe-Taylor, J., Zemel, R.S., Bartlett, P.L., Pereira, F., Weinberger, K.Q. (Eds.), Advances in Neural Information Processing Systems 24. Curran Associates, Inc., pp. 1341–1349.

Miller, R.E., Tadmor, E.B., 2002. The Quasicontinuum Method: Overview, applications and current directions. J. Comput.-Aided Mater. Des. 9, 203–239. https://doi.org/10.1023/A:1026098010127

Millman, K.J., Aivazis, M., 2011. Python for Scientists and Engineers. Comput. Sci. Eng. 13, 9–12. https://doi.org/10.1109/MCSE.2011.36

Monasterio, P.R., Wirth, B.D., Odette, G.R., 2007. Kinetic Monte Carlo modeling of cascade aging and damage accumulation in Fe–Cu alloys. J. Nucl. Mater., TMS 2007:Wechsler Symposium 361, 127–140. https://doi.org/10.1016/j.jnucmat.2006.12.022

Morawiec, A., Field, D.P., 1996. Rodrigues parameterization for orientation and misorientation distributions. Philos. Mag. A 73, 1113–1130. https://doi.org/10.1080/01418619608243708

Mori, H., 2017. Temperature and Stress Dependence of Mobility of Screw Dislocation in BCC Iron. Solid State Phenom. 258, 17–20. https://doi.org/10.4028/www.scientific.net/SSP.258.17

Mulvey, J.M., Vanderbei, R.J., Zenios, S.A., 1995. Robust Optimization of Large-Scale Systems. Oper. Res. 43, 264–281. https://doi.org/10.1287/opre.43.2.264

Naamane, S., Monnet, G., Devincre, B., 2010. Low temperature deformation in iron studied with dislocation dynamics simulations. Int. J. Plast. 26, 84–92. https://doi.org/10.1016/j.ijplas.2009.05.003

Narayanan, S., McDowell, D.L., Zhu, T., 2014. Crystal plasticity model for BCC iron atomistically informed by kinetics of correlated kinkpair nucleation on screw dislocation. J. Mech. Phys. Solids 65, 54–68. https://doi.org/10.1016/j.jmps.2014.01.004

National Research Council, 2008. Integrated Computational Materials Engineering: A Transformational Discipline for Improved Competitiveness and National Security. The National Academies Press, Washington, DC. https://doi.org/10.17226/12199

Niezgoda, S.R., Turner, D.M., Fullwood, D.T., Kalidindi, S.R., 2010. Optimized structure based representative volume element sets reflecting the ensemble-averaged 2-point statistics. Acta Mater. 58, 4432–4445. https://doi.org/10.1016/j.actamat.2010.04.041

Oskay, C., Fish, J., 2007. On calibration and validation of eigendeformation-based multiscale models for failure analysis of heterogeneous systems. Comput. Mech. 42, 181–195. https://doi.org/10.1007/s00466-007-0197-3

Ostoja-Starzewski, M., 2006. Material spatial randomness: From statistical to representative volume element. Probabilistic Eng. Mech. 21, 112–132. https://doi.org/10.1016/j.probengmech.2005.07.007

Park, I., Amarchinta, H.K., Grandhi, R.V., 2010. A Bayesian approach for quantification of model uncertainty. Reliab. Eng. Syst. Saf. 95, 777–785. https://doi.org/10.1016/j.ress.2010.02.015

Patra, A., McDowell, D.L., 2012. Crystal plasticity-based constitutive modelling of irradiated bcc structures. Philos. Mag. 92, 861–887. https://doi.org/10.1080/14786435.2011.634855

Patra, A., Zhu, T., McDowell, D.L., 2014. Constitutive equations for modeling non-Schmid effects in single crystal bcc-Fe at low and ambient temperatures. Int. J. Plast. 59, 1–14. https://doi.org/10.1016/j.ijplas.2014.03.016

Paulson, N.H., Priddy, M.W., McDowell, D.L., Kalidindi, S.R., 2017. Reduced-order structure-property linkages for polycrystalline microstructures based on 2-point statistics. Acta Mater. Complete, 428–438. https://doi.org/10.1016/j.actamat.2017.03.009

Pederson, S.P., Johnson, M.E., 1990. Estimating Model Discrepancy. Technometrics 32, 305–314. https://doi.org/10.2307/1269107

Pedregosa, F., Varoquaux, G., Gramfort, A., Michel, V., Thirion, B., Grisel, O., Blondel, M., Prettenhofer, P., Weiss, R., Dubourg, V., Vanderplas, J., Passos, A., Cournapeau, D., Brucher, M., Perrot, M., Duchesnay, É., 2011. Scikit-learn: Machine Learning in Python. J. Mach. Learn. Res. 12, 2825−2830.

Plimpton, S., Battaile, C., Ch, M., Holm, L., Thompson, A., Tikare, V., Wagner, G., Zhou, X., Cardona, C.G., Slepoy, A., 2009. Crossing the Mesoscale No-Man's Land via Parallel Kinetic Monte Carlo.

Priddy, M.W., 2016. Exploration of forward and inverse protocols for property optimization of Ti-6Al-4V.

Proville, L., Rodney, D., Marinica, M.-C., 2012. Quantum effect on thermally activated glide of dislocations. Nat. Mater. 11, 845–849. https://doi.org/10.1038/nmat3401

Qidwai, S.M., Turner, D.M., Niezgoda, S.R., Lewis, A.C., Geltmacher, A.B., Rowenhorst, D.J., Kalidindi, S.R., 2012. Estimating the response of polycrystalline materials using sets of weighted statistical volume elements. Acta Mater. 60, 5284–5299. https://doi.org/10.1016/j.actamat.2012.06.026

Qin, Q., Bassani, J.L., 1992. Non-schmid yield behavior in single crystals. J. Mech. Phys. Solids 40, 813–833. https://doi.org/10.1016/0022-5096(92)90005-M

Rao, R.V., 2008. A decision making methodology for material selection using an improved compromise ranking method. Mater. Des. 29, 1949–1954. https://doi.org/10.1016/j.matdes.2008.04.019

Rasmussen, C.E., Williams, C.K., 2006. Gaussian process for machine learning. MIT press.

Reddy, J.N., 1993. An introduction to the finite element method. McGraw-Hill New York.

Rieh, S.Y., Danielson, D.R., 2008. Credibility: A multidisciplinary framework. Annu. Rev. Inf. Sci. Technol. 41, 307–364. https://doi.org/10.1002/aris.2007.1440410114

Riley, M.E., Grandhi, R.V., 2011. Quantification of model-form and predictive uncertainty for multi-physics simulation. Comput. Struct., Computational Fluid and Solid Mechanics 2011 89, 1206–1213. https://doi.org/10.1016/j.compstruc.2010.10.004

Rizzi, F., Najm, H., Debusschere, B., Sargsyan, K., Salloum, M., Adalsteinsson, H., Knio, O., 2012a. Uncertainty Quantification in MD Simulations. Part II: Bayesian Inference of Force-Field Parameters. Multiscale Model. Simul. 10, 1460–1492. https://doi.org/10.1137/110853170

Rizzi, F., Najm, H., Debusschere, B., Sargsyan, K., Salloum, M., Adalsteinsson, H., Knio, O., 2012b. Uncertainty Quantification in MD Simulations. Part I: Forward Propagation. Multiscale Model. Simul. 10, 1428–1459. https://doi.org/10.1137/110853169

Roters, F., Eisenlohr, P., Hantcherli, L., Tjahjanto, D.D., Bieler, T.R., Raabe, D., 2010. Overview of constitutive laws, kinematics, homogenization and multiscale methods in crystal plasticity finite-element modeling: Theory, experiments, applications. Acta Mater. 58, 1152–1211. https://doi.org/10.1016/j.actamat.2009.10.058

Rudd, R. e., Broughton, J. q., 2000. Concurrent Coupling of Length Scales in Solid State Systems. Phys. Status Solidi B 217, 251–291. https://doi.org/10.1002/(SICI)1521-3951(200001)217:1<251::AID-PSSB251>3.0.CO;2-A

Salloum, M., Sargsyan, K., Jones, R., Najm, H., Debusschere, B., 2015. Quantifying Sampling Noise and Parametric Uncertainty in Atomistic-to-Continuum Simulations Using Surrogate Models. Multiscale Model. Simul. 13, 953–976. https://doi.org/10.1137/140989601

Scholten, L., Scheidegger, A., Reichert, P., Maurer, M., 2013. Combining expert knowledge and local data for improved service life modeling of water supply networks. Environ. Model. Softw. 42, 1–16. https://doi.org/10.1016/j.envsoft.2012.11.013

Schwartzbart, H., Jones, M.H., Brown Jr, W.F., 1951. Observations on Bauschinger Effect in Copper and Brass.

Seeger, A., 1956. LXV. On the theory of the low-temperature internal friction peak observed in metals. Philos. Mag. 1, 651–662. https://doi.org/10.1080/14786435608244000

Shahba, A., Ghosh, S., 2016. Crystal plasticity FE modeling of Ti alloys for a range of strain-rates. Part I: A unified constitutive model and flow rule. Int. J. Plast. 87, 48–68. https://doi.org/10.1016/j.ijplas.2016.09.002

Simulia, 2007. ABAQUS. Dassault Systemes, Providence, RI.

Smith, B.D., 2013. Microstructure-sensitive plasticity and fatigue of three titanium alloy microstructures (Thesis). Georgia Institute of Technology.

Smith, R.C., 2013. Uncertainty Quantification: Theory, Implementation, and Applications. SIAM-Society for Industrial and Applied Mathematics, Philadelphia.

Sobie, C., Bertin, N., Capolungo, L., 2015. Analysis of Obstacle Hardening Models Using Dislocation Dynamics: Application to Irradiation-Induced Defects. Metall. Mater. Trans. A 46, 3761–3772. https://doi.org/10.1007/s11661-015-2935-z

Song, J.E., 2010. Hierarchical multiscale modeling of Ni-base superalloys (Thesis). Georgia Institute of Technology.

Spencer, P.J., 2008. A brief history of CALPHAD. Calphad 32, 1–8. https://doi.org/10.1016/j.calphad.2007.10.001

Spitzig, W.A., Keh, A.S., 1970a. Orientation and temperature dependence of slip in iron single crystals. Metall. Trans. 1, 2751–2757. https://doi.org/10.1007/BF03037811

Spitzig, W.A., Keh, A.S., 1970b. The role of internal and effective stresses in the plastic flow of iron single crystals. Metall. Trans. 1, 3325–3331. https://doi.org/10.1007/BF03037859

Spitzig, W.A., Keh, A.S., 1970c. Orientation dependence of the strain-rate sensitivity and thermally activated flow in iron single crystals. Acta Metall. 18, 1021–1033. https://doi.org/10.1016/0001-6160(70)90058-1

statsmodels: Statsmodels: statistical modeling and econometrics in Python, 2018. . statsmodels.

Stopka, K., Kalidindi, S.R., McDowell, D.L., n.d. Reduced-order structure-property linkages for multiphase polycrystalline microstructures.

Storlie, C.B., Lane, W.A., Ryan, E.M., Gattiker, J.R., Higdon, D.M., 2015. Calibration of Computational Models With Categorical Parameters and Correlated Outputs via Bayesian Smoothing Spline ANOVA. J. Am. Stat. Assoc. 110, 68–82. https://doi.org/10.1080/01621459.2014.979993

Sundararaghavan, V., Zabaras, N., 2005. Classification and reconstruction of three-dimensional microstructures using support vector machines. Comput. Mater. Sci. 32, 223–239. https://doi.org/10.1016/j.commatsci.2004.07.004

Suzuki, T., Koizumi, H., Kirchner, H.O.K., 1995. Plastic flow stress of b.c.c. transition metals and the Peierls potential. Acta Metall. Mater. 43, 2177–2187. https://doi.org/10.1016/0956-7151(94)00451-X

Tadmor, E.B., Ortiz, M., Phillips, R., 1996. Quasicontinuum analysis of defects in solids. Philos. Mag. A 73, 1529–1563. https://doi.org/10.1080/01418619608243000

Tallman, A.E., Swiler, L.P., Wang, Y., McDowell, D.L., 2017. Reconciled Top-down and Bottom-up Hierarchical Multiscale Calibration of bcc Fe Crystal Plasticity. Int. J. Multiscale Comput. Eng. 15. https://doi.org/10.1615/IntJMultCompEng.2017021859

Tanner, A.B., McGinty, R.D., McDowell, D.L., 1999. Modeling temperature and strain rate history effects in OFHC Cu. Int. J. Plast. 15, 575–603. https://doi.org/10.1016/S0749-6419(98)00062-X

Tong, J., Zhan, Z.-L., Vermeulen, B., 2004. Modelling of cyclic plasticity and viscoplasticity of a nickel-based alloy using Chaboche constitutive equations. Int. J. Fatigue 26, 829–837. https://doi.org/10.1016/j.ijfatigue.2004.01.002

Tran, A.V., Wang, Y., 2017. Reliable Molecular Dynamics: Uncertainty quantification using interval analysis in molecular dynamics simulation. Comput. Mater. Sci. 127, 141–160. https://doi.org/10.1016/j.commatsci.2016.10.021

Trucano, T.G., Swiler, L.P., Igusa, T., Oberkampf, W.L., Pilch, M., 2006. Calibration, validation, and sensitivity analysis: What's what. Reliab. Eng. Syst. Saf., The Fourth International Conference on Sensitivity Analysis of Model Output (SAMO 2004)SAMO 2004The Fourth International Conference on Sensitivity Analysis of Model Output (SAMO 2004) 91, 1331–1357. https://doi.org/10.1016/j.ress.2005.11.031

Tzeng, G.-H., Huang, J.-J., 2011. Multiple Attribute Decision Making: Methods and Applications. CRC Press.

van der Sluis, O., Schreurs, P.J.G., Brekelmans, W.A.M., Meijer, H.E.H., 2000. Overall behaviour of heterogeneous elastoviscoplastic materials: effect of microstructural modelling. Mech. Mater. 32, 449–462. https://doi.org/10.1016/S0167-6636(00)00019-3

Vitek, V, Mrovec, M., Bassani, J.., 2004. Influence of non-glide stresses on plastic flow: from atomistic to continuum modeling. Mater. Sci. Eng. A 365, 31–37. https://doi.org/10.1016/j.msea.2003.09.004

Vitek, V., Mrovec, M., Gröger, R., Bassani, J.L., Racherla, V., Yin, L., 2004. Effects of non-glide stresses on the plastic flow of single and polycrystals of molybdenum. Mater. Sci. Eng. A 387–389, 138–142. https://doi.org/10.1016/j.msea.2004.04.066

Voter, A.F., 2007. INTRODUCTION TO THE KINETIC MONTE CARLO METHOD, in: Sickafus, K.E., Kotomin, E.A., Uberuaga, B.P. (Eds.), Radiation Effects in Solids, NATO Science Series. Springer Netherlands, pp. 1–23. https://doi.org/10.1007/978-1-4020-5295-8_1

Wagner, G.J., Liu, W.K., 2003. Coupling of atomistic and continuum simulations using a bridging scale decomposition. J. Comput. Phys. 190, 249–274. https://doi.org/10.1016/S0021-9991(03)00273-0

Wagoner, R.H., 1982. Plastic behavior of 70/30 brass sheet. Metall. Mater. Trans. A 13, 1491–1500.

Weaver, J.S., Khosravani, A., Castillo, A., Kalidindi, S.R., 2016. High throughput exploration of process-property linkages in Al-6061 using instrumented spherical microindentation and microstructurally graded samples. Integrating Mater. Manuf. Innov. 5, 10. https://doi.org/10.1186/s40192-016-0054-3

Weber, G., Anand, L., 1990. Finite deformation constitutive equations and a time integration procedure for isotropic, hyperelastic-viscoplastic solids. Comput. Methods Appl. Mech. Eng. 79, 173–202. https://doi.org/10.1016/0045-7825(90)90131-5

Wheeler, D., Brough, D., Fast, T., Kalidindi, S., Reid, A., 2014. PyMKS: Materials Knowledge System in Python. https://doi.org/10.6084/m9.figshare.1015761.v2

White, D.J., Anandalingam, G., 1993. A penalty function approach for solving bi-level linear programs. J. Glob. Optim. 3, 397–419. https://doi.org/10.1007/BF01096412

Wilkinson, R.D., 2010. Bayesian Calibration of Expensive Multivariate Computer Experiments, in: Biegler, L., Biros, G., Ghattas, O., Heinkenschloss, M., Keyes, D., Mallick, B., Marzouk, Y., Tenorio, L., van Bloemen Waanders, B., Willcox, K. (Eds.), Large-Scale Inverse Problems and Quantification of Uncertainty. John Wiley & Sons, Ltd, pp. 195–215. https://doi.org/10.1002/9780470685853.ch10

Xiong, L., Xu, S., McDowell, D.L., Chen, Y., 2015. Concurrent atomistic–continuum simulations of dislocation–void interactions in fcc crystals. Int. J. Plast. 65, 33–42. https://doi.org/10.1016/j.ijplas.2014.08.002

Yalcinkaya, T., Brekelmans, W. a. M., Geers, M.G.D., 2008. BCC single crystal plasticity modeling and its experimental identification. Model. Simul. Mater. Sci. Eng. 16, 085007. https://doi.org/10.1088/0965-0393/16/8/085007

Yapo, P.O., Gupta, H.V., Sorooshian, S., 1998. Multi-objective global optimization for hydrologic models. J. Hydrol. 204, 83–97. https://doi.org/10.1016/S0022-1694(97)00107-8

Yeniay, Ö., 2005. Penalty Function Methods for Constrained Optimization with Genetic Algorithms. Math. Comput. Appl. 10, 45–56. https://doi.org/10.3390/mca10010045

Yin, X., Chen, W., To, A., McVeigh, C., Liu, W.K., 2008. Statistical volume element method for predicting microstructure–constitutive property relations. Comput. Methods Appl. Mech. Eng., Stochastic Modeling of Multiscale and Multiphysics Problems 197, 3516–3529. https://doi.org/10.1016/j.cma.2008.01.008

Zhan, Z.-L., Tong, J., 2007. A study of cyclic plasticity and viscoplasticity in a new nickel-based superalloy using unified constitutive equations. Part I: Evaluation and determination of material parameters. Mech. Mater. 39, 64–72. https://doi.org/10.1016/j.mechmat.2006.01.005

Zhang, M., Zhang, J., McDowell, D.L., 2007. Microstructure-based crystal plasticity modeling of cyclic deformation of Ti–6Al–4V. Int. J. Plast. 23, 1328–1348. https://doi.org/10.1016/j.ijplas.2006.11.009